Design and characterisation of MgB_2 bulk superconducting magnets containing Y_2O_3 and Mg additions

Guillaume Matthews

The Queen's College

University of Oxford

A thesis submitted for the degree of

Doctor of Philosophy

Michaelmas MMXX

"No great mind has ever existed without a touch of madness."

Aristotle

"Nothing in life is to be feared, it is only to be understood. Now is the time to understand more, so that we may fear less."

Marie Curie

"Your vision will become clear only when you can look into your own heart. Who looks outside, dreams; who looks inside, awakes."

Carl Jung

"Imagination is more important than knowledge. For knowledge is limited to all we now know and understand, while imagination embraces the entire world, and all there ever will be to know and understand."

Albert Einstein

Acknowledgements

After five years in Oxford, it would be an understatement to say that I could not have made it on my own, and I am very grateful to everyone that has contributed to my magical experience as a student at the University of Oxford and The Queen's College.

First of all, I want to express all my gratitude to my supervisors Susie Speller and Chris Grovenor who always supported my ideas, gave me a lot of freedom and provided me with excellent supervision throughout my three years on the MgB_2 project. They have inspired me to be a better researcher, tutor and lecturer, and more than my supervisors I consider them as my mentors.

I would also like to thank Richard Todd and Patrick Grant for their support and interest in my work, and for giving me my first role as a tutor in Oxford. I am very grateful to the Materials Department for the continuous financial support I received during my five years in Oxford, and all the teaching opportunities I was able to take. I would like to thank the EM staff for their support and contribution in my microscopy training. I am grateful to Tony, Pete and Robin for their help in my lab work, even if on some occasions it involved significant risks...

I would like to thank all the Masters and DPhil students in my research group, Tim, Danielle, Laura, Morris, Marco, Stephen, Yatir and Will for their help and all the fun moments we shared and which made my work environment much more enjoyable. I am thankful to Junliang, Sangeeta, Tayebeh and Matt for their contribution to my research. I am very grateful to John Waite for being a great friend and for supporting me when I most needed it.

Last but not least, I am immensely grateful to my family, in particular my mum, sister and brother: Véronique, Victoria and Charles-Emmanuel for always believing in me and supporting me throughout my five years in Oxford. I feel blessed to have them in my life and I could not have made it this far without them. Thank you for helping me follow my dreams and allowing me to go on my Oxford adventure.

Publications

- **G.A.B. Matthews**, P.S. Grant, C.R.M. Grovenor, S. Speller. Large critical current density improvements in composite MgB_2 bulks containing Mg and Y_2O_3 additions manufactured by an innovative liquid phase/reactive sintering route.
  In preparation (2020)

- **G.A.B. Matthews**, T. Mousavi, P.S. Grant, C.R.M. Grovenor, S. Speller. Improving connectivity in MgB_2 bulks by an innovative liquid phase/reactive sintering route.
  In preparation (2020)

- **G.A.B. Matthews**, J. Liu, P.S. Grant, C.R.M. Grovenor, S. Speller. Design and characterisation of ex-situ bulk MgB_2 superconductors containing a nanoscale dispersion of artificial pinning centres. *Superconductor Science and Technology* 33(3), 2020

- **G.A.B. Matthews**, S. Santra, R. Ma, P.S. Grant, C.R.M. Grovenor, S. Speller. Effect of the sintering temperature on the microstructure and superconducting properties of MgB_2 bulks manufactured by the field assisted sintering technique. *Superconductor Science and Technology* 33(5), 2020.

- S. Santra, T. Davies, **G.A.B. Matthews**, J. Liu, C.R.M. Grovenor, S. Speller. The effect of the size of NbTi filaments on interfacial reactions and the properties of InSn-based superconducting solder joints. *Materials & Design* 176, 2019

- D. Moseley, **G.A.B. Matthews**, D. Zhou, V. Cientanni, M. Ainslie, S. Speller, J. Durrell, Improved pulsed field magnetisation in MgB_2 trapped-field magnet. *In preparation* (2020)

- S. Santra, **G.A.B. Matthews**, T. Mousavi, C.R.M. Grovenor, S. Speller, Understanding the role of alloying HCP metals with different (c/a) ratios on superconducting properties of A15 based intermetallics. *In preparation* (2020)

Acronyms and parameters

List of acronyms:

- BPR - ball to powder ratio
- BSE - backscattered electron
- CTE - coefficient of thermal expansion
- DC - direct current
- DSC - differential scanning calorimetry
- EBSD - electron backscatter diffraction
- EDX - energy dispersive X-ray spectroscopy
- FAST - field assisted sintering technology
- FIB - focussed ion beam
- GB - grain boundary
- HAADF - high angle annular dark field
- HTS - high temperature superconductor
- LPS - liquid phase sintering
- LTS - low temperature superconductor
- MRI - magnetic resonance imaging
- ODS - oxide dispersion strengthened
- PID - proportional integral derivative
- PPMS - physical property measurement system
- SEM - scanning electron microscopy
- SPS - spark plasma sintering
- SQUID - superconducting quantum interference device
- STEM - scanning transmission electron microscopy
- TEM - transmission electron microscopy

- TKD - transmission Kikuchi diffraction
- UHP - ultra high pressure
- VSM - vibrating sample magnetometer
- XRD - X-ray diffraction
- ZFC - zero field cooled

List of parameters:

- T - temperature
- $\mu_0 H$ - magnetic field
- B - internal magnetic field
- m - magnetic moment
- M - magnetisation
- χ - magnetic susceptibility
- T_c - superconducting transition temperature
- $T_{c,onset}$ - onset criteria of the superconducting transition temperature
- ΔT_c - width of the superconducting transition
- $\mu_0 H_c$ - critical field
- $\mu_0 H_{c1}$ - lower critical field
- $\mu_0 H_{c2}$ - upper critical field
- B_{irr} - irreversibility field
- J_c - critical current density
- J_{c0} - self-field critical current density
- λ - superconducting penetration depth
- ξ - superconducting coherence length
- κ - Ginzburg-Landau parameter
- Φ_0 - magnetic flux quantum
- v_F - Fermi velocity
- ω_D - Debye frequency
- G - Gibbs free energy
- $d_{0.5}$ - particle median size
- ρ_0 - residual resistivity

Contents

Introduction

In 2001 Nagamatsu *et al.* [1] discovered that MgB_2, a material produced commercially since the 1950s, was a type II superconductor showing promising superconducting properties. MgB_2 has a relatively high critical temperature (T_c) of 39 K and can be processed easily in multiple forms (bulks, wires and tapes) by readily available powder routes. Today MgB_2 has been recognised as a promising material for practical applications and a serious competitor to "older" low temperature superconductors (LTS) such as NbTi.

The aim of this work is to investigate new processing methods and powder treatments (prior to consolidation) in order to manufacture MgB_2 bulk specimens with improved superconducting properties. The initial idea behind this work, imagined by Prof. Susie Speller, was to transpose a successful concept used for improving the mechanical properties of steels and superalloys to superconductors. In the 1970s, Benjamin [2] developed a new concept, known as Oxide Dispersion Strengthening (ODS), to improve the mechanical properties at high temperature of nickel alloys. The process consists in obtaining a fine dispersion of stable oxide (usually Y_2O_3) precipitates in a metallic matrix. The size of these precipitates can be finely tuned during a controlled re-precipitation thermal treatment. In structural alloys, these precipitates effectively pin the dislocations and also the grain boundaries, leading to improved high temperature strength and creep properties. Since the early 1970s the ODS concept has been successfully applied to different superalloys and steels, and commercial ODS materials were produced by several companies [2–8].

The main goal of this work is to investigate if the ODS concept can be successfully applied to MgB_2 bulk superconductors. In this case, the nano precipitates need to act as effective pinning centres for magnetic flux vortices to improve the superconducting properties, in contrast with conventional ODS materials in which they pin dislocations.

The first chapter starts with an introduction on superconductivity, followed by a brief review of MgB_2. Almost all the samples manufactured and analysed in this work were produced by the Field Assisted Sintering Technique (FAST), so the concept of sintering is first introduced, followed by a description of the FAST process. Finally, articles studying the manufacture of MgB_2 bulks by FAST are summarised and discussed, before introducing relevant papers on the main types of MgB_2 modifications: carbon doping, oxide and metallic additions and ball milling.
The second chapter details all the processing equipment and manufacturing routes used to produce the specimens studied in this work. It also introduces the different characterisation techniques and data analysis procedures performed to extract material parameters. The precision and reliability of some of these characterisation techniques and analyses are also discussed here, and for conciseness will not be repeated in the results and discussion chapters.
The three results and discussion chapters are presented in order of increasing complexity to gradually build up comprehension of the interplay between processing parameters, microstructure and superconducting properties.
Chapter 3 is dedicated to the characterisation of MgB_2 bulks made from unmodified powder and sintered by FAST at temperatures ranging from 900 to 1200 °C.
Chapter 4 first introduces the ODS process developed in this work and the analyses performed on ODS powders, then discusses the consolidation of these powders and the characterisation of ODS MgB_2 bulks.
Chapter 5 explores an idea I had to improve the properties of MgB_2 bulks sintered at low temperature. In an attempt to improve densification at low processing temperatures, I developed a liquid phase/reactive sintering process. This process is first described, followed by the characterisation of Mg-MgB_2 bulks made from MgB_2 powders containing Mg additions. Chapter 5 ends on the concept of Mg-Y_2O_3-MgB_2 composite bulks and investigates if these two additions can work in synergy to produce high-performance composite superconductors.

Chapter 1

Literature review

1.1 Superconductivity

At the beginning of the 20th century, the research group of Heike Kamerlingh Onnes was leading the race towards ultra low temperatures and during the summer of 1908 Onnes achieved the liquefaction of He. He was then able to conduct experiments at temperatures as low as 1 K and decided to tackle one of the great questions unanswered at that time in the physics community: what was the behaviour of the electrical resistivity in metals when the temperature approaches the absolute zero. Two years later, while performing an experiment on mercury, they found that the electrical resistivity of mercury dropped suddenly to zero below 4.2 K. On the 28th April 1911, these results were communicated to the Royal Academy of the Netherlands and superconductivity had just been discovered [9].

1.1.1 Superconducting phenomena and critical parameters

There are several phenomena observed with the superconducting state. The first one, discovered by H.K. Onnes, is that below a critical temperature (T_c) superconductors do not show any DC electrical resistivity and act as perfect conductors of electricity.

Meissner [10] observed that when a superconductor was subjected to an external magnetic field, the field was expelled from the superconductor and the magnetic field inside the superconductor vanished i.e. $B = 0$. This effect is shown in Figure 1.1 and is known as the Meissner effect. In the Meissner state, superconductors act as perfect diamagnetic materials and have a magnetic susceptibility $\chi = -1$.

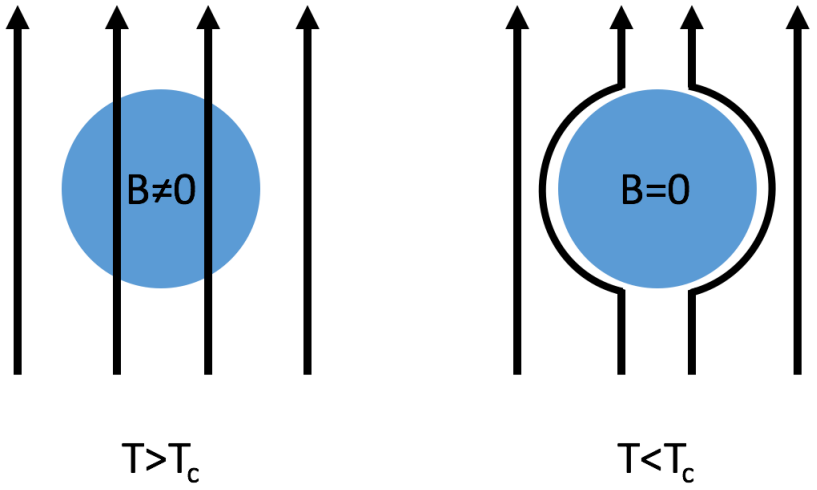

Figure 1.1: Schematic of the Meissner effect.

London [11] described the Meissner effect in a formal way and showed that if the magnetic field vanished at the core of the superconductor, it could still penetrate a distance of the order of λ at the surface. This distance is known as the London penetration depth, and was the first characteristic length associated with the superconducting state.

Later, Pippard generalised London's equations and introduced a second characteristic length, the coherence length ξ, that defines the characteristic distance over which the number of superconducting electrons varies. These two characteristic lengths are represented in the schematic of a normal-superconducting interface shown in Figure 1.2.

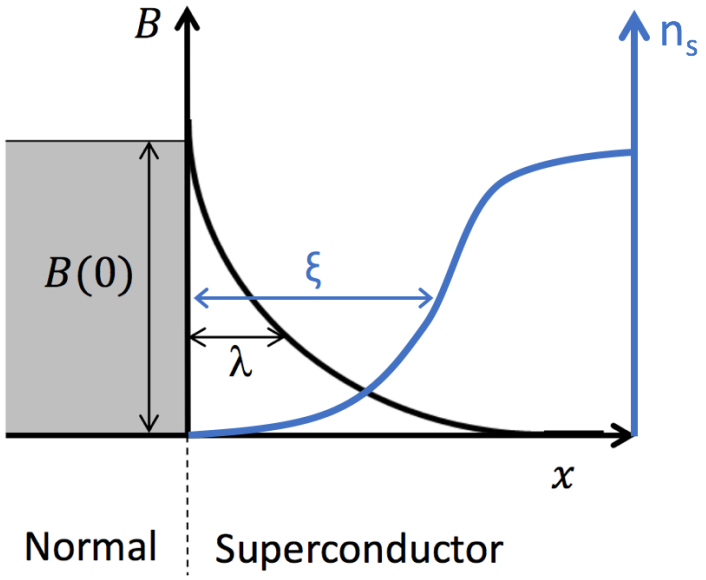

Figure 1.2: Schematic of the evolution of B and the number of superconducting electrons (n_s) at a normal-superconducting interface. Redrawn from [12].

It was also observed that superconductivity was lost above a critical field H_c and a critical current density J_c. These three parameters are not independent and form a critical surface in the temperature - magnetic field - current density space which defines the superconducting phase of a superconductor. A schematic of this critical surface is shown in Figure 1.3. Inside the critical surface, the material is in the superconducting state whereas outside the material is in the normal state.

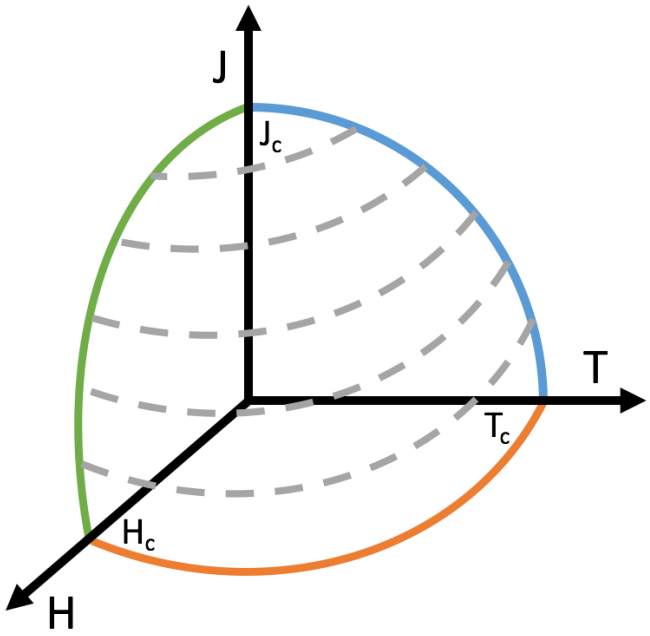

Figure 1.3: Schematic of the critical surface delimiting the phase boundary between the normal and superconducting states.

1.1.2 Superconductors

Although some superconductors only exhibit the normal and superconducting state, most of the superconductors used in real applications also show a third "mixed" state in which some magnetic flux can penetrate the material in the form of magnetic flux vortices. Superconductors are classified into two categories; type I or type II, based on whether or not they can exist in this mixed state.

The Ginzburg-Landau [13] theory is a phenomenological model that describes the superconducting transition from a thermodynamic point of view. In this model, the normal and superconducting states are two distinct thermodynamic states and the superconducting transition is a second order phase transition. The Ginzburg-Landau parameter $\kappa = \frac{\lambda}{\xi}$ indicates if a superconductor is

of type I ($\kappa < \frac{1}{\sqrt{2}}$) or II ($\kappa > \frac{1}{\sqrt{2}}$). This comes from thermodynamic considerations behind the creation of normal cores inside the superconductor that allow some magnetic flux to penetrate the material. If the creation of these normal cores is energetically favourable, the superconductor can show a mixed state and is thus of type II; otherwise it is of type I [12, 14].

Type I superconductors

Many pure elements such as Hg, Pb and Sn are type I superconductors. These superconductors have relatively low $T_c < 10$ K and very small H_c values ($\mu_0 H_c < 0.1$ T) which prevent their use in most real applications. They show a simple magnetisation behaviour with increasing magnetic field, as shown in Figure 1.4. Below H_c, the material is in the superconducting state and acts as a perfect diamagnet i.e. its magnetisation $M = -H$. Above H_c, the material abruptly turns into the normal state and superconductivity is lost. In type I superconductors, the critical current density J_c can be calculated from H_c by simply considering the geometry of the superconductor. Superconductivity is destroyed when the current flowing through the superconductor produces a magnetic field[1] equal to H_c at its surface. This is known as the Silsbee effect. For instance, in the absence of an external magnetic field $J_c = \frac{2H_c}{R}$ in the case of a wire of radius R. This simply comes from Ampere's law applied to the outer surface of the superconducting wire [12, 14].

Type II superconductors

Almost all type II superconductors are alloys, intermetallics or complex ceramics such as NbTi, MgB_2 and $YBa_2Cu_3O_{7-\delta}$ (YBCO). In contrast with type I materials, some type II superconductors such as the cuprates[2] can still show superconductivity at very large magnetic fields as high as 100 T [14]. However, they show a different behaviour when subjected to an external magnetic field, as shown in Figure 1.5. Below a lower critical field (H_{c1}), type II superconductors are similar to type I materials and also behave like perfect diamagnets i.e. $M = -H$ and $B = 0$. However, above H_{c1}, superconductivity is not lost suddenly as in type I superconductors. Instead, type II superconductors enter a mixed state where part of the material remains superconducting and normal cores are formed within the superconducting "matrix", as shown in Figure 1.5. Magnetic

[1] In case an external magnetic field is also applied H is the sum of the externally applied field and the field produced by the current.

[2] Cuprate superconductors are high temperature superconductors that have a specific crystal structure made of alternating layers of CuO_2 and oxides of other metals acting as charge reservoirs. A few examples are: $YBa_2Cu_3O_{7-\delta}$, $Bi_2Sr_2CaCu_2O_{8+\delta}$, $HgBa_2CaCu_2O_{6+\delta}$.

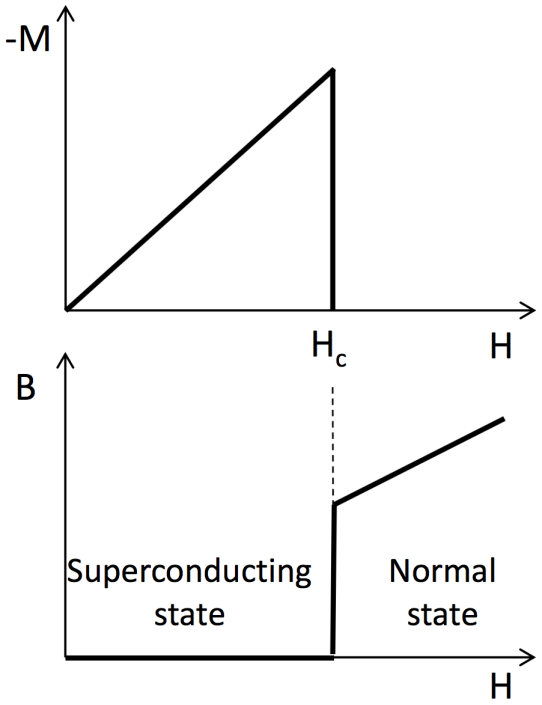

Figure 1.4: Typical magnetisation (M) and magnetic field inside the superconductor (B) evolution with an applied magnetic field (H) for type I superconductors [12].

flux can thus penetrate the superconductor through these normal cores in the form of quantised flux lines, each carrying a magnetic flux $\Phi_0 = \frac{h}{2e}$, where h is the Planck constant and e is the electronic charge. The number of these normal cores gradually increases with H until an upper critical field H_{c2} is reached, above which superconductivity is lost and the whole material becomes normal. Between H_{c1} and H_{c2} the magnetic field inside the superconductor is not zero and the magnetic susceptibility χ gradually increases from -1 to 0.

These flux lines are also known as flux vortices due to the permanent circular currents that are induced at the interface between the normal core and the superconducting matrix, as shown in Figure 1.6. These currents circulate in the opposite direction to the screening currents at the edge of the specimen, and they are induced in a cylinder of radius λ around the centre of the normal core. At the centre of the normal core, the local magnetic field B is a maximum and it decreases exponentially over a distance λ in the superconducting matrix. The number density of superconducting electrons (also known as the order parameter) quickly falls from its bulk value in the surrounding superconducting matrix to zero in the normal core over a distance ξ, as shown in Figure 1.6. The diameter of the normal core is thus approximately 2ξ [12, 14].

A complete derivation of the Ginzburg-Landau equations is outside the scope of this review,

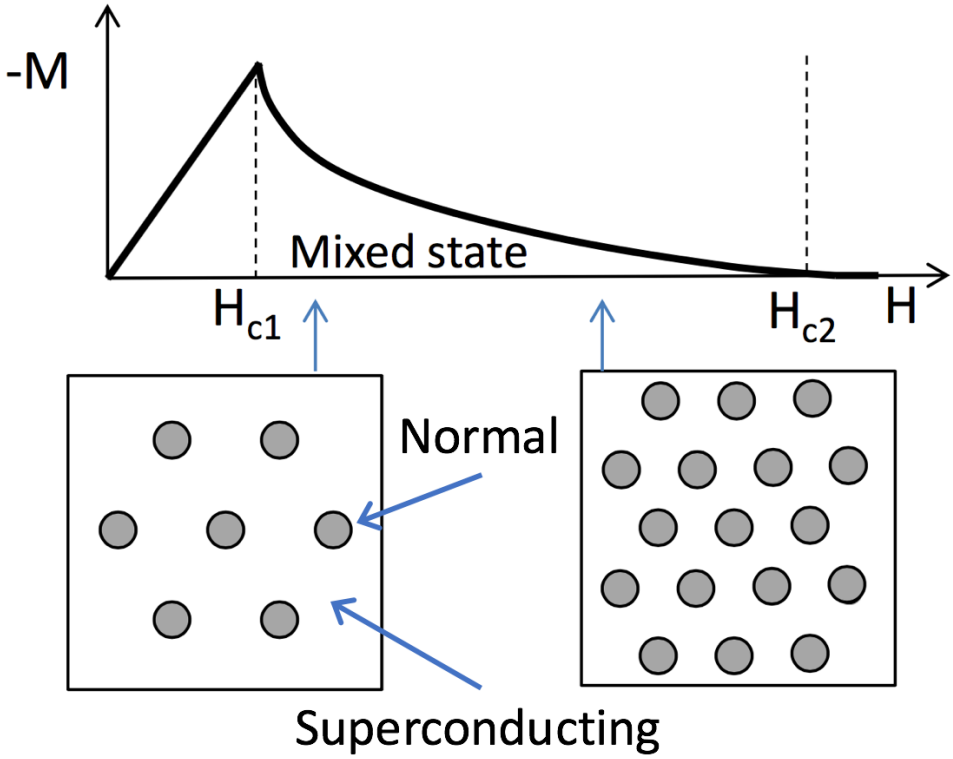

Figure 1.5: Typical magnetisation (M) evolution with an applied magnetic field (H) for type II superconductors. Note that $H_{c1} \ll H_{c2}$. Redrawn from [12].

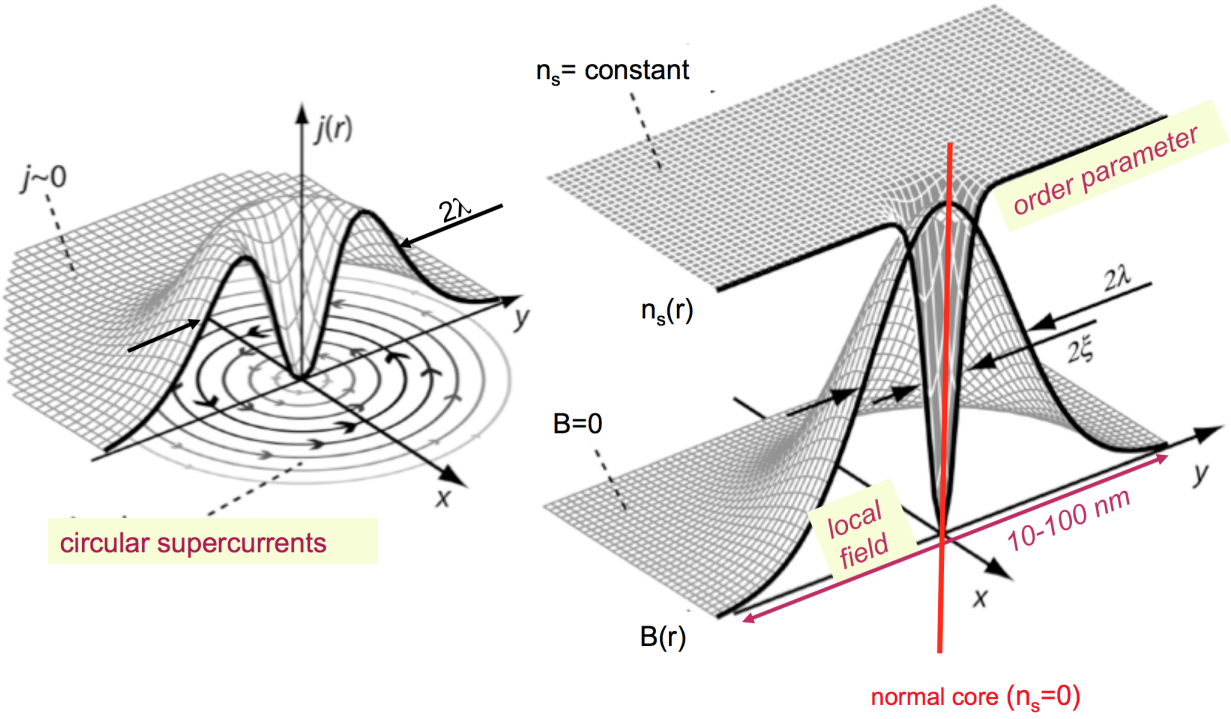

Figure 1.6: Schematic of a flux vortex in a type II superconductor [14].

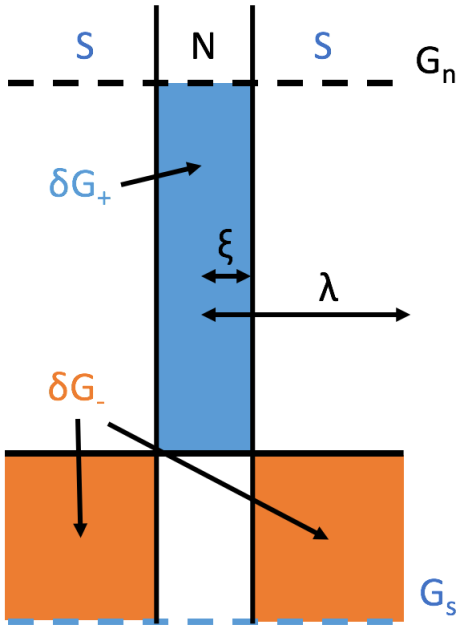

Figure 1.7: Simplified diagram illustrating the thermodynamics of the creation of a flux vortex in a type II superconductor for $H > H_{c1}$.

but it is important to understand the basic thermodynamics aspects behind the creation of flux vortices. As with any transformation, thermodynamics tell us that a system transforms spontaneously if this causes a reduction in the system's free Gibbs energy G. Let us imagine the formation of a normal core of radius ξ in a superconducting matrix, as shown in Figure 1.6. This transformation is associated with two energetic contributions: δG_+, that leads to an increase in G and thus opposes the vortex formation and δG_- which reduces G and favours the vortex. This is represented graphically by the schematic shown in Figure 1.7. δG_+ comes from the loss in condensation energy due to the formation of the normal core of radius ξ, and is thus proportional to ξ^2. δG_- is due to the magnetic flux that can penetrate a cylinder of radius[3] λ around the normal core and is proportional to λ^2. The vortex can thus form if the beneficial contribution δG_- is larger than the detrimental contribution δG_+. Naturally, it follows that if $\lambda > \xi$, the formation of this vortex is more likely to be energetically favourable. A more exact calculation leads to the condition introduced above: $\kappa = \dfrac{\lambda}{\xi} > \dfrac{1}{\sqrt{2}}$ or equally $\lambda > \dfrac{\xi}{\sqrt{2}}$, which is consistent with the conclusion reached intuitively.

Whereas in type I superconductors J_c is intrinsically related to H_c (Silsbee effect), in type II superconductors J_c depends strongly on the microstructure of the material and can vary by

[3]Expelling the magnetic field requires magnetostatic energy. Consequently, allowing magnetic field to penetrate the superconductor reduces the magnetostatic energy of the system

orders of magnitude for the same superconductor.

When a transport current flows across a type II superconductor in the mixed state, a Lorentz force $\mathbf{F_L} = \mathbf{B} \times \mathbf{J}$ (per unit volume) is induced on the flux lines going through the superconductor. In a perfect type II superconductor, there is nothing to counteract this Lorentz force and thus the flux lines are free to move. Since each vortex carries a magnetic flux Φ_0, N vortices per unit area moving at a velocity $\mathbf{v}$ will induce an electric field $\mathbf{E} = N\mathbf{v} \times \mathbf{\Phi_0}$. Consequently, flux lines motion produces an electric field and the superconductor becomes resistive and dissipates energy.

The critical current density is defined as the maximum current that can flow in a superconductor without generating any resistance. Therefore, in type II superconductors J_c is the maximum current that can flow without causing the movement of these flux vortices.

Since some type II superconductors such as NbTi and MgB_2 can reach colossal J_c values above 10^9 A/m^2, it means that there must be some force counteracting the Lorentz force and preventing the vortices from moving. This concept, known as flux pinning, is crucial for technological superconductors and describes how the vortices can be pinned by defects in superconducting materials. Superconductors are thus engineered to contain specific defects, known as pinning sites, which stop the movement of the vortices in order to allow transport currents to flow without dissipating any energy. Stronger pinning leads to higher J_c values and is thus central to the improvement in properties of technological superconductors. The next section, will explore further this important concept of flux pinning.

1.1.3 Flux pinning

The concept of pinning is crucial for many engineering materials. High strength steels, superalloys, hard ferromagnets and superconductors all contain defects that interact with specific features such as dislocations, grain boundaries, magnetic domain walls and flux vortices.

In the case of superconductors, these pinning sites (or centres) prevent the movement of flux vortices by acting as potential energy wells. As explained above and shown in Figure 1.7, the creation of a vortex is associated with two energy contributions: a favourable one due to the flux that can penetrate locally the superconductor and a detrimental one due to the loss of condensation energy in the normal core. If a vortex coincides with an interface or a normal particle

such as a small precipitate, this condensation energy loss is decreased[4] and thus the detrimental contribution is lower which makes the vortex more stable. Pinning is thus provided by defects that effectively lower the energy of vortices [12, 14]. In order to move vortices away from their pinning centres, energy must be introduced in the system (a certain force is required). The maximum force that can be exerted on a vortex before it becomes unpinned is known as the pinning force. The pinning force can be estimated from $J_c - B$ data since at J_c, the Lorentz force exerted on the vortices is balanced by the pinning force [15].

Based on the Bean critical state model [16], Dew-Hughes modelled different pinning mechanisms that occur in type II superconductors [15]. These pinning mechanisms can be represented by different functions $F_p(B)$ that each have a characteristic shape. These pinning force curves can be normalised and plotted in function of the reduced field $b = \dfrac{B}{B_{c2}}$, which allows the theoretical pinning force curves to be compared with experimental curves and identify which pinning mechanisms are dominant.

In the majority of commercial superconducting materials there are two types of pinning centres that are referred as "$\Delta\kappa$ pinning" and "normal pinning" [15]. The first type arise from small local changes in κ (Ginzburg-Landau parameter) which can be caused by fluctuations in composition or non uniform distributions of dislocations. The second type originates from the presence of small non superconducting particles that can be a normal metal, an insulator or void. These two types of pinning centres can be further classified into three categories depending on their relative dimensions with respect to the flux line spacing[5], d, in the superconductor. Point pins are features for which all three dimensions are smaller than d. When features such as grain boundaries, sub grains and stacking faults have two dimensions larger than d they act as surface pins. Larger features such as large precipitates that have all three dimensions greater than d are volume pins. The most common pinning centre types and their associated theoretical pinning force curve are summarised in Table 1.1 and shown graphically in Figure 1.8.

[4] This decrease can come from either a reduction of the volume of superconductor that needs to transform into the normal state at the core or a local decrease in the condensation energy at a defect

[5] The flux line spacing is given by the following expression: $d = 1.07\left(\dfrac{\phi_0}{B}\right)^{1/2}$ [15]

Geometry of pin	Type of centre	Pinning function F_p(b)	Peak position*
Point	Normal	$b(1-b)^2$	0.33
	Δk	$b^2(1-b)$	0.67
Surface	Normal	$b^{1/2}(1-b)^2$	0.2
	Δk	$b^{3/2}(1-b)$	0.6
Volume	Normal	$(1-b)^2$	-
	Δk	$b(1-b)$	0.5

Table 1.1: Different types of pinning centres in type II superconductors [15].* In terms of reduced field $b = \dfrac{B}{B_{c2}}$.

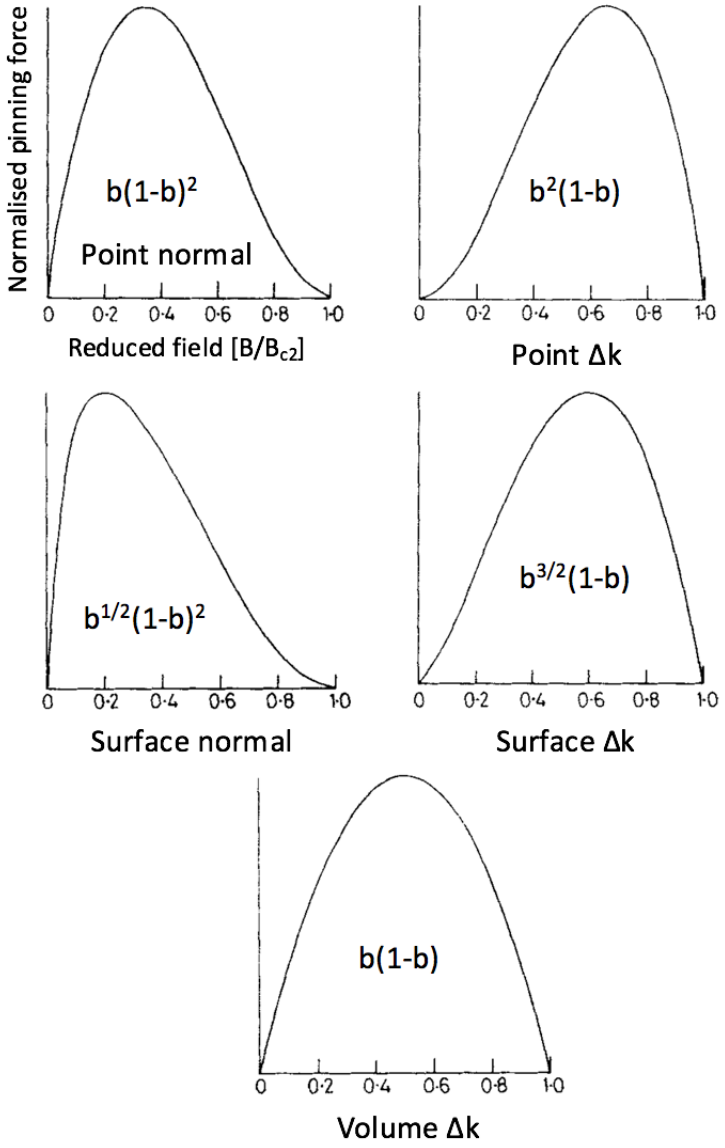

Figure 1.8: Theoretical pinning functions for different pinning mechanisms predicted by Dew-Hughes [15].

1.1.4 Theories of superconductivity

The first phenomenological theory of superconductivity was only published by Ginzburg and Landau [13] in 1950, almost 40 years after the discovery of superconductivity. The Ginzburg-Landau model describes the superconducting phase transition from a thermodynamic point of view. In this model the superconducting and normal states are two distinct thermodynamic phases and the transition is second order as indicated by the singularity observed in the specific heat at T_c. The set of equations proposed by Ginzburg and Landau to describe the behaviour of the order parameter of the transition led to useful predictions such as the classification of type I and type II superconductors based on the two characteristic lengths in superconductivity: the penetration depth λ and the coherence length ξ. The Ginzburg-Landau theory also provided an explanation for the Meissner effect.

Despite the progress made to understand superconductivity following the Ginzburg-Landau theory, at the beginning of the 1950s the microscopic origin of superconductivity still remained mysterious. The first microscopic theory of superconductivity was published a few years later in 1957 with Bardeen, Cooper and Schrieffer and is known as the "BCS" theory [17]. The BCS theory was formulated after the discovery of two fundamental results: the role of the phonons (lattice vibrations) in superconductivity and the concept of Cooper pairs. In 1950, Fröhlich [18] postulated that two electrons of opposite velocities and spins could be subjected to an attractive interaction mediated by phonons. This effect, also called phonon drag, is represented by the model shown schematically in Figure 1.9. As the first electron (blue) travels from right to left, the lattice is deformed due to the attraction between the electron and the protons on the lattice. Compared with the high velocity of the electron (Fermi velocity $v_F \sim 10^8$ cm/s) the lattice oscillation (i.e. phonon) follows very slowly and the maximum lattice deformation occurs at a distance[6] of ~ 1000 Å (in the case of Al) behind the first (blue) electron which corresponds to the "size of a Cooper pair". The second (green) electron travelling in the opposite direction thus experiences an attractive force due to the lattice deformation that was induced by the first blue electron that has now travelled a distance of ~ 1000 Å. This relatively large distance (on the atomic level) also explains why the Coulomb repulsion between these two electrons is insignificant. Cooper pairs can thus form due to the attractive force existing between two electrons

[6] This can be estimated for metallic superconductors (e.g. Al) by considering that the first electron travelling at the Fermi speed v_F generates a phonon which has a typical frequency ω_D (Debye frequency). The maximum deformation of the lattice occurs after the electron has travelled a distance $d = v_F \frac{2\pi}{\omega_D} \sim 1000$ Å [14].

of opposite velocities and spins that are effectively "exchanging" phonons [14]. The concept of Cooper pairs was introduced in 1956 [19] showing that two electrons of opposite wave-vector and spin on the Fermi surface can form a bound pair whose energy is lower than the sum of the kinetic energy of the individual electrons.

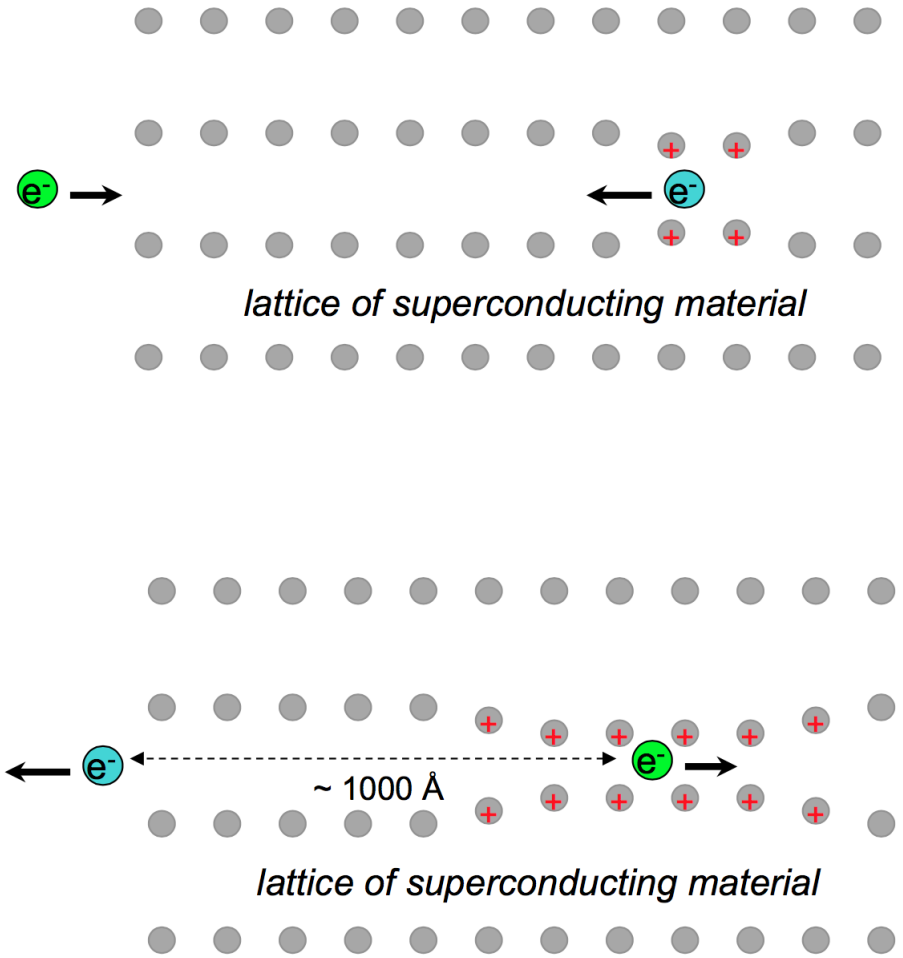

Figure 1.9: Schematic of the phonon drag [14].

Based on these results Bardeen, Cooper and Schrieffer developed the BCS theory one year later (1957) and managed to explain most of the experimental results observed: the Meissner effect, the critical field, the critical current density, the nature of the coherence length etc. They showed that due to their momentum and spin that are both equal to 0, Cooper pairs did not follow Fermi statistics and behaved more like bosons and could condense into the same energy level. They also showed the existence of a small energy gap 2Δ (a few meV) at the Fermi level between the normal and superconducting states. This theory also explained why superconductors show zero resistance. When individual electrons travel through the lattice, they can be easily scattered by

impurities or lattice vibrations and this result in a macroscopic resistive behaviour. However, when Cooper pairs condense they form a coherent macroscopic ground state. This means that Cooper pairs cannot be scattered individually like single conduction electrons but need to be scattered all at once. The probability of scattering all the Cooper pairs condensate at the same time is simply zero and thus the superconductor does not show any resistance [14].

1.1.5 Superconducting magnets

The very high current that engineering superconductors such as NbTi, MgB_2 and YBCO can carry without any dissipation makes them ideal materials to build bulk superconducting magnets or electromagnets that generate large magnetic fields. Whereas permanent ferromagnets such as Nd-Fe-B are intrinsically limited to 1.6 T, bulk superconducting magnets can produce magnetic fields that are one order of magnitude larger (e.g. 17.6 T at 26 K for an YBCO bulk) [20, 21]. Although conventional electromagnets made from copper or aluminium can be water cooled and achieve large magnetic fields in the 10 T range, these require a very large power to operate which makes them very costly and inefficient. On the other hand, superconducting electromagnets do not dissipate any energy in the coil itself but require cooling to very low temperatures. They are also much more compact than conventional electromagnets. Overall the energy required to operate large superconducting electromagnets is much lower than their Cu or Al equivalent. As an example, the conventional electromagnet used in the ALICE experiment at CERN uses 4.2 MW of power whereas its superconducting equivalent in the CMS experiment at CERN only uses 0.5 MW [14].

The main difference between ferromagnets, bulk superconducting magnets and electromagnets is shown in Figure 1.10. In ferromagnets, the magnetic field comes from the coupling of the spin magnetic moment of unpaired electrons that all align in the same direction within a macroscopic region called a magnetic domain. Upon application of an external magnetic field, all these domains can align and the remanent magnetisation can attain up to 1.6 T in hard ferromagnets such as Nd-Fe-B. In ferromagnets the magnetic field is spatially uniform as shown in Figure 1.10. The main advantage of bulk superconducting magnets is that they are not bound by this ferromagnetic limit and also that the total magnetic field trapped by the superconducting magnet scales up with its size, unlike ferromagnets. The magnetic field originates from permanent cur-

rents induced in the magnet and its magnitude depends on the $J_c - B$ characteristics of the superconductor, the temperature, the connectivity of the bulk and its shape and size. Bulk superconducting magnets offer the advantage of showing high magnetic field values in very compact samples (e.g. YBCO bulk traps 17.6 T in 25 mm sample [20]), and also do not need to be connected to an external power supply like electromagnets.

Electromagnets, whether made of Cu/Al or superconductors, are wires wound into solenoids and produce large magnetic fields due to the large currents induced in the wires by an external power supply. Superconducting electromagnets can generate huge magnetic fields > 30 T, although they are less compact than bulk superconducting magnets and require a power supply[7] [21].

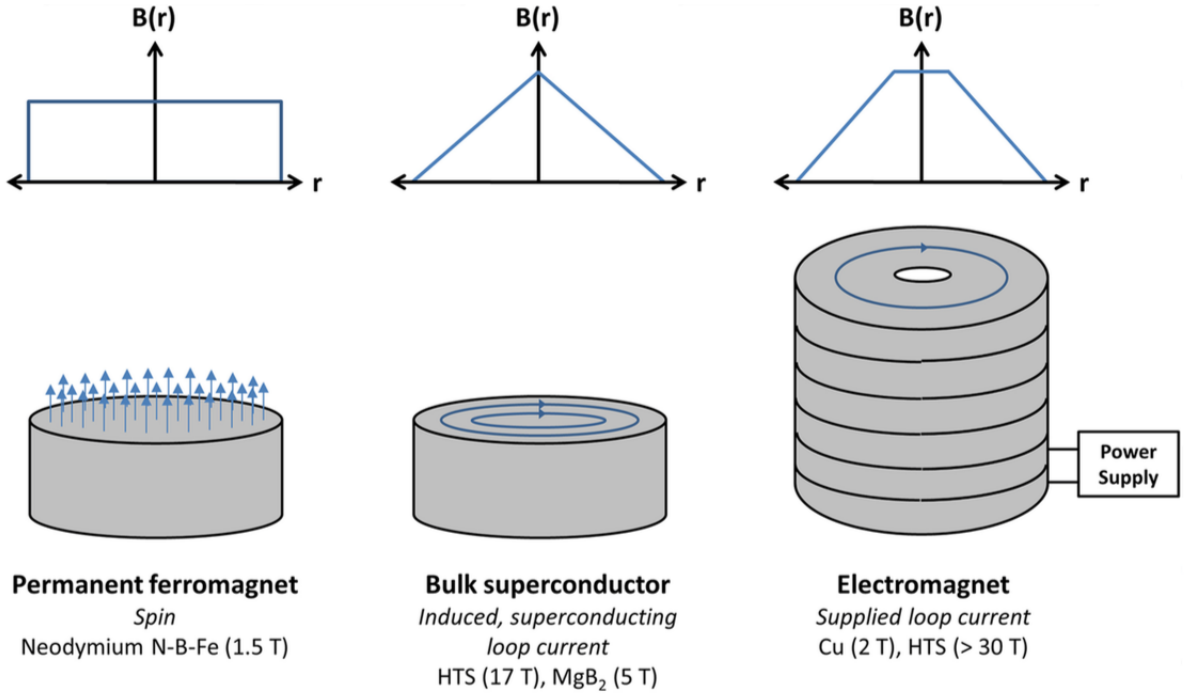

Figure 1.10: Magnetic field distribution in ferromagnets, bulk superconducting magnets and electromagnets [21].

[7] Note that persistent mode superconducting electromagnets do not require any power in operation but do need a power supply when the magnetic field is first initiated.

1.1.6 Applications

Superconducting magnets can generate high magnetic fields from 1.5 T up to 30 T for a broad range of applications:

- **Magnetic Resonance Imaging (MRI) machines** are one of the most powerful tools in medical imaging and allow quick acquisition of highly detailed images of the organs and tissues inside the body. It's a non invasive technique and unlike CT scans or radiography it does not use any harmful ionising radiation. In fact, magnets for MRI machines represent the largest fraction of the global commercial use of superconductors (60% of the global production of superconducting wires [22]). A typical MRI machine is shown in Figure 1.11.

Figure 1.11: Typical example of an MRI machine.

- **High energy particle accelerators** make extensive use of superconducting magnets to accelerate and shape beams of highly energetic particles. A good example is the Large Hadron Collider (LHC) at CERN which is the largest particle accelerator in the world and is composed of no less than 8000 superconducting magnets. The LHC is mainly used to conduct particle physics experiments and led to the discovery of the Higgs boson in 2012.

- **Nuclear fusion reactors** such as the experimental ITER reactor are built around a set of superconducting coils that magnetically confine, shape and control the plasma that can soar to temperatures up to 300 millions °C (this magnetic "container" is called a tokamak). The ITER reactor contains some of the largest superconducting solenoids ever built, as shown in Figure 1.12.

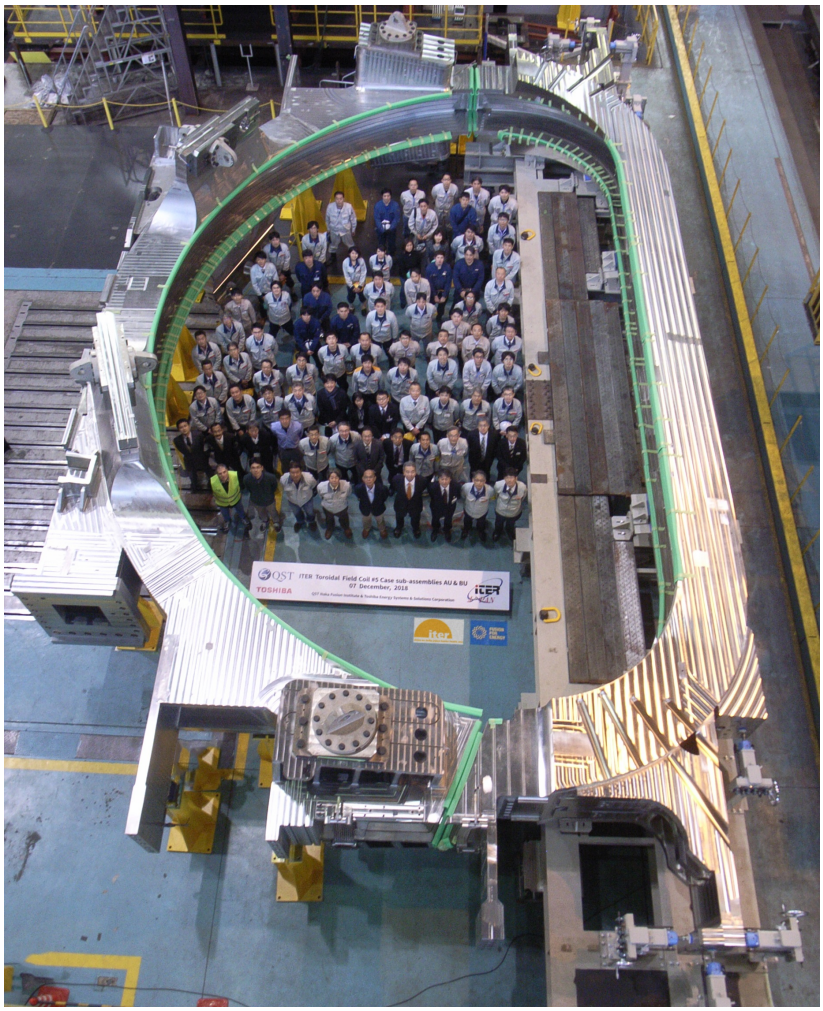

Figure 1.12: Superconducting solenoid used in the ITER reactor to confine the plasma.

- **Maglev (magnetically levitating) trains** use superconducting magnets to levitate a few cm above the tracks, virtually eliminating any friction between the train and the tracks (only the friction between the air and the train remains). Maglev trains not only provide much quieter and smoother journeys but also travel significantly faster than conventional trains, with a speed record of 600 km/h established in Japan.

Superconductors are also used in high power applications where the absence of resistance is a major advantage compared with metallic conductors. Due to their high critical current density, superconductors can transport large currents in very compact cables and thus increase the power transported in dense urban areas and also reduce the visual impact and electromagnetic pollutions of overhead lines. Figure 1.13 shows the huge size difference between copper cables and a superconducting line both rated for 12500 A. In addition, superconducting cables reduce the energy transport loss.

Superconductors are also used in a variety of specialised detectors and high frequency electronics [12, 14]. Superconducting Quantum Interference Device (SQUID) magnetometers are based on the Josephson effect[8] [23] and can detect incredibly subtle magnetic fields that are over a billion times weaker than the earth's magnetic field. In fact, SQUID magnetometers are so sensitive that they are used in magnetoencephalography to map the local electrical activity in the brain by detecting the associated magnetic fields emanating from the brain [14].

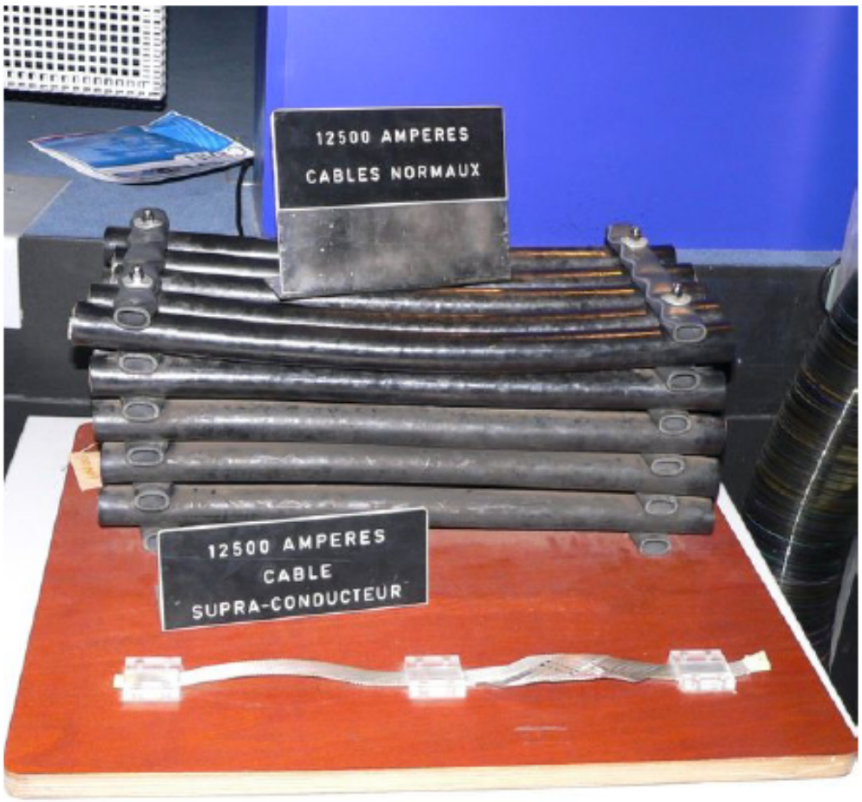

Figure 1.13: Comparison between copper cables and a superconducting line both rated for 12500 A [14].

[8] Josephson discovered that Cooper pairs could tunnel through a normal or insulating barrier having a width similar to the coherence length ξ [23].

1.2 MgB_2

1.2.1 Introduction and general properties

MgB_2 has been known since the 1950s but its popularity suddenly increased in 2001 when Nagamatsu *et al.* [1] discovered its superconducting properties. It has been recognised as a promising material for practical applications owing to its relatively high critical temperature (T_c) and the fact that MgB_2 can be processed easily by readily available powder routes. MgB_2 has a T_c of 39 K, which is the highest of any binary compound and makes it more suitable for helium-free applications than conventional low temperature superconductors (LTS) such as NbTi and Nb_3Sn. Unlike the cuprate high temperature superconductors, grain boundaries in MgB_2 act as pinning sites not weak links because the coherence length[9] in MgB_2 is $\sim 4-10$ nm [24], and thus show good current carrying ability in polycrystalline samples. This also enables MgB_2 samples to be processed by standard ceramic processing methods which are scalable to mass production [24].

MgB_2 has an hexagonal AlB_2 (space group P6/mmm) type crystal structure, as shown in Figure 1.14. Its structure is made of graphite type boron planes separated by hexagonal closed packed layers of magnesium. The magnesium atoms are located at the centre of the hexagons formed by the boron atoms.

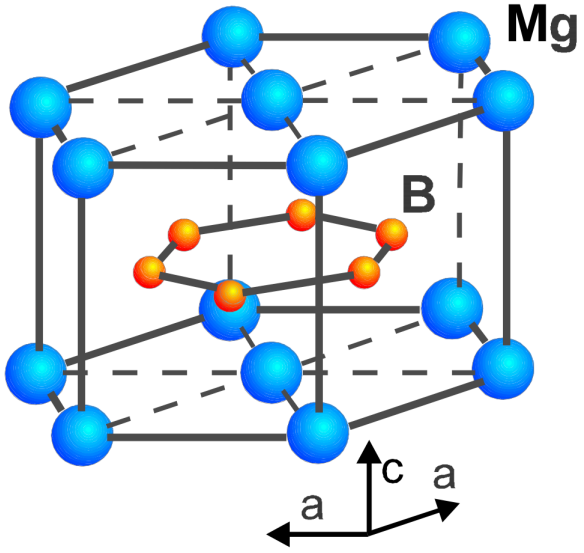

Figure 1.14: MgB_2 crystal strucure, space group P6/mmm [24].

[9]Estimated from B_{c2} measurements in polycrystalline bulk specimens.

MgB_2 is a relatively brittle intermetallic with a density of 2.63 g/cm^3 and exhibits high hardness values (1700-2800 HV) when fully dense [24,25]. The phase diagrams calculated by Liu *et al.* [26] for the Mg-B system at 1 atm and 1 Torr (0.0013 atm) are presented in Figure 1.15. In addition to the solid, liquid and gas magnesium phases and the solid boron phase, three intermediate compounds exist in the Mg-B system, MgB_2, MgB_4 and MgB_7. At ambient pressure MgB_2 coexists with the solid, liquid or gas Mg phase at various temperatures for Mg-rich compositions. Above 1545 °C MgB_2 decomposes into MgB_4 and magnesium vapour. When the pressure is reduced to 1 Torr, the phase diagram changes drastically. At 1 Torr, the pressure is lower than the triple-point of Mg (650 °C, 2.93 Torr) and the liquid phase of Mg disappears. The decomposition temperature of MgB_2 into MgB_4 and $Mg_{(g)}$ also decreases to 912 °C [26].
Another study by Balducci *et al.* [27] showed that an additional phase, MgB_{20} also exists for boron rich compositions.
Guo *et al.* [28] found experimentally that MgB_2 starts decomposing into MgB_4 at 932 °C by a combination of XRD and thermogravimetry analysis performed in Ar at 1 atm. This value is much lower than the theoretical decomposition temperature calculated by Liu [26] but is in better agreement with several experimental studies on MgB_2 [29–32].

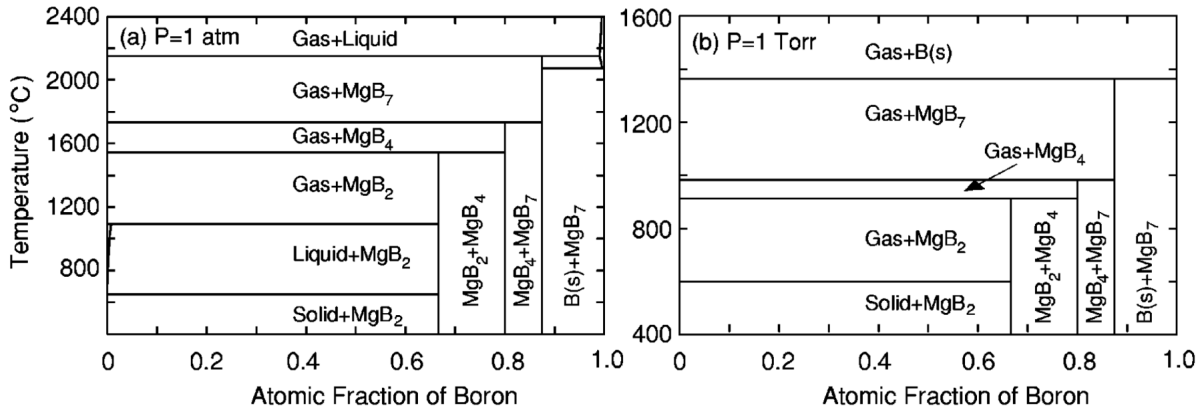

Figure 1.15: Phase diagrams of the Mg-B system under 1 atm and 1 Torr [26].

Unmodified MgB_2 has a T_c of 39 K but samples made from modified powders can exhibit much lower values (5-30 K) for carbon doped [33] or ball milled powders [34]. In contrast, modified MgB_2 often leads to larger J_c and B_{c2} values due to higher defect concentrations. J_c values depend strongly on the type of sample (wire, tape, bulk or thin film), the method of processing and the characteristics of the initial powder or precursors. The best MgB_2 samples usually show J_{c0}(4.2 K) values between 10^9 and 10^{10} A/m^2 [35–37]. In MgB_2 bulks, B_{c2} values can reach up to

17 T at 4.2 K. In polycrystalline samples the coherence length[10] $\xi \sim 4 - 10$ nm at temperatures between 4.2 and 20 K, and the penetration depth λ ranges from 85 to 200 nm [24].

1.2.2 Manufacturing MgB_2

MgB_2 has been successfully manufactured in different forms: powder, single crystal, wire, tape, bulk and thin film. Single crystals can be obtained by high pressure techniques or solid-liquid reaction methods from Mg-rich precursors [33]. The powder-in-tube method (PIT) is a reliable route to produce high quality wires and tapes [38]. Bulks have been manufactured using multiple techniques: conventional sintering, hot pressing, field assisted sintering, infiltration-growth and high pressure methods [25, 29, 39, 40]. MgB_2 films can be made by typical thin film manufacturing routes such as pulsed laser deposition (PLD), magnetron sputtering and chemical vapour deposition (CVD) [24].

A technique is referred to as in-situ or ex-situ depending on the precursor materials used to manufacture MgB_2. The in-situ method starts with elemental Mg and B, and MgB_2 is formed during a solid, liquid or gas phase reaction between these two elemental precursors. This method has led to samples having high J_c values but often showing very porous microstructures [35,38,41]. The ex-situ processing route, in which pre-synthesised MgB_2 powder is consolidated at high temperature, usually with the assistance of pressure, can produce samples with significantly higher density than in-situ methods. This is because the formation of MgB_2 from Mg and B precursor powders is accompanied by a large increase in theoretical density from 2.10 g/cm^3 for the powder mixture to 2.63 g/cm^3 for the MgB_2 phase, leading to a maximum relative density of 80%, assuming full densification during the in-situ process [39]. In contrast, ex-situ MgB_2 samples with a relative density above 95% have been produced by several research groups using the field assisted sintering technique (FAST), also called spark plasma sintering (SPS), or ultra-high pressure methods [25, 31, 39, 42–44].

[10] Estimated from B_{c2} values for polycrystalline samples by using the Ginzburg-Landau model: $B_{c2} = \frac{\phi_0}{2\pi\xi^2}$ [24].

1.3 Sintering

1.3.1 Thermodynamics of sintering

Sintering is a solid state process during which powder particles in contact with each other form physical links (called necks) between each other, and porosity is gradually reduced. The two schematics in Figure 1.16 depict the microscopic changes taking place during sintering. First, the contact region between powder particles form a neck, transforming the loose powder into a solid porous body. Then the size and volume fraction of the pores gradually decrease. This microscopic evolution also causes macroscopic changes: an increase in density and the shrinkage of the green body [45].

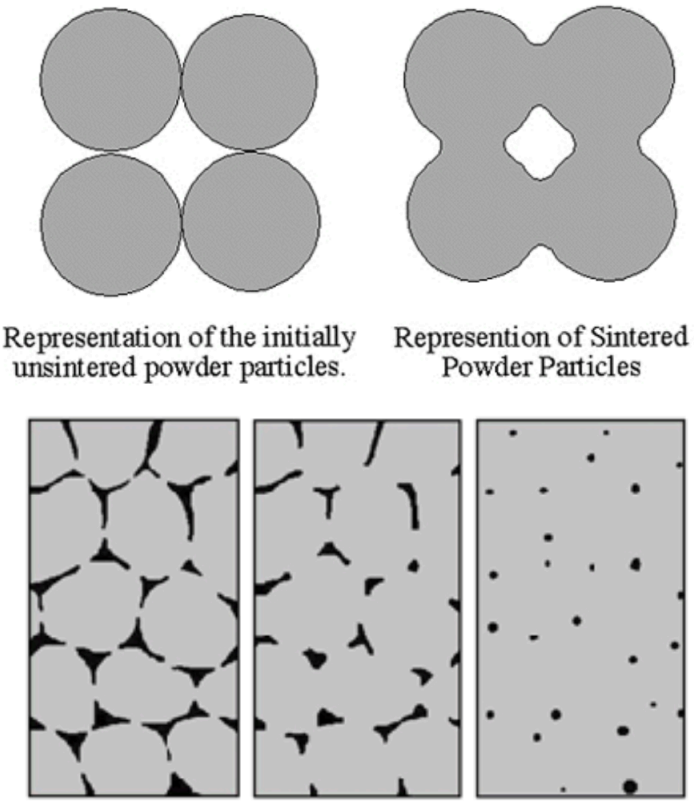

Figure 1.16: Schematic of the neck formation (top) and the reduction of porosity (bottom) during the sintering process [45].

In order to understand the driving force behind the sintering process, the simplest form of sintering is discussed. Sintering, like any other physical transformation in materials, follows the rules of thermodynamics which describe how a system evolves with a change in one or several of the state variables such as temperature, pressure etc. A system can only transform from one state into another if the change in free energy G associated with this transformation is negative

$\Delta G < 0$ i.e. the system reduces its free Gibbs energy. In the case of conventional pressure-less sintering, the system contains two phases: a solid phase of volume V_s and a gaseous phase of volume V_g separated by an interface of area A. For this particular case, the exact differential of the free Gibbs energy dG is given by equation 1.1 [45].

$$dG = -(S_g + S_s)dT + V_g dP_g + V_s dP_s + \sum \mu_i dn_i + \gamma dA \tag{1.1}$$

Where S_g and S_s are the entropy of the gaseous and solid phase, P_g and P_s are the pressure of the gaseous and solid phase, μ_i and n_i are the chemical potential and number of moles of phase i and γ is the interface energy between the gaseous and solid phase.
If we consider a steady-state case where sintering occurs at constant temperature and pressure and without any change in composition, equation 1.1 becomes equation 1.2 [45].

$$dG = \gamma dA \tag{1.2}$$

Equation 1.2, shows that the driving force for sintering comes from the reduction of the interface energy between the gaseous and solid phases in the green body. Since this interface energy is relatively low, the change in free Gibbs energy ΔG is relatively small in sintering. This explains why pressure-less sintering is a very slow process and has now been replaced by more elaborate sintering techniques such as hot pressing, reactive and liquid phase sintering and field assisted sintering (FAST), which use pressure, chemical reactions, liquid phase or high electrical currents to activate sintering and increase the driving force [45].
In order to understand the effect of the sintering conditions on densification, it is important to look into the transport mechanisms that occur during sintering. There are essentially two types of mechanisms: surface and bulk transport, as shown in Figure 1.17 [45].
Surface transport does not increase the density and simply reduces the total surface area of the particles by making the necks grow. The different mechanisms contributing to surface transport are shown in Figure 1.18 and listed here:

- Diffusion of vacancies to the surface along the surface of the pores (1)
- Diffusion of vacancies to the surface through the bulk (2)
- Evaporation and condensation processes (3)

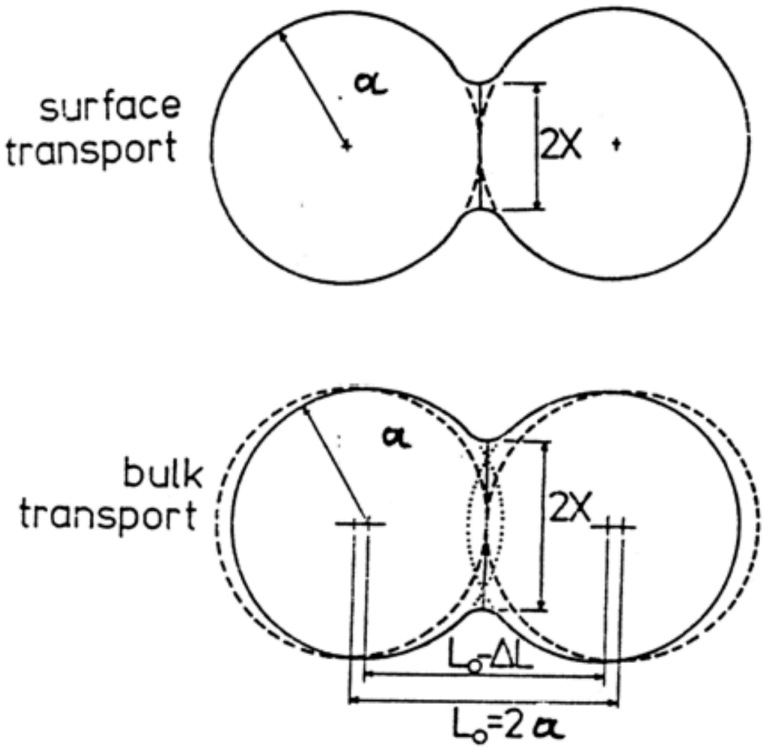

Figure 1.17: Schematic showing surface and bulk transport that occur during the sintering process [45].

Bulk transport moves matter from the bulk of the particles to the surface of the pores causing a net movement of the center of mass of the particles toward each other leading to an increase in density, as shown in Figure 1.17. The mechanisms contributing to bulk transport are shown in Figure 1.18 and listed below:

- Diffusion of vacancies to grain boundaries along grain boundaries (4)
- Diffusion of vacancies to grain boundaries through the bulk (5)
- Diffusion of vacancies to the bulk through the bulk (6)
- Plastic flow

If we consider the case of a monophasic powder, the transport of matter can be described by a simple version of Fick's law and depends on the self-diffusion constant D^* [45]:

$$D^* = D_0 \exp\left(-\frac{\Delta H_m}{RT}\right) \tag{1.3}$$

where D_0 is the diffusion coefficient of vacancies, ΔH_m the formation enthalpy of vacancies per

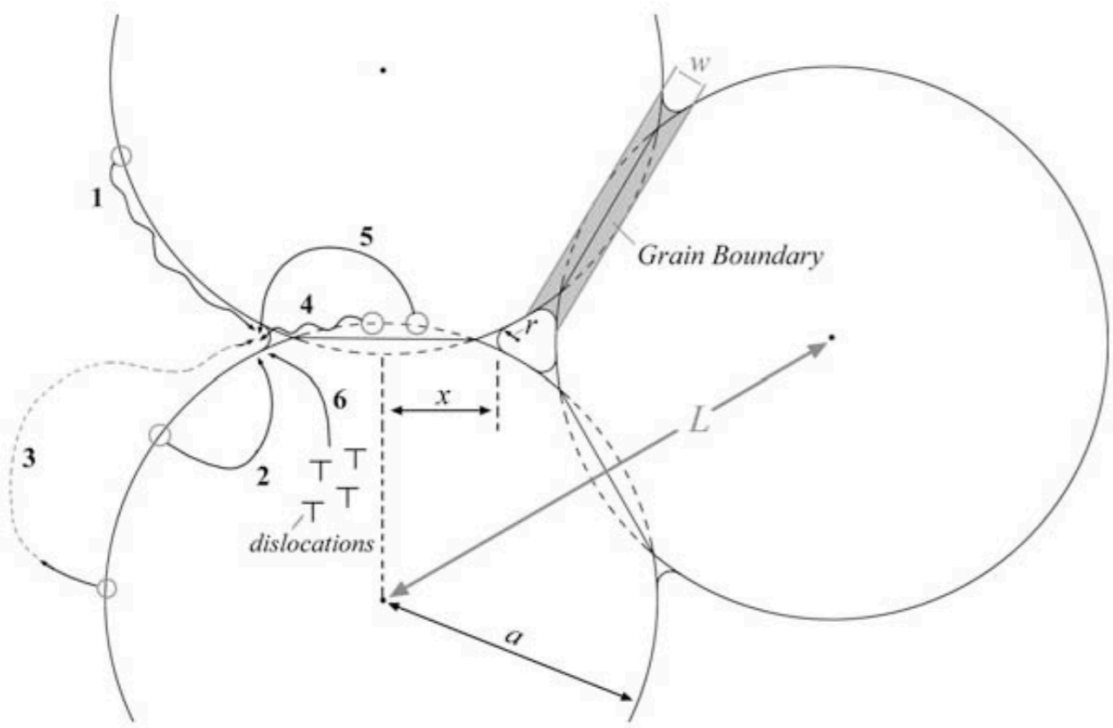

Figure 1.18: Schematic of the different transport mechanisms occuring during the sintering process [45].

unit mole and R the ideal gas constant. ΔH_m is highest in the bulk, lower at grain boundaries and lowest at the surface of the particle, thus $\Delta H_{surface} < \Delta H_{GB} < \Delta H_{bulk}$. Therefore, low sintering temperatures only promote surface transport whereas high temperatures also activate grain boundary and bulk transport which contribute to densification. High sintering temperatures and fast heating rates are thus preferred to enhance densification [45]. The next section describes a modern sintering technique, known as the Field Assisted Sintering Technology, which was used to manufacture most of the MgB_2 samples presented in this work.

1.3.2 Field Assisted Sintering Technology

The Field Assisted Sintering Technology (FAST), also known as Spark Plasma Sintering, is a relatively new processing technique that uses pressure and high electric currents to quickly sinter conductive and non-conductive materials. It uses a low voltage DC pulsed current to heat a powder enclosed in a graphite die between two graphite punches, as shown in Figure 1.19. Two electrodes mounted on a hydraulic system apply pressure and transmit high currents (typically between 1 and 10 kA) to the powder through the graphite punches. The combination of pressure

and high currents (leading to large joule heating) results in efficient sintering of the powder to very high density values. For non-conductive samples, the current flows mainly in the grahite die which transmits heat to the powder by conduction. The whole system is enclosed in a chamber which enables the sintering process to be held in a specific atmosphere, typically under vacuum or argon [46, 47].

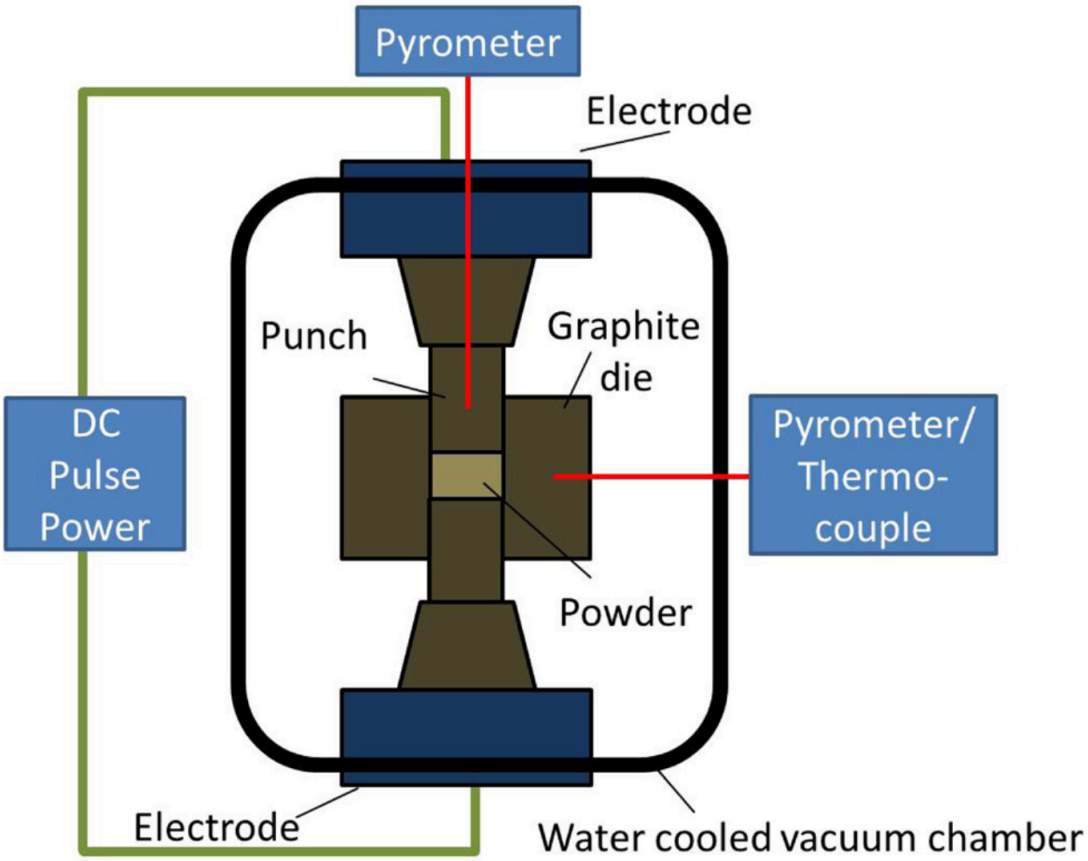

Figure 1.19: Schematic of a FAST apparatus [46].

FAST is a flexible process that allows a wide range of sintering conditions with heating and cooling rates up to 1000 °C/min and 150 °C/min respectively, and temperatures up to 2400 °C with standard graphite dies [46, 48]. The main advantage of FAST is that unlike conventional sintering where a whole furnace is heated up or cooled down, in FAST only the sample and the graphite die are maintained at a specific temperature. Consequently, the temperature response is faster and much larger heating and cooling rates can be achieved compared to conventional sintering techniques. This allows the design of novel sintering routes that cannot be achieved with

conventional furnaces and also makes the sintering process faster and more energy efficient [46,48]. The rest of this section focusses on different effects observed in FAST and its advantages compared to conventional sintering. These effects are divided into three categories: mechanical, thermal and electrical effects.

Mechanical effects The pressure applied to the powder leads to better contacts between particles and enhances densification mechanisms (bulk and grain boundary diffusion). Pressure can also activate new mechanisms such as plastic deformation and/or grain boundary sliding which promote densification [46]. On the other hand, non-densifying mechanisms such as surface diffusion and evaporation/condensation are not affected by compressive stress [46].
Pressure is also beneficial to maintain a fine microstructure because compressive stress tends to slow down grain growth taking place at high temperature [46,49]. In addition, high compressive stress can break agglomerates that tend to form in very fine powders, and thus lead to particle rearrangement and better powder packing. This increases the green body density and promotes faster and more homogeneous densification. Finally, the additional densification mechanisms (plastic deformation and power law creep) that are activated by high pressure enable full density to be reached at lower temperatures than in conventional sintering, reducing microstructure coarsening [46].

Thermal effects The main advantage of FAST is the very high heating and cooling rates that can be achieved compared to conventional sintering. As discussed in section 1.3.1, densifying mechanisms (grain boundary and bulk diffusion) are activated at higher temperatures than non-densifying mechanisms (surface diffusion) which only contribute to coarsening. In FAST, the higher heating rates allow us to reach these temperatures rapidly and thus promote densifying mechanisms much quicker than in conventional sintering. This reduces considerably the overall processing time and the operation cost.
The high heating rates in FAST also allow us to reduce considerably the total time at intermediate and high temperatures leading to an efficient reduction in grain growth. This has been confirmed experimentally by Shen [50] and Zhou [51] who found that higher heating rates led to smaller grain size in alumina made by FAST.

Electrical effects The electrical effects that occur when high electrical currents flow through the green body are still under investigation and debated in the literature [46,47,52,53]. FAST is still known by many as Spark Plasma Sintering which has raised a big debate in the sintering community. Some maintain that a plasma is formed and spark discharge occurs within the green body, but this has never been observed and is strongly doubted by others [46,47]. The following electrical effects may occur during FAST: percolation effects, the Peltier effect, electrochemical reactions and electromigration [46,47,52–54].

Due to the nature of the green body, current does not flow homogeneously through its cross section but rather follows complex percolation paths that fluctuate with time as densification occurs. Consequently, Joule heating occurs along these percolation paths and fluctuating hotspots form within this percolation network. The temperature at these hotspots can be much higher than the average temperature of the green body. These local conditions can lead to specific mechanisms such as partial melting or recrystallisation [46]. Densification also occurs much faster along this percolation network which can lead to heterogeneous microstructures [52,53]. Olevsky *et al.* [54] investigated the effect of electromigration on densification by modelling the consolidation of aluminium powder by FAST. The authors showed that for low porosity values ($<$10 %) electromigration could become the main driving force for densification. These results suggest that electromigration could have a significant effect on densification during the final stage of sintering, when the driving force is very low.

1.4 Field assisted sintering of MgB_2

Many research groups have successfully manufactured MgB_2 by FAST for almost two decades [39,42,43,55–57]. Pre-synthesised MgB_2 was found to be difficult to sinter by conventional sintering techniques, which made FAST popular to manufacture ex-situ bulks. A few groups also investigated the in-situ route by FAST, but the ex-situ method is usually preferred due to the much higher density values that can be obtained. [39,55,57].

The following sections summarise the effect of the processing conditions on the microstructure and superconducting properties of MgB_2 bulks manufactured by FAST. The main sintering parameters that have been investigated in the literature are the temperature, pressure, heating rate and dwell time.

1.4.1 Temperature

A rigorous study on the effect of the sintering temperature on the properties of MgB_2 manufactured by FAST could not be found in the literature. In fact, I decided to investigate this matter myself and this will be the topic of Chapter 3, which has been published in Superconductor Science and Technology [37]. Nonetheless, some general trends have been observed. Most of the MgB_2 samples manufactured by FAST have been sintered between 850 and 1250 °C [30,39,42–44]. The main effects reported in the literature were an increase in density and in the fraction of secondary phases with higher sintering temperatures.

Lee *et al.* [42] manufactured MgB_2 at 1250 °C and measured a density of 99%, and also found a higher fraction of MgO in the consolidated specimen compared to the as-received powder. Unfortunately, no quantitative information on MgO were given and the authors also did not make any comment on the presence of several extra peaks in their XRD patterns which probably correspond to higher borides such as MgB_4.

Dancer *et al.* [39] manufactured MgB_2 bulks at 1250 °C and found a density of 97%. They also observed an increase in the fraction of MgO and MgB_4 in sintered specimens, compared to the initial powder. The fraction of MgO was estimated to ~ 7 wt.% by XRD, but the authors could not measure the MgB_4 content.

Shim *et al.* observed a significant increase in density from 78% to 99% by increasing the sintering temperature from 900 to 1050 °C. This seems abnormally large compared to the density values reported by Lee and Dancer for samples processed at 1250 °C.

Habler *et al.* [30] manufactured MgB_2 between 850 and 950 °C, and measured a density of 86% for the 950 °C sample. They found that the fraction of MgO (~ 8 wt.%) was almost constant with the processing temperature whereas the amount of MgB_4 increased sharply from < 0.5 wt.% in the 850 °C sample up to 8 wt.% in the 950 °C specimen.

In summary, the sintering temperature has two effects on the properties of MgB_2 samples made by FAST; the density and fraction of MgB_4 increase significantly with higher processing temperatures. In contrast, the sintering temperature has almost no effect on the fraction of MgO, although several research groups have found that the amount of MgO detected in the consolidated material is higher than in the initial powder.

1.4.2 Pressure

Dancer *et al.* [39] investigated the effect of pressure by manufacturing MgB_2 samples at 1250 °C and using 16, 50 and 80 MPa. The density of these three specimens were respectively 92, 97 and 97%. They suggested that above a certain value, increasing the pressure only had a marginal effect on density. They measured similar fractions of MgO (estimated by XRD) for the three samples, suggesting that the pressure probably had a negligible effect on the formation of MgO. The authors characterised the superconducting properties of the bulks processed at 16 and 80 MPa by performing magnetic measurements and found that J_c values of both samples were very similar, indicating that pressure only had a limited influence on J_c. They also performed SEM on fractured samples and observed that grain growth was higher in the denser sample processed at 80 MPa, suggesting that grain boundary pinning became less effective as the porosity level decreased. They concluded that the negative effect of grain growth on J_c might negate the positive influence of increased density, which could explain why the specimens processed at 16 and 80 MPa had similar J_c values.

1.4.3 Heating rate

Aldica *et al.* [31] studied the effect of the heating rate by manufacturing MgB_2 samples at 1150 °C using heating rates of 20, 100, 235, 355 and 475 °C/min. All the samples showed similar density values above 99% except the bulk processed at 100 °C/min which had a density of 95%. They did not provide any explanation for this difference and concluded that the heating rate did not have a significant influence on densification. The fraction of MgO and MgB_4 was estimated by XRD and they found that the samples processed using the highest heating rates contained slightly less impurities. The authors suggested that higher heating rates led to a shorter exposition of the material to high temperatures, limiting the following reactions: $2MgB_2 \rightleftharpoons MgB_4 + Mg$ and $Mg + \frac{1}{2}\ O_2 \Rightarrow MgO$

They also characterised the superconducting properties of the samples by magnetic measurements. All the specimens showed a sharp superconducting transition with an onset T_c at 38.8 K. The J_c values of all the samples were relatively similar and their results did not show any trend

between the heating rate and J_c. The best J_c and H_{irr} values were obtained in the sample processed at 100 °C/min, from which they concluded that 100 °C/min was the optimal heating rate. This statement was not supported by any further evidence or additional characterisation. They suggested that J_c might be influenced by a complex combination of different factors such as crystallite size and the fraction and size of the impurity phases. Further characterisation is needed to understand their results and confirm their statement about the optimal heating rate.

1.4.4 Dwell time

Shim *et al.* [43] manufactured MgB_2 between 950 and 1050 °C for 10 and 30 min. The samples processed at 950 and 1000 °C for 30 min showed density values of 91 and 99% respectively, compared to 84 and 94% for the samples sintered for only 10 min. They only characterised further two samples manufactured at different temperatures which does not allow us to draw any conclusion on the influence of the dwell time.

Aldica *et al.* [31] recently investigated more rigorously the influence of dwell time on MgB_2 sintered by FAST. The samples were processed at 1150 °C for 1, 4, 7, 10 and 20 min. They observed that the density increased slightly with the dwell time, going from 95 to 97% for the samples sintered for 1 and 20 min respectively. The composition of the samples was estimated by XRD and they found very similar MgO and MgB_4 fraction for all the specimens. They concluded that for short processing times ($\leq$ 20 min), the dwell time had no influence on the composition of consolidated MgB_2. The crystallite size of MgB_2, MgO and MgB_4 were also relatively similar and the authors did not see any clear trend with the dwell time.

They also characterised the superconducting properties of the samples by performing magnetic measurements. J_c values at 10 K are shown in Figure 1.20. They observed a small decrease in J_{c0} with the dwell time and found that all the samples showed almost identical normalised $J_c - B$ curves. They reported that all the samples had similar pinning behaviour and that point pinning was the dominant pinning mechanism. The authors finally concluded that the dwell time had only a limited influence on J_c.

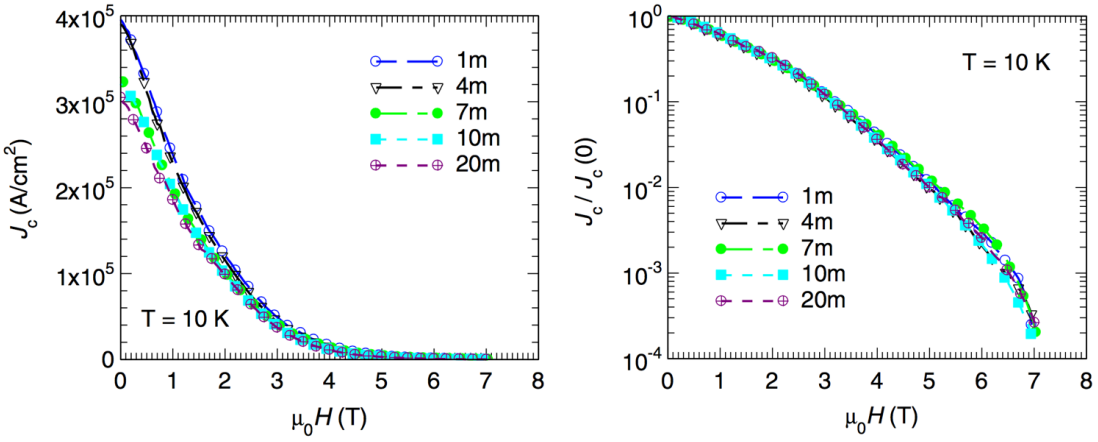

Figure 1.20: $J_c - B$ and normalized $J_c - B$ curves at 10 K for bulks processed by FAST using different dwell times [31].

1.5 MgB_2 modification

1.5.1 Carbon doping

Carbon doping is the most popular form of doping for MgB_2 and has been studied extensively in the literature. Many research groups have investigated the effect of carbon additions on the superconducting properties of MgB_2 in various forms such as single crystals [33, 58], wires [35, 59, 60] and bulks [61–64].

Lee *et al.* [33] investigated the effect of carbon doping on MgB_2 single crystals prepared by a high pressure technique. Mg, B and C powders were mixed together and MgB_2 single crystals were formed at 1600-1700 °C and 5 GPa by the in-situ method. The single crystals had a nominal composition $Mg(B_{1-x}C_x)_2$ with $x = 0.02 - 0.15$, and were characterized by XRD and magnetic measurements. Figure 1.21 shows the evolution of the a and c-axis lattice parameters and T_c with the amount of substituted carbon.

They observed that c was constant while a decreased significantly with higher carbon substitution. Their magnetic measurements showed that T_c decreased drastically with the carbon concentration.

Deemyad *et al.* [65] investigated the effect of hydrostatic pressure on the cell volume and T_c of MgB_2 single crystals. They found that the reduction of the unit cell volume caused by pressure led to a linear decrease in T_c, as shown in the onset of Figure 1.21. Although Lee found that carbon substitution also caused a reduction in the unit cell volume, they observed a much larger decrease in T_c in their carbon substituted samples than in Deemyad's specimens that were

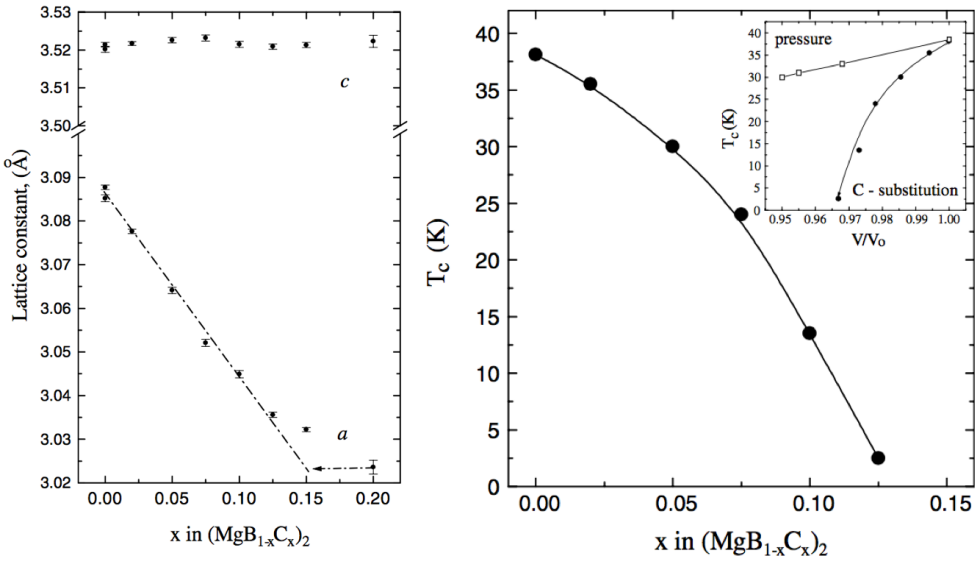

Figure 1.21: Left: Influence of the carbon content on the lattice parameters of carbon doped MgB_2 single crystals. Right: Influence of the carbon content on the critical temperature. Inset: Comparison of the effect of the lattice volume change caused by pressure or carbon substitution on the critical temperature [33].

subjected to hydrostatic pressure. Lee concluded that additional effects such as electron doping should be considered to explain the large decrease in T_c observed in carbon substituted single crystals. The authors suggested that carbon doping caused a major change in the electronic structure of MgB_2 leading to this drastic reduction in T_c.

Wilke *et al.* [59] manufactured carbon doped MgB_2 wires by the in-situ method and also observed a significant reduction in T_c with increasing carbon concentrations. In addition, they showed that H_{c2} increased significantly (2 fold) in their specimen containing $\sim 3\%$ carbon compared to unmodified MgB_2.

Yamamoto *et al.* [61] manufactured B_4C doped MgB_2 tapes using the powder-in-closed-tube (in-situ) method and also observed a reduction in T_c with increasing B_4C concentrations. They found that H_{c2} and J_c at 20 K increased slightly with small B_4C fractions but decreased drastically for larger concentrations. The authors suggested that J_c improvements were due to the reduction in the coherence length caused by carbon substitution which improved grain boundary pinning. J_c eventually decreased for higher carbon concentrations due to the competition between two opposite effects: the improvement in grain boundary pinning and the decrease in T_c.

1.5.2 Oxide and metal additions

Several research groups investigated the effect of oxide and metallic additions on the microstructure and superconducting properties of MgB_2 [36, 66–72].

Aldica *et al.* [66] prepared ex-situ MgB_2 bulks containing Te and TeO_2 additions by FAST. The samples were sintered at 1150 °C for 3 min (95MPa, 160° C/min) and the nominal compositions were: $MgB_2(Te)_x$ and $MgB_2(TeO_2)_x$ where $x = 0.005$, 0.01 and 0.03.

All the samples containing additions showed high density values between 96 and 99% compared to 94% for unmodified MgB_2. All the Te/TeO_2 samples and unmodified MgB_2 had similar lattice parameters and T_c values, suggesting a lack of Te substitution in the MgB_2 lattice. Four distinct phases were identified by XRD: MgB_2, MgO, MgB_4 and MgTe. TeO_2 specimens contained higher concentrations of MgB_4, MgO and MgTe with increasing TeO_2 additions. Te samples showed a similar trend except for the fraction of MgO which was almost constant and lower than in TeO_2 specimens. Despite the large errors on the crystallite size values estimated by XRD, the authors concluded that the samples $MgB_2(Te)_{0.01}$ and $MgB_2(TeO_2)_{0.01}$ had smaller crystallite size for MgB_2, MgO, MgB_4 and MgTe. The samples were further characterized by magnetic measurements and $J_c - B$ curves at 20 K were calculated. At low magnetic field, J_c decreased with increasing additions in TeO_2 samples. In contrast, J_c at low field was constant in Te specimens. The TeO_2 and Te samples containing 1% additions showed the best J_c values at high field.

The authors concluded that for both additions, the optimal concentration was 1%. They attributed this improvement to the fine microstructure observed in these two specimens, which showed smaller crystallite size than the samples containing 0.5 and 3% Te or TeO_2. Further characterisation in particular by SEM and TEM is needed to understand the microscopic role of Te and TeO_2 additions on J_c.

Batalu *et al.* [36] manufactured ex-situ MgB_2 containing GeO_2 by FAST. MgB_2 and GeO_2 powders were mixed to give the nominal compositions $MgB_2(GeO_2)_x$ where $x = 0.005$, 0.01 and 0.03. The powders were then consolidated at 1150 °C for 3 min (95 MPa).

All their samples showed relatively high density values (>93%), but no clear trend between the fraction of GeO_2 and the density could be observed. XRD analysis detected 4 phases: MgB_2, MgB_4, MgO and Mg_2Ge. The concentrations of the three secondary phases increased with GeO_2 additions. The GeO_2 samples had smaller MgB_2, MgO and MgB_4 crystallite size than unmodified

MgB_2, with the 1% sample showing the finest microstructure. The lattice parameters and onset T_c of all the samples were very similar suggesting only very limited Ge substitution in the MgB_2 lattice. The $J_c - B$ curves at 20 K of their GeO_2 samples and unmodified MgB_2 are shown in Figure 1.22.

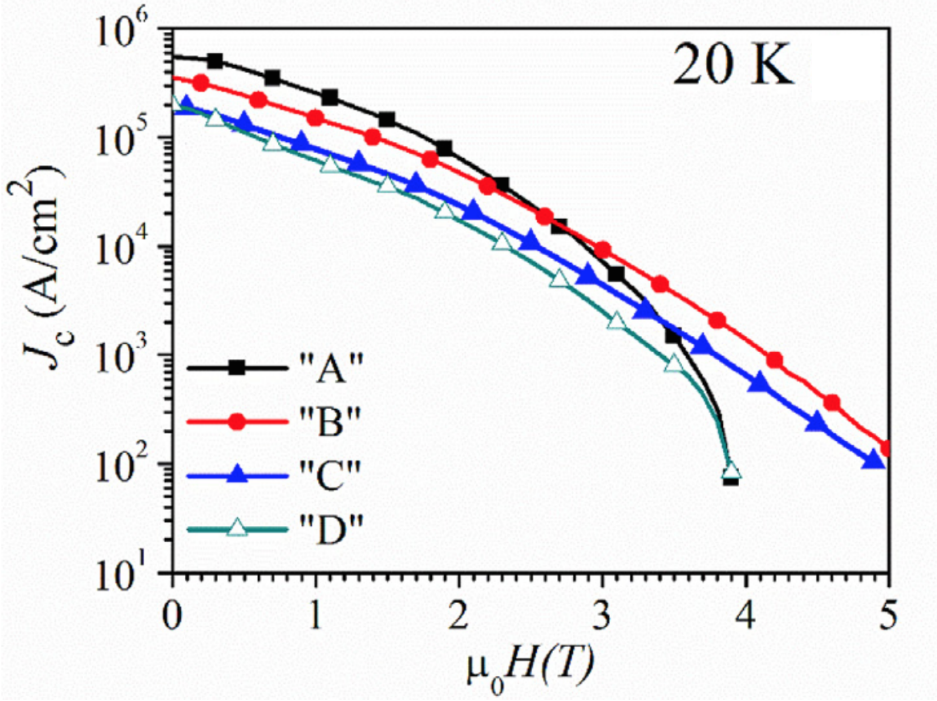

Figure 1.22: $J_c - B$ curves at 20 K for (A) unmodified MgB_2 and (B-D) $MgB_2(GeO_2)_x$ samples with $x = 0.005$, 0.01 and 0.03 respectively [36].

Although the authors did not analyse the low field properties, Figure 1.22 clearly shows a reduction in J_c at low field with increasing GeO_2 additions. This is in good agreement with the results of Aldica [66] on TeO_2-MgB_2. At high field, the 0.5 and 1% GeO_2 samples showed an increase in J_c compared to unmodified MgB_2. In contrast, the 3% GeO_2 sample had lower J_c values than unmodified MgB_2 for the entire field range. This is also consistent with the results on Te and TeO_2-MgB_2 samples of Aldica which suggested that only relatively small amount of additions ($\leq$1%) improved J_c values at high field.

SEM analysis showed that the microstructure of GeO_2-MgB_2 samples was composed of clean MgB_2 grains and Ge rich regions. TEM analysis showed the presence of very fine 25-100 nm particles containing Mg, B, C and O. They also observed spherical nano particles containing Mg-O and Mg-Ge with an average size of 100 nm. This was consistent with the crystallite size for the MgO and Mg_2Ge phases estimated by XRD. Thick layers containing mainly Mg-O or Mg-Ge

were also found in their samples. The authors suggested that this layer morphology could come from the formation of liquid Mg and GeO_2 during the sintering process. They also mentioned the presence of some pure Ge layers. The authors concluded that J_c improvements at high field were mainly due to "composite" microstructural effects, without developing this concept.

Xu *et al.* [71] manufactured in-situ MgB_2 bulks containing nano TiO_2 additions. Mg, B and TiO_2 powders were ground together and pressed into pellets before being heat treated at 800 °C for 30 min. Three compositions were investigated: 5, 10 and 15 wt.% TiO_2.
Only two phases were detected by XRD: MgB_2 and MgO. The fraction of MgO increased gradually with TiO_2 additions. Despite the fact that no TiO_2 or Ti-containing phase could be detected by XRD, the authors suggested that Ti did not substitute in the MgB_2 lattice. This was supported by their magnetic measurements that showed TiO_2 only had a limited effect on T_c. They observed a small reduction in the a-axis lattice parameter with increasing TiO_2 additions, but they attributed this to a difference in MgO fraction. The authors suggested that higher MgO fractions could be regarded as Mg deficiency, causing a reduction of the a-axis lattice parameter. In contrast with the studies of Batalu [36] and Aldica [66] on ex-situ bulks, these in-situ samples showed high J_c values at low field that were similar to unmodified MgB_2 even for large concentrations of TiO_2. All the TiO_2 samples (5, 10 and 15 wt.%) also showed higher J_c values at high field and H_{irr} values compared to unmodified MgB_2. They found that 10 wt.% TiO_2 gave the best J_c performance, which was much larger than the optimal concentrations found by Batalu and Aldica for their ex-situ samples containing Te, TeO_2 and GeO_2 additions. This suggests that the effect of oxide or metal additions might depend on the type of processing method (in-situ or ex-situ) used.
The authors suggested different explanations for the J_c and H_{irr} improvements. They first mentioned that MgO, TiO_2 and/or other Ti-rich nano particles could lead to an increase in H_{irr}. They also explained that TiO_2 additions could cause a Mg-deficiency leading to Mg vacancies and the formation of small MgB_4 particles. The authors suggested that Mg vacancies might generate strain in the MgB_2 lattice and that small MgB_4 particles could act as pinning centres which could improve J_c at high field and H_{irr}, but further characterization is needed to confirm the origin of these improvements. (S)TEM analysis could confirm the presence of these nano particles and provide important information on their size and distribution.

Wang *et al.* [69] prepared in-situ MgB_2 bulks containing 5, 10 and 15 wt.% nano Y_2O_3. The powders were pressed into pellets and heated up to 900 °C for 15 min. All the Y_2O_3-MgB_2 samples and unmodified MgB_2 had a density of 50% ± 5, and light microscopy confirmed that the pellets were macroscopically porous. Only 3 phases were detected by XRD: MgB_2, MgO and YB_4. The lack of Y_2O_3 peaks suggested that Y_2O_3 fully reacted with B to form YB_4. The authors found that the fraction of MgO and the MgB_2 unit cell volume increased with Y_2O_3 additions. They attributed this increase in unit cell volume change to oxygen dissolved in the MgB_2 lattice and/or strain generated by the YB_4 nano particles. TEM analysis showed small $\sim$ 10 nm YB_4 precipitates located at MgB_2 grain boundaries and smaller $3-5$ nm particles inside MgB_2 grains.

Unmodified MgB_2 and the samples containing 5 and 10 wt.% Y_2O_3 had very similar onset T_c at $\sim$ 39 K. However, the 15 wt.% sample showed a slightly lower onset T_c at $\sim$ 38 K. The authors concluded that Y_2O_3 neither alloyed MgB_2 nor caused significant disorder.

$J_c - B$ curves at 20 K showed that all the Y_2O_3 samples had higher J_c values at low and intermediate field (<4 T) than unmodified MgB_2. The optimal Y_2O_3 concentration was found to be 10 wt.%, which is consistent with the study of Xu [71] on TiO_2-MgB_2. However, at high fields (> 5 T) unmodified MgB_2 outperformed the Y_2O_3 specimens. The authors attributed this to a better connectivity at the grain boundaries in unmodified MgB_2 explaining that additional phases were present at the grain boundaries in Y_2O_3-MgB_2 samples.

Cai *et al.* [70] manufactured in-situ MgB_2 bulks containing SiC and Y_2O_3. Mg and B powders were mixed with 10 wt.% nano SiC and 10 wt.% nano Y_2O_3 before being pressed into pellets and heated up to 900 °C for 30 min.

Five phases were detected by XRD: MgB_2, MgO, YB_4, Y_2O_3 and Mg_2Si. The average YB_4 crystallite size was estimated to 36 nm by XRD. High resolution SEM showed very fine intragranular YB_4 precipitates consistent with the average size estimated by XRD. Their SEM analysis also confirmed the presence of residual Y_2O_3 at MgB_2 grain boundaries. These results are relatively different from the study of Wang [69] who observed much smaller 3-10 nm YB_4 particles and could not find any residual Y_2O_3. The SiC-Y_2O_3 sample showed a small improvement in J_c at high field compared to unmodified MgB_2. In contrast, J_c values at low field were lower than in

unmodified MgB_2. This was attributed to the presence of residual Y_2O_3 at MgB_2 grain boundaries which hindered intergranular connectivity. The SiC-Y_2O_3 specimen had a T_c of $\sim$ 37 K, slightly lower than unmodified MgB_2. The authors concluded that J_c improvements at high field were probably due to a combination of additional pinning by Mg_2Si and YB_4 nano particles, and intragrain dislocations caused by carbon substitution from SiC.

Muralidhar *et al.* [72] manufactured in-situ MgB_2 bulks containing between 2 and 10 wt.% silver. Mg, B and Ag powders were ground together and pressed into pellets heat treated at 775 °C for 3 h.

XRD analysis indicated that the main phase was MgB_2 with a few additional peaks that could correspond to either Ag_2O or $AgMg_3$. The fraction of these Ag-containing phases increased with Ag additions. The authors claimed that silver additions promoted sintering but did not give any information about the density of the bulk samples. SEM analysis showed that unmodified MgB_2 had a very porous microstructure containing numerous pores of different size and shape. In contrast, large (5-20μm) Ag and Ag_2O particles filled some of these voids in the samples containing Ag additions. Smaller (<1μm) precipitates were also observed inside MgB_2 grains and were identified as $AgMg_3$ by EDX. The samples containing more silver additions showed a higher fraction of $AgMg_3$ particles. $AgMg_3$ precipitates were also larger and were distributed less homogeneously in samples containing more Ag additions. Atomic Force Microscopy (AFM) analysis confirmed the presence of nano $AgMg_3$ particles, as small as 10-20 nm, and also coarser ones up to several microns.

The superconducting properties of the bulks were investigated by magnetic measurements using a SQUID magnetometer. All the Ag samples showed a sharp superconducting transition and had very similar T_c values almost identical to unmodified MgB_2. J_c analysis at 20 K showed that all the samples containing Ag additions showed better J_c at low field than unmodified MgB_2. This is in contrast with most of the studies on oxide additions presented above and suggests that silver additions have a different effect than oxide additions. Most of the samples containing oxide additions showed reduced J_c values at low field compared to unmodified MgB_2. Several authors attributed the J_c degradation at low field to poor intergranular connectivity due to the presence of oxides at MgB_2 grain boundaries. In the case of Ag additions, the opposite trend was observed and J_c at low field was improved. The sample containing 4 wt.% Ag showed the highest

J_c values. The authors explained that 4 wt.% Ag probably gave the best distribution of nano $AgMg_3$. They attributed the J_c improvements at low field to additional pinning provided by these nano $AgMg_3$ precipitates in the MgB_2 matrix. The authors did not show any J_c values at high field so the effect of Ag additions in this regime could not be investigated and compared to the effect of oxide additions. Connectivity measurements would also be valuable to understand the origin of J_c improvements at low field.

1.5.3 Ball milling

Many research groups ball mill Mg and B powders to produce precursor powders for the manufacture of in-situ MgB_2. Ball milling is also used for doping purpose where Mg and B powders or pre-synthesised MgB_2 are milled with a carbon source for instance. Since my work focusses on sintering pre-synthesised MgB_2 and the previous section covers carbon doping and oxide and metallic additions, this section focusses on ball milling unmodified MgB_2.

Kario *et al.* [32] ball milled MgB_2 powder from Alfa Aesar using a high energy planetary ball mill. The powder was milled in Ar for $0.5-20$ h at a speed of 250 rpm and with a ball-to-powder ratio (BPR) of 36:1. These powders were cold pressed into pellets that were hot pressed at 700 °C for 10 min at 640 MPa. The samples were finally annealed at 900 °C for 1 h.
Wires were also made from the powder milled 2 h using the PIT method. These wires were rolled into tapes that were sintered between 600 and 925 °C for $1-80$ h.
The Differential Scanning Calorimetry (DSC) curves for the milled powders are shown in Figure 1.23. Unmilled MgB_2 showed a very small endothermic peak above 1000 °C which corresponds to the decomposition of MgB_2 into $Mg_{(g)}$ and MgB_4. Figure 1.23 shows that the peak shifted to lower temperatures and increased in intensity with longer milling times. The author suggested that ball milling made the powder more reactive and promoted the decomposition reaction.
XRD analysis showed that the MgB_2 crystallite size was reduced drastically during the first few hours of milling before reaching a plateau at $10-15$ nm after 10 h. No MgB_4 could be detected in the bulk sample made from unmodified MgB_2 powder. In contrast, the samples ball milled for 2 h and longer contained a large fraction ($\sim$ 20 wt.%) of MgB_4. This was consistent with the DSC measurements and supported the fact that ball milling made MgB_2 more reactive and promoted the decomposition reaction. The authors did not provide a quantitative analysis for

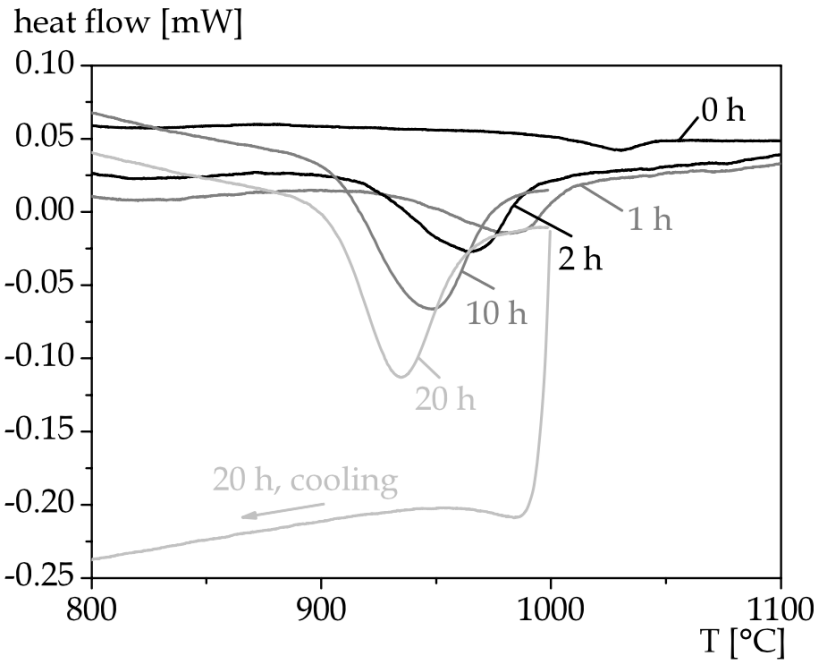

Figure 1.23: DSC curves (first heating) of MgB_2 powders ball milled for different times [32].

the MgO phase and just mentioned that the fraction of MgO increased with longer ball milling times.

The superconducting properties of the bulk samples are shown in figure 1.24. T_c decreased gradually from $\sim$ 39 K down to $\sim$ 37 K. The authors attributed this reduction to the mechanical stress induced by the ball milling process. H_{irr} increased up to $4.5 - 5$ T in the samples milled for 2 h and longer compared to $\sim$ 3.5 T for unmodified MgB_2. The $J_c - B$ curves at 20 K were only shown between 1 and 5 T. In this field range the samples milled for longer than 1 h had higher J_c values than unmodified MgB_2, in particular at high field. The best J_c values were obtained for the sample milled for 2 h. The authors explained that the J_c improvements were due to a combination of reduced crystallite size, better connectivity and moderate increase in the fraction of secondary phases.

Kario also prepared tapes from the powder milled for 2 h. These tapes were sintered between 500 and 925 °C for $1 - 80$ h. The tape processed at 500 °C had a relatively low T_c of 32 K. T_c gradually increased in samples sintered at higher temperatures, reaching 37.5 K in the 850 and 900 °C samples. The authors only presented $J_c - B$ curves at 4.2 K for the samples processed between 800 and 925 °C, which showed similar J_c values. No comparison with unmodified MgB_2 was made.

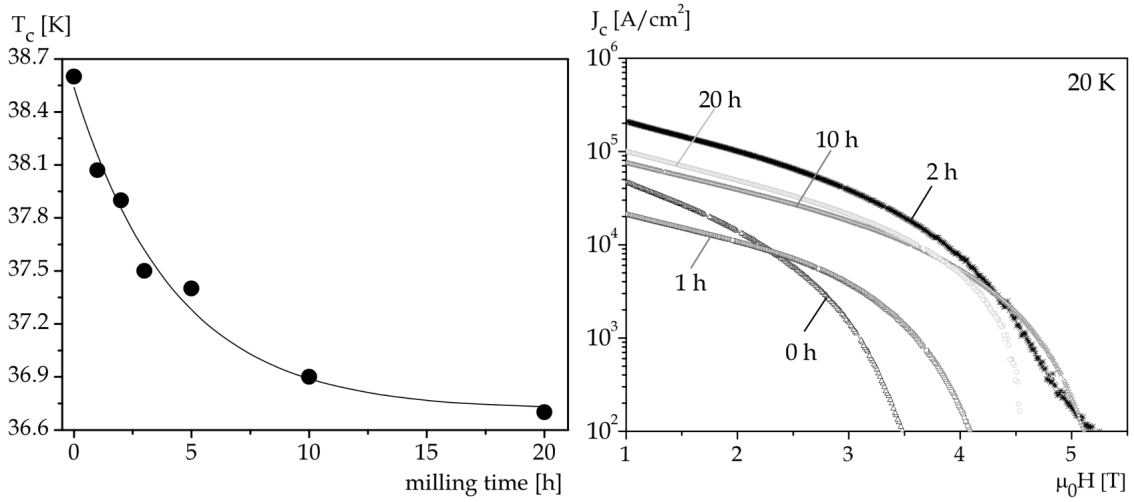

Figure 1.24: T_c (left) and J_c-B curves (right) of ex-situ MgB_2 bulks manufactured from ball milled powders [32].

TEM analysis of the tape sintered at 900 °C showed a fine dispersion (5-24 nm) of what the authors called "oxidised" MgB_2 particles (probably simply MgO). In contrast, these nano particles were not found in unmodified MgB_2 sintered at the same temperature. The authors also claimed that MgB_2 grains were better connected in the ball milled sample, but did not provide further explanation.

XRD analysis showed a significant increase in the fraction of secondary phases (MgB_4 and MgO) with increasing sintering temperature. In contrast, the sintering time did not have a significant influence on the composition. The total fraction of secondary phases (MgB_4 + MgO) increased from less than 5 wt.% in the 650 °C sample up to 40 wt.% in the specimen processed at 925 °C. The authors concluded that T_c and J_c improvements observed with higher sintering temperatures were due to a better grain connectivity without further explanation. This should be confirmed with connectivity measurements and other factors such as coarsening of MgB_2 grains and MgO particles should also be investigated to understand further the influence of the microstructure on the superconducting properties.

Sun *et al.* [73] ball milled MgB_2 powder from Alfa Aesar for $5-200$ h in Ar with a BPR of 10:1. Three bulk samples were manufactured from the powder ball milled for 200 h by hot pressing at 600 °C for 10 and 30 min at 3 GPa and for 10 min at 5 GPa.

The MgB_2 crystallite size decreased drastically from several hundred nm in the initial powder to 7 nm in the powder ball milled for 200 h. The fraction of MgO in the powder (estimated by

XRD) increased gradually with milling time up to 2 wt.% in the powder ball milled for 200 h. The strain also increased significantly up to 1.2% after 200 h of milling. After hot pressing, all the bulks made from the 200 h powder showed an identical MgB_2 crystallite size of 8 nm, suggesting the absence of coarsening. Dark field TEM showed MgB_2 grains with a size ranging from 5 to 11 nm, in good agreement with the XRD analysis. The three bulk samples showed a similar strain of $0.7-0.8\%$ suggesting that part of the strain induced by ball milling was released during sintering.

SEM analysis showed that the sample sintered for 10 min at 3 GPa contained large voids and isolated particles whereas the samples processed for 30 min at 3 GPa and 10 min at 5 GPa were dense and well connected. The density of these specimens was 77, 92 and 91% respectively.

The three bulk samples had similar onset T_c at ~ 32 K, but the sample processed for 10 min at 3 GPa had a much broader superconducting transition than the specimens sintered for longer or at higher pressure. The authors attributed this broader transition curve to inhomogeneities in the microstructure and impurities.

The samples sintered for 10 min at 5 GPa and for 30 min at 3 GPa showed higher J_c values than the sample processed 10 min at 3 GPa. This was attributed to the large difference in density and connectivity between these specimens. The bulk sample sintered for 10 min at 5 GPa showed the best J_c values at low field, whereas the sample processed for 30 min had slightly higher J_c values at high field. The fraction of MgO was slightly higher in the 30 min specimen and the authors explained that MgO hindered intergranular connectivity and thus was detrimental to J_c at low field.

They concluded that the sintering time and pressure were crucial parameters to obtain dense and well connected MgB_2 bulks with high J_c values.

Rodrigues *et al.* [74] ball milled MgB_2 powder from Alfa Aesar for 5 and 67 h in nitrogen. Bulk samples were manufactured by hot isostatic pressing (HIP) at 1000 °C for 24 h at 200 MPa. Similar to Kario [32] and Sun [73] they observed a reduction in MgB_2 crystallite size and an increase in MgO with milling time. The bulks made from the powders milled 5 and 67 h had T_c values of ~ 38 and ~ 34 K respectively, consistent with the trends observed by Kario and Sun. The samples manufactured from the milled powders showed larger H_{irr} and J_c values at high field, and a large reduction in J_c at low field compared to unmodified MgB_2. The authors

simply concluded that J_c improvements at high field were probably due to ball milling induced effects increasing electron scattering.

Naito *et al.* [75] ball milled ex-situ MgB_2 powder from Furuuchi Chemical Co. at 250 and 600 rpm for 12 h. The powders were then sintered by FAST at $950 - 1050$ °C for $5 - 15$ min at 50 MPa. The authors found that higher ball milling speeds resulted in a reduction of the crystallite size and an increase in MgO, similar to the effects caused by longer ball milling times described above. T_c decreased with the ball milling speed, reaching 35 K in the 600 rpm sample. This reduction in T_c was attributed to a degraded crystallinity of the MgB_2 lattice.
Both samples made from the powders milled at 250 and 600 rpm showed higher J_c values than unmodified MgB_2, and the intermediate ball milling speed (250 rpm) gave the best J_c values. This is consistent with the results of Kario [32] suggesting that intermediate ball milling times gave the best J_c. The authors concluded that the optimal microstructure in terms of J_c was determined by the balance between the increase in pinning centres and the degradation of superconductivity.

Fujii *et al.* [76] ball milled MgB_2 powders from Sigma Aldrich and Alfa Aesar at speeds of 150, 300 and 500 rpm for up to 30 h. Tapes were made by the PIT method and subsequently annealed at 700-940 °C for 1 h.
Powders ball milled at 150, 350 and 500 rpm for 30 h showed a crystallite size of 70, 10 and 5 nm respectively. The authors observed that the crystallite size reached a constant value after 10 h of milling at 350 and 500 rpm. SEM analysis showed that the initial powder contained particles several microns in diameter. The powder milled at 150 rpm for 30 h still contained large micron sized particles. However, the powder milled at 350 rpm for 30 h was composed of much smaller particles $< 1\mu$m. After only 5 h of milling at 500 rpm, very fine particles of few hundred nanometers were observed in the powder. Longer milling times at 500 rpm did not lead to further reduction of the particle size. This suggests that the crystallite size and particle size reduction have different kinetics.
The authors also observed a reduction in T_c with ball milling. Similar to the study of Kario [32] and Naito [75], J_c at high field was higher in ball milled samples compared to unmodified MgB_2. At 500 rpm, the specimen ball milled for 10 h showed the highest J_c values, and longer milling

times caused a reduction in J_c. This is consistent with the studies presented above and supports the fact that J_c values first increase with milling time, up to a point where additional milling degrades J_c.

In a more recent article Fujii *et al.* [34] investigated the effect of the heat treatment temperature on J_c values at high field for tapes manufactured from ball milled powders. The evolution of J_c(10 T) and J_c(12 T) at 4.2 K in function of the heat treatment temperature is shown in Figure 1.25. J_c first increased with higher temperatures until an optimal temperature where a further increase caused a large reduction in J_c. The authors found that the optimal heat treatment temperature was shifted to lower temperatures for powders ball milled longer. They suggested that the improvement in J_c was a compromise between two opposite effects. Higher temperatures helped recover crystallinity but also caused microstructure coarsening and MgB_2 decomposition. The authors concluded that powders milled for longer were more reactive and decomposed at lower temperatures reducing the optimal heat treatment temperature. This is consistent with the DSC and XRD results of Kario *et al.* [32].

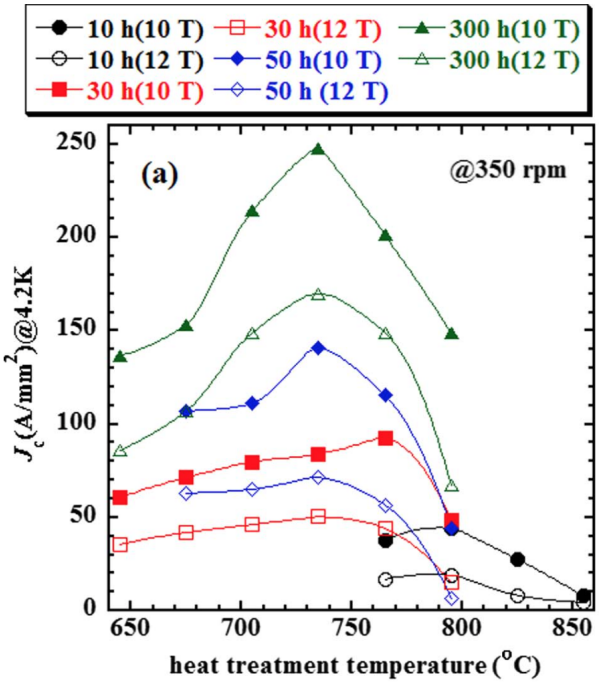

Figure 1.25: J_c(10 T) and J_c(12 T) at 4.2 K in function of the heat treatment temperature for tapes manufactured from ball milled powders [34].

Chapter 2

Experimental methods

2.1 Manufacturing

All the powder processing and most of the sintering work was performed by myself in the Advanced Processing Laboratory (APL) at the Materials Department in Oxford. A few specimens were also hot pressed at Element 6 (research centre for manufacturing diamond in Oxfordshire) with the help of Dr Edwin Eardley. The raw materials used in this work are listed in table 2.1.

Material	Form	Manufacturer	Purity	Size
MgB_2	Powder	Alfa Aesar	99%	< 150 μm
Y_2O_3	Powder	PI KEM ltd.	99.999%	$20 - 40$ nm
Mg	Powder	Alfa Aesar	99.8%	< 45 μm

Table 2.1: Raw materials used in this work.

2.1.1 Powder processing

Two powder processing operations were performed, mechanical alloying and manual mixing of different powders.

Y_2O_3-MgB_2 powders were made by mechanical alloying. Mixtures of pre-synthesised MgB_2 and nano Y_2O_3 powders were sealed into stainless steel jars with stainless steel balls in a glove box under an Ar atmosphere. The total mass of the powder was 10 g with a ball-to-powder ratio (BPR) of 10:1. These conditions were chosen due to the high yields ($80-90\%$) obtained. Different milling conditions were explored, in particular larger amounts of powder and higher BPRs, but these were not used subsequently due to the smaller yields ($40 - 50\%$) causing large powder

waste. Mechanical alloying was conducted in a Fritsch P5 planetary ball mill rotated at 350 rpm in repeating cycles of 10 min of milling followed by a 20 min pause to prevent the powders from overheating. After different milling times (10 min, 1 h, 3 h, 6 h and 12 h) the powders were recovered in a glove box under Ar.

Mixtures of unmodified MgB_2 or Y_2O_3-MgB_2 powders and pure Mg powder were obtained by manual mixing. The two powders were simply put into a small glass jar and shaken manually for 5 min in a glove box under Ar.

2.1.2 Field Assisted Sintering Technique

Bulk samples were manufactured using a Dr Fritsch DSP 507 FAST apparatus, shown in Figure 2.1 (a). For consolidation, powders were poured into a 20 mm diameter graphite die lined with a double layer of graphite paper and gently enclosed between two graphite punches also covered by a double layer of graphite paper, as shown in Figure 2.1 (b). The powders were then cold compacted in a glove box using a uni-axial pressure of 30 MPa before being transferred in the die into the FAST apparatus. The consolidation chamber was evacuated to 1 mbar and maintained at this pressure during the sintering process. Later, an Ar gas line was fitted on the FAST which allowed the chamber to be flushed with Ar before sintering.

The cold compacted green bodies were heated from room temperature to the maximum sintering temperature at a rate of 120 °C/min then held for durations between 1 and 60 min at this temperature before cooling down naturally. During the first heating step, the pressure was gradually increased to 50 MPa and then maintained during the high temperature dwell time, before being progressively released during the final cooling step. Samples manufactured using a different cooling process are clearly identified in subsequent chapters. The FAST current and voltage passing through the die/punch/green body arrangement was typically 300 to 900 A and 0.6 to 1.2 V respectively.

Most of the specimens were made using 3 g of powder and had a diameter of 20 mm and a typical thickness between 3 and 5 mm depending on the final density of the bulk pellet.

Good temperature control is crucial during the sintering process and was obtained by finding the right values for the Proportional Integral Derivative (PID) controller. The PID values were found by using the *Auto Tune* function built into the FAST software, followed by further manual

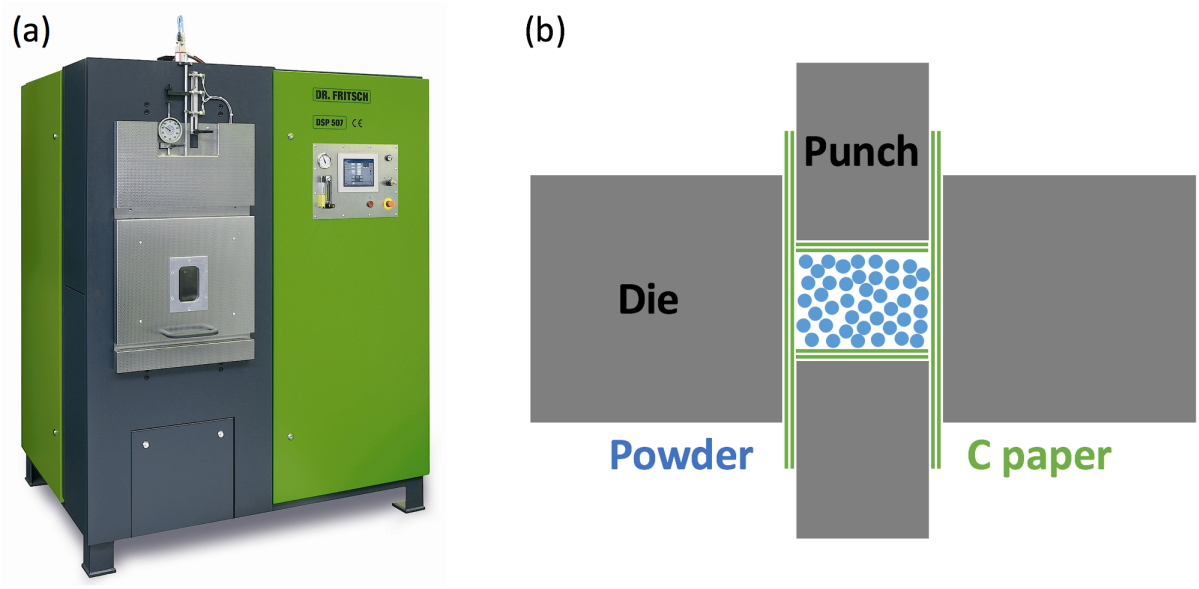

Figure 2.1: (a) Dr Fritsch DSP 507 FAST apparatus. (b) Schematic of the die assembly.

fine tuning. The PID values used for all the consolidated samples were: P=1.3, I=31.3 and D=7.8. These values gave an excellent temperature control with almost no overshoot. A typical sintering cycle using optimised PID values is compared to another cycle using non-optimised values in Figure 2.2.

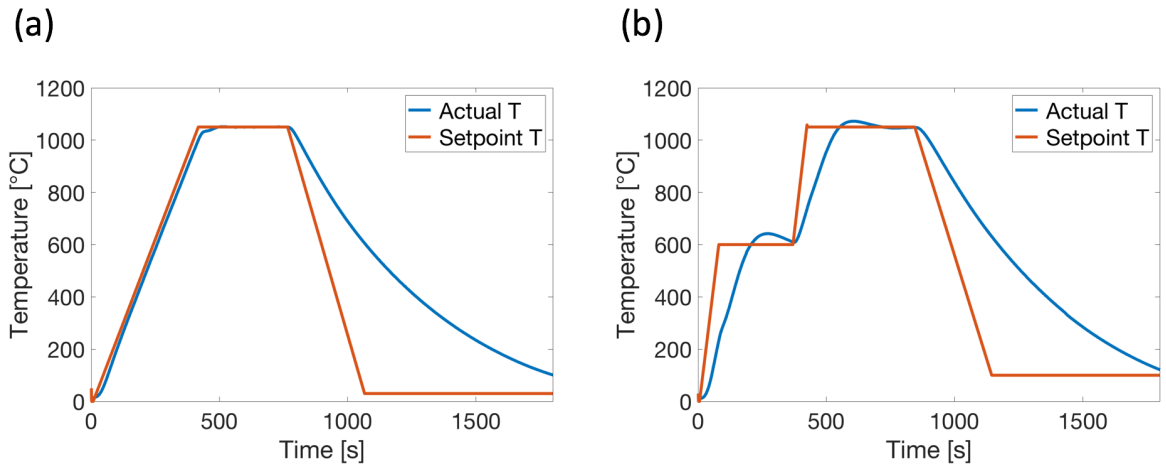

Figure 2.2: Temperature control using (a) optimised PID values and (b) non-optimised PID values.

2.1.3 Ultra high pressure hot pressing

A few samples were manufactured at the Element 6 research centre using their ultra high pressure cubic press. A schematic of their cubic press is shown in figure 2.3. Pressure is applied to a cubic sample cell by 6 large steel anvils with tungsten carbide inserts at their tip. The design and materials used in the sample cell produce a near hydrostatic pressure at its core where the powder is located inside a capsule made of niobium. The temperature inside the cell is controlled by driving a current through heating elements placed in the sample cell. Bulk specimens were sintered at 900 °C for 15 min and under 5.5 GPa of pressure. Typical sintering cycles were comprised of three steps: a heating ramp, a high temperature dwell and a natural cool down. The pressure was ramped up before the maximum temperature was reached and then slowly released after the cooling step. This procedure was necessary to avoid the pressure-transferring media to flash[1] between the anvils. The fine details of the sintering process and sample cell design cannot be disclosed for intellectual property reasons.

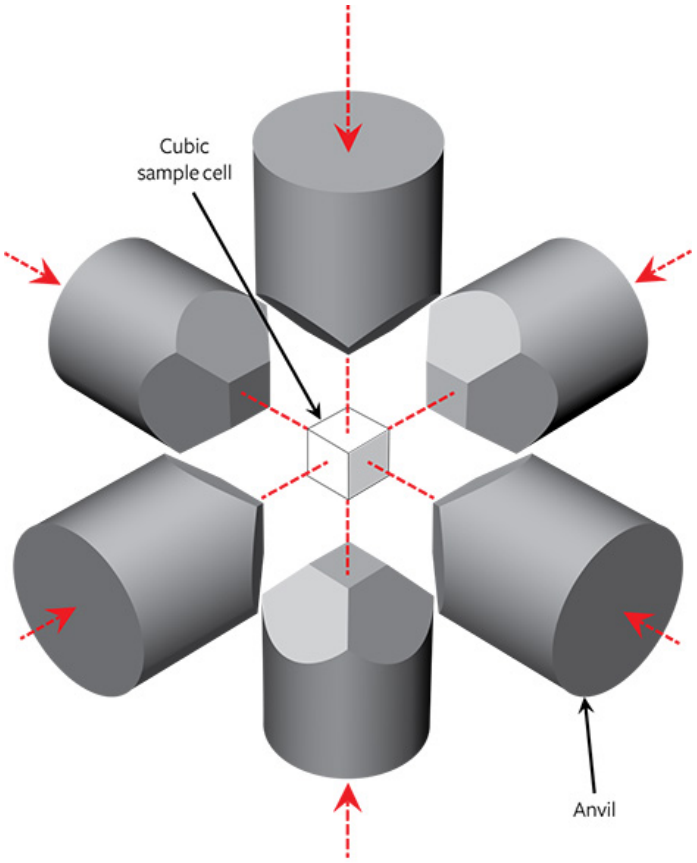

Figure 2.3: Schematic of the cubic press used at Element 6.

[1]Flashing refers to the flow of material between two surfaces of a mould.

2.2 Characterisation

All the sample preparation and material characterisation, except the high resolution analytical Scanning Electron Microscopy (SEM) and electrical transport measurements, have been done by myself at the Materials Department in Oxford. Dr Sangeeta Santra and Dr Tayebeh Mousavi performed SEM, Junliang Liu realised Transmission Kikuchi Diffraction (TKD) and Runsen Ma performed transport measurements. All the disc-shaped samples made by FAST or ultra high pressure hot pressing have been prepared in a systematic way for different characterisation techniques, as shown in Figure 2.4.

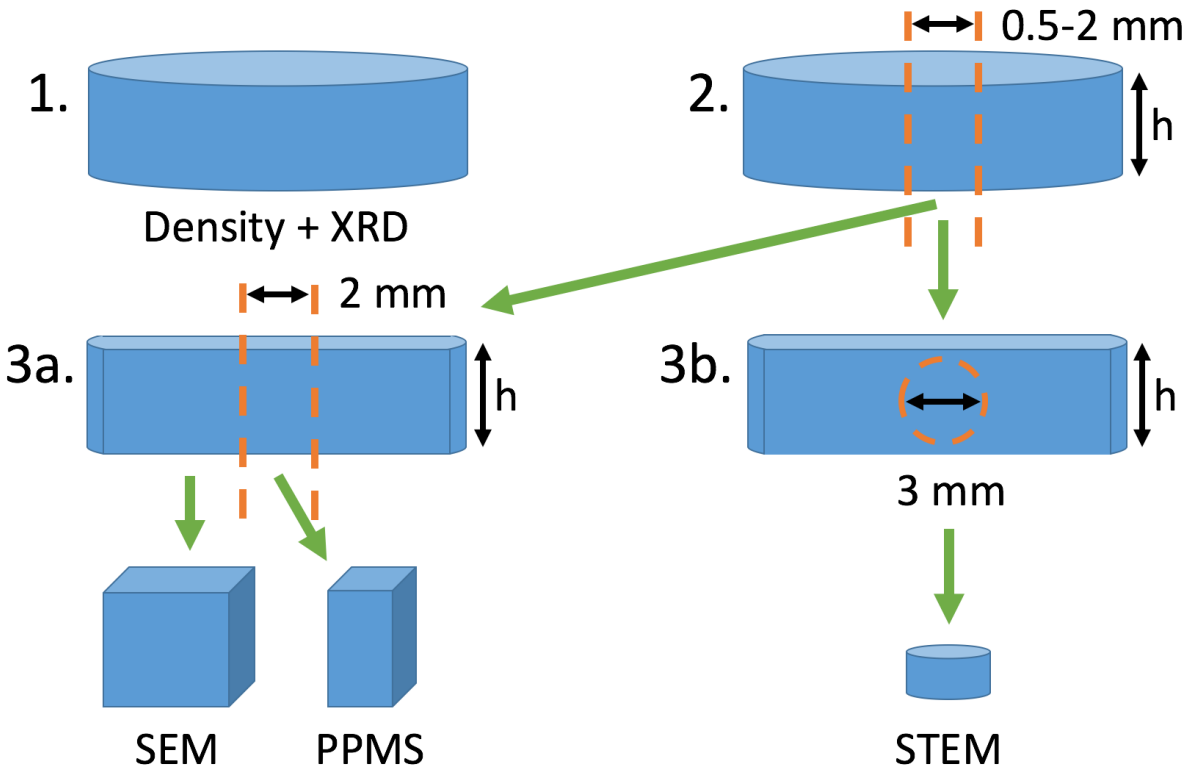

Figure 2.4: Schematic of the specimen preparation.

Density and XRD measurements were first realised on the whole disc. A first central slice with a thickness of approximately 2 mm was cut with a low speed saw equipped with a diamond blade. A cuboid with a cross section of $\sim$ 2 mm x 2 mm and a height equal to the initial disc thickness was then cut from the centre of that first slice. This cuboid specimen was used for magnetic measurements (PPMS) of superconducting properties. One of the off-cuts was used for SEM. For some specimens, two additional slices were cut and prepared for STEM and electrical transport measurements.

2.2.1 Density measurements

Most of the density measurements were performed on the whole specimen. After sintering, the specimen was coated with a thin layer of graphite paper which was removed using coarse SiC grinding paper before taking the measurements. The bulk density of the specimens, i.e. including both open and closed porosity, was measured using the Archimedes' method. Isopropanol was chosen as the measuring medium since MgB_2 reacts with water. The pellet was first weighed dry and then weighed again while immersed in isopropanol. The wet mass (when immersed) was recorded as soon as the pellet was fully immersed to give a measure of the total porosity. The bulk density was then computed using equation 2.1.

$$\rho = \frac{m}{V} = \frac{m_{dry}}{(m_{dry} - m_{wet})/\rho_{iso}} \tag{2.1}$$

Where m_{dry} and m_{wet} are the dry mass and the mass measured while immersed in isopropanol and $\rho_{iso} = 0.785$ g/cm^3 is the density of isopropanol. The measurement was repeated 3 times to ensure consistency and the mean value was used. The measurements were very consistent and the uncertainty was estimated to $\pm 0.5\%$ (relative density) for most of the specimens and up to $\pm 1\%$ for a few very porous samples. The relative bulk density was then computed by normalising the bulk density by the theoretical density calculated by using the sample composition estimated by XRD. The following density values were used for the different phases present in the consolidated samples: MgB_2 = 2.63 g/cm^3, MgO = 3.58 g/cm^3, MgB_4 = 2.49 g/cm^3, Mg = 1.74 g/cm^3.

2.2.2 Powder particle size analysis

The particle size distribution of powders was measured by using a Malvern Master-Sizer laser diffractometer. A small amount of powder was dispersed into deionised water and four 30 s long ultrasound cycles were used to break agglomerates. A first measurement was taken before the first ultrasound cycle and then four additional measurements were made after each ultrasound cycle. The measurement which gave the smallest median particle size was chosen. Two types of measurement will be presented in this work. The median particle size ($d_{0.5}$) is defined as the size at which 50% (in volume) of the particles in the sample are smaller and 50% are larger. The size distribution histogram gives the fraction (in volume %) of particles with a particular diameter.

2.2.3 X-ray Diffraction

The XRD measurements were performed using a PANalytical Empyrean diffractometer with Cu kα radiation ($\lambda = 0.154$ nm) at 40 kV and 40 mA and a Pixcel 1D scanning detector. A 5 mm incident beam mask and a programmable variable incident slit were used to provide a constant irradiated area of 5 mm x 5 mm on the specimen. $\theta - 2\theta$ measurements were carried out in a Bragg-Bretano geometry using a scan range of $2\theta = 5 - 120°$ with a step size of 0.013° and a time per step of 100 s. The lattice parameter, crystallite size, strain and weight fraction of the different phases present in the samples were estimated from the XRD spectra using Rietveld refinement. The following procedure was used to perform the Rietveld refinement using the PANalytical HighScore Plus software:

- The instrumental broadening was corrected by using a recent scan taken on a Si standard
- The background was fitted using the determine background function
- Peaks were located using the search peaks function
- MgB_2, MgO, MgB_4 and for some samples Mg or YB_4 reference patterns were found in the database and matched to the experimental peaks
- The experimental pattern was fitted using the Rietveld phase fit function
- The calculated patterns of the different phases were checked visually to ensure a good fit

The weight fraction of the different phases was estimated by using the Hill and Howard method [77], implemented in HighScore Plus. Instrumental broadening of peaks was corrected using a Si standard measured under the same beam optics and scan conditions.

Estimation of the uncertainty

Estimating the standard deviation of the parameters computed by Rietveld refinement is a difficult task which is often poorly performed [78–80]. The most common method uses the estimated standard deviation (esd) values, also called standard uncertainty (s.u.) calculated when fitting the computed data to the observed XRD data. The esd value is derived from statistical analysis

and represent the mathematical uncertainty coming from the misfit between the computed and observed data. The esd value mainly estimates the uncertainty coming from counting statistics and is often extremely small. This has led researchers to use another method which involves multiplying the esd value by the goodness of fit G defined by $G^2 = \chi^2$ [80]. These two methods have been strongly debated in the literature and only provide a reliable estimation of the uncertainty in specific cases [78–80].

A different approach was chosen to estimate the typical uncertainty. The precision rather than the accuracy of the values computed by Rietveld refinement was estimated by performing the same analysis on 11 different specimens made under identical processing conditions. By characterising 11 specimens instead of only 1, this method also gives an indication of the process reproducibility. Table 2.2 shows the values estimated by Rietveld refinement and the estimated precision which is defined by half the difference between the maximum and minimum value.

Sample	MgO [wt.%]	MgB_4 [wt.%]	MgB_2 crystallite size [nm]	MgB_2 strain [%]	MgO crystallite size [nm]	MgB_2 a-axis [Å]	MgB_2 c-axis [Å]
1	8.0	13.0	151	0.14	50	3.08377	3.52785
2	8.6	13.5	141	0.14	43	3.08374	3.52765
3	8.5	14.8	137	0.13	44	3.0837	3.52773
4	7.9	12.6	127	0.14	45	3.08391	3.52758
5	8.0	12.7	138	0.14	50	3.08354	3.52809
6	8.7	13.5	144	0.14	48	3.08358	3.52783
7	8.5	13.8	141	0.14	47	3.08361	3.52786
8	8.7	15.1	139	0.14	45	3.08371	3.52782
9	8.7	13.3	132	0.14	46	3.08361	3.52783
10	8.2	13.3	133	0.14	49	3.08377	3.52762
11	8.6	14.2	138	0.14	46	3.08372	3.52779
Precision	±0.4	±1.3	±12	±0.005	±4	±0.0002	±0.0003

Table 2.2: XRD characterisation of 11 bulk samples processed under the same conditions (5 min at 1150 °C, 50 MPa). The precision ($\frac{max-min}{2}$) is provided for each parameter.

Comparison with SEM and STEM measurements

It is good practice to compare the values of parameters (e.g. particle size or composition) derived from XRD with values obtained by a different characterisation technique, for instance SEM or STEM, to check that the XRD analysis is well calibrated and gives meaningful results.

The composition of a MgB_2 specimen sintered for 5 min at 1200 °C using FAST was characterised by XRD and SEM analysis. The method used to estimate the composition from backscattered SEM images is explained in the next section. The sample contained 8 ±0.4 wt.% MgO and 16 ±1.3 wt.% MgB_4 according to XRD and 7 ±1 MgO wt.% and 12 ±2.5 wt.% MgB_4 by SEM. Due to the sharp MgO contrast in the SEM images, the XRD and SEM values were in good agreement and the small difference was within the uncertainty. The amount of MgB_4 found by XRD was slighlty higher than by the SEM method. This can be explained by the following observations. First, MgB_4 peaks had a much smaller intensity than the two other phases. In consequence the signal to noise ratio of the MgB_4 peaks was lower which probably led to overestimating the MgB_4 fraction since these small peaks were difficult to fit. Secondly, the weak contrast between MgB_2 and MgB_4 in SEM images, and the porous nature of MgB_4 probably also caused the fraction of MgB_4 found by the SEM method to be underestimated. Nonetheless, both methods gave relatively similar results.

The YB_4 and MgO particle size of similar Y_2O_3-MgB_2 ODS samples sintered 5 min at 1150 °C by FAST were found by XRD and STEM analysis. XRD gave a particle diameter of 35 ±4 nm and 50 ±4 nm for YB_4 and MgO respectively. The corresponding particle diameters were 28 ±10 nm and 60 ±30 nm by STEM analysis. The values found by XRD and STEM were in good agreement and the small difference was within the uncertainty.

2.2.4 Scanning Electron Microscopy

SEM specimens were cut following the procedure shown in Figure 2.4 and mounted into carbon-loaded bakelite. Specimens were progressively ground using finer SiC grinding paper up to 4000 grit. Samples were then polished for approximately 30 min using colloidal silica.

The SEM analysis was performed by Dr Sangeeta Santra and Dr Tayebeh Mousavi in a Zeiss Merlin Field Emission Gun (FEG) SEM system operating at 10 kV, equipped with an Oxford Instrument 150 mm^2 Xmax EDX detector. SEM images were acquired with a backscattered electron (BSE) detector. Images acquired with a BSE detector show a contrast which is sensitive to the atomic number (Z contrast) and the crystallography.

Transmission Kikuchi Diffraction (TKD) investigations were carried out by Junliang Liu in a Zeiss Merlin Field Emission Gun (FEG) SEM system operating at 20 kV, equipped with a Bruker e-flash high resolution Electron Backscatter Diffraction (EBSD) detector and an OPTIMUS TKD head. The samples used for TKD were STEM specimens made by the procedure described in the next section.

Image processing

The volume fraction of the different phases present in MgB_2 specimens was estimated by measuring their area fraction from BSE SEM images. The area fraction was computed by image thresholding on contrast using the software Image J. A systematic method was used to ensure consistent estimation of the area fraction, as illustrated in the following example.

To estimate the volume fraction of the MgB_4 phase, low magnification images (250x) were used since the MgB_4 islands were relatively large (several tens of microns). The initial BSE image is shown in Figure 2.5.

The first step involved transforming the grey scale image into a binary image where the feature of interest, here the MgB_4 phase which has the darker contrast in the image, is separated from the rest of the image (background). This step is known as thresholding and was done manually using the interactive thresholding function in the Image J software. The result is shown in Figure 2.6. At this point, the area fraction of the dark phase can be computed simply as the ratio of the black pixels to the total number of pixels in the image. The area fraction of the dark phase in Figure 2.6 is 11.4%. Looking at the initial image in Figure 2.5, this value seems to underestimate the actual MgB_4 fraction.

Owing to the complex contrast in the image, a single thresholding operation does not give a good estimation of the area fraction of MgB_4. The problem mainly comes from the porous nature of MgB_4 which led to a non-uniform contrast within the MgB_4 islands. During the initial thresholding operation, lighter regions within the MgB_4 islands were assigned to the background and thus led to underestimate the MgB_4 area fraction. This is a classic image processing problem, which is well known in the steel community where the quantification of pearlite is made difficult by its zebra like contrast [81]. One way to solve this problem is to use mathematical morphology

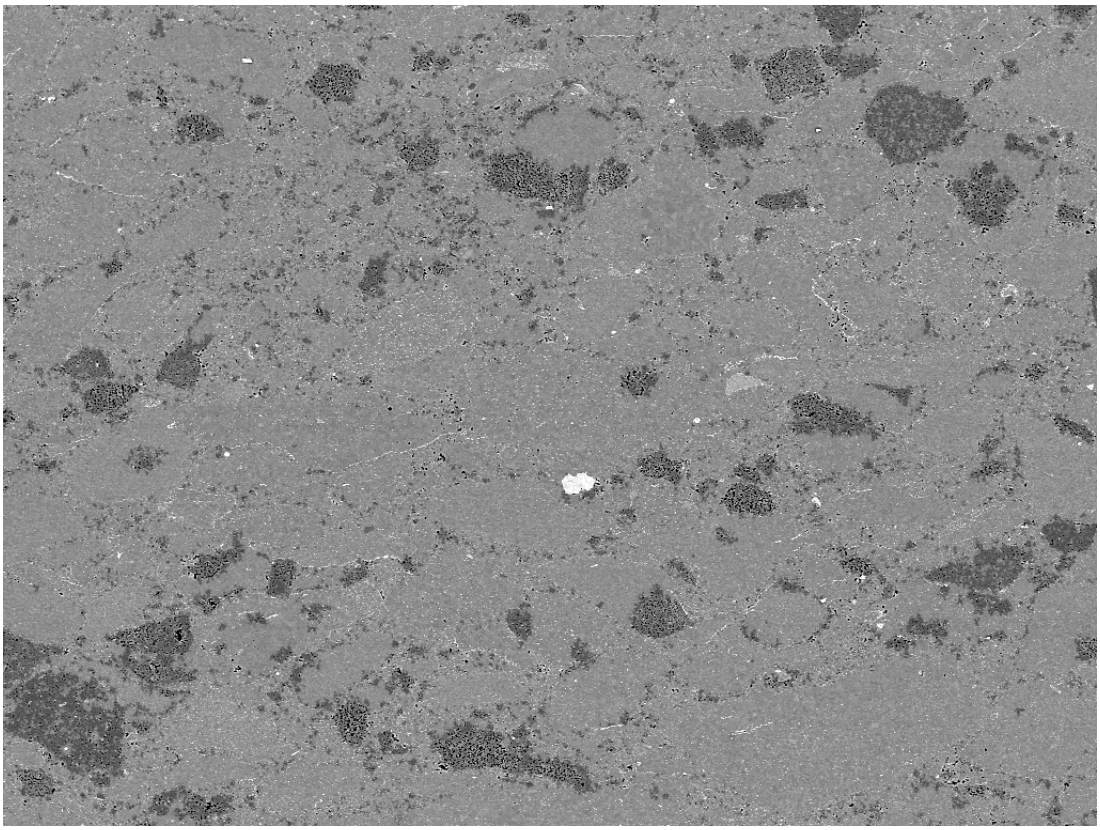

Figure 2.5: Initial backscattered image used for the image processing method (250x magnification).

operations to modify the binary image. The idea is to remove the white pixels in the MgB_4 islands to make them a solid black phase. This is exactly what the "closing" operation in Image J does by first dilating and then eroding[2] the image. The "Fill Holes" operation in the Image J software was also used after the closing operation to remove larger white pixel areas within the MgB_4 islands. The result of the closing and Fill Holes operations performed on Figure 2.6 is shown in Figure 2.7.

After performing the closing and Fill Holes operations on the thresholded image, the MgB_4 islands are solid and the area fraction of MgB_4 is now calculated as 16.8%. However, the image showed in Figure 2.7 can be further improved by removing the individual black pixels located in the middle of MgB_2 grains or at grain boundaries. These small regions correspond to porosity which was assigned to the MgB_4 phase during thresholding. This was performed using the "opening" operation which is an erosion followed by a dilation, the opposite of the closing operation. The result of this operation on Figure 2.7 is shown in Figure 2.8. After opening the image,

[2]Dilation and erosion are basic mathematical morphology operations defined by the following equations. Dilation of A by the structuring element B: $A \oplus B = \bigcup_{b \in B} A_b$. Erosion of A by the structuring element B: $A \ominus B = \bigcap_{b \in B} A_{-b}$

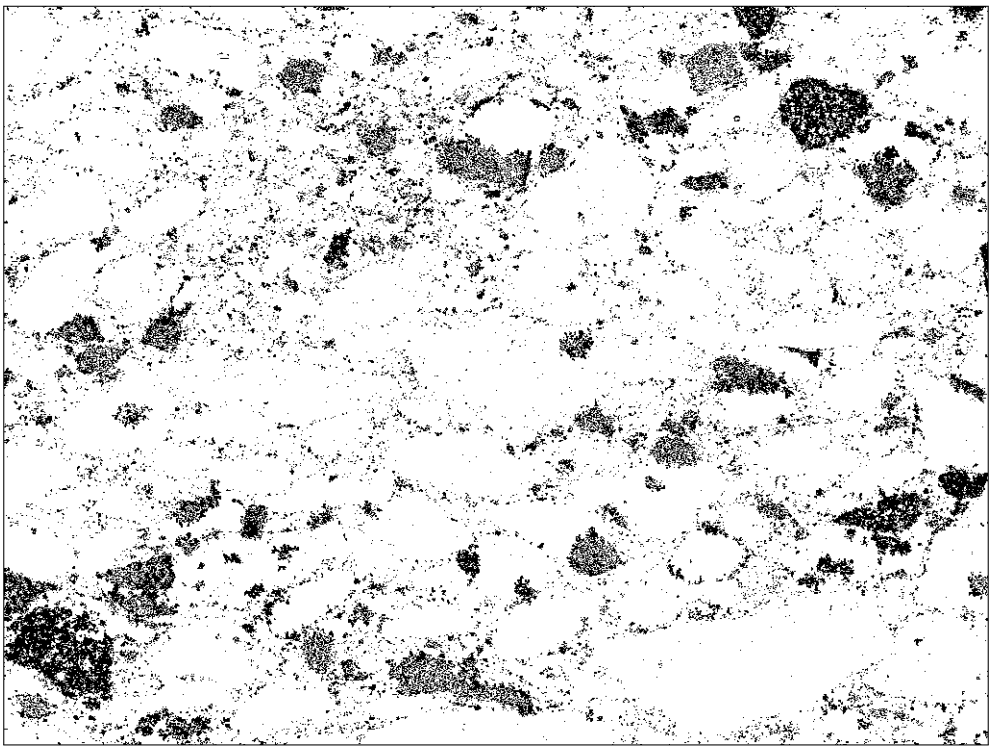

Figure 2.6: Binary image after the thresholding operation. MgB_4 is in black and the background is white (250x magnification).

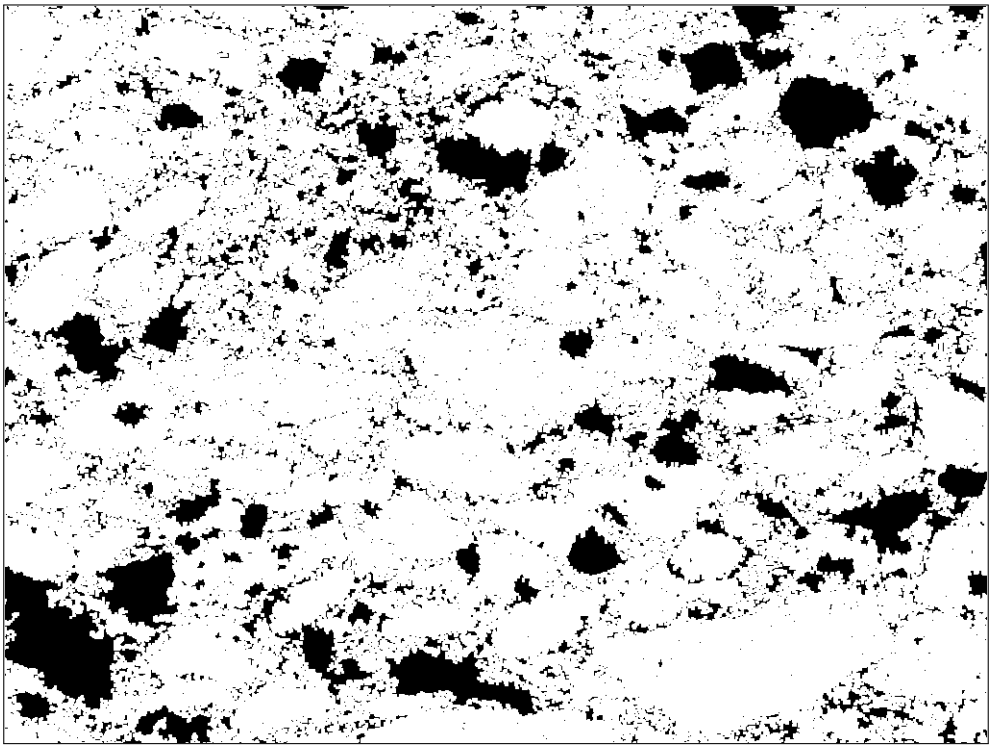

Figure 2.7: Binary image after performing the closing and Fill Holes operations. MgB_4 is in black and the background is white (250x magnification).

the MgB_4 area fraction is 13.4%. This procedure was repeated on 9 images taken from different areas of the same sample and averaged to give a volume fraction of 13 ±2.5 %.

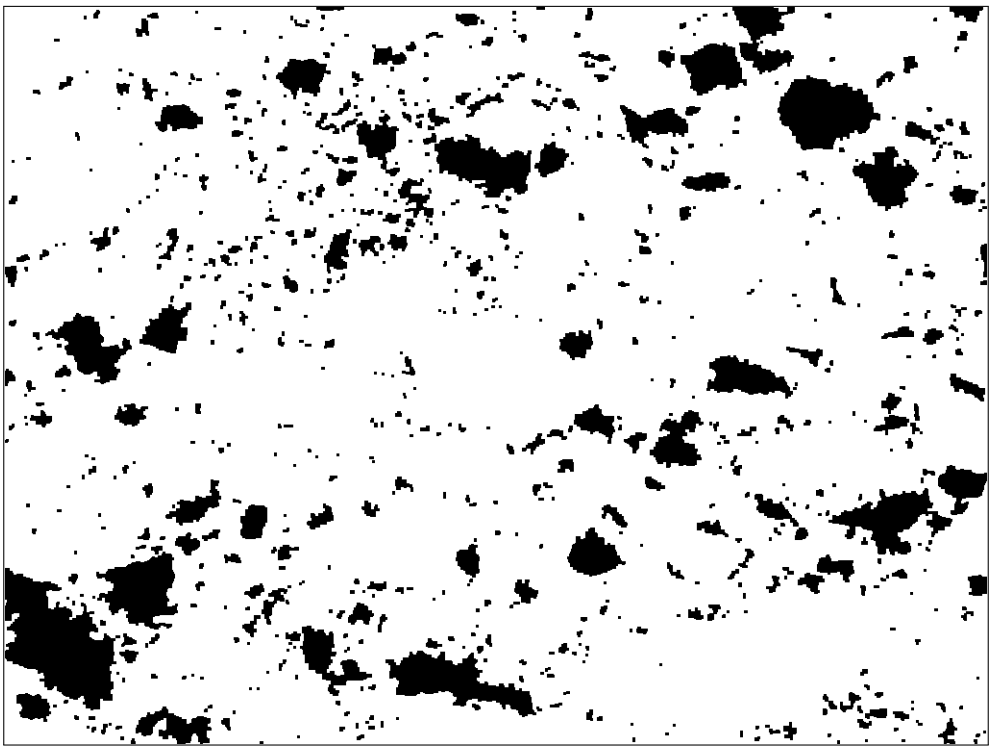

Figure 2.8: Binary image after performing the opening operation. MgB_4 is in black and the background is white (250x magnification).

Finding the fraction of MgO was a simpler task since MgO particles showed a clear bright contrast compared to the rest of the sample and had a solid nature. In the case of MgO, the thresholding and opening operations were carried out on higher magnification images (5000x). This procedure was performed on 9 different images and gave a MgO volume fraction of 5 ±1 %. Typical initial and modified images used for the MgO procedure are shown in Figure 2.5.

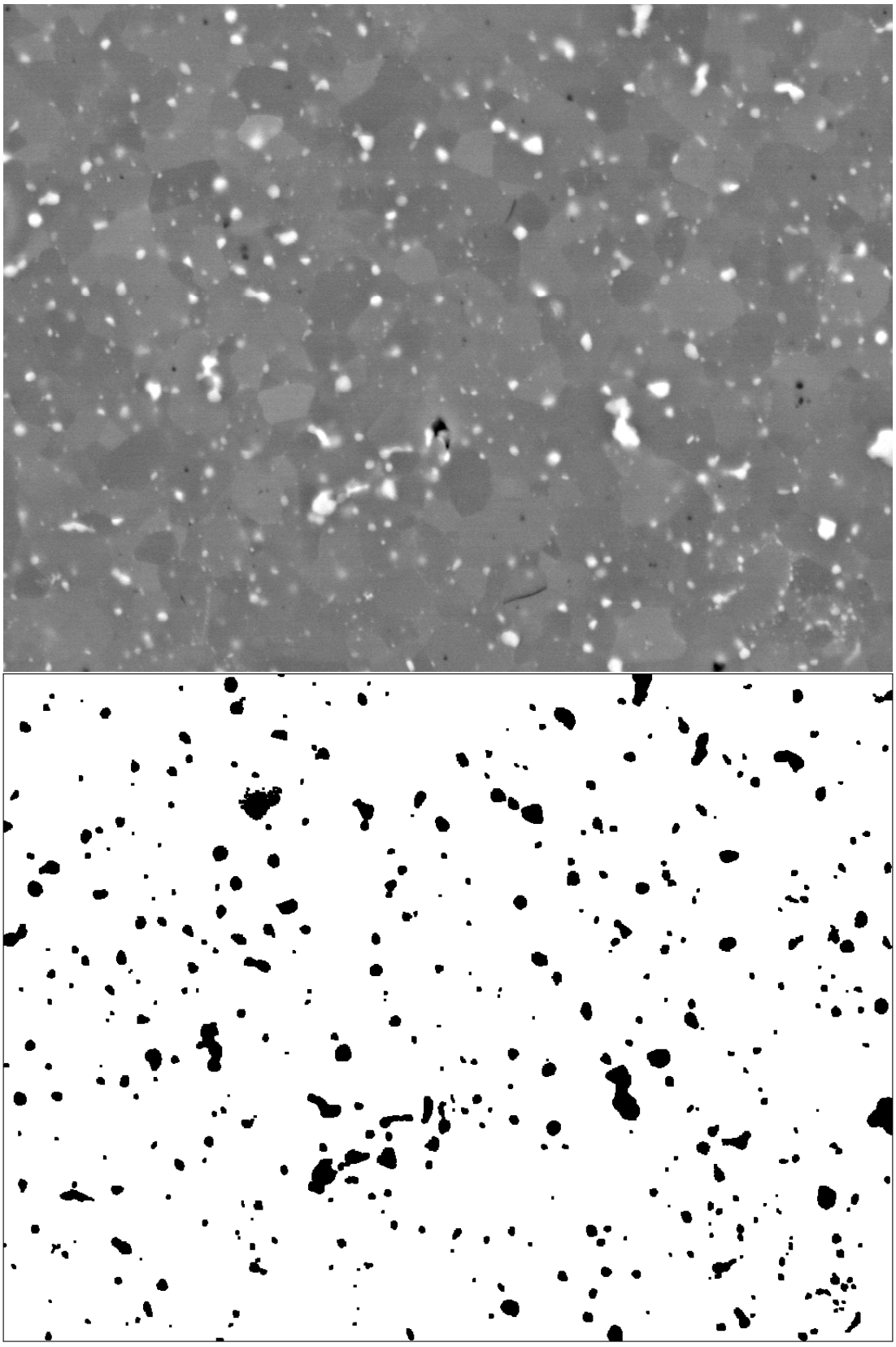

Figure 2.9: Initial grey scale image (top). Thresholded and opened image (bottom). In the binary image, MgO is in black and the background is white (5000x magnification).

2.2.5 Scanning Transmission Electron Microscopy

STEM MgB_2 specimens were found to be very difficult to prepare by the Focussed Ion Beam (FIB) lift-out technique due to the very low milling rate of MgB_2. If the sample was not lost or damaged during the FIB preparation, around 6 FIB sessions were required to prepare one specimen which due to the large number of FIB users and frequent instrument shut downs would take at least one month. Since, the STEM analysis was not site specific and due to time considerations, another preparation method was developed by myself. Specimens were typically prepared in less than a week with this method.

STEM specimens were prepared by cutting 3 mm discs from thin slices made from consolidated pellets, as shown in Figure 2.4. The slice was first thinned down manually using coarse SiC paper to approximately $300 - 350$ μm. A 3 mm disc was cut using a Gatan ultrasonic cutter with an oil-SiC slurry as the cutting medium. The discs were mechanically ground to approximately 100 μm by using fine SiC paper and a precision grinding wheel. The discs were then dimpled using a Gatan dimple grinder with an oil-SiC slurry before finally being thinned to perforation with a Fischione 1010 Ion Mill. Coarse milling was first realised at 15° and 10° using a voltage and current of 5 kV and 5 mA until a small hole was obtained at the centre of the specimen. A final polishing step was then performed at 6° and 4° using a voltage and current of 1 kV and 3 mA for a few minutes.

Some powders were also prepared for STEM analysis. A small amount of powder was first poured into a small beaker containing isopropanol. A fine suspension was created by putting the beaker in an ultrasound bath for 5 min. The STEM sample was finally made by dip coating a carbon coated copper grid into the suspension and letting the isopropanol evaporate.

The STEM analysis was performed in a JEOL 3000F TEM at an accelerating voltage of 300 kV, equipped with a High Angle Annular Dark Field (HAADF) detector and an Oxford Instruments EDX detector. Initially, images were acquired with a probe size of 1 nm and a camera length of 12 cm. Unfortunately, the 3000F had a significant breakdown which lead to the STEM instrument being unavailable for almost 6 months. After repair, the 3000F could only be operated at 200 kV and with a fixed camera length of approximately 25 cm in STEM mode, which was not appropriate for my STEM work. In consequence, the images acquired later in the project are not as well defined in terms of contrast between the MgB_2, MgO and YB_4 phases.

Due to the sample preparation method it was difficult to find an amorphous region which made the STEM alignments more difficult than with standard FIB lift-out specimens. In order to obtain good alignments in STEM mode, the following procedure was developed:

- The 3 mm disc was placed on a double tilt holder and the microscope was first aligned in TEM mode.
- A suitable area was found and the height of the specimen was adjusted. The X, Y and Z values of the specimen position were written down.
- The sample holder was taken out of the TEM with the specimen left inside.
- A carbon coated copper grid was placed in a second specimen holder and the microscope was aligned in STEM mode using the Ronchigram formed with the carbon film.
- The second sample holder was taken out and the first sample holder was put back in the microscope without changing any of the settings.
- The specimen was moved back to the X, Y and Z values written down in step 2.

2.2.6 Magnetic measurements

PPMS

Magnetic measurements were acquired with a Quantum Design Physical Property Measurement System (PPMS) Vibrating Sample Magnetometer (VSM) on cuboid samples cut from consolidated discs as shown in Figure 2.4. The cuboid samples had a cross section of approximately 2 mm x 2 mm and a length between 3 and 5 mm, depending on the density of the disc. The magnetic field was applied parallel to the long axis of the specimen, which is the pressing direction during sintering. A few powder samples were also prepared by packing a small amount of powder in a PPMS powder capsule.

Two types of measurements were taken on bulks and powders. First, a zero field cooled (ZFC) curve was obtained by cooling the specimen to 10 K (below the superconducting transition temperature) followed by applying a small field of 5 mT ($H_{c1}(10K) \sim 20$ mT for MgB_2 bulks [24]). The magnetic moment of the specimen was then measured while the temperature of the cryostat

increased up to 42 K. This measurement was used to find the critical temperature (T_c) of the specimen. Second, magnetic hysteresis loops were measured at 4.2 K and 20 K. The specimens were first cooled to the measuring temperature without applying any magnetic field. Then the field was ramped up and down at 50 Oe/s according to the following 5 quadrants sequence:

- 1: 0 T → -4 T
- 2: -4 T → 0 T
- 3: 0 T → 10 T
- 4: 10 T → 0 T
- 5: 0 T → -4 T

At 20 K the field was ramped between -2 T and 8 T because the irreversibility field (B_{irr}) was smaller at higher temperature.

MPMS

Magnetisation measurements were acquired with a Quantum Design Magnetic Property Measurement System 3 (MPMS-3) SQUID Magnetometer on powder samples. A small amount of powder was weighted using a high precision scale and then packed in a powder capsule.
ZFC curves were obtained by cooling the specimen to 6 K and then applying a small field of 1 mT. The magnetic moment of the specimen was then measured while the temperature of the cryostat increased up to 42 K. This measurement was used to find T_c of the powders.

Estimating the superconducting transition temperature (T_c)

In this work, the superconducting transition was defined by 3 values: T_c, onset T_c and offset T_c. The critical temperature (T_c) was defined as the temperature where the slope of the ZFC curve was the steepest. T_c was computed by finding the temperature at which the derivative of the ZFC curve was maximum, as shown in Figure 2.10. The onset and offset of the superconducting transition were taken as the intersection between a linear fit of the transition and the normal and superconducting plateaus respectively, as illustrated in Figure 2.11. All the data processing was performed using functions that I wrote in MATLAB.

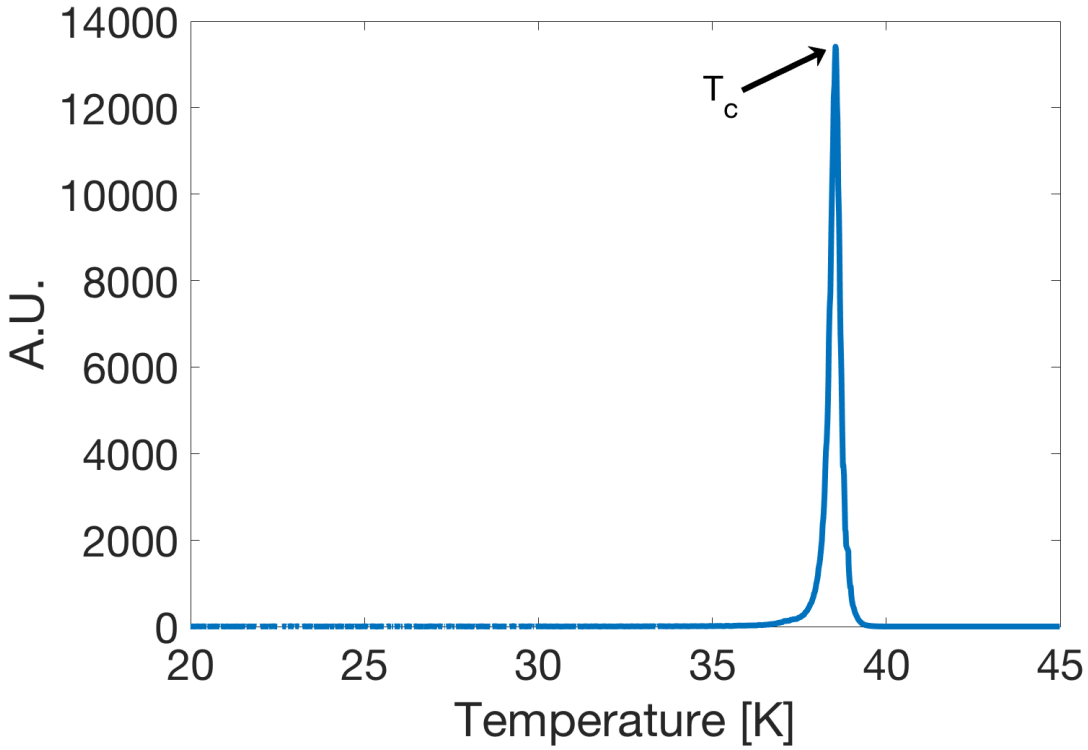

Figure 2.10: Method used to find T_c from the derivative of ZFC curves.

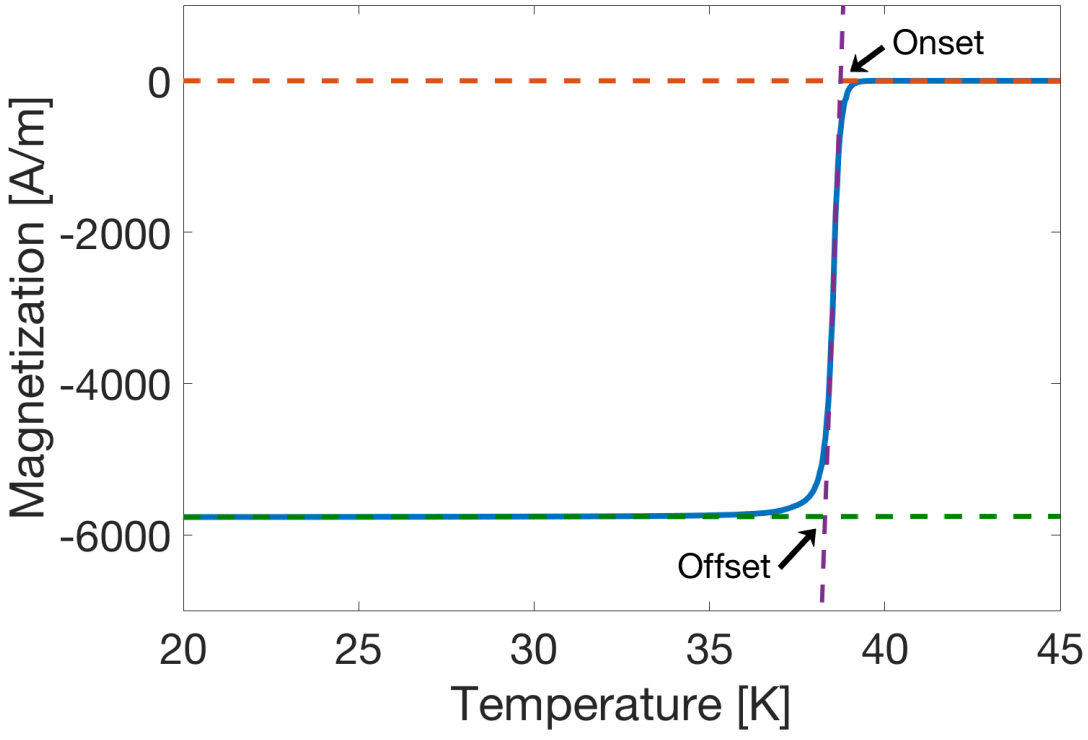

Figure 2.11: Method used to find onset T_c and offset T_c values from ZFC curves.

Estimating the critical current density (J_c)

For solid specimens, J_c values are usually extracted from $\Delta M - B$ data using the standard Bean model for samples with dimensions a, b and c with the applied field $\parallel$ c and $b > a$, given in equation 2.2 [16].

$$J_c = \frac{2\Delta M}{a(1 - \frac{a}{3b})} \tag{2.2}$$

where ΔM is the width of the magnetic hysteresis loops ($M - B$), as shown in Figure 2.12, and defined as $\mid \Delta M \mid = \frac{|m_+ - m_-|}{V} = 2M_{irr}$, where m_+ and m_- are the magnetic moments corresponding to the increasing and decreasing field branches respectively, M_{irr} is the irreversible component of the magnetisation and V is the sample volume.

This model assumes that circulating supercurrents flow macroscopically around the entire specimen. This ideal case corresponds to a fully dense, homogeneous and well connected sample as represented in Figure 2.13 (b). In this case, the macro-scale J_c value estimated from the Bean model is a good approximation of the intrinsic (intragrain), micro-scale J_c.

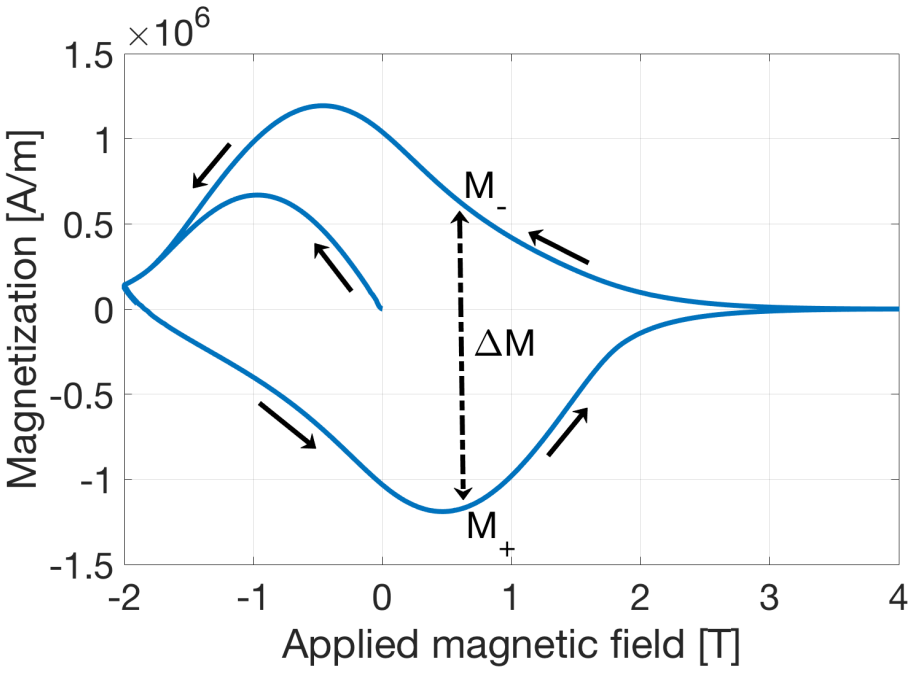

Figure 2.12: Typical hysteresis loops plotted as magnetisation versus applied field ($M - B$).

Figure 2.13 (a) shows a schematic microstructure of a poorly sintered material in which supercurrents are only able to circulate within the particles (each of which may contain many micron-sized grains) owing to the poor particle connectivity. In that case, the total magnetic moment gen-

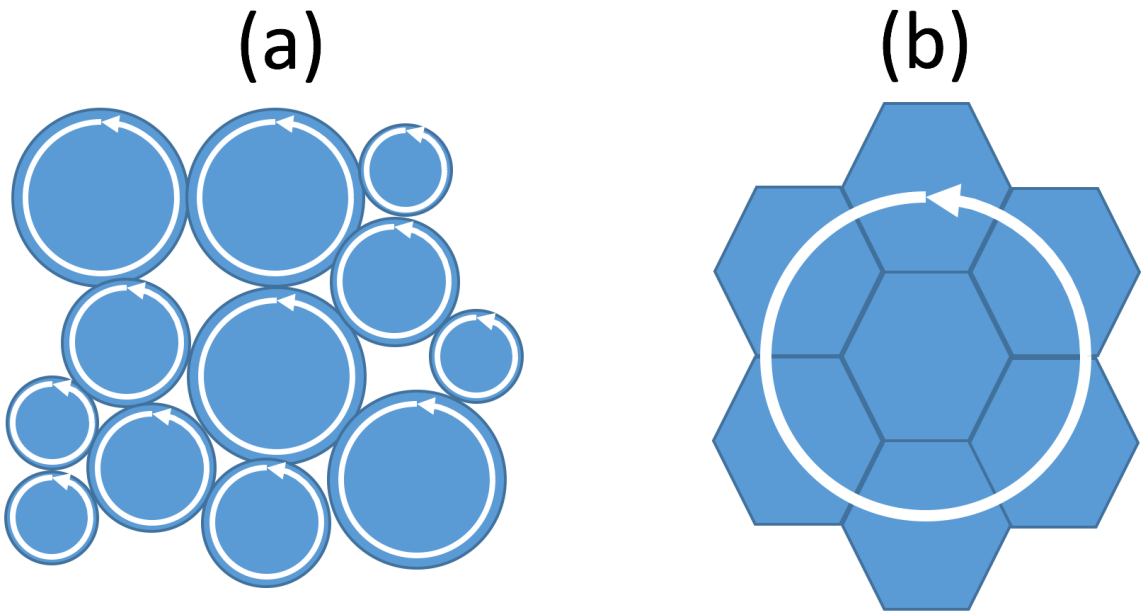

Figure 2.13: (a) A porous and poorly connected microstructure leading to small intraparticle supercurrent loops. (b) A dense and well connected microstructure resulting in large intergranular supercurrent loops.

erated by these micro-scale supercurrents is much smaller, and the J_c values extracted using equation 2.2, which assumes currents are circulating around the entire sample, will dramatically underestimate the micro-scale J_c values inside the particles. A different model is commonly used to estimate intragrain J_c values of poorly connected materials [82]. In the case of cuprate HTS, where the grain boundaries act as weak links, the average grain size is used to compute intragrain J_c values, instead of the macroscopic dimensions of the specimen. However, grain boundaries in MgB_2 do not act as weak links and thus another length scale needs to be considered: the powder particle size.

The micro-scale model considers that the sample is made of individual (spherical) particles that are electrically isolated from one another (i.e. supercurrents cannot flow between adjacent particles). In this case, the particle median size ($d_{0.5}$) is used in Bean's model, instead of the dimensions of the whole sample, to calculate J_c using equation 2.3.

$$J_c = \frac{32}{3\pi}\frac{\Delta M}{d_{0.5}} \tag{2.3}$$

The macro and micro-scale models give estimated lower and upper bounds of the material intrinsic J_c.

The micro-integral model

The micro-scale model introduced in the previous section is based on the strong assumption that the specimen is composed of identical particles with a diameter equal to the median size $d_{0.5}$. However, this model poorly represents real powders which often show a complex size distribution. In order to obtain a better estimation of J_c for powders and poorly connected materials, I have developed the micro-integral model.

The micro-integral model is similar to the micro-scale model and also assumes that the specimen is composed of individual spheres that are electrically insulated from each other. However, instead of assuming that the specimen is made of identical spherical particles of diameter $d_{0.5}$, the model considers the actual particle size distribution of the powder or sintered material. The powder particle size distribution can be measured with a laser diffractometer and most instruments provide a size distribution in the form of the volume fraction of particles of a specific diameter d. Let us define $f_v(r)$, which is the size distribution measured by the laser diffractometer and expressed in radius. $f_v(r)$ can be normalised to obtain the probability density function $p_v(r)$ defined by equation 2.4 and which satisfies equation 2.5.

$$p_v(r) = \frac{f_v(r)}{\int_0^\infty f_v(r)dr} \tag{2.4}$$

$$\int_0^\infty p_v(r)dr = 1 \tag{2.5}$$

Let us now consider a sample of volume V_{tot} composed of particles that follow the probability density function $p_v(r)$ defined in equation 2.4. The number of particles of radius r in this sample of volume V_{tot} can be expressed by equation 2.6.

$$N(r) = \frac{V_{tot} \cdot p_v(r)}{V(r)} = \frac{V_{tot} \cdot p_v(r)}{\frac{4}{3}\pi r^3} \tag{2.6}$$

Using Bean's model for a superconducting sphere of radius r, equation 2.7 can be derived.

$$\Delta m(r) = \frac{J_c \pi^2 r^4}{4} \tag{2.7}$$

Where $\mid \Delta m \mid = \mid m_+ - m_- \mid = 2m_{irr}$ and m_+ and m_- are the magnetic moments corresponding

to the increasing and decreasing field branches of a magnetic hysteresis loop ($m-B$) respectively, m_{irr} is the irreversible component of the moment.

Let us now consider a macroscopic specimen composed of a large number of spherical particles that follow a size distribution described by the probability density function $p_v(r)$. The width of the hysteresis loops, Δm_{tot}, measured for the macroscopic specimen is the sum of all the microscopic $\Delta m(r)$ generated by spherical particles of radius r. By combining equations 2.6 and 2.7, equation 2.8 is obtained.

$$\Delta m_{tot} = \int_0^\infty N(r)\Delta m(r)dr = \int_0^\infty \frac{V_{tot}\cdot p_v(r)}{\frac{4}{3}\pi r^3}\frac{J_c\pi^2 r^4}{4}dr = J_c V_{tot}\frac{3\pi}{16}\int_0^\infty p_v(r)rdr \tag{2.8}$$

Finally, an expression for J_c can be obtained by rearranging equation 2.9:

$$J_c = \frac{16}{3\pi}\frac{\Delta m_{tot}}{V_{tot}}\frac{1}{\int_0^\infty p_v(r)rdr} = \frac{16}{3\pi}\frac{\Delta M}{\int_0^\infty p_v(r)rdr} \tag{2.9}$$

The micro-scale model expressed by equation 2.3 is a particular case of the micro-integral model. If the specimen is made entirely of identical powder particles of diameter $d_{0.5}$ then it follows that $\int_0^\infty p_v(r)rdr = \frac{d_{0.5}}{2}$ and equation 2.9 reduces to equation 2.3. In order to evaluate the difference between the micro-scale and micro-integral model, $J_c(B)$ of the unmodified MgB_2 powder was computed using both models, as shown in Figure 2.14. There is almost a factor 3 between the two models, which is a significant difference. The micro-scale model tends to overestimate J_c due to the assumption that the powder particles follow a perfect monomodal size distribution. In fact, real powders usually show much more complex particle size distributions, as shown in figure 2.15. By considering the actual particle size distribution the micro-integral model gives a better estimation of J_c values in powders and poorly connected materials.

The comparison between the two models was also made with ball milled powders which often show more complex particle size distributions than sieved commercial powders. The size distributions of powders ball milled between 10 min and 12 h are shown in Figure 2.15 along with the unmilled powder. The difference in J_c values between the micro-scale and micro-integral models is shown for these powders in Figure 2.16. For powders ball milled more than 3 h, there

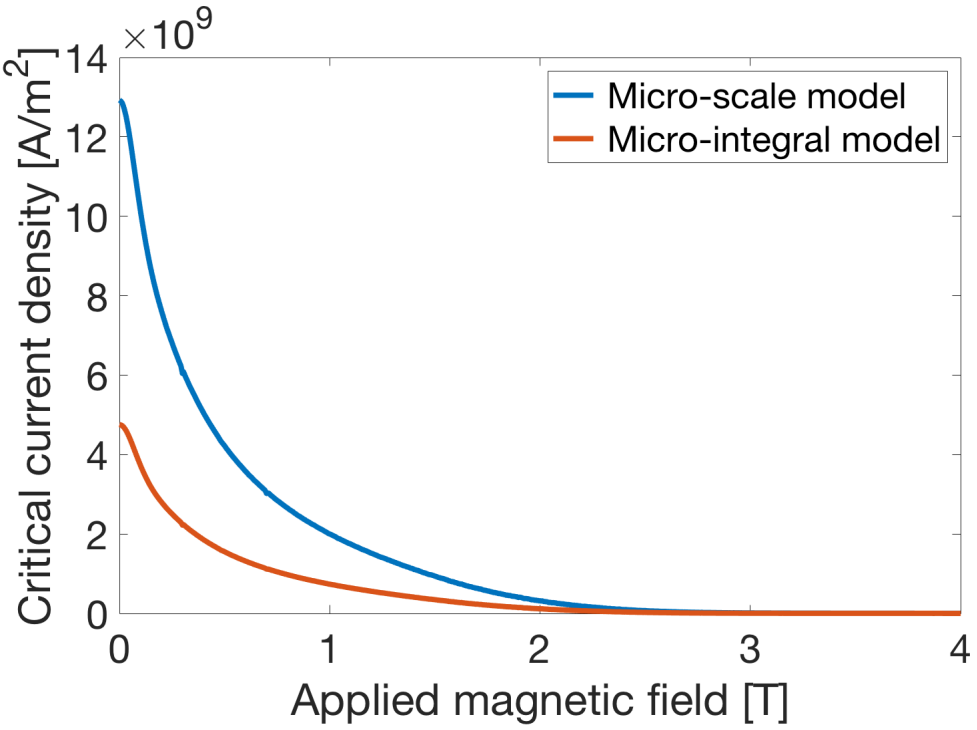

Figure 2.14: Comparison of the $J_c - B$ curves of MgB_2 powder computed with the micro-scale and micro-integral models.

was almost a factor 70 between the J_c values computed with the two models. These results indicate that for milled powders showing a complex particle size distribution, the micro-scale approximation is inadequate and substantially overestimates J_c.

Estimating B_{irr}

The irreversibility field (B_{irr}) values were estimated using the same method as Martinez *et al.* [83] by extrapolating the high field region of Kramer plots ($B^{\frac{1}{4}} J_c^{\frac{1}{2}} - B$), ignoring the tail which is attributed to flux creep. B_{irr} values were computed by finding the intersection between the linear regression of the high field region of the Kramer plots and the x axis. Since the Kramer plots were not linear, the uncertainty in B_{irr} values was estimated by interpolating different intervals of the high field region of the plots. The uncertainty was found to be as high as ± 0.5 T for some specimens. In addition, our magnetisation measurements were realised in VSM mode which can lead to the underestimation of the true irreversibility field due to the field inhomogeneity the sample is exposed to as it vibrates [84].

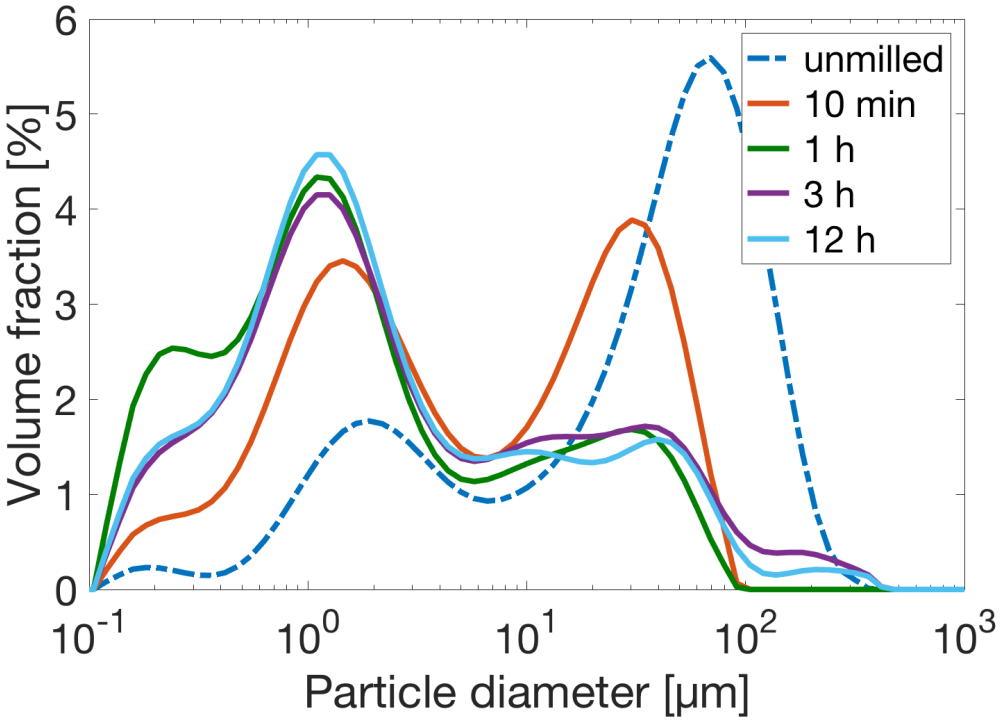

Figure 2.15: Powder size distributions of MgB_2 powders ball milled between 10 min and 12 h and the unmilled powder.

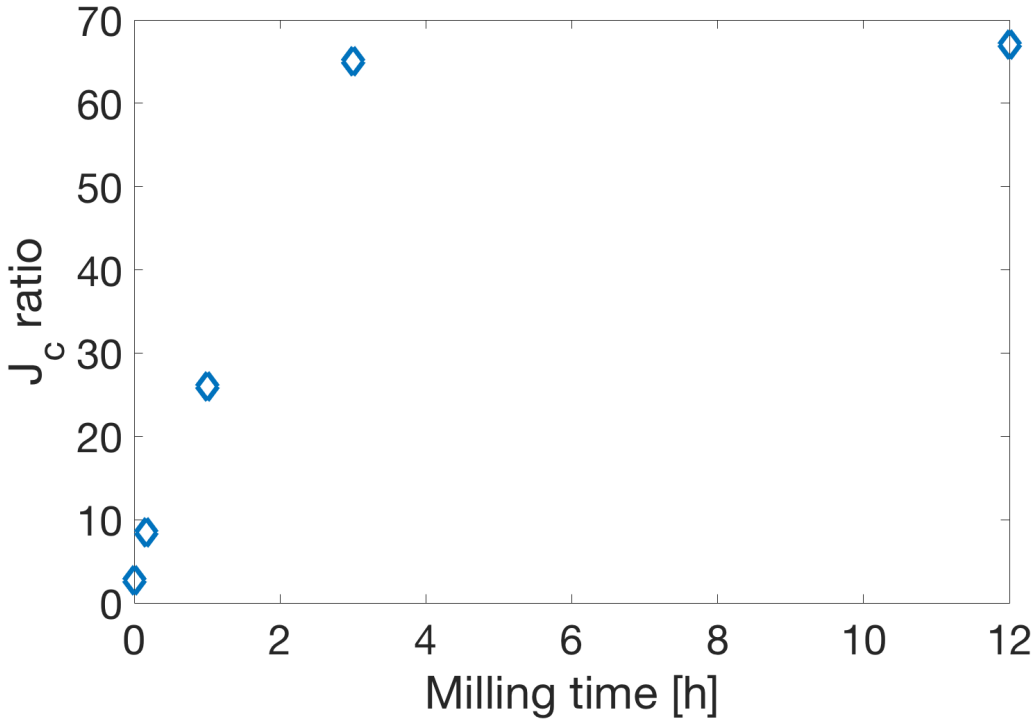

Figure 2.16: Ratio between the J_c values estimated with the micro-scale and micro-integral models for powders ball milled between 10 min and 12 h and the unmilled powder.

2.2.7 Transport measurements

To estimate the effective cross-sectional area for macroscopic current transport in bulk samples, four-point transport measurements have been peformed by Runsen Ma. The normal state electrical resistivity was obtained as a function of temperature. Measurements were performed using a CTICryogenics closed cycle helium cryocooler (22C CRYODYNE) using samples $2.6 - 4.8$ mm in width and $0.6 - 0.8$ mm thick, with voltage taps 4 mm apart. A DC current of 0.2 A was provided by a Keysight E36311A Programmable DC Power Supply and a Keithley 2000 Digital Multimeter was used to measure the voltage. Gold coatings were first made by plasma deposition using a mask with 2 mm wide slits. The contacts were then made on these gold coated regions using electrodag.

Following the analysis of Collings *et al.* [85], the Bloch-Gruneisen function (2.10) was fitted to the data, enabling to extract the residual resistivity ρ_0, the Debye temperature θ_D, and the scale factor F, which is related to the percentage connectivity by $K = \frac{146}{F}$ [85, 86]. To obtain the materials constant k, equation 2.10 was initially fitted to the reference single crystal data from Eltsev *et al.* [87].

$$\rho(T) = F\left[\rho_0 + \frac{k}{\theta_D}\left(\frac{T}{\theta_D}\right)^5 \int_0^{\theta_D/T} \frac{z^5 dz}{(e^z - 1)(1 - e^{-z})}\right] \tag{2.10}$$

Chapter 3

Sintering MgB_2 by FAST

The aim of this part of the project was to investigate the influence of the sintering temperature on the microstructure and superconducting properties of MgB_2 bulks manufactured by FAST using unmodified MgB_2 powder.

Sample details

Table 3.1 describes the manufacturing conditions used for MgB_2 specimens analysed in this section. In order to understand the effect of the temperature on the microstructure and superconducting properties, 4 sintering temperatures were chosen between 900 and 1200 °C, and the other process parameters were kept constant. Several research teams have successfully manufactured dense MgB_2 bulks by FAST using sintering times between 1 and 30 min and uniaxial pressure ranging from 16 to 95 MPa. [31,39,43]. In particular, Dancer *et al.* [39] obtained 97% dense specimens by sintering commercial MgB_2 powder at 1200 °C for 5 min under a pressure of 50 MPa. They showed that densification was enhanced with higher pressure, which is commonly observed for most sintered materials [45,46]. I decided to choose a pressure of 50 MPa because it is the highest pressure that can be safely used when using graphite dies and punches in the DSP 507 FAST apparatus described in section 2.1.2. Pressure above 50 MPa were found to cause graphite dies and punches to break during the sintering process.

Aldica *et al.* [31] manufactured MgB_2 bulks using sintering times between 1 and 20 min and showed that the sintering time had only a small influence on the density and superconducting properties of the bulks. I chose to use a sintering time of 5 min to keep the sintering process relatively short.

Initial Powder	Sintering T [°C]	Sintering time [min]	Heating rate [°C/min]	Pressure [MPa]
MgB_2	900	5	120	50
MgB_2	1000	5	120	50
MgB_2	1100	5	120	50
MgB_2	1200	5	120	50

Table 3.1: Processing conditions for MgB_2 bulks manufactured by FAST

The heating rate is well known to influence the densification and grain growth kinetics in sintered materials [45, 46, 50]. Fast heating rates are preferred because bypassing the low temperature sintering steps favours densification over coarsening and can produce materials with both high densities and fine microstructures. For this reason, I decided to use the maximum heating rate that also gave stable temperature control [1], and this was found to be approximately 120 °C/min for the setup used in the DSP 507 FAST apparatus.

XRD and density measurements

XRD patterns of MgB_2 samples processed between 900 and 1200 °C are presented in Figure 3.1, and Table 3.2 shows the results of the XRD analysis (described in section 2.2.3) and the density measurements. The relative density of the samples was found to increase systematically with processing temperature[2], from 68% up to 96% for the specimens sintered at 900 and 1200 °C respectively. The differences in density observed between these four specimens were much larger than the uncertainty estimated to ±1%, as discussed in section 2.2.1. The relative density of the 1200 °C specimen was very similar to the value of 97% measured by Dancer *et al.* [39] on a bulk sample manufactured at 1250 °C by FAST. Shim *et al.* [43] also observed an increase in density with higher sintering temperatures. However they measured unusually high relative density values for their samples processed between 900 and 1050 °C. In particular, their sample sintered 10 min at 1050 °C had a density above 99% which is higher than the density of my sample sintered at 1200 °C and the specimen made by Dancer *et al.* [39] at 1250 °C. This could be caused by a difference in the manufacturing process or the measurement method. First, the authors do not mention how and where the temperature was recorded, which could lead to a

[1] In systems controlled by a PID controller there is a trade-off between the response time and the stability of the system. In the case of FAST, if the PID controller is set to give a very sharp response (i.e. high heating rates), the system stability is degraded and the overshoot and settling time increase.

[2] This behaviour is expected for most sintered materials due to faster diffusion rates at high temperature [45].

large difference between the measured temperature and the actual temperature of the powder inside the die. If the temperature was measured with a pyrometer on the external surface of the die, the actual temperature inside the die could be much higher, which could explain the higher density values.

Second, both Dancer and I have calculated the relative density by considering the fraction of MgO in the bulk pellets[3]. Shim *et al.* do not give any details about the procedure they used to compute density. If the authors did not consider the MgO fraction, the density values will be overestimated.

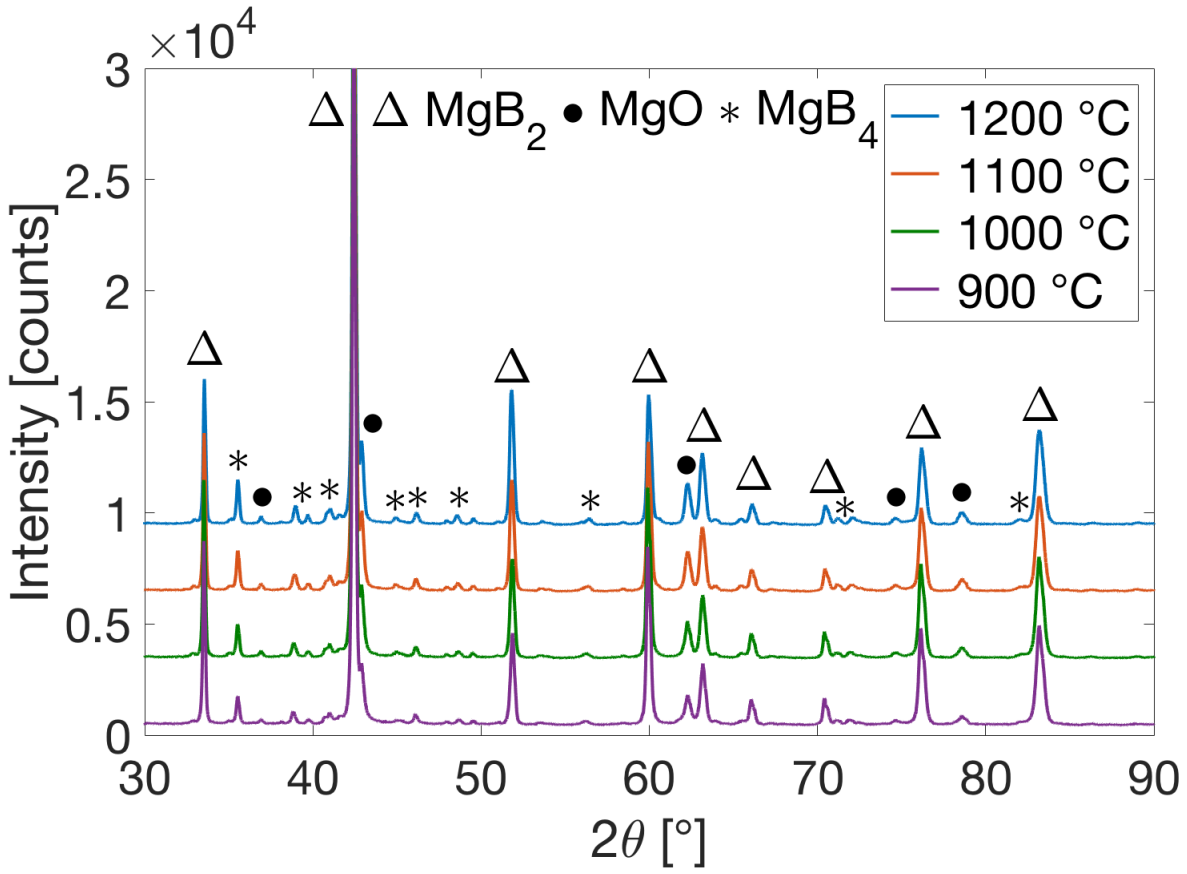

Figure 3.1: XRD patterns of MgB_2 samples processed at 900, 1000, 1100 and 1200 °C.

The precision of the XRD analysis was discussed in section 2.2.3. Most of the trends observed below were based on differences between samples that were larger than the uncertainty estimated in Table 2.2. Table 3.2 shows that the impurity phase content in the bulk samples increased with increasing processing temperature. The MgO content increased slightly from 5 wt.% in the as-received powder up to 8 wt.% in the sample sintered at 1200 °C. The amount of MgB_4 increased

[3]MgO has a density of 3.58 g/cm^3 which is significantly higher than MgB_2 at 2.63 g/cm^3

Sample	MgO [wt.%]	MgB_4 [wt.%]	Relative density [%]	MgB_2 crystallite size [nm]	MgB_2 strain [%]	MgO crystallite size [nm]	MgB_2 a-axis [Å]	MgB_2 c-axis [Å]
Powder	5	7	-	100	0.11	45	3.086	3.524
900 °C	7	11	68	120	0.12	30	3.085	3.525
1000 °C	8	13	75	130	0.12	38	3.085	3.526
1100 °C	8	16	86	140	0.13	44	3.084	3.527
1200 °C	8	16	96	170	0.14	54	3.084	3.528

Table 3.2: XRD characterisation and relative density of the bulk samples sintered between 900 and 1200 °C using the FAST, and the as-received MgB_2 powder.

more significantly, reaching 16 wt.% in the sample processed at 1200 °C, more than double the concentration found in the as-received powder. This trend has also been observed by several other research teams [30,39,42]. In particular, Habler *et al.* [30] reported a slightly higher MgO fraction and a large increase in MgB_4 with higher sintering temperatures. Dancer *et al.* [39] measured a MgO fraction of 7.3 wt.% in a sample processed at 1250 °C, which is in good agreement with the 8 wt.% estimated for my specimen made at 1200 °C. The decomposition reaction $2MgB_2 \rightleftharpoons MgB_4 + Mg_{(g)}$ that occurs above $\sim$ 900 °C [26,32], explains the increase in MgB_4 at higher processing temperatures.

In addition, MgB_2 crystallite size was found to increase systematically with temperature, reaching 170 nm in the highest temperature sample compared to 100 nm in the as-received powder. A similar trend was observed for MgO, with the sample processed at 1200 °C having an average MgO size almost twice that in the specimen sintered at 900 °C. However, the MgO crystallite size of the as-received powder was larger than for the bulk samples sintered at 900 and 1000 °C. This may indicate the formation of fine MgO particles during the sintering process, lowering the average crystallite size compared to the as-received powder. Indeed, all the consolidated samples showed higher MgO fractions which suggests that new MgO particles were formed during sintering. The sintering process being performed under a vacuum of 0.5-1 mbar, it is likely that a small amount of residual oxygen was still present in the chamber and reacted with MgB_2 at high temperature to form MgO.

The a-axis lattice parameter was found to decrease with increasing processing temperature, as previously observed by Aldica *et al.* [31] in samples processed at the same temperature but for longer dwell times. They attributed this effect to a higher level of carbon substitution (coming from the graphite die) which is well known to reduce the a-axis lattice parameter

of MgB_2 [33]. Higher processing temperatures can have a similar effect to longer sintering times by increasing the diffusion rate of carbon in MgB_2, potentially leading to a higher carbon content in the specimens manufactured at higher temperatures. However, a slight increase in c-axis lattice parameter was also observed with higher processing temperatures, which is not expected for carbon doping. The inhomogeneous strain, derived using Rietveld analysis from the peak broadening, increased slightly with processing temperature. This could be because larger residual strains were induced when cooling from higher sintering temperatures. Alternatively, it may indicate that there is chemical inhomogeneity, possibly as a result of increased carbon doping of the outer edges of the samples from the graphite die during the high temperature process, leading to spatially varying lattice parameters which present as inhomogeneous strain.

SEM

Figures 3.2 and 3.3 show backscattered SEM images at different magnifications of the samples processed at (a) 900, (b) 1000, (c) 1100 and (d) 1200 °C. At low magnification (Figure 3.2), 4 different contrast levels can be observed. These correspond to 3 solid phases: MgB_2 (light grey), MgB_4 (dark grey) and MgO (white), and to porosity (black). This phase assignation was confirmed by EDX and a typical backscattered image with the corresponding Mg, B and O EDX maps for the sample sintered at 1200 °C are shown in Figure 3.4.

The sample sintered at 900 °C (Figure 3.2 (a)) showed a poorly connected microstructure containing a significant volume fraction of pores, and composed of large $50-100$ μm MgB_2 particles surrounded by smaller $5-50$ μm MgB_2 particles. In contrast, the sample processed at 1200 °C had a very dense microstructure with hardly any porosity. The large reduction in porosity with increasing temperature observed by SEM is in good agreement with the density measurements presented in table 4.5.

The micrograph in Figure 3.3 (a) shows the internal structure of one of the large, MgB_2 particles in the 900 °C sample at higher magnification. It is clear that even these apparently dense particles contain considerable internal porosity. The size and volume fraction of these pores were drastically reduced by increasing the sintering temperature, as expected from the increased diffusion rates at high temperature. The sample processed at 1200 °C showed only a very small number of sub-micron pores, in contrast with the specimen sintered at 900 °C which contained a large fraction of $1-5$ μm pores.

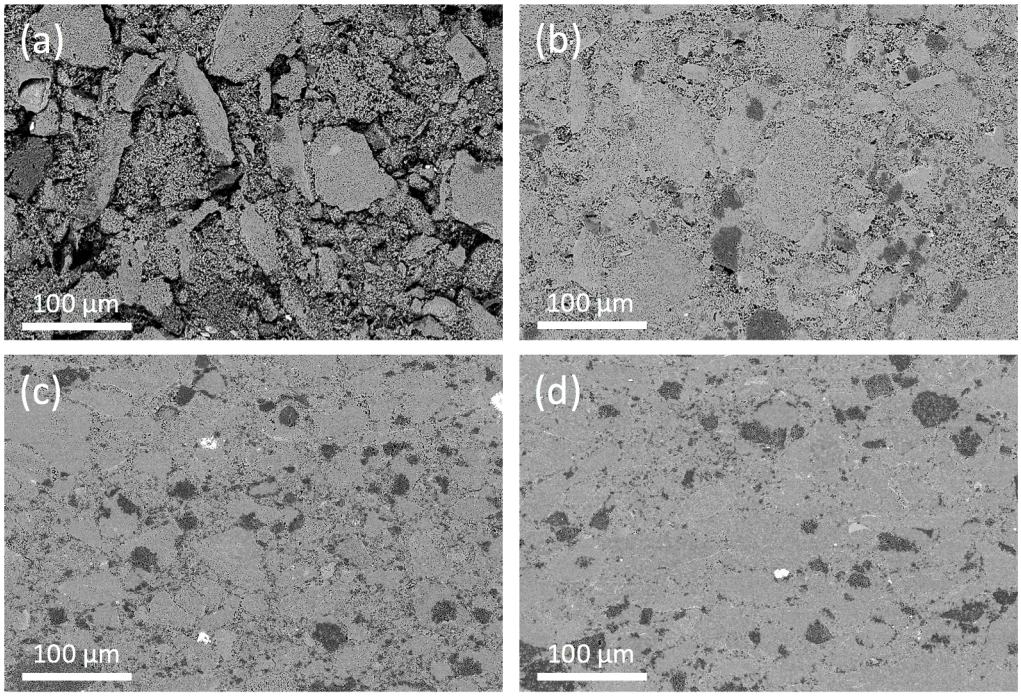

Figure 3.2: Typical backscattered SEM images of the samples processed at (a) 900, (b) 1000, (c) 1100 and (d) 1200 °C. These images were taken by Dr Sangeeta Santra

Figure 3.3 (d) also shows backscattered electron channelling contrast which reveals that the matrix of these well compacted samples is actually a fine polycrystalline MgB_2 microstructure composed of grains with diameters ranging from 0.5 to $2-3$ μm.

The MgB_4 phase occurred as large particles $10-50$ μm in diameter, randomly distributed in the MgB_2 matrix, as shown in Figure 3.2. Samples processed at higher temperatures contained a larger volume fraction of MgB_4. The volume fraction of MgB_4 in the sample processed at 1200 °C was estimated to be 13 vol. % by analysing 9 images using the procedure described in section 2.2.4. This corresponds to $\sim$ 12 wt.% MgB_4 which is slightly smaller but similar to the value of 16 wt.% calculated from the XRD results on the same sample. This small difference probably comes from the limitations of the XRD and SEM techniques explained in section 2.2.3. The sintering temperature also had a significant effect on the size of the MgO particles. Very fine MgO particles with a diameter under 100 nm can be seen in all the specimens, but large MgO particles with a diameter up to 1 μm were only found in the sample processed at 1200 °C, which on close (Figure 3.3 (d)) inspection were located at grain boundaries where diffusion is fast enough for considerable coarsening to occur. The volume fraction of MgO in the sample sintered at 1200 °C was estimated to be 5 vol.% ($\sim$ 7 wt.%) by analysing 9 images, using the procedure described in section 2.2.4. This is consistent with 8 wt.% estimated by XRD.

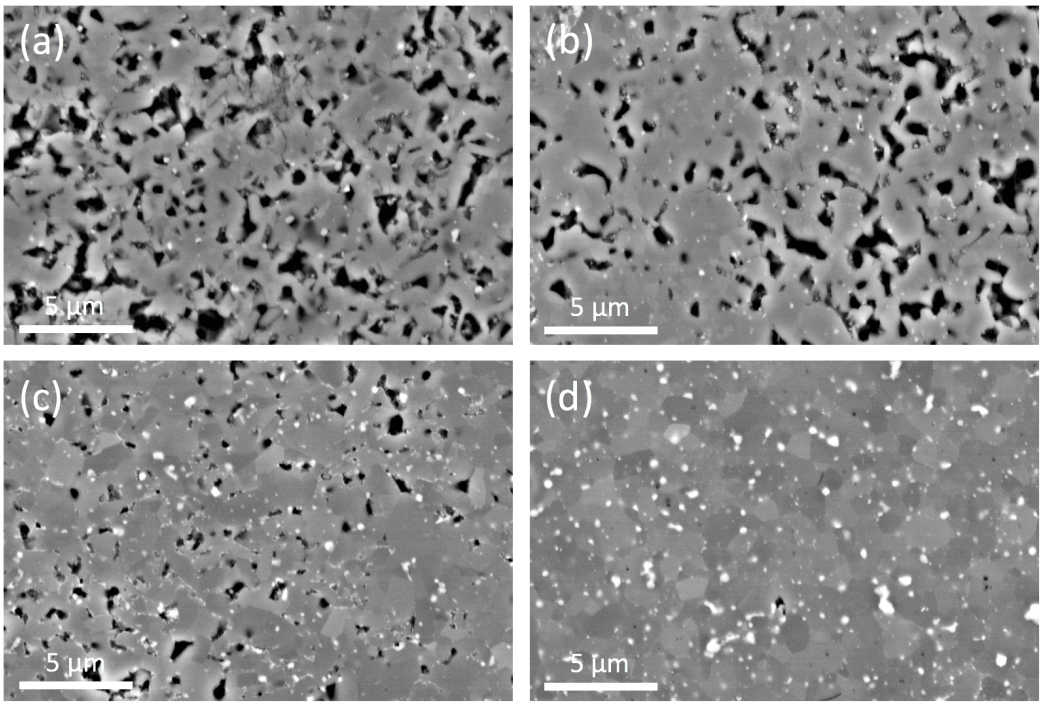

Figure 3.3: Typical backscattered SEM images of the samples processed at (a) 900, (b) 1000, (c) 1100 and (d) 1200 °C. These images were taken by Dr Sangeeta Santra.

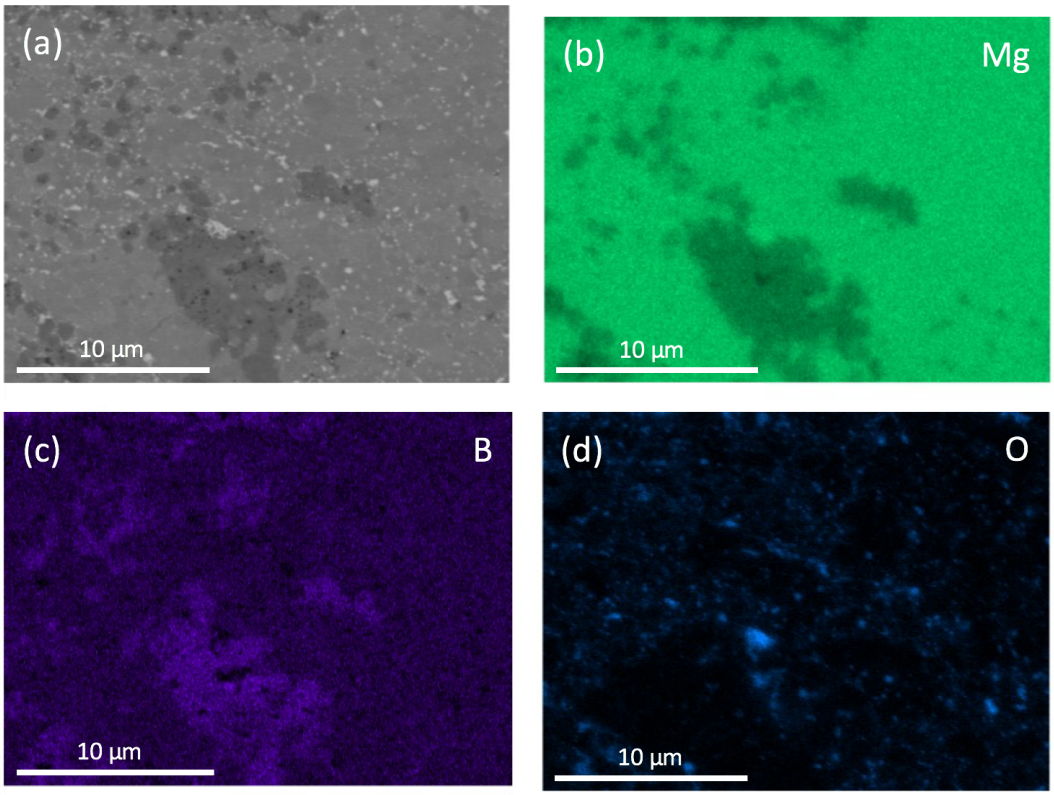

Figure 3.4: (a) Typical backscattered SEM image and corresponding EDX maps showing the (b) Mg, (c) B and (d) O distribution in the sample processed at 1200 °C.

Magnetic measurements

Figure 3.5 and Table 3.3 summarise the superconducting properties of the samples extracted from magnetisation-temperature curves and magnetic hysteresis loops, as described in section 2.2.6. Figure 3.5 (a) shows the normalised susceptibility of the samples sintered at 900-1200 °C as a function of temperature obtained using a measurement field of 5 mT and after correcting for demagnetising effects. All the samples showed a very similar onset critical temperature (T_c) around 38.7 K, but the width of the superconducting transition ΔT_c decreased from 1.7 to 0.4 K with higher processing temperatures. This suggests that the lower processing temperatures were not sufficient to fully anneal out inhomogeneities that were present in the as-received MgB_2 powder. Figures 3.5 (b) and (c) show the effect of applied field on J_c at 4.2 and 20 K respectively. Increasing the processing temperature increased the measured J_c values[4] over the majority of the field range at both 4.2 K and 20 K. The J_c values presented in Table 3.3 were extracted from $\Delta M - B$ data using the macro-scale model (see section 2.2.6). However, this model assumes that macroscopic currents can flow around a perfectly connected and homogeneous bulk sample. In poorly sintered materials the value of J_c calculated will be a lower bound of the intraparticle J_c.

Sample	$T_{c,onset}$ [K]	ΔT_c [K]	J_c(5 T,4.2 K) [A/m^2]	J_c(0 T,20 K) [A/m^2]	J_c(3 T,20 K) [A/m^2]
900 °C	38.6	1.7	1.2×10^7	0.55×10^9	0.9×10^7
1000 °C	38.6	0.6	2.6×10^7	1.8×10^9	2.2×10^7
1100 °C	38.7	0.4	4.6×10^7	3×10^9	3.8×10^7
1200 °C	38.7	0.4	4.6×10^7	3.3×10^9	3.8×10^7

Table 3.3: Superconducting properties of the MgB_2 specimens processed at $900-1200$ °C. J_c values were estimated using the macro-scale model.

Understanding the origin of the differences in J_c (extracted from magnetic measurements on macroscopic specimens) behaviour in sintered materials is complicated because it depends on the intraparticle J_c of the material, as well as extrinsic factors such as the effective cross-sectional area for current flow (electrical connectivity) and the length scale of the circulating current paths in the sample. The intraparticle[5] $J_c(B,T)$ is itself influenced both by the micro/nano scale pinning landscape and how "dirty" the superconducting phase is. Increasing disorder and chemical impurity substitution in the MgB_2 lattice makes the superconductor dirtier, and is known to

[4]Using the macro-scale model described in section 2.2.6. Unless explicitly indicated, J_c refers to the critical current density values calculated using the macro-scale model.

[5]The intraparticle J_c is the theoretical J_c value that could be observed in a single microscopic powder particle.

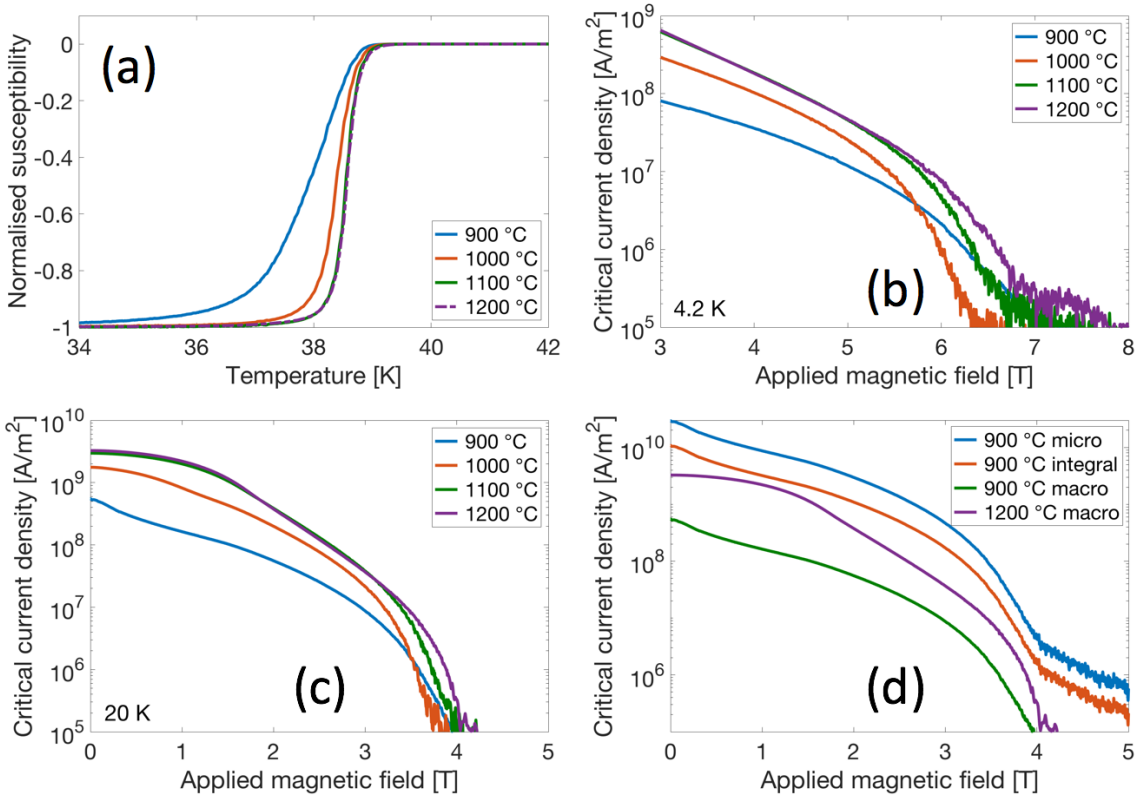

Figure 3.5: Superconducting properties of the MgB_2 samples processed at 900-1200 °C. (a) normalised susceptibility, (b) $J_c - B$ at 4.2 K, (c) $J_c - B$ at 20 K, (d) $J_c - B$ at 20 K calculated using the 3 models described in section 2.2.6.

lead to higher upper critical fields and reduced anisotropy [88] which will increase J_c values at a particular magnetic field. In the low field region, vortices are separated by relatively large distances and so it is relatively easy to achieve strong pinning and high intrinsic J_c. Therefore changes in J_c at low field are likely to be dominated by extrinsic factors.

The volume fraction of MgB_2 was estimated from the XRD weight fractions in Table 3.3 to be 83 vol.% and 77 vol.% for the samples processed at 900 and 1200 °C, respectively. The total superconducting fraction is then estimated from the product of the MgB_2 volume fraction and the relative density of the sample. The samples sintered at 900 and 1200 °C have an estimated total superconducting fraction of 56 and 73 vol.% respectively, which represents an improvement of 30 % by processing at higher temperature. This suggests that the large (6 fold) increase in J_c(0 T, 20 K) between the samples sintered at 900 and 1200 °C cannot be only attributed to the total superconducting fraction and must mainly come from a difference in electrical connectivity between particles.

To explore whether the reduction in J_c in the low density samples can be explained simply by extrinsic effects, $J_c(B)$ values at 20 K for the sample processed at 900 °C have been calculated using macro-scale, micro-scale and micro-integral models representing the extremes of connectivity (see section 2.2.6). In the macro-scale model, the sample was considered as a perfectly connected, homogeneous cuboid. In contrast, the micro-scale model considers that the sample is made of individual (spherical) particles that are electrically isolated from one another (i.e. supercurrents cannot flow between adjacent particles). In this case, the particle median size (measured on the powder before sintering by laser diffraction) was used to calculate $J_{c,micro}$ instead of the macroscopic dimensions of the specimen. In the micro-integral model, the exact particle size distribution (measured on the as-received powder by laser diffraction) was used instead of considering that the powder was made of identical particles of diameter $d_{0.5}$.
The macro and micro-scale models give estimated lower and upper bounds of the intraparticle J_c of the material, as shown in Figure 3.5 (d). The micro-integral model gives a more realistic estimation of the upper bound, as discussed in section 2.2.6. Comparing $J_{c,integral}$ of the porous 900 °C sample with $J_{c,macro}$ of the dense and well connected 1200 °C bulk suggests that lower processing temperatures actually lead to higher intraparticle J_c values. This is consistent with the microstructural observations (Figure 3.3) that lower processing temperatures lead to finer microstructures and retains the dirtier superconducting phase, both of which should result in higher intraparticle J_c values. It also confirms that the reduction in J_c(0 T, 20 K) observed in the samples sintered at low temperatures probably comes from extrinsic effects, and especially poor interparticle connectivity.

Connectivity measurements

To estimate the effective cross-sectional area for macroscopic current transport in my bulk samples, four-point transport measurements and analysis of connectivity have been performed by Runsen Ma to obtain the normal state electrical resistivity as a function of temperature. Following the analysis of Collings *et al.* [85], values of connectivity were extracted from the data using the procedure described in section 2.2.7.

Figure 3.6 clearly shows that the connectivity (effective cross-sectional area for macroscopic current transport) in the 900 °C sample is very low, improving by a factor of ~ 6 on increasing the

processing temperature to 1200 °C. This confirms that it is appropriate to use the micro-integral model for estimating J_c from magnetisation data for the 900 °C sample. The 1200 °C sample also has a reduced cross-sectional area for current transport, as indicated by its relatively low connectivity of 35%, so the macro-scale model is also likely to underestimate the true intrinsic J_c in this sample.

This suggests that there are still lots of possibilities to improve the connectivity in bulk MgB_2 specimens, in particular by reducing the fraction of impurities. A first improvement could be to use a cleaner MgB_2 powder. In fact, XRD analysis (Table 3.2) revealed that the "99%" pure MgB_2 powder from Alfa Aesar actually contained 5 wt.% MgO and 7 wt.% MgB_4. Unfortunately, there are only a few MgB_2 powder manufacturers and Alfa Aesar is known to produce some of the best MgB_2 powder commercially available. Higher quality powders need to be made in smaller quantity by a custom lab process, which is very time consuming and requires special facilities. Another possibility could be to reduce commercial MgB_2 powder to remove impurities, but this process also requires special equipment and presents additional risks due to the reactivity of high purity reduced powders.

The sharp increase in connectivity with higher temperatures can be correlated to the significant improvement in J_c observed in samples sintered at high temperature. In fact, the improvement in J_c(0 T, 20 K) between the samples sintered at 900 and 1200 °C almost exactly matches the improvement in connectivity between these samples. This confirms that the increase in J_c observed in samples processed at high temperature comes from extrinsic effects. These results suggest that connectivity has a significant effect on the maximum magnetic moment that can be generated by macroscopic samples, even at the relatively small scale of PPMS specimens (2 mm x 2 mm x 3-5 mm). Connectivity is expected to play a major role in the trapped field performance of large MgB_2 superconducting magnets.

The residual resistivity ρ_0 (Figure 3.6) is seen to decrease systematically with increasing processing temperature, suggesting the MgB_2 lattice contains fewer defects and/or less impurity in solid solution. This is likely to result in the superconductor becoming "cleaner" according to the definition of Anderson [89].

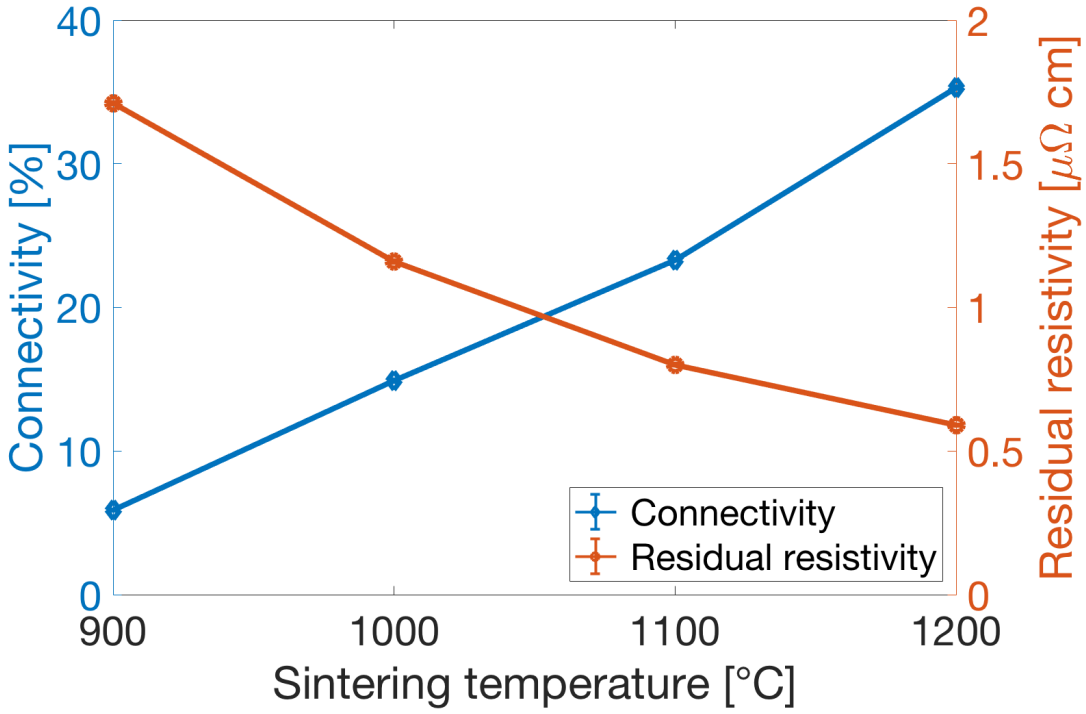

Figure 3.6: Connectivity and residual resistivity of the bulk samples estimated from normal state electrical transport measurements following the analysis outlined by Collings *et al.* [85]. The measurements and analysis were performed by Runsen Ma.

Pinning Force Analysis

To explore whether the dominant pinning mechanisms were affected by the processing temperature, normalised pinning force curves at 4.2 K and 20 K were extracted from $M - B$ data (method described in section 2.2.6), and are shown in Figures 3.7 and 3.8 respectively. Theoretical curves representing the point pinning and grain boundary pinning models formulated by Dew-Hughes [15] are also shown in Figures 3.7 and 3.8 for comparison. The reduced field $b = \frac{B}{B_{irr}}$ has been calculated using irreversibility field (B_{irr}) values estimated using the method described in section 2.2.6.

Sample	4.2 K		20 K	
	B_{irr} [T]	b_{peak}	B_{irr} [T]	b_{peak}
1200 °C	-	-	3.8	0.28
1100 °C	6.5	0.28	3.8	0.28
1000 °C	6.2	0.21	3.7	0.23
900 °C	6.8	0.22	3.8	0.3

Table 3.4: Irreversibility field values estimated from the Kramer extrapolation and b_{peak} values at 4.2 K and 20 K. The data for the 1200 °C sample at 4.2 K is not included due to the large flux jump in the magnetisation data.

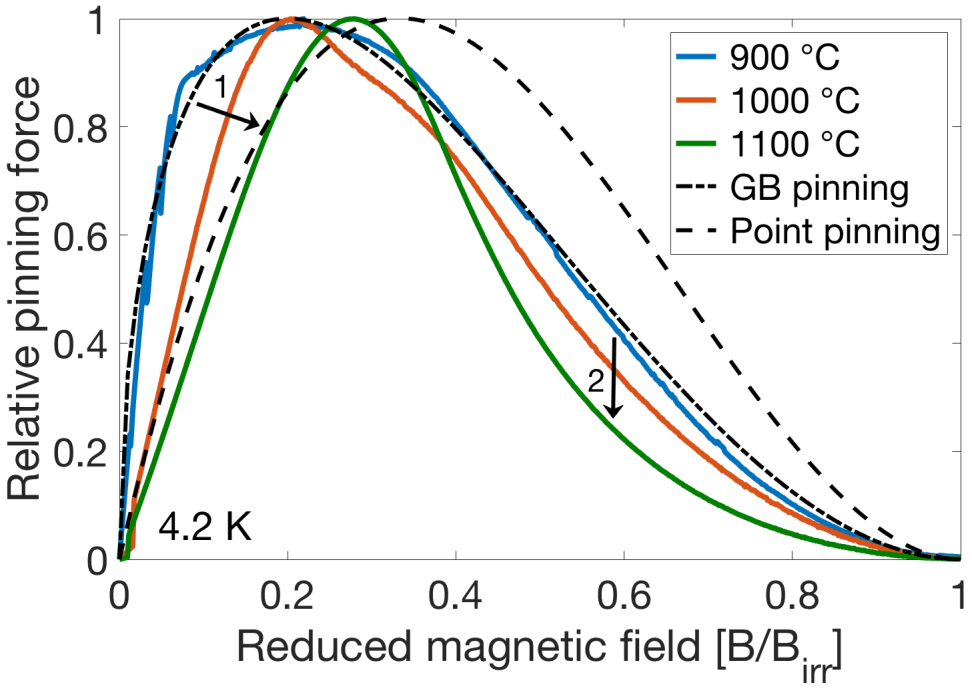

Figure 3.7: Normalised pinning force curves at 4.2 K compared to the grain boundary normal ($f_p \propto b^{\frac{1}{2}}(1-b)^2$) and point normal ($f_p \propto b(1-b)^2$) pinning models. The data for the 1200 °C sample is not included due to the large flux jump in the magnetisation data

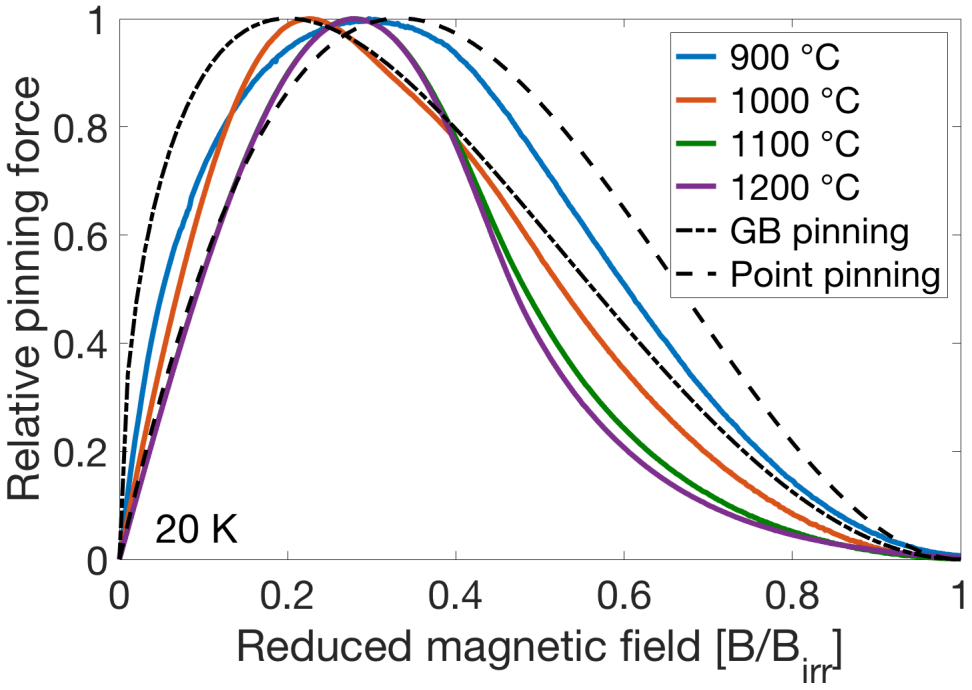

Figure 3.8: Normalised pinning force curves at 20 K compared to the grain boundary normal ($f_p \propto b^{\frac{1}{2}}(1-b)^2$) and point normal ($f_p \propto b(1-b)^2$) pinning models.

Table 3.4 shows the B_{irr} values used in the analysis, together with the peak position of the pinning force curves. Pinning in MgB_2 is generally considered to be dominated by two-dimensional grain boundary (GB) pinning [90,91]. At 4.2 K, the curve of the sample sintered at 900 °C shown in Figure 3.7 was relatively close to the shape predicted by the GB pinning model which suggests that it was the dominant pinning mechanism in this sample. However, the samples processed at 1000 and 1100 °C had curves deviating considerably from the $f_p = b^{\frac{1}{2}}(1-b)^2$ function predicted by the core-pinning model of Dew-Hughes for "surface normal" pinning [15] or Kramer's flux line lattice (FLL) shear model [92]. In particular, the 1100 °C sample had a peak position at around $b_{peak} = 0.3$ rather than the $b_{peak} = 0.2$ predicted for GB pinning, and the 1000 °C sample showed two peaks, the main one at $b_{peak} \sim 0.2$ and a secondary peak at $b_{peak} \sim 0.35$. This may indicate that there was a significant contribution from "point normal" pinning, described by the function $f_p = b(1-b)^2$ and having a peak at $b_{peak} = 0.33$ [15]. This could arise from the presence of non-superconducting secondary phase particles (e.g. MgO) with all dimensions smaller than the flux line spacing. Indeed, SEM observations presented in Figure 3.3, have revealed the presence of small MgO particles having diameters below 100 nm.

The low field side (before the peak) of the 3 curves in Figure 3.7 gradually changed from having a shape similar to the GB pinning model for the 900 °C sample to a shape close to the point pinning model for the 1100 °C sample, going through an intermediate shape having two peaks for the 1000 °C specimen. This gradual change from GB to point pinning is shown in Figure 3.7 by arrow 1, and suggests that the dominant pinning mechanism changed from GB to point pinning with increasing sintering temperature. On the other hand, for samples sintered at higher temperature the high field side of the curve gradually became more concave, as shown by arrow 2 in Figure 3.7, and deviates from both the GB and point pinning models. This seems to be in contradiction with the trend observed for the low field side of the curve, but this concave shape has been observed by other groups [83,85] and may arise from anisotropy effects. Eisterer *et al.* [88] suggested that anisotropy needs to be taken into account to explain the shape of $J_c(B)$ curves in polycrystalline MgB_2. At high fields, superconductivity in grains aligned in unfavourable directions relative to the applied field will "switch off", causing a reduction in the effective cross sectional area for supercurrents. The analysis by Speller [37] on my data investigated the effect of anisotropy on the shape of pinning force curves by including the Eisterer percolation model in three different pinning models; the classic grain boundary model, the point pinning model and the modified

grain boundary model using the Brandt[6] correction [95]. The results of Speller's analysis are presented in Figure 3.9 with the data at 20 K of the MgB_2 specimen sintered at 1100 °C.

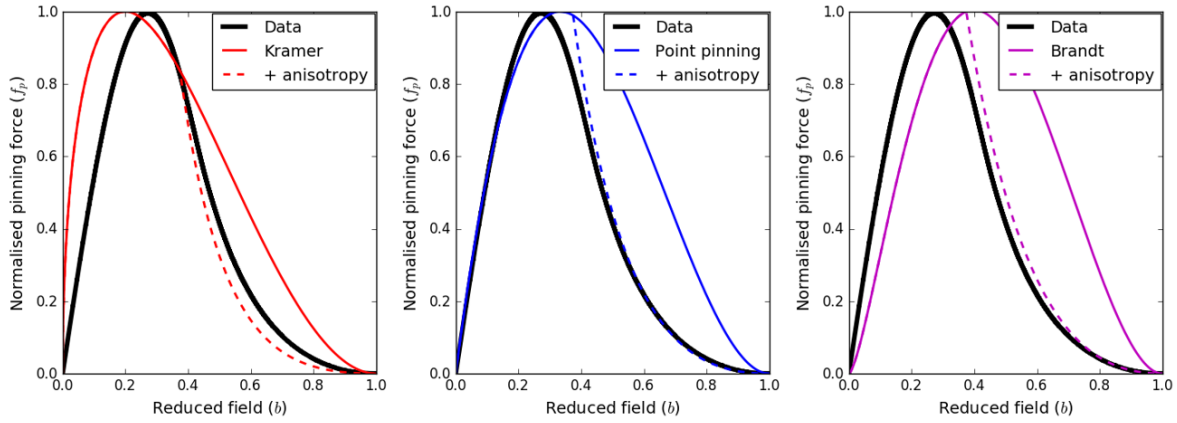

Figure 3.9: Experimental normalised pinning force curves for the 1100 °C processed sample at 20 K compared with the Kramer grain boundary, point pinning and Brandt modified grain boundary models, showing the effect of taking into account anisotropy using the Eisterer percolation model with $B_{c2}^{ab} = 10$ T, $\gamma = 4$ and $B_{irr} = 4$ T [37].

From Figure 3.9, it is clear that anisotropy had a large effect on the high field side of the curve. Including anisotropy in the pinning models allowed us to reproduce the sharp drop and concave shape observed after the peak, on the high field side of the curve. To understand the evolution of the pinning force curves at 4.2 K in Figure 3.7, the low and high field side of the curves need to be analysed individually (this is highlighted by arrows 1 and 2 in Figure 3.7). The low field side of the curve changed from a shape similar to the GB pinning model to a shape closer to the point pinning model (arrow 1) with increasing processing temperature. This suggests a change in the dominant pinning mechanism from GB to point pinning with increasing processing temperature. The high field side of the curve gradually changes into a more concave shape (arrow 2). While this could also be interpreted as a change in pinning mechanism, it is more likely that the change in shape on the high field side of the curve comes from the anisotropy effects discussed above. The sample processed at 900 °C is reasonably well fitted by the classical grain boundary pinning model (at 4.2 K) without taking anisotropy into account. Since the MgB_2 samples processed at low temperature are likely to be dirtier as discussed above, increased B_{c2} and decreased γ values[7]

[6]It is well known that the Labusch form of the shear modulus of the flux line lattice used in the classical Kramer model (GB pinning) is only accurate at high field [93, 94]. Brandt derived a different form of the shear modulus that is valid over almost the entire field range [95].

[7]Anisotropy is defined by $\gamma = \frac{B_{c2}^{ab}}{B_{c2}^{c}}$ where B_{c2}^{ab} and B_{c2}^{c} are the critical fields with the applied field parallel to the ab and c planes respectively.

are expected, both of which will reduce the effect of anisotropy. On the other hand, samples processed at higher temperature deviate considerably from the standard pinning models and much better fits are obtained by considering anisotropy. These results suggest that the shape of the pinning force curves of samples sintered at higher temperature is much more sensitive to anisotropy effects. This can be explained by the large difference in connectivity between the samples processed at low and high temperature. In poorly connected samples (low sintering temperature) the size of the current loops is already very limited, and therefore, the effect of anisotropy on the $J_c - B$ curve (and consequently also on the pinning force curve) is not significant. However, the size of these current loops is much larger in well connected specimens (high sintering temperature), which means that as the field increase, more grains that are unfavourably aligned with the applied field switch off, until the percolation threshold is reached, then leading to a sudden drop in J_c, which is observed as the concave shape of the high field side (after the peak) of the pinning force curves in well connected samples.

XRD and SEM results both showed an increase in MgO fraction (Table 3.2) and coarsening of the microstructure (Figure 3.3) with increasing processing temperature. Whereas the grain boundary density decreased monotonically with higher sintering temperature, the density of MgO particles acting as efficient point pinning centres might increase with higher processing temperature. This is supported by the increase in MgO fraction observed in Table 3.2 with higher sintering temperature and the fact that even in the sample processed at 1100 °C, MgO particles remained relatively fine, with an average size around 40 nm. This could explain the evolution of the shape of the pinning force curves at 4.2 K (Figure 3.7) with increasing sintering temperature.
At 20 K, the effect of anisotropy is also clearly visible on the high field side of the pinning force curves, as shown in Figure 3.8. However, the low field side of the curve is more difficult to interpret than at 4.2 K, and no conclusion on an eventual change in pinning mechanism can be drawn with confidence.

Chapter 4

Oxide Dispersion Strengthened MgB_2

4.1 Manufacturing Y_2O_3-MgB_2 ODS powders

This section focusses on the characterisation of different Y_2O_3-MgB_2 powders manufactured by mechanical alloying, as described in section 2.1.1. Manufacturing these powders is the first step toward the realisation of oxide dispersion strengthened (ODS) superconductors. The ODS concept has been investigated since the 1970s, and consists in obtaining a fine dispersion of stable oxide precipitates in a metallic matrix to improve mechanical properties. This concept has mainly been used to improve the high temperature strength and creep properties of steels and superalloys, where the oxide particles act as pinning centres for dislocations and grain boundaries [2–4].

The aim of this project is to investigate if the ODS concept can be successfully applied to superconductors to improve their functional properties rather than mechanical properties. In this case, oxide particles would act as pinning centres for magnetic vortices and improve the functional properties such as the critical current density (J_c) and the irreversibility field (B_{irr}) of superconductors. Y_2O_3 is an extremely stable oxide and has been successfully used by many research groups to improve the mechanical properties of steels and superalloys. Y_2O_3 has also been used by several companies to produce commercial ODS materials [3–8]. For this reason, I decided to use Y_2O_3 to manufacture Y_2O_3-MgB_2 ODS powders. In this section, two parameters have been investigated, the mechanical alloying time and the fraction of Y_2O_3 in Y_2O_3-MgB_2 ODS powders. Part of the results presented in Chapter 4 have been published in Superconductor Science and Technology [96].

4.1.1 Effect of mechanical alloying time

Several research groups have investigated the effect of the mechanical alloying time on the microstructure of ODS steel and superalloys for durations up to $50 - 100$ h. However, most of the microstructural changes happen in the first $10 - 20$ h [5–8]. In addition, one can expect the ball milling dynamics of a brittle powder such as MgB_2 to be faster than for steel or superalloy powders showing significant ductility [3]. Consequently, I decided to explore milling times up to 12 h.

Particle size distribution and XRD

The median diameter and the particle size distribution of 0.5 wt.% Y_2O_3-MgB_2 ODS powders ball milled for up to 12 h are shown in Figure 4.1 (a) and (b) respectively. There was an initial sharp reduction in particle diameter from approximately 40 μm for the unmilled powder to 4 μm after only 10 min of milling. The particle diameter then stabilised at 1.5 μm after 1 h of milling, and this is usually interpreted as the point where the rate of fragmentation equals the rate of agglomeration [3]. MgB_2 is intrinsically relatively brittle, leading to a rapid diameter reduction. Figure 4.1 (b) shows that ball milling also had a drastic effect on the particle size distribution. The unmilled powder showed a trimodal distribution with the main mode (peak in the distribution) at 70 μm and two smaller ones at 2 and 0.2 μm. Ball milling led to an increase in the volume fraction of smaller particles (< 5 μm) at the expense of larger ones (> 10 μm) due to particle fracture. The powders ball milled for more than 1 h showed complex multimodal distributions with up to 5 modes. A small fraction of large particles were still found in powders ball milled for 3, 6 and 12 h which is probably due to a second stage in the milling process where the fragmentation rate was lower than during the initial stage, leading to more agglomeration.

Only three phases were detected in the XRD patterns shown in Figure 4.2 for powders ball milled for various times: MgB_2, MgB_4 and MgO. The small fraction of Y_2O_3 added (0.5 wt.%) was below the XRD detection limit, hence no Y_2O_3 peaks were observed. Table 4.1 summarises the results of Rietveld refinement of the XRD patterns. After milling, the characteristic peaks of all three phases in Figure 4.2 decreased progressively in intensity and became broader, resulting in both an increase in inhomogeneous strain and/or a reduction in effective crystallite size.

The pristine powder contained approximately 5 wt.% MgO and 7 wt.% MgB_4, and the fraction of these impurities increased with milling time. In particular, the MgO fraction increased up

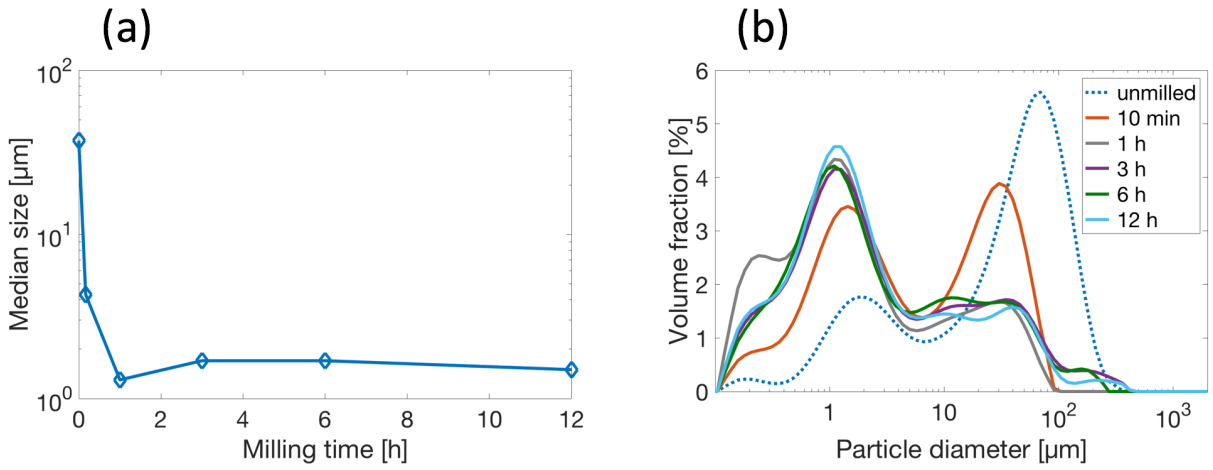

Figure 4.1: (a) Median size (b) particle size distribution of 0.5 wt.% Y_2O_3-MgB_2 ODS powders ball milled for different times.

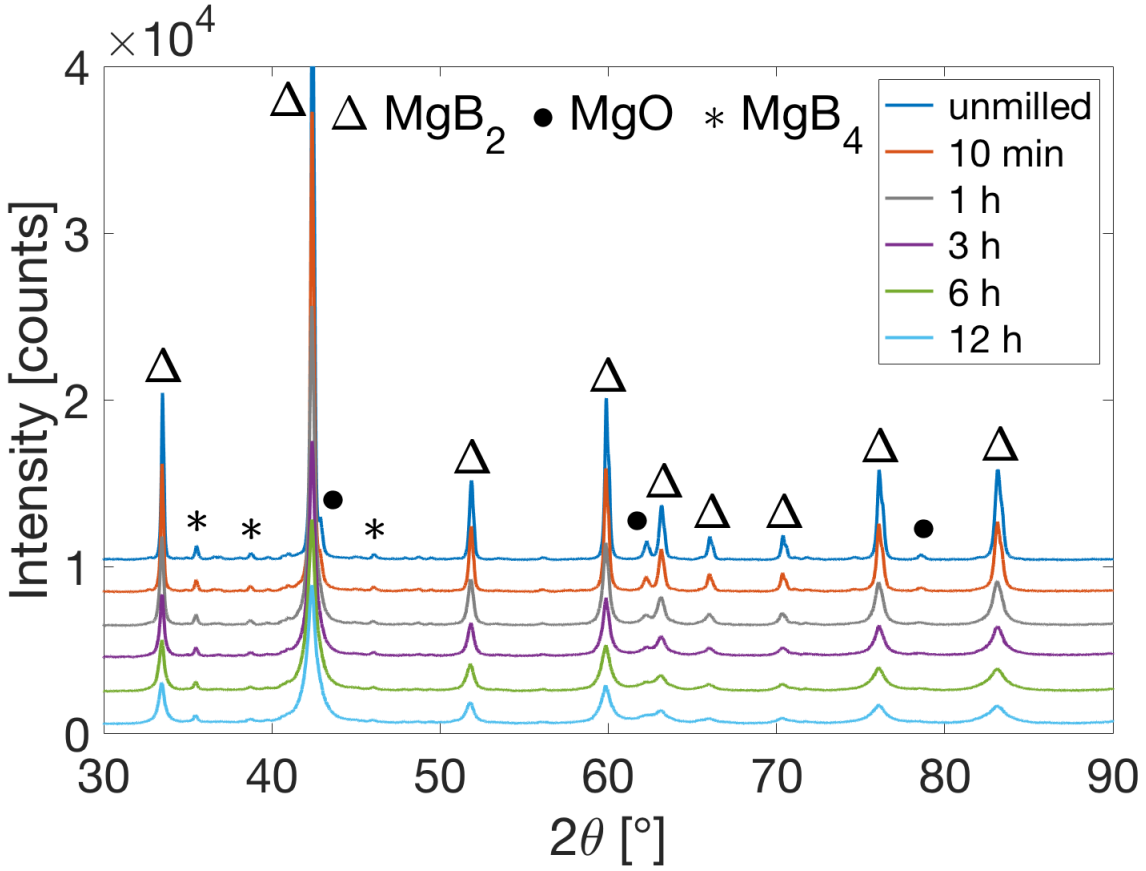

Figure 4.2: XRD patterns of 0.5 wt.% Y_2O_3-MgB_2 ODS powders ball milled for different times.

to 11 wt.% after 12 h. Therefore, despite using an Ar filled glove box, it was not possible to fully exclude residual oxygen that reacted with the freshly formed surface of the MgB_2 particles during ball milling. The small increase in MgB_4 fraction was probably a refinement artifact rather than a change in composition. The MgB_4 peaks were relatively weak and difficult to fit

Milling time	MgO [wt.%]	MgB_4 [wt.%]	MgB_2 crystallite size [nm]	MgB_2 strain [%]	MgB_2 a-axis [Å]	MgB_2 c-axis [Å]
0 h	5	7	100	0.11	3.086	3.524
10 min	5	7	110	0.13	3.086	3.524
1 h	6	7	100	0.23	3.087	3.525
3 h	8	8	80	0.31	3.087	3.525
6 h	10	9	70	0.45	3.088	3.527
12 h	11	11	50	0.52	3.088	3.528

Table 4.1: Characteristics of the 0.5 wt.% Y_2O_3-MgB_2 powder ball milled for different times, estimated using Rietveld refinement.

during the Rietveld refinement, and the signal to noise ratio decreased with ball milling time which may have led to an overestimation of the total intensity of the MgB_4 peaks relative to the total diffracted intensity.

As commonly seen in mechanically alloyed powders, the crystallite size of MgB_2 decreased and the strain increased with milling time (Table 4.1). Although the refinement of the particle diameter stopped after 1 h of milling, the XRD patterns suggested that refinement of the microstructure (crystallite size) continued. While qualitatively this behaviour is similar to that widely reported for ODS steels, it is perhaps surprising that a brittle compound shows essentially identical trends. Further, there was a gradual increase in the a and c-axis of the MgB_2 lattice with increasing milling time. Yttrium has a larger atomic size (2.32 Å) than either magnesium or boron (1.73 Å and 1.92 Å respectively), and the increase in lattice volume may be an indication of the dissociation and dissolution of Y_2O_3 into the MgB_2 lattice. Again, similar phenomena were seen in metallic ODS solid solutions at long milling times [5,6].

STEM analysis

The ODS powders were further characterized by STEM analysis. High angle annular dark field (HAADF) images of individual powder particles were acquired along with the corresponding Y and O EDX maps. Analyses were conducted on several particles for each milling condition, and representative images and EDX maps of powder ball milled for 10 min, 1 h and 12 h are shown in Figure 4.3.

After 10 min of milling, undissolved Y_2O_3 particles approximately $20-50$ nm in diameter were located on the surface of MgB_2 powder particles. The corresponding Y and O maps indicated that Y and O concentrations were co-located. After 1 h of milling, the image contrast was

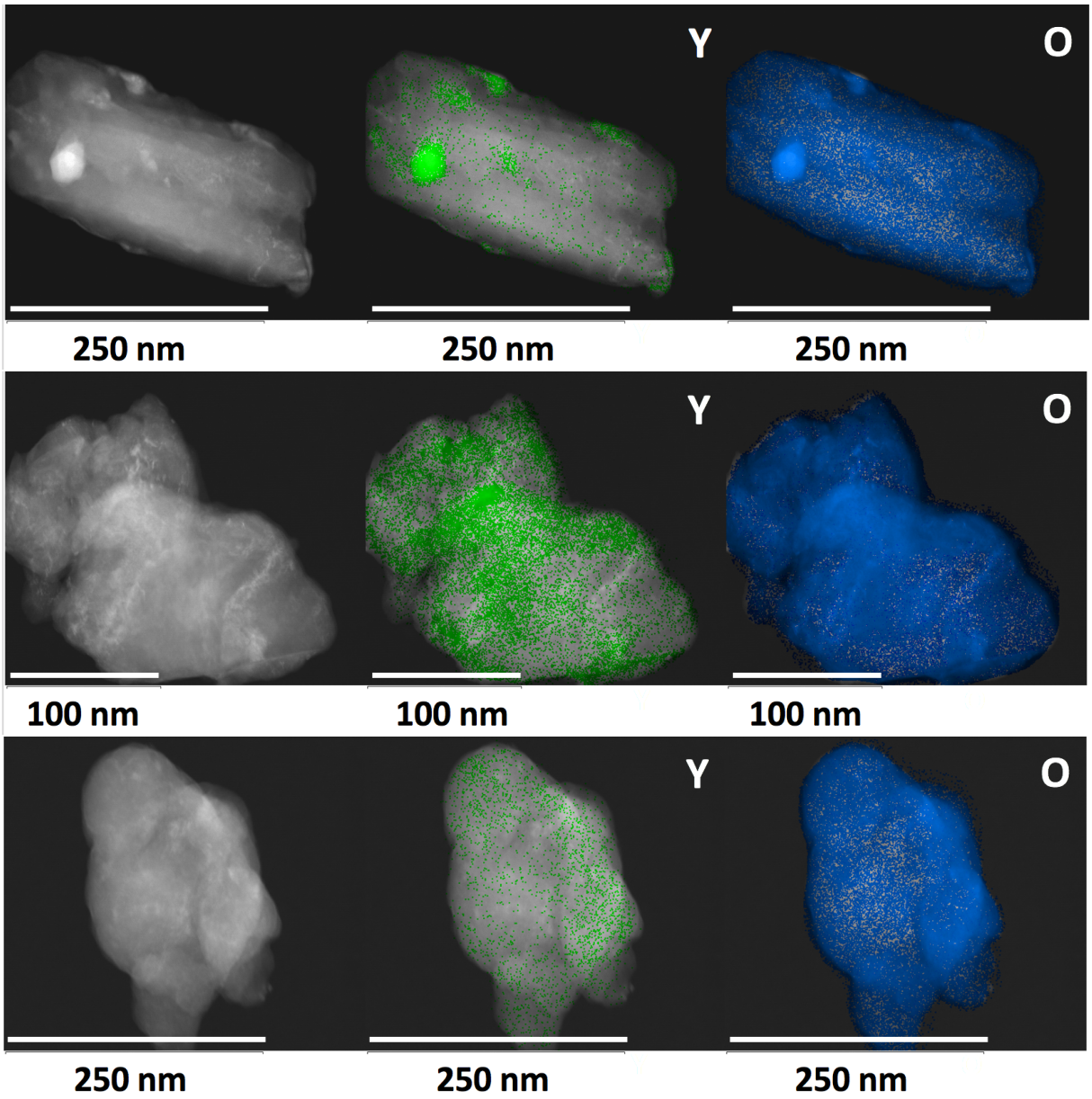

Figure 4.3: STEM HAADF images, and corresponding Y and O EDX maps of 2 wt.% Y_2O_3-MgB_2 ODS powders ball milled for 10 min, 1 h and 12 h (top to bottom).

more difficult to interpret due to the high concentration of defects (vacancies and dislocations) introduced by mechanical alloying, and few discrete Y_2O_3 particles could be resolved. Again, in the EDX maps there were areas comparatively richer in both Y and O, but both elements were now more widely dispersed. This trend was confirmed after 12 h of milling where no Y_2O_3 particles could be resolved, and the EDX maps showed a much more homogeneous distribution of both Y and O. Consistent with the XRD results above, this suggests that the Y_2O_3 nano particles have dissolved into the MgB_2 lattice.

XRD analysis of 10 wt.% Y_2O_3-MgB_2 ODS powders

In order to further investigate the evolution of the Y_2O_3 phase during the mechanical alloying process, ODS powders containing a much higher fraction of Y_2O_3, so that it might be more easily detected, were fabricated. This method has been used by several research groups to investigate the evolution of the Y_2O_3 phase in ODS steels and superalloys powders during ball milling [5–8]. Figure 4.4 shows XRD patterns of 10 wt.% Y_2O_3-MgB_2 ODS powders as a function of milling time.

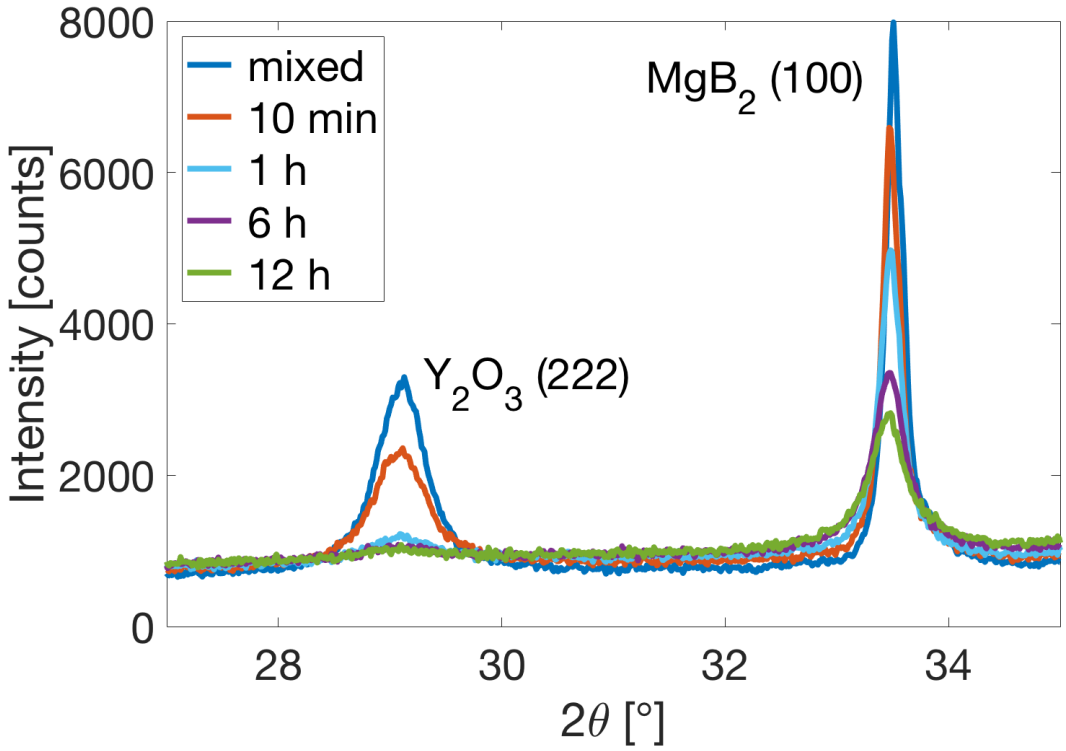

Figure 4.4: XRD patterns of 10 wt.% Y_2O_3-MgB_2 ODS powders showing the evolution of the (222) Y_2O_3 and (100) MgB_2 reflections with ball milling time.

The initial mix of powders showed a strong (222) Y_2O_3 reflection, which was still visible after 10 min of milling. However, this peak decreased in intensity after 1 h, and vanished at longer ball milling times. Thus it was concluded that for the ODS powders, even when relatively large fractions of Y_2O_3 were added, all the Y_2O_3 was dissolved (presumably as dissociated Y and O from the EDX maps) into the MgB_2 lattice during mechanical alloying. This is in good agreement with the study of Zhang *et al.* [6] on 10 wt.% Y_2O_3-Fe-14Cr ODS steels. The authors showed that the Y_2O_3 peaks almost completely disappeared after 12 h of ball milling and concluded that Y_2O_3 particles had dissolved in the steel matrix.

A further possibility, suggested for some cases of ODS steels, but for which there was no compelling evidence in this particular study, is that the Y_2O_3 becomes first very finely divided and then effectively amorphous (glassy) due to the excessive cold work and ultra-high defect density induced by cold milling [7, 8].

Magnetic measurements

ZFC curves were measured on powders ball milled up to 12 h with a SQUID magnetometer using the procedure described in section 2.2.6. Normalised magnetic susceptibility curves of unmilled MgB_2 and ball milled 0.5 wt.% Y_2O_3-MgB_2 ODS powders are shown in figure 4.5. The curves were all scaled to ensure that the unmilled MgB_2 powder reached a magnetic susceptibility of -1 at 10 K. Without this correction, the unmilled powder showed a susceptibility of -1.36 which is not a meaningful value. This probably comes from the fact that a demagnetising factor of 1/3 (commonly used for ideal spheres) was used to compute the magnetic susceptibility. Bjork *et al.* [97] have computed demagnetising factors for powders made of randomly packed spherical particles using a numerical model. They found that the sample aspect ratio had the largest effect on the value of the demagnetising factor but the relative density of the sample had only a small effect on the value of the demagnetising factor and the particle size distribution was almost negligible. For example, a sample with an aspect ratio of 2 and a relative density of 0.55 led to a demagnetising factor of 0.42 instead of 0.33 for ideal spheres. All my powder samples were pressed in a SQUID capsule and had a disc geometry with a relatively large aspect ratio (3-5). Consequently, the demagnetising factor of my powder samples are expected to deviate significantly from the theoretical value of 0.33 for ideal spheres. Exact values of the demagnetising factor for each powder would require extensive numerical modelling and is beyond the scope of this work. Instead, a simple empirical correction[1] was made to give estimated values of the magnetic susceptibility. As shown above, the ball milled powders and unmilled MgB_2 powder had complex and relatively different particle size distributions, but Bjork [97] showed that the particle size distribution had only a very small effect on the demagnetising factor. Therefore, correcting the magnetic susceptibility value of all the powders with the same empirical factor should be a good estimation.

[1]The susceptibility of the unmilled powder was normalised to -1 and the same demagnetising correction was applied to all the ball milled powders.

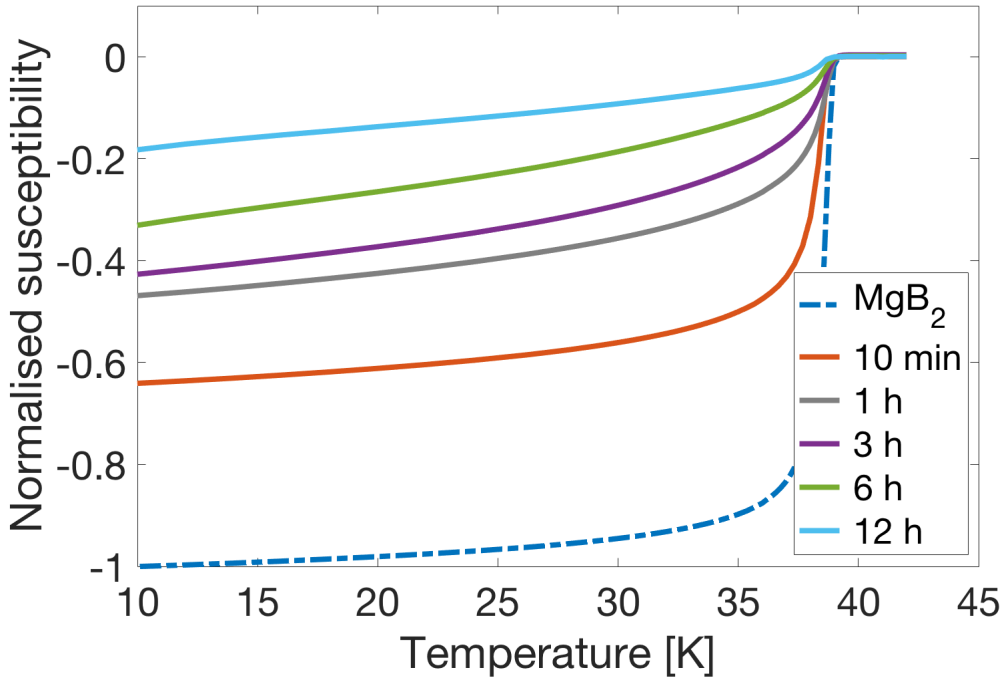

Figure 4.5: Normalised magnetic susceptibility curves computed from ZFC data measured with an applied field of 1 mT of unmilled MgB_2 and 0.5 wt.% Y_2O_3-MgB_2 ODS powders ball milled up to 12 h. All the curves were scaled by a factor 1.36 in order to account for the powder demagnetising factor.

Table 4.2 summarises the superconducting properties derived from the ZFC curves in Figure 4.5. $T_{c,onset}$ was not affected by ball milling and remained at 39.0 K for all the ball milled powders, even after 12 h of milling. On the other hand, the superconducting transition became wider with longer ball milling times, increasing from 1.5 K to $\sim$ 2.5 K for the powders milled for 3, 6 and 12 h. This is likely to be caused by the higher level of inhomogeneity introduced by the ball milling process.

The value of the normalised susceptibility at 10 K gives some indication[2] of the evolution of the superconducting fraction during the ball milling process. Table 4.2 shows that the normalised susceptibility at 10 K gradually decreased with the milling time, suggesting a reduction in the superconducting fraction. This was probably caused by the severe cold work and ultra high defect density induced by cold milling as indicated by the large reduction in intensity and the significant broadening of the MgB_2 XRD Bragg reflections shown in Figure 4.2.

[2]In the case of powders, individual particles are electrically insulated from each other and thus susceptibility values can give an estimation of the superconducting fraction. This would not be the case for well connected macroscopic specimens [98].

Sample	$T_{c,onset}$ [K]	ΔT_c [K]	Normalised magnetic susceptibility (10 K)
MgB_2	39.0	1.5	-1
10 min	39.0	2.2	-0.64
1 h	39.0	2.1	-0.47
3 h	39.0	2.6	-0.43
6 h	39.0	2.6	-0.33
12 h	39.0	2.5	-0.18

Table 4.2: Superconducting properties of unmilled MgB_2 and 0.5 wt.% Y_2O_3-MgB_2 ODS powders ball milled up to 12 h.

4.1.2 Effect of Y_2O_3 fraction

ODS steels and superalloys used in real applications only contain a very small fraction of oxide particles, usually below 1 wt.%. Due to the very small size of the oxide particles (tens of nanometres) that can be achieved through mechanical alloying and controlled precipitation during high temperature consolidation, even small fractions < 1 wt.% can have a large effect on the mechanical properties [3, 4, 6]. Consequently, I decided to manufacture ODS powders with 0.2, 0.5 and 2 wt.% Y_2O_3.

Particle size distribution and XRD

Figure 4.6 shows the particle size distribution of Y_2O_3-MgB_2 ODS powders containing 0.2, 0.5 and 2 wt.% Y_2O_3 and ball milled for 12 h. All three powders showed a relatively similar particle size distribution with the main mode at approximately 1 μm. The ODS powders containing 0.2, 0.5 and 2 wt.% Y_2O_3 had particle median sizes ($d_{0.5}$) of 1.9, 1.5 and 2.2 μm respectively.
Table 4.3 summarises the results of the XRD analysis performed on the ODS powders containing 0.2, 0.5 and 2 wt.% Y_2O_3 and ball milled for 12 h. All three powders had almost identical characteristics, suggesting that for fractions of $Y_2O_3 \leq 2$wt.%, the amount of Y_2O_3 does not have a significant effect on the microstructure of the ODS powder. This is in contrast with the effect of the ball milling time presented in the previous section, which had a significant effect on the microstructure of ODS powders.
The next section is dedicated to the characterisation of ODS bulks made by FAST using the Y_2O_3-MgB_2 ODS powders presented here. The characterisation and observations made on the different ODS powders in this section will be useful to understand the effect of the milling time and fraction of Y_2O_3 on the microstructure and final properties of the ODS bulks made by FAST.

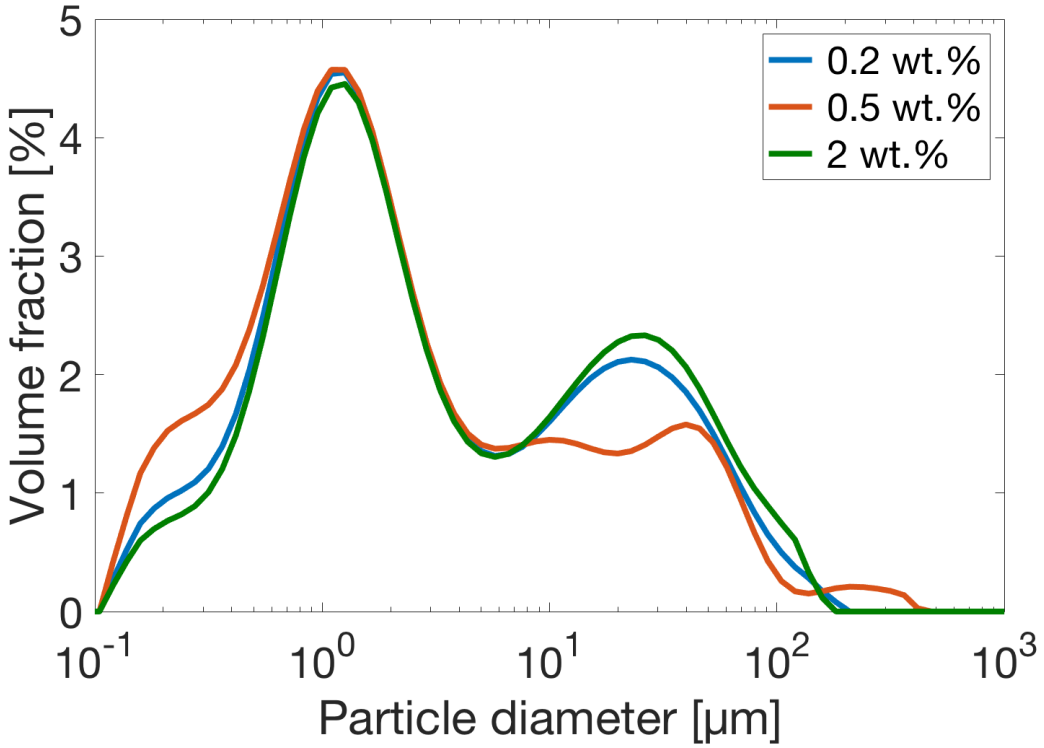

Figure 4.6: Particle size distribution of Y_2O_3-MgB_2 ODS powders containing 0.2, 0.5 and 2 wt.% Y_2O_3 and ball milled for 12 h.

Y_2O_3 [wt.%]	MgO [wt.%]	MgB_4 [wt.%]	MgB_2 crystallite size [nm]	MgB_2 strain [%]	MgB_2 a-axis [Å]	MgB_2 c-axis [Å]
0.2	11	11	50	0.48	3.088	3.527
0.5	11	11	50	0.52	3.088	3.528
2	12	12	50	0.5	3.088	3.527

Table 4.3: Characteristics of Y_2O_3-MgB_2 ODS powders containing 0.2, 0.5 and 2 wt.% Y_2O_3 and ball milled for 12 h, estimated using Rietveld refinement.

4.2 Manufacturing Y_2O_3-MgB_2 ODS bulks

Three parameters were investigated: the milling time, fraction of Y_2O_3 and sintering temperature. In order to study these 3 parameters independently, 3 sets of specimens were manufactured in which only one parameter was varied while the other processing parameters were kept constant.

4.2.1 Effect of milling time

Sample details

The effect of milling time was investigated by manufacturing bulk samples using 0.5 wt.% Y_2O_3-MgB_2 ODS powders ball milled for 1 h, 6 h and 12 h. The sintering conditions were kept constant for all the specimens and are summarised in Table 4.10.

Initial Powder	Sintering T [°C]	Sintering time [min]	Heating rate [°C/min]	Pressure [MPa]
MgB_2	1150	5	120	50
MgB_2 + 0.5 wt.% Y_2O_3 milled 1 h	1150	5	120	50
MgB_2 + 0.5 wt.% Y_2O_3 milled 6 h	1150	5	120	50
MgB_2 + 0.5 wt.% Y_2O_3 milled 12 h	1150	5	120	50

Table 4.4: Processing conditions for Y_2O_3-MgB_2 ODS bulks manufactured by FAST.

XRD and density measurements

The results of the density measurements and the XRD analysis are summarised in Table 4.5. Unmodified MgB_2 had the highest relative density of 93% while the ODS samples milled for 1 h and 6 h had a lower density of 90%, and the ODS specimen milled for 12 h had the lowest density of 87%. This suggests that the addition of Y_2O_3 and/or longer milling times had a detrimental effect on densification. The XRD analysis of the ball milled powders presented in Table 4.1 showed a significant increase in MgO fraction with longer milling times, from 5 wt.% in the unmodified powder up to 11 wt.% in the ODS powder milled for 12 h. MgO has a higher intrinsic sintering temperature than MgB_2 and is thus expected to slow down the sintering kinetics and hinder densification [99]. This explains the lower density observed in samples made from ODS powders balled milled for longer times.

The three ODS specimens showed relatively similar MgO and MgB_4 fractions, much higher than in the unmodified MgB_2 sample. ODS powders already showed higher MgO fractions than the

Sample	MgO [wt.%]	MgB_4 [wt.%]	Relative density [%]	MgB_2 crystallite size [nm]	MgB_2 strain [%]	MgO crystallite size [nm]	MgB_2 *a*-axis [Å]	MgB_2 *c*-axis [Å]
MgB_2	8	13	93	150	0.14	50	3.084	3.528
milled 1 h	13	21	90	110	0.16	47	3.084	3.528
milled 6 h	14	20	90	90	0.19	45	3.083	3.528
milled 12 h	15	17	87	90	0.2	49	3.085	3.529

Table 4.5: XRD characterisation and relative density of bulk samples made from 0.5 wt.% Y_2O_3-MgB_2 ODS powders milled for 1, 6 and 12 h and unmodified MgB_2 powder.

MgB_2 powder, as shown in Table 4.1. Table 4.5 suggests that the ODS bulks contained slightly higher MgO fractions than their respective ODS powder. This is due to the fact that ball milled powders have a much larger surface area than the initial MgB_2 powder. Consequently, a larger fraction of MgB_2 oxidised and turned into MgO during the sintering process at high temperature. By performing Differential Scanning Calorimetry (DSC) measurements on ball milled MgB_2 powders, Kario *et al.* [32] showed that the decomposition temperature of the reaction $2MgB_2 \rightleftharpoons MgB_4 + Mg_{(g)}$ decreased from $\sim$ 1050 °C for the unmodified powder to $\sim$ 950 °C in powders ball milled for 10 h. These results suggest that ball milling renders MgB_2 particles less stable and favours the decomposition reaction. They also found that bulks made from ball milled MgB_2 powders showed higher MgB_4 fractions compared to the unmodified powder. Table 4.5 shows that all three ODS samples have higher MgB_4 fractions than unmodified MgB_2, in good agreement with Kario's results.

The MgB_2 crystallite sizes of all the consolidated samples were larger than in their respective powders before sintering. This suggests that coarsening occurred during the sintering process at 1150 °C. However, the crystallite size was smaller in samples milled for longer durations, suggesting that part of the microstructural refinement obtained with ball milling was preserved after sintering. In particular, the crystallite sizes of the 6 and 12 h samples were 90 nm, significantly smaller than 150 nm for unmodified MgB_2. As expected, the strain was higher in bulk samples made from powders ball milled longer, following the trend observed in the ODS powders before sintering (Table 4.1). However, a reduction in strain was observed in the bulks compared to their respective powders before sintering, indicating that some strain relief occurred during the sintering process.

STEM analysis

ODS samples were studied by STEM, and typical HAADF images along with Y and O EDX maps from the 1 h and 12 h ODS specimens are shown in figure 4.7. The ODS bulks showed relatively fine MgB_2 grains, typically of a diameter of a few hundred nanometres, and numerous MgO and YB_4 nano particles.

MgO and YB_4 particles had similar shape and size which made their identification difficult by TEM. Dark field TEM did not offer much contrast due to the low concentration of YB_4 and the proximity of some MgB_2, MgO and YB_4 diffraction spots/rings. On the other hand, the combination of HAADF STEM and EDX mapping proved to be a successful (although time consuming) method to identify both particles. By working at a small camera length, the contrast in HAADF STEM is highly dependent on Z (atomic number) and less influenced by difference in crystallographic orientations than TEM. This makes HAADF STEM ideal to characterise heavier nano particles in a light matrix and gives a clear Z contrast, relatively free of diffraction effects. Figure 4.7 shows that YB_4 (having the highest Z number) was brighter than MgO and that the difference in contrast between these two phases was usually enough to tell them apart. However, EDX maps were also taken alongside HAADF images to make the analysis more reliable, as shown in Figure 4.7 (d).

The 1 h ODS sample had a noticeably inhomogeneous YB_4 particle distribution, which mainly formed large agglomerates at grain boundaries, as shown in Figure 4.7 (a) and (b). This probably arises from the relatively short milling time not providing sufficient mixing between the nano Y_2O_3 and MgB_2 powders, resulting in Y_2O_3 being located at the surface of MgB_2 particles in the ball milled powder.

On the other hand, Figures 4.7 (c) and (d) show that the 12 h ODS specimen had a much more homogeneous YB_4 particle distribution. YB_4 precipitates had a diameter ranging from 20 to 60 nm, and were mainly located at the surface of the larger MgO particles and also within MgB_2 grains. No trace of discrete Y_2O_3 particles was detected. Fine $20-30$ nm MgO particles were found within MgB_2 grains, as well as coarser MgO up to 150 nm located at grain boundaries.

In order to confirm the presence of YB_4 by XRD, a sample was manufactured by FAST using an ODS powder containing 10 wt.% Y_2O_3 so that YB_4 peaks could be detected. Figure 4.8 shows that several YB_4 peaks were observed in the XRD pattern whereas no trace of Y_2O_3 could be detected. Finally, YB_4 was also observed by Transmission Kikuchi Diffraction (TKD), as shown

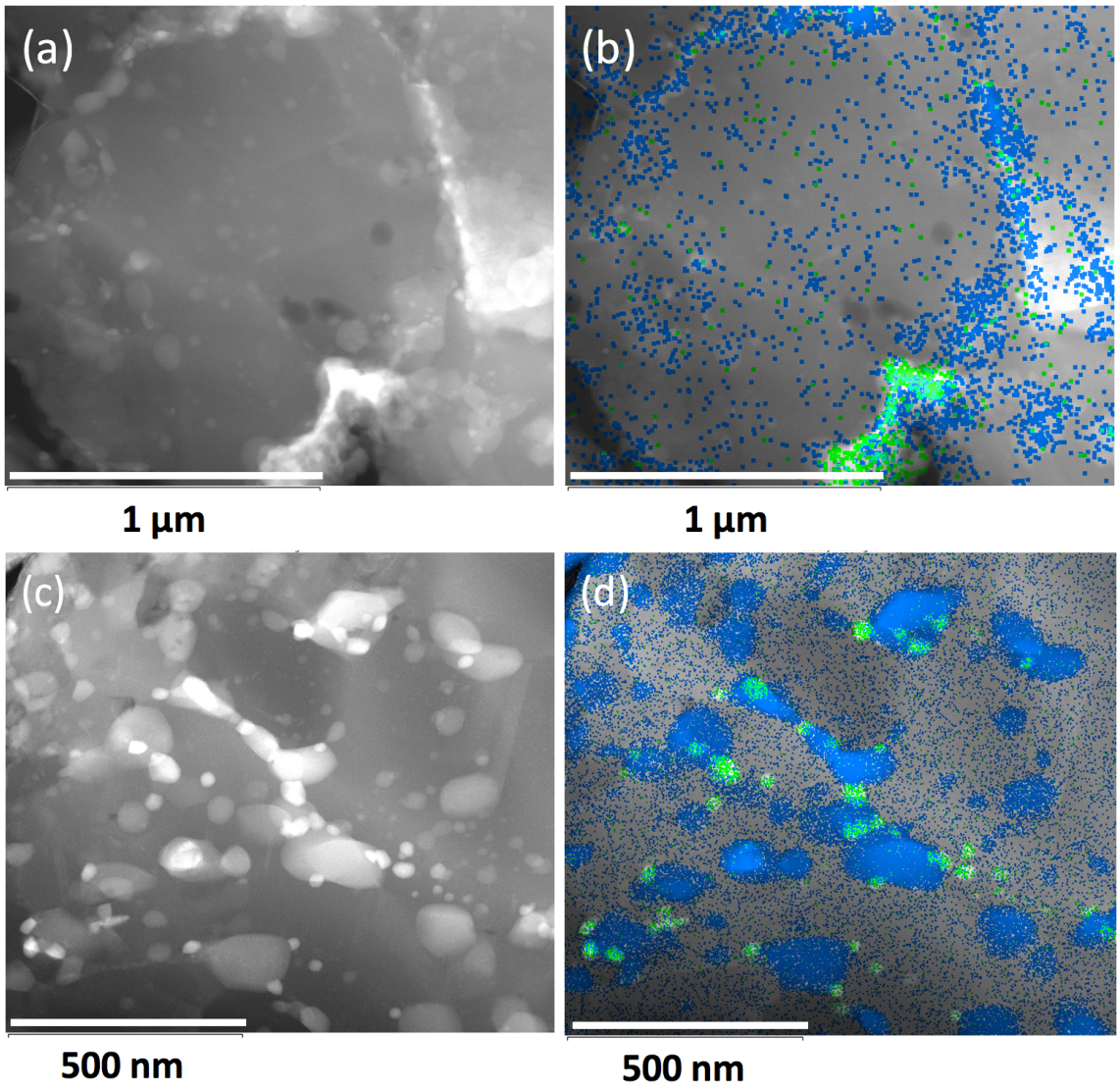

Figure 4.7: Typical STEM HAADF images and Y (green) and O (blue) EDX maps of bulk ODS specimens made from ODS powders ball milled for (a, b) 1 h and (c, d) 12 h.

in the example given in Figure 4.9. Wang *et al.* [69] also found that YB_4 was formed in Y_2O_3 doped MgB_2. In fact, YB_4 can also be synthesised through the borothermal reduction of Y_2O_3 at temperatures around 2000 °C [100]. Although the sintering temperature (here of 1150 °C) was lower, local temperatures in the FAST are known to sometimes be very much higher than the "bulk" reading from a pyrometer or thermocouple, even if only for a few seconds. In addition, as previously suggested, Y may be dissolved in MgB_2 by milling and may react directly with MgB_2 and re-precipitate to form YB_4. At the same time, dissolved oxygen precipitates as MgO.

The size distributions of the MgO and YB_4 particles extracted from the HAADF images are shown in Figure 4.10 for the 12 h ODS sample. YB_4 particles followed a monomodal distribution with most diameters between 20 and 30 nm, and an average diameter of 28 ± 10 nm. XRD

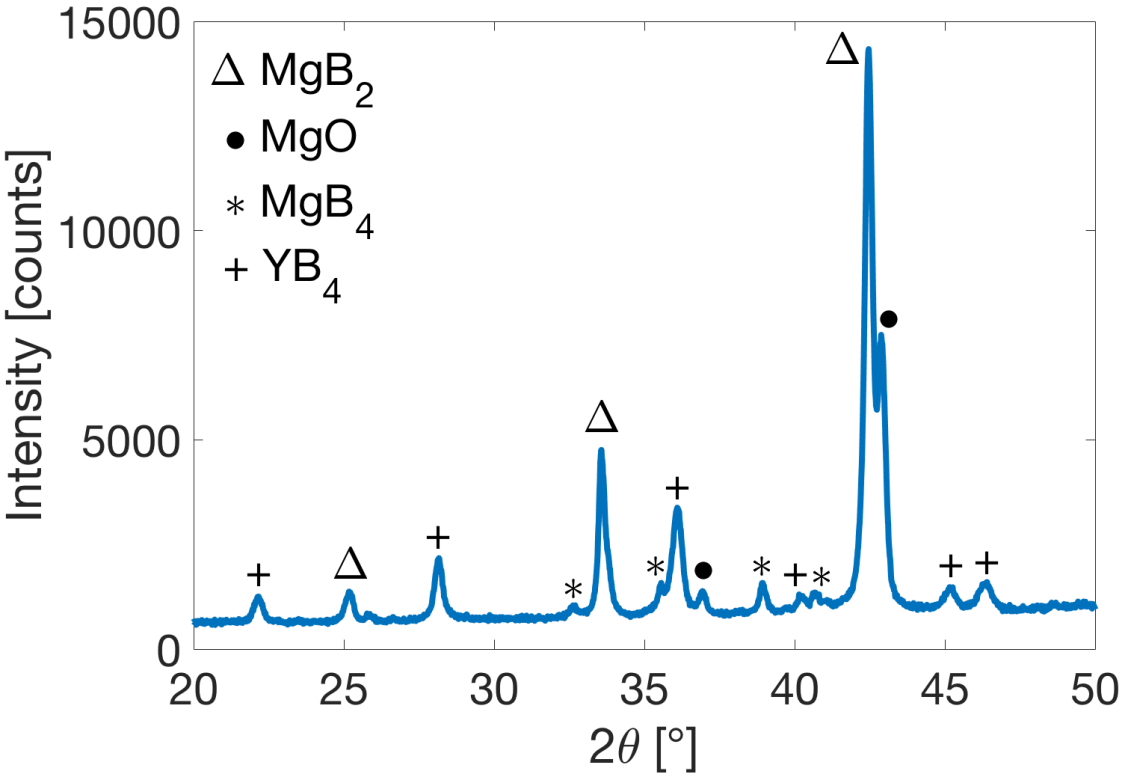

Figure 4.8: XRD pattern of a 10 wt.% Y_2O_3-MgB_2 ODS sample made by FAST at 1150 °C.

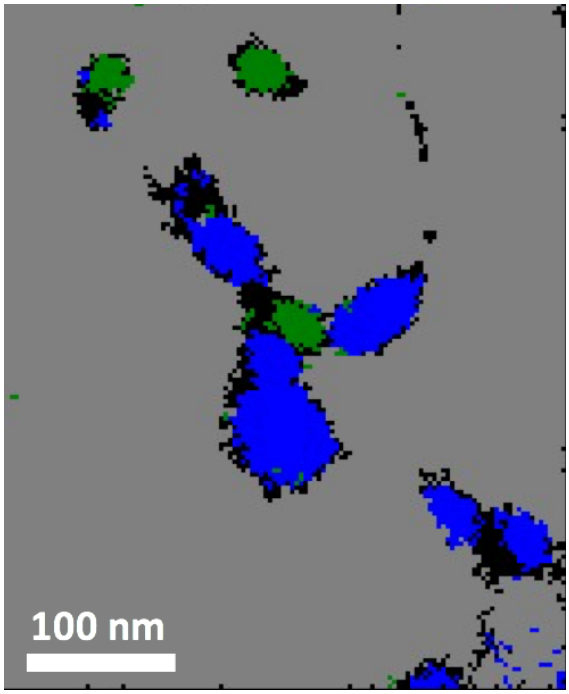

Figure 4.9: Typical TKD phase map of a 2 wt.% Y_2O_3-MgB_2 ODS specimen showing MgB_2 (grey), YB_4 (green) and MgO (blue). This analysis was performed by Junliang Liu.

patterns of 10 wt.% Y_2O_3-MgB_2 ODS samples processed under the same conditions gave YB_4 fractions high enough to be detected, and Rietveld analysis gave an average diameter of 35 nm, in good agreement with the STEM results. The size distribution of MgO was bimodal, composed of fine 20 to 50 nm and coarser 80 to 120 nm particles, with an average diameter of 60 ± 30 nm, again similar to the 50 nm extracted from the XRD measurements.

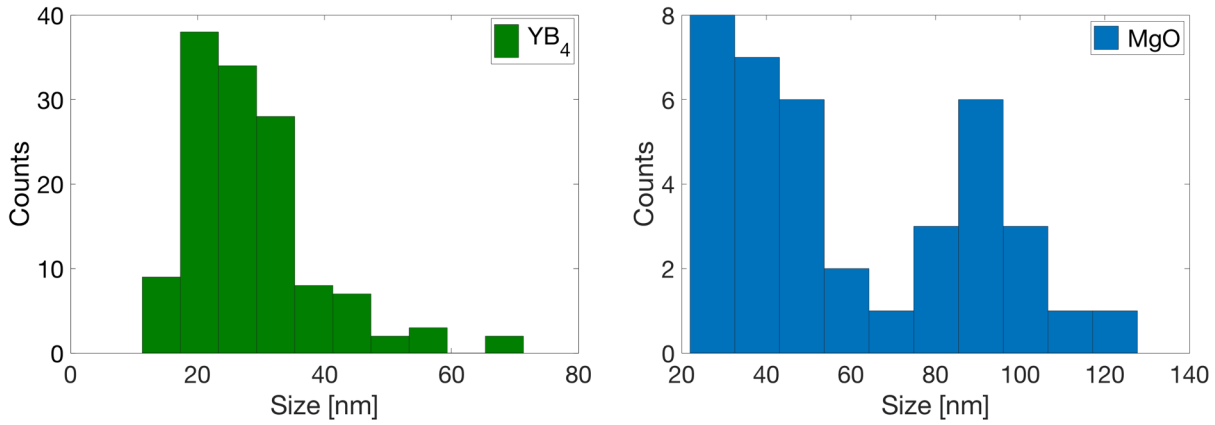

Figure 4.10: Size distributions of YB_4 and MgO particles found in the ODS specimen made from the ODS powder ball milled for 12 h. Measurements were performed on several HAADF images.

Overall, most of the YB_4 particles nucleated on larger MgO particles, which suggests that some MgO was present before YB_4 precipitation, i.e. before sintering. These large MgO particles were probably pre-existing in the as-supplied MgB_2 powder. The finer MgO particles were mainly located inside the MgB_2 grains with a diameter similar to the YB_4 precipitates, which may indicate they were formed and coarsened during the FAST process. This suggests that the addition and dissolution of Y_2O_3 in the MgB_2 matrix during mechanical alloying had the double effect of producing a fine dispersion of both YB_4 and MgO during sintering. This is dissimilar to ODS alloys where predominantly Y_2O_3 is re-precipitated, albeit with more complex transition phases sometimes involved, such as Y-Ti-O phases in Ti containing matrices [6].

Magnetic measurements

The superconducting properties of the ODS samples and unmodified MgB_2 are shown in Figure 4.11 and Table 4.6. Figure 4.11 (a) and Table 4.6 show that the normalised susceptibility curves of the ODS specimens were shifted to lower temperatures with increasing milling times. T_c in MgB_2 is well-known to be affected by any deviation from an ideal MgB_2 crystal structure, and is thus sensitive to doping, strain and defect concentrations, explaining the gradual degradation

in T_c in samples ball milled for longer durations. Nonetheless, all the ODS samples showed only a small reduction in T_c, indicating that Y_2O_3 does not have as severe an effect on T_c as carbon doping [33].

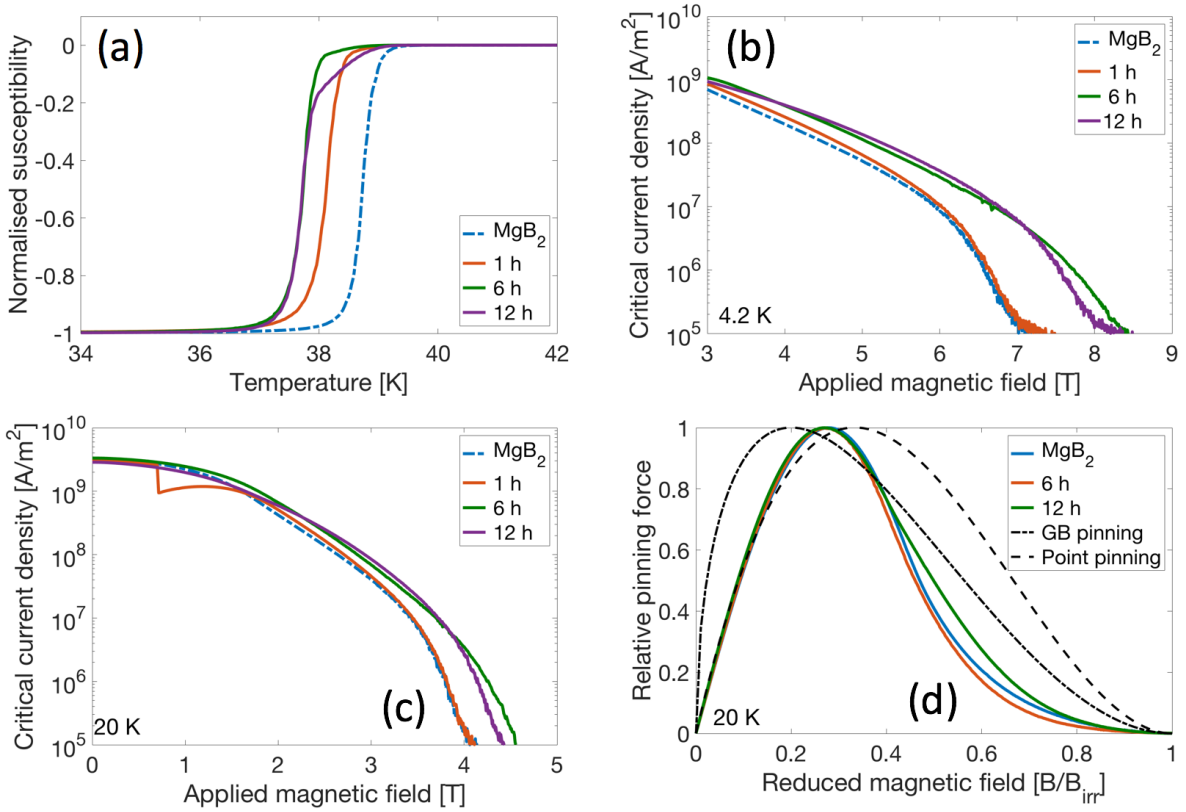

Figure 4.11: Superconducting properties of the ODS bulks made from 0.5 wt.% Y_2O_3-MgB_2 powders ball milled for 1, 6 and 12 h. J_c values were estimated using the macro-scale model.

Sample	T_c [K]	ΔT_c [K]	B_{irr}(4.2 K) [T]	B_{irr}(20 K) [T]	b_{peak}(20 K)	J_c(7 T,4.2 K) [A/m^2]	J_c(0 T,20 K) [A/m^2]
MgB_2	38.7	0.4	6.8	3.9	0.28	1.5 $\times 10^5$	3.3 $\times 10^9$
1 h	38.1	0.5	6.8	3.9	-	1.8 $\times 10^5$	3.1 $\times 10^9$
6 h	37.7	0.4	8	4.4	0.27	5.8 $\times 10^6$	3.3 $\times 10^9$
12 h	37.7	0.5	7.8	4.3	0.27	6 $\times 10^6$	2.9$\times 10^9$

Table 4.6: Superconducting properties of the ODS bulks made from 0.5 wt.% Y_2O_3-MgB_2 powders ball milled for 1, 6 and 12 h. J_c values were estimated using the macro model.

$J_c - B$ curves at 4.2 K are shown in Figure 4.11 (b). Measurements at lower fields were often compromised by excessive flux jumps below 3 T, so this is not shown in Figure 4.11 (b). The ODS sample milled for 1 h showed no improvement compared with unmodified MgB_2. On the other hand, both the 6 and 12 h milled samples showed an appreciable improvement in J_c over

the entire field range ($3 - 8$ T). This strong difference in performance can be directly related to the STEM observations. The 1 h sample showed a relatively poor distribution of YB_4 particles (Figure 4.7 (a, b)), which formed agglomerates that were much larger than the coherence length of MgB_2 ($\xi = 4 - 10$ nm [24]). In consequence, these agglomerates could not act as efficient pinning centres to improve J_c. In contrast, STEM analysis showed that the 12 h ODS specimen had a much more homogeneous dispersion of finer YB_4 precipitates (Figure 4.7 (c, d)). Since the 6 h sample had similar J_c values to the 12 h specimen, it was concluded that 6 h of ball milling is sufficient to obtain a homogeneous dispersion of YB_4 particles. At 4.2 K, the ODS samples ball milled for 6 and 12 h showed J_c(7 T) values 40 times higher than unmodified MgB_2, and B_{irr} was also improved by 1 T.

At 20 K, all four samples showed similar self-field J_c (J_{c0}) values, as shown in Table 4.6. Figure 4.11 (c) also shows that at 20 K, J_c at high field followed a similar trend to J_c at 4.2 K: the samples ball milled for 6 and 12 h had higher J_c values and showed a small improvement in B_{irr} compared to unmodified MgB_2.

These results are in good agreement with the studies of Wang [69] and Mikheenko [101] who observed similar J_c improvements in Y_2O_3 and Dy_2O_3 doped MgB_2. The authors found that nano-scale YB_4 or DyB_4 particles were formed during sintering and acted as efficient pinning centres that enhanced J_c, in particular at high field. They reported higher J_c values than we have obtained in our specimens, but direct comparisons are difficult owing to the fact that both Wang and Mikheenko used an in-situ processing method which tends to lead to higher grain connectivity [41].

Pinning force curves at 20 K were extracted from $M - B$ loop data as explained in section 2.2.6 and are shown in Figure 4.11 (d) for the 6 and 12 h ODS samples and unmodified MgB_2. The curves at 4.2 K are not displayed due to flux jumps in the $M - B$ data. Figure 4.11 (d) shows that the pinning force curves of the ODS samples and unmodified MgB_2 have very similar shapes, with a peak at $b \sim 0.27$ which is in between the theoretical values expected for the GB and point pinning models at 0.2 and 0.33 respectively [15]. This suggests that ODS samples and unmodified MgB_2 show similar pinning mechanisms, with the simple interpretation being that they have contributions from both GB and point pinning. However, care must be taken with extracting pinning mechanism information from these curves as suggested by Speller [37].

4.2.2 Effect of Y_2O_3 fraction

Sample details

The effect of the fraction of Y_2O_3 was investigated by manufacturing ODS powders containing 0.2, 0.5 and 2 wt.% Y_2O_3 ball milled for 12 h. All the bulks were sintered using the same conditions, as shown in Table 4.7.

Initial Powder	Sintering T [°C]	Sintering time [min]	Heating rate [°C/min]	Pressure [MPa]
MgB_2	1150	5	120	50
MgB_2 + 0.2 wt.% Y_2O_3 milled 12 h	1150	5	120	50
MgB_2 + 0.5 wt.% Y_2O_3 milled 12 h	1150	5	120	50
MgB_2 + 2 wt.% Y_2O_3 milled 12 h	1150	5	120	50

Table 4.7: Processing conditions of Y_2O_3-MgB_2 ODS bulks manufactured by FAST

XRD and density measurements

The results of the XRD analysis and density measurements are summarised in Table 4.8. All the ODS samples showed lower density values than unmodified MgB_2. This is consistent with the results presented in the previous section (4.2.1), where ODS samples containing higher fractions of MgO showed lower density values. In addition, the density of the ODS specimens decreased with increasing Y_2O_3 fraction. Since all three ODS samples had almost identical MgO fractions, this suggests that Y_2O_3 additions have a detrimental effect on densification. Similar to MgO, Y_2O_3 has a much higher intrinsic sintering temperature than MgB_2 and usually requires temperatures in excess of 1800 °C to sinter [102]. The presence of undissolved Y_2O_3 in the ODS powder (which could not be found by XRD and STEM analysis) could thus hinder densification. Another explanation is that dissolved Y and/or O in the MgB_2 lattice leads to slower diffusion rates and thus slows down sintering kinetics.

Sample	MgO [wt.%]	MgB_4 [wt.%]	Relative density [%]	MgB_2 crystallite size [nm]	MgB_2 strain [%]	MgO crystallite size [nm]	MgB_2 *a*-axis [Å]	MgB_2 *c*-axis [Å]
MgB_2	8	13	93	150	0.14	50	3.084	3.528
0.2 wt.%	16	9	91	90	0.18	49	3.084	3.529
0.5 wt.%	15	17	87	90	0.2	49	3.085	3.529
2 wt.%	15	19	86	80	0.21	44	3.084	3.528

Table 4.8: XRD characterisation and relative density of bulk samples made from ODS powders containing 0.2, 0.5 and 2 wt.% Y_2O_3 and milled for 12 h.

All three ODS specimens showed a significant increase in the fraction of MgO compared to unmodified MgB_2. This increase comes from the ball milling process as discussed in section 4.2.1. All the ODS samples also showed similar MgB_2 and MgO crystallite size, suggesting that the fraction of Y_2O_3 does not have a significant effect on microstructure refinement. The strain values increased slightly with higher Y_2O_3 fractions which is probably due to residual strain induced by YB_4 particles in the MgB_2 matrix upon cooling from high temperature.

STEM

ODS samples were characterised by STEM, and typical HAADF images and corresponding Y and O EDX maps of 0.5 and 2 wt.% specimens are shown in figure 4.12. As already discussed in section 4.2.1, the ODS samples showed relatively fine MgB_2 grains containing numerous MgO and YB_4 nano-particles. As expected, Figures 4.12 (c, d) show that the 2 wt.% specimen contained a larger number of YB_4 particles and that a large fraction of these particles were located at MgB_2 grain boundaries. In contrast, the 0.5 wt.% sample showed a more homogeneous YB_4 distribution.

Magnetic measurements

The superconducting properties of the ODS bulks made from powder containing 0.2, 0.5 and 2 wt.% Y_2O_3 are shown in Figure 4.13 and Table 4.7. Figure 4.13 (a) shows that T_c gradually decreased with increasing Y_2O_3 fraction. In addition, Table 4.7 suggests that ΔT_c slightly increased with higher Y_2O_3 fractions. As already discussed in Chapter 3 (magnetic measurements section), the superconducting transition in MgB_2 is sensitive to several factors such as the defect density and elements in solid solution in the MgB_2 lattice. The reduction in T_c observed in samples containing larger Y_2O_3 fractions was probably caused by higher concentrations of Y and O dissolved in the lattice and/or higher defect concentrations. Although Figures 4.12 (a-d) show the presence of numerous YB_4 precipitates in the ODS bulks, a small fraction of Y and O might still be dissolved in the MgB_2 lattice, reducing T_c. The fraction of residual Y and O in solid solution is likely to be higher in ODS samples made from powders containing higher Y_2O_3 fractions, which could explain the larger T_c reduction observed in these specimens. However, the a and c-axis lattice parameters of all three ODS specimens were almost identical, which does not allow any firm conclusion on the relative amount of Y and O dissolved in these samples to be

drawn. On the other hand, the inhomogeneous strain was slightly higher in the 2 wt.% sample, suggesting a higher defect concentration.

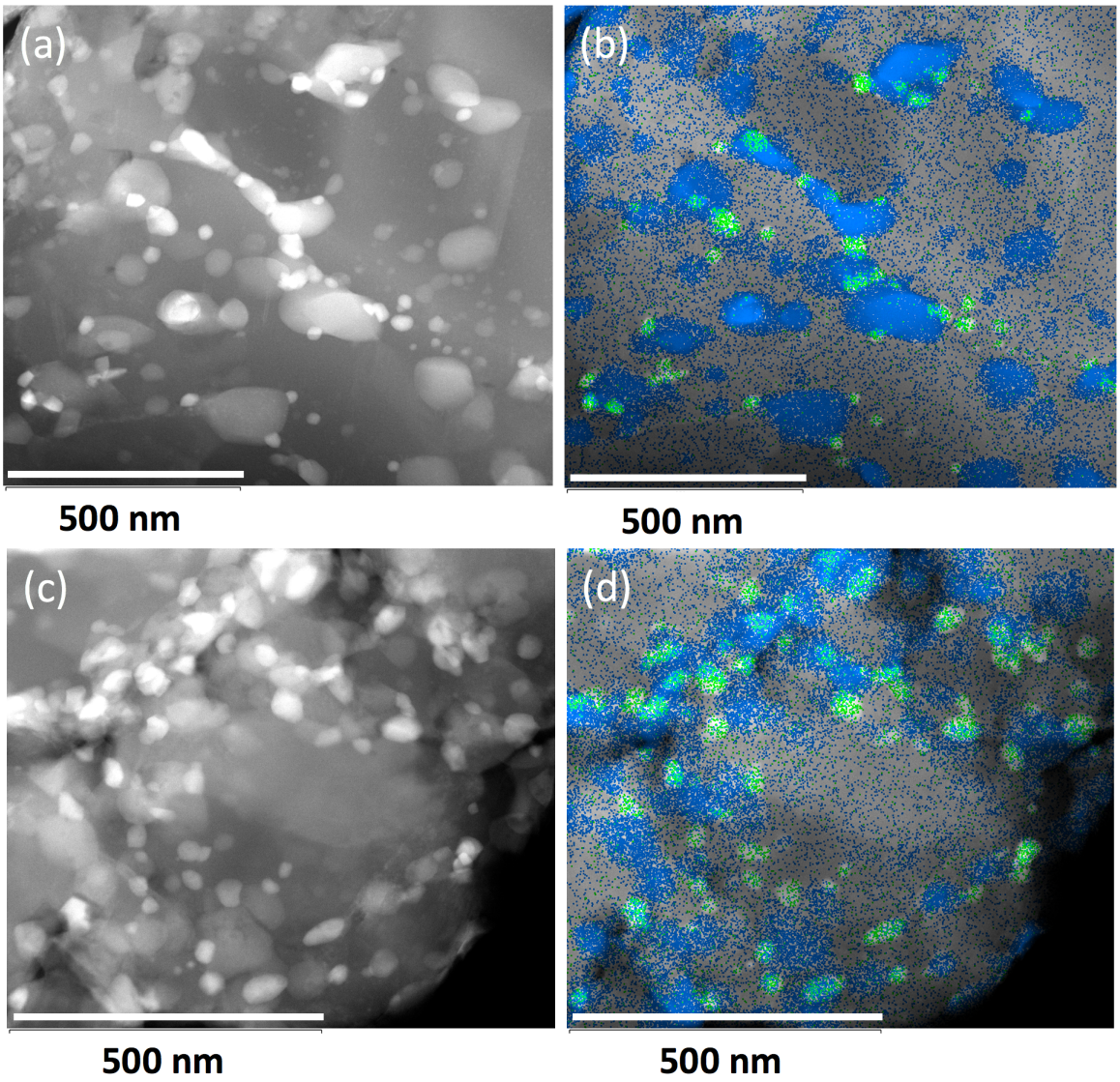

Figure 4.12: Typical STEM HAADF images and Y (green) and O (blue) EDX maps of ODS specimens made from ODS powders containing (a, b) 0.5 wt.% and (c, d) 2 wt.% Y_2O_3.

Sample	T_c [K]	ΔT_c [K]	B_{irr}(4.2 K) [T]	B_{irr}(20 K) [T]	b_{peak}(20 K)	J_c(7 T,4.2 K) [A/m^2]	J_c(0 T,20 K) [A/m^2]
MgB_2	38.7	0.4	6.8	3.9	0.28	1.5 $\times 10^5$	3.3 $\times 10^9$
0.2 wt.%	38.3	0.5	7.2	4.1	0.27	5 $\times 10^5$	3.2 $\times 10^9$
0.5 wt.%	37.7	0.5	7.8	4.3	0.27	6 $\times 10^6$	2.9$\times 10^9$
2 wt.%	37.2	0.7	7.4	4.0	0.26	3 $\times 10^6$	2.5 $\times 10^9$

Table 4.9: Superconducting properties of the ODS bulks manufactured by FAST using ODS powders containing 0.2, 0.5 and 2 wt.% Y_2O_3 and ball milled for 12 h. J_c values were estimated using the macro model.

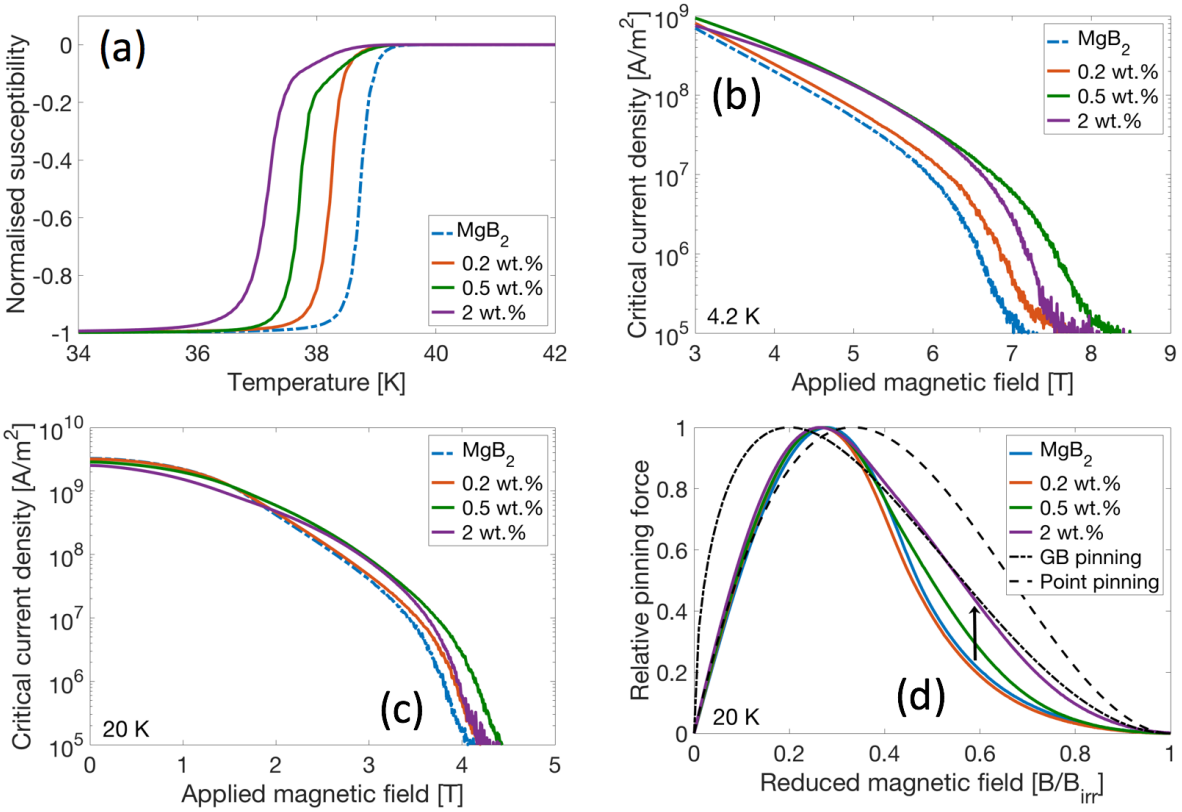

Figure 4.13: Superconducting properties of the ODS bulks manufactured by FAST using ODS powders containing 0.2, 0.5 and 2 wt.% Y_2O_3 and ball milled for 12 h. J_c values were estimated using the macro model.

Figure 4.13 (b) shows the $J_c - B$ curves at 4.2 K for the samples made from the ODS powders containing 0.2, 0.5 and 2 wt.% Y_2O_3. All three ODS specimens had higher J_c values at high field $(3 - 8$ T$)$[3] than unmodified MgB_2, with the 0.5 wt.% specimen showing the best performance. The J_c improvement observed in the ODS samples is probably a compromise between increasing the number of efficient pinning centres while maintaining high connectivity. While the 2 wt.% specimen had a larger number of YB_4 particles (thus more pinning centres), Figures 4.12 (c, d) show that most of these were located at grain boundaries and some also formed agglomerates which presumably led to a degradation in electrical connectivity. These results suggest that intermediate fractions of Y_2O_3 (< 2 wt.%) are better to maintain a high connectivity, and lead to better J_c values overall.

At 20 K, similar trends are observed in Figure 4.13 (c). Table 4.9 shows that J_c(0 T, 20 K) gradually decreased with increasing Y_2O_3 fraction. As discussed in section 3, J_c values at low field depend mostly on extrinsic factors such as connectivity and the superconducting fraction.

[3]The data below 3 T is not shown due to flux jumps

It was concluded that connectivity had the largest effect on J_{c0}. This suggests that ODS powders containing higher fractions of Y_2O_3 lead to ODS bulks showing lower connectivity.

Pinning force curves at 20 K are shown in Figure 4.13 (d). All three ODS specimens and unmodified MgB_2 had a peak at $b \sim 0.27$ and almost identical shapes on the low field side of the curve (before the peak). The only difference arose from the shape of the curves after the peak, where ODS samples containing higher fractions of Y_2O_3 showed less pronounced concave shapes, in contrast with unmodified MgB_2, as shown by the arrow in Figure 4.13 (d). The same trend was observed in unmodified MgB_2 specimens sintered at low temperature (section 3). MgB_2 samples processed at low temperature also showed broader superconducting transitions (Table 3.3), similar to the ODS samples containing higher Y_2O_3 fractions, as shown in Table 4.9. It was concluded in section 3 that the concave shape observed after the peak was caused by anisotropy effects, rather than a change in pinning mechanism. In consequence, the pinning force curves shown in Figure 4.13 (d) suggest that samples containing higher Y_2O_3 fractions show lower connectivity values, and that the ODS samples and unmodified MgB_2 have similar pinning mechanisms having contributions from both GB and point pinning.

4.2.3 Effect of sintering temperature

Sample details

The effect of the sintering temperature was investigated by manufacturing ODS bulks by FAST at $950 - 1200$ °C. The same 0.5wt.% Y_2O_3-MgB_2 ODS powder ball milled for 12 h was used to make all the specimens. The processing parameters are summarised in Table 4.10.

Initial Powder	Sintering T [°C]	Sintering time [min]	Heating rate [°C/min]	Pressure [MPa]
MgB_2 + 0.5 wt.% Y_2O_3 milled 12 h	950	5	120	50
MgB_2 + 0.5 wt.% Y_2O_3 milled 12 h	1000	5	120	50
MgB_2 + 0.5 wt.% Y_2O_3 milled 12 h	1100	5	120	50
MgB_2 + 0.5 wt.% Y_2O_3 milled 12 h	1200	5	120	50

Table 4.10: Processing conditions of Y_2O_3-MgB_2 ODS bulks manufactured by FAST

XRD and density

Table 4.11 shows the results of the XRD analysis and the density measurements for Y_2O_3-MgB_2 ODS samples sintered between 950 and 1200 °C, and the as-milled ODS powder. As

expected, the density increased with higher sintering temperatures. However, the density of the ODS bulks sintered at high temperature were much lower than for unmodified MgB_2 samples processed at the same temperature. Figure 4.14 shows the relative density of unmodified MgB_2 and 0.5 wt.% Y_2O_3-MgB_2 samples sintered at temperatures between 1000 and 1200 °C. Although unmodified MgB_2 and the ODS sample sintered at 1000 °C have the same density, ODS specimens manufactured at higher temperature showed density values much lower than unmodified MgB_2. As already discussed in section 4.2.2, this further confirms that Y_2O_3 additions have a detrimental effect on densification, and lead to slower sintering kinetics.

Sample	MgO [wt.%]	MgB_4 [wt.%]	Relative density [%]	MgB_2 crystallite size [nm]	MgB_2 strain [%]	MgO/YB_4^* crystallite size [nm]	MgB_2 a-axis [Å]	MgB_2 c-axis [Å]
Powder	11	11	-	50	0.52	11 / -	3.088	3.528
950 °C	16	18	72	60	0.27	22 / 19	3.085	3.527
1000 °C	16	19	75	60	0.26	25 / 19	3.084	3.527
1100 °C	16	20	78	70	0.23	34 / 25	3.084	3.527
1200 °C	16	6	86	100	0.16	48 / 36	3.085	3.527

Table 4.11: XRD characterisation and relative density of 0.5 wt.% Y_2O_3-MgB_2 ODS samples made by FAST, and as-milled ODS powder.*The YB_4 crystallite size was estimated from 10 wt.% Y_2O_3-MgB_2 samples processed under the same conditions.

Table 4.11 shows that the sintering temperature had no effect on the MgO fraction. All four ODS samples had an identical MgO content of 16 wt.%. The specimens sintered at 950, 1000 and 1100 °C also contained very similar amount of MgB_4. However the sample sintered at the highest temperature (1200 °C) showed a much smaller fraction of MgB_4. A few very weak peaks indexed as MgB_7 were seen in the XRD pattern of the sample sintered at 1200 °C, which suggests that at this temperature MgB_4 decomposes into $Mg_{(g)}$ and MgB_7. This is consistent with the phase diagram calculated by Liu *et al.* [26].

The MgB_2 crystallite size increased slightly to 60 nm in the bulks sintered at 950 and 1000 °C compared to 50 nm in the powder. The crystallite size increased more rapidly for the samples sintered at temperatures above 1000 °C, reaching 100 nm at 1200 °C. The strain was drastically reduced with increasing sintering temperature, reaching values as low as 0.16% in the 1200 °C sample compared to 0.52% in the powder. This indicates that high sintering temperatures relieve the residual strain induced in the powder during the ball milling process.

Similar crystallite size values $\sim$ 20 nm are found for MgO and YB_4 in the specimen sintered at 950 °C. Both phases showed significant coarsening with higher sintering temperatures, in

particular MgO and YB_4 particles grew to an average size of 48 nm and 36 nm respectively in the 1200 °C sample.

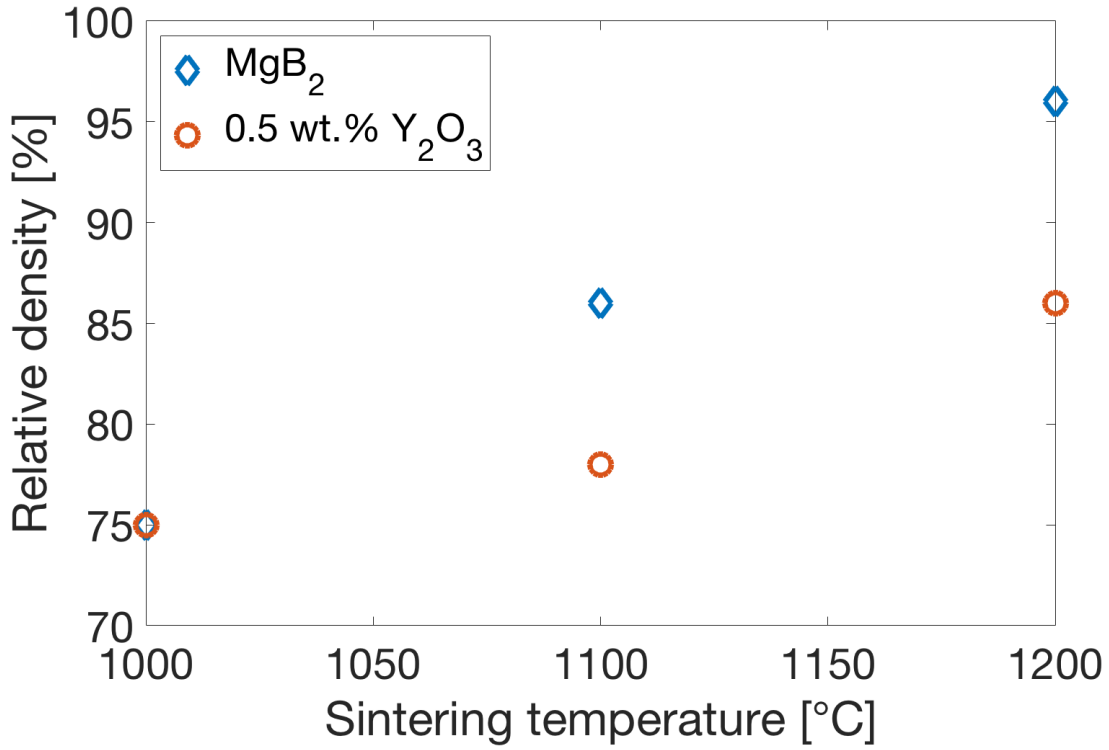

Figure 4.14: Relative density of MgB_2 and 0.5 wt.% Y_2O_3-MgB_2 samples sintered between 1000 and 1200 °C.

SEM

Figures 4.15 (a) and (b) show low magnification backscattered SEM images of the ODS samples sintered at 950 and 1200 °C respectively. The sample sintered at 950 °C looks like cold compacted powder and does not show any sign of sintering. The microstructure was composed of a mixture of small MgB_2 particles a few microns in diameter and very fine sub-micron particles, both having relatively spherical shapes. A few large 10-50 μm particles were also seen in Figure 4.15 (a). This is in good agreement with the particle size distribution measured by laser diffraction shown in Figure 4.1 (b). This microstructure is completely different from the one observed in unmodified MgB_2 sintered at 900 °C, shown in Figure 3.2 (a). The main difference comes from the shape and size of the powder particles, which were much larger (5-100 μm) and angular in unmodified MgB_2.

Figure 4.15 (b) shows that the 1200 °C ODS sample has sintered to a much greater extent, but

still shows a higher fraction of porosity than unmodified MgB_2 sintered at 1200 °C (Figure 3.2 (d)). This is consistent with the large difference in density observed between the ODS specimen and unmodified MgB_2 sintered at 1200 °C (Figure 4.14). As discussed in section 1.3.1, the driving force for sintering is the reduction in surface area of the powder. Let us approximate the MgB_2 and ODS powders by spherical particles of diameter $d_{0.5}$. The median size of the MgB_2 and ODS powders are respectively ~ 40 μm and 1.5 μm. It follows that the specific surface area of the ODS powder is almost 30 times larger than for the unmodified MgB_2 powder. Since the driving force is 30 times larger for the ODS powder, one would expect the ODS powder to sinter more easily than unmodified MgB_2. However, despite the larger driving force, the opposite trend is observed. Again this confirms that ball milling (through the oxidation of the MgB_2 surface and formation of MgO) and Y_2O_3 additions are detrimental to the sintering process.

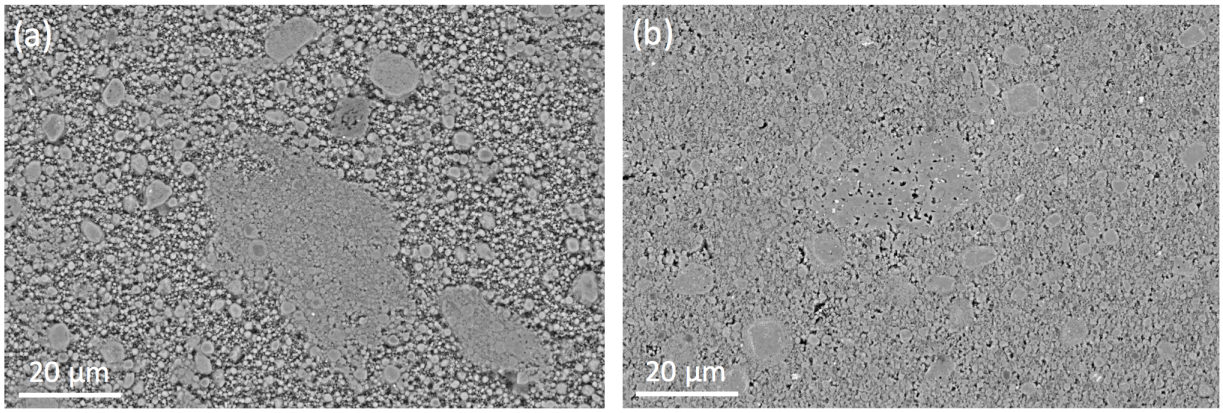

Figure 4.15: Backscattered SEM images of 0.5 wt.% Y_2O_3-MgB_2 ODS samples sintered at (a) 950 °C and (b) 1200 °C.

Higher magnification images of the ODS samples sintered at 950 and 1200 °C are shown in Figures 4.16 (a) and (b) respectively. Figure 4.16 (a) confirms that the microstructure of the sample processed at 950 °C is mainly composed of small $0.2 - 2$ μm spherical particles "aggregated together" that does not show any sign of sintering. Figure 4.16 (b) reveals that even after sintering at 1200 °C, the ODS powder has only sintered to a small extent. In contrast, unmodified MgB_2 sintered at 1200 °C (Figure 3.3 (d)) showed a well sintered microstructure with hardly any porosity. Obtaining dense ODS bulks is thus a real challenge due to the negative effect of MgO and Y_2O_3 on densification.

Very fine MgO particles (< 100 nm) can be seen in Figure 4.16 (b) and were located on the surface of particles and also at grain boundaries within individual particles. This is in good

agreement with the XRD analysis in Table 4.11 which gave an average MgO particle size of ~ 50 nm.

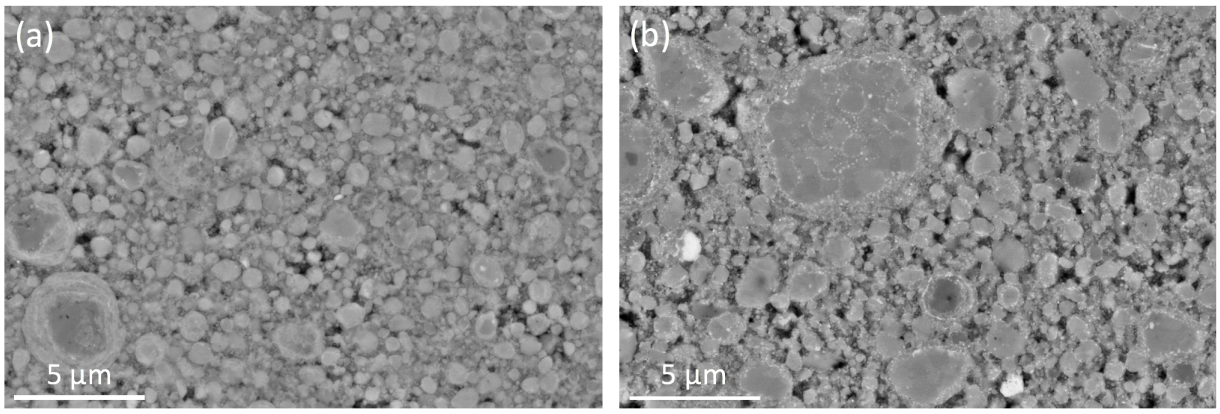

Figure 4.16: Backscattered SEM images of 0.5 wt.% Y_2O_3-MgB_2 ODS samples sintered at (a) 950 °C and (b) 1200 °C.

Magnetic measurements

The normalised susceptibility curves for all four ODS samples (Figure 4.17 (a)) showed a step in the superconducting transition. A first onset was observed at approximately 38.7 K for all the ODS samples, followed by a second one at lower temperature and at a similar susceptibility value of ~ -0.2. This can be explained by inhomogeneity using a "two powders" model. The first powder was composed of unaltered particles with high T_c, similar to unmodified MgB_2. The second powder was constituted of particles that have undergone severe cold work and contained dissolved Y and O, and for which the MgB_2 lattice was heavily damaged, thus showing much lower T_c. A possible explanation is that after mechanical alloying, the powder particles could have a damaged external layer. For small and medium particles, the damaged layer was similar in size to the particle radius and thus these particles were strongly affected by ball milling and associated to the low T_c transition. In larger particles, the damaged layer was smaller than the radius of the particle and thus there was an unaffected core region that led to the high T_c transition. It was shown in section 4.1 that ODS powders ball milled for longer showed weaker and broader XRD Bragg reflections (Figure 4.2), and slightly larger a and c-axis lattice parameters for MgB_2 (Table 4.1), suggesting that some Y and O were dissolved in the MgB_2 lattice. As discussed in section 4.1, the magnetic susceptibility of the ODS powder ball milled for 12 h (Figure 4.5),

reached a value of ~ -0.2 at low temperature (10 K), instead of -1 for a perfect superconductor in the Meissner phase, suggesting that only ~ 20 vol.% of the powder was still superconducting while the remaining ~ 80 vol.% had been heavily damaged during the ball milling process. This is in good agreement with the fact that the second onset in the superconducting transition of all four ODS bulks (Figure 4.17 (a)) was located at a susceptibility value of approximately -0.2. The two powders model is useful to understand the step in the susceptibility curves of the ODS bulks and its evolution with the sintering temperature.

All four ODS bulks have been made from the same powder ball milled for 12 h. Following the two powders model, the ball milled powder is composed of "two powders" prior to sintering, ~ 20 vol.% of unaltered powder having high T_c (~ 39 K), and ~ 80 vol.% of damaged powder which is not superconducting. The 20 vol.% of unaltered powder does not undergo any significant change during the sintering process. This is reflected by the first small superconducting transition (at ~ 39 K) shown by all four ODS samples in Figure 4.17 (a), regardless of the sintering temperature.

The main transition that ranges from -0.2 to -1, corresponds to the remaining 80 vol.% of damaged powder which recovered superconductivity after the sintering process. Some of the defects and elements in solid solution in the MgB_2 lattice were presumably annealed out at high temperature. This is supported by the reduction in inhomogeneous strain with higher sintering temperature (Table 4.11) and the precipitation of YB_4 particles discussed above. Figure 4.17 (a) shows that as the sintering temperature increased, the main superconducting transition (corresponding to the damaged powder) was pushed to higher temperatures, and eventually almost merged with the secondary transition in the 1200 °C sample. This is confirmed by the significant increase in T_c with higher sintering temperatures, as shown in Table 4.12. This progressive shift can be explained by the fact that damaged powders exposed to higher temperatures benefit from higher diffusion rates leading to quicker and more complete recovery of the defective MgB_2 lattice.

Figure 4.17 (b) shows that the sintering temperature had a large effect on J_c(4.2 K) values at high field. Table 4.12 shows that the 950 and 1000 °C samples had J_c(7 T, 4.2 K) values 2 orders of magnitude larger than for unmodified MgB_2. All four ODS specimens also showed higher J_c values than unmodified MgB_2 at fields > 5 T. The ODS samples sintered at 950 and 1000 °C showed the largest increase in B_{irr} (estimated with the method described in section 2.2.6) at

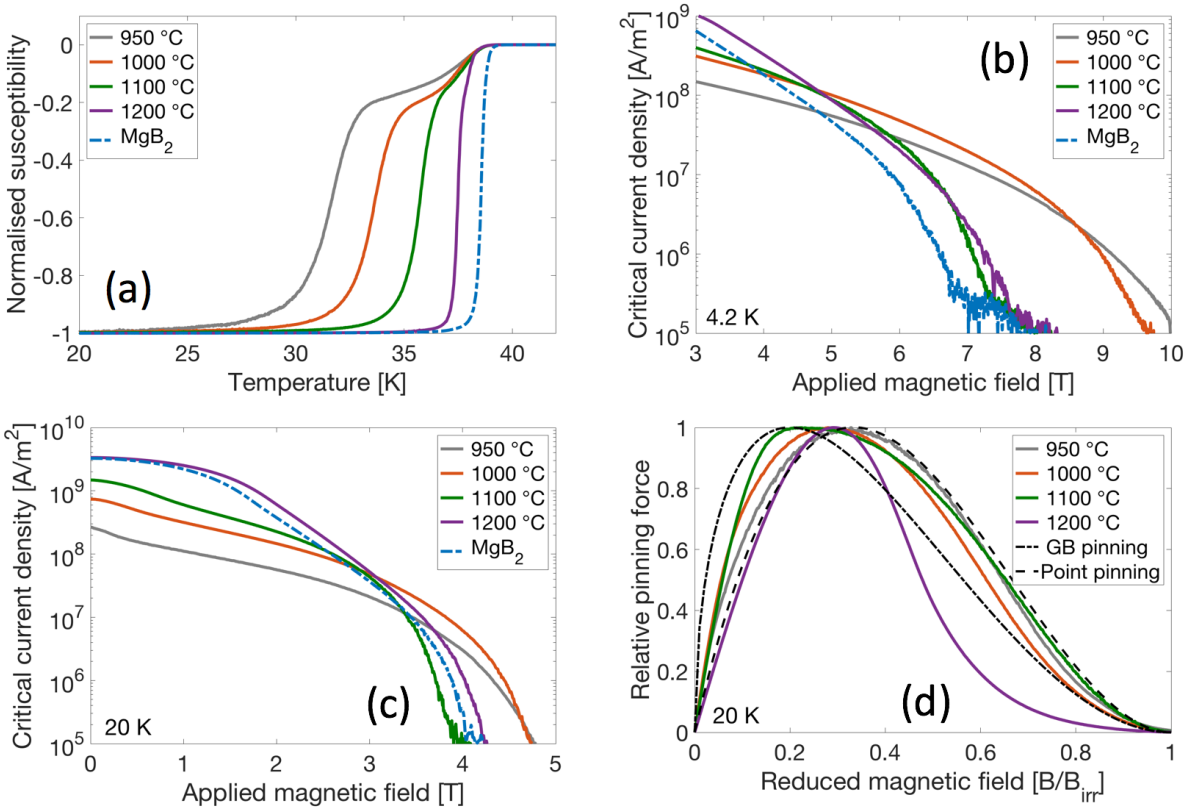

Figure 4.17: Superconducting properties of 0.5 wt.% Y_2O_3-MgB_2 ODS samples sintered at 950 – 1200 °C and unmodified MgB_2 sintered at 1200 °C. J_c values were estimated using the macro-scale model.

Sample	T_c [K]	ΔT_c [K]	B_{irr}(4.2 K) [T]	B_{irr}(20 K) [T]	b_{peak}(20 K)	J_c(7 T,4.2 K) [A/m^2]	J_c(0 T,20 K) [A/m^2]
950 °C	31.5	2.9	10.0	4.7	0.33	1.3 $\times 10^7$	2.7 $\times 10^8$
1000 °C	33.6	2.4	9.5	4.7	0.29	2.0 $\times 10^7$	7.4 $\times 10^8$
1100 °C	35.7	1.6	7.3	3.8	0.22	1.3 $\times 10^6$	1.5 $\times 10^9$
1200 °C	37.5	0.5	7.4	4.1	0.29	2.2 $\times 10^6$	3.4 $\times 10^9$
MgB_2	38.6	0.4	6.9	4.0	0.27	1.5 $\times 10^5$	3.3 $\times 10^9$

Table 4.12: Superconducting properties of 0.5 wt.% Y_2O_3-MgB_2 ODS samples sintered at 950 – 1200 °C and unmodified MgB_2 sintered at 1200 °C. J_c values were estimated using the macro-scale model.

10 T and 9.5 T respectively, compared to $\sim$ 7 T for the ODS samples and unmodified MgB_2 processed at higher temperature.

Figure 4.17 (c) shows that the sintering temperature had a smaller, but rather similar effect on J_c(20 K) values at high field. On the other hand, low sintering temperatures severely reduced J_c(20 K) values at low field (0 – 3 T). In particular, J_c(0 T, 20 K) of the 1200 °C sample increased 10 fold compared to the 950 °C specimen. This was also observed in unmodified MgB_2 sintered between 900 and 1200 °C, where J_c(0 T, 20 K) increased 6 fold by raising the sintering

temperature from 900 °C to 1200 °C. As discussed in section 3, this large increase in J_{c0} values was attributed to connectivity improvements. This increase in J_{c0} observed in ODS samples sintered at higher temperatures is probably due to similar connectivity improvements. This is supported by the density measurements and SEM analysis above, suggesting that the 1200 °C ODS specimen had sintered to a much greater extent than the 950 °C sample, as shown in Figure 4.15.

Table 4.12 also shows that the 1200 °C ODS sample had almost the same J_c(0 T, 20 K) value as unmodified MgB_2. This is surprising considering the large difference in density between the 2 samples. Unmodified MgB_2 had a density of 96% and showed a well sintered microstructure with hardly any porosity, as shown in Figure 3.3 (d). On the other hand, the 1200 °C ODS sample had a much lower density of 86%, and Figure 4.16 (d) revealed a microstructure that contained a significant fraction of porosity. Nonetheless, both samples had almost identical J_{c0}(20 K) values which suggests that both specimens had relatively similar connectivity. Therefore it appears that connectivity is difficult to judge from SEM images alone and might not depend strongly on density in relatively dense specimens (> 86%). This was already observed in Chapter 3, where unmodified MgB_2 sintered at 1100 °C and 1200 °C showed similar J_{c0}(20 K) despite having different densities. Transport measurements are thus crucial to characterise quantitatively the connectivity in ODS bulks. Future work should include a systematic analysis of the connectivity by transport measurements in order to investigate more rigorously the effect of the composition and sintering conditions on the connectivity of ODS bulks.

Pinning force curves at 20 K for the ODS samples sintered between 950 and 1200 °C are shown in Figure 4.17 (d). As discussed in Chapter 3 (pinning force analysis section), the shape of the high field side of the curve (after the peak) can be strongly affected by anisotropy. It was also shown that well connected samples (sintered at high temperature) tend to show a pronounced concave shape on the high field side of the curve (Figure 3.8). Figure 4.17 (d) shows that only the 1200 °C sample had this concave shape, whereas all three specimens sintered at lower temperature showed relatively similar pinning force curves, close to the point pinning model. This confirms that the 1200 °C specimen showed higher connectivity than the samples sintered at lower temperature.

Figure 4.17 (d) shows that the 950 °C sample had a shape fitting very well to the point pinning model with a peak located at $b_{peak} = 0.33$, which is the exact value predicted by the point pinning

model. Simple interpretation[4] suggests that point pinning is the dominant pinning mechanism in the ODS sample sintered at 950 °C. This can be explained by the presence of very fine ($\sim$ 20 nm) MgO and YB_4 particles which act as efficient point pins, as shown in Table 4.11. Future work should involve STEM to confirm the average size of MgO and YB_4 precipitates estimated by XRD.

The pinning force curve of the 1000 °C sample is very similar to the 950 °C sample, only slightly shifted to lower fields, as indicated with its peak located at $b_{peak} = 0.29$. This suggests that there is a small GB pinning contribution in the 1000 °C sample, and that the pinning mechanism is between point and GB pinning, but still with point pinning as the main contribution. Table 4.11 shows that the 1000 °C sample had almost identical characteristics (composition and crystallite size) to the 950 °C specimen. However, these two samples show different pinning force curves which suggests that there are subtle differences in their microstructures. One possible explanation is that MgO and YB_4 particles coarsened slightly while the grain size remained mostly unchanged. This would cause an increase in the GB pinning contribution and lead to a peak shift toward the predicted value of 0.2 for the GB pinning model.

The pinning force curve of the 1100 °C sample follows the same trend, and was pushed even further to the left (lower fields), with a peak located at $b_{peak} = 0.22$. This is consistent with the microstructure evolution shown in Table 4.11. Indeed, the MgB_2 crystallite size only increased slightly compared to the specimens processed at lower temperature, whereas MgO and YB_4 particles grew more significantly. The relative contribution of GB pinning thus becomes larger, which is reflected by the peak shifting to $b_{peak} = 0.22$, close to the value of $b_{peak} = 0.2$ predicted by the GB pinning model.

The pinning force curve of the 1200 °C sample does not follow the same trend as the first three specimens (a gradual shift of the peak from $b_{peak} = 0.33$ to $b_{peak} = 0.22$). The peak of this specimen is located at b_{peak}=0.29 and the low field side of the curve (before the peak) is closer to the point pinning model. As explained above, the high field side of the curve deviates significantly from both models due to anisotropy effects. This suggests that the 1200 °C sample shows an hybrid pinning behaviour, with contributions from both GB and point pinning. In contrast with the samples sintered at 950, 1000 and 1100 °C where the GB pinning contribution increased with the sintering temperature, it decreased in the 1200 °C sample. This can be correlated with the

[4]Speller [37] showed that modified pinning models lead to different position of the peaks for the point and surface pinning models.

sudden increase in MgB_2 crystallite size at 1200 °C (Table 4.11).

These results suggest that coarsening of MgO and YB_4 particles occurred first between 950 and 1100 °C, followed by a delayed grain growth taking place above 1100 °C. This explains why the GB pinning contribution (relative to point pinning) first increased with sintering temperature before decreasing above 1100 °C.

This delayed grain growth might seem surprising at these high sintering temperatures but can be explained by Zener drag [103, 104]. In addition to dislocation pinning, oxide particles in ODS steels also pin grain boundaries, which contributes to their superior high temperature strength [7, 105]. This technique of slowing down grain growth by having a fine dispersion of particles pinning grain boundaries is known as the Zener drag or Zener pinning, and has been used in several commercial applications including tungsten filaments, transparent alumina and High Stength Low Alloy (HSLA) steels [103,105]. Therefore, it is expected that MgO and YB_4 particles have a similar effect in ODS superconductors, and thus hinder coarsening of MgB_2 grains through Zener pinning. In fact, the evolution of the microstructure with increasing sintering temperature shown in Table 4.11 suggests a behaviour that is consistent with Zener pinning. MgO and YB_4 particles grew gradually with the processing temperature, but the MgB_2 crystallite size increased suddenly only above 1100 °C. This suggests that MgO and YB_4 particles were small enough to act as efficient Zener pinning centres in the samples sintered below 1100 °C. However, these particles were too large in the ODS specimen sintered at 1200 °C and did not lead to efficient Zener drag, allowing grain growth to occur.

4.2.4 Ultra-high pressure hot pressing

A few specimens were made at Element 6 using their ultra high pressure (UHP) hot press in order to investigate the effect of extreme pressure on the microstructure and superconducting properties of ODS and unmodified MgB_2 bulks. The details of this process were presented in section 2.1.3. In this section, two samples made by UHP hot pressing are compared with FAST samples made from the same powder and using similar sintering conditions.

The Element 6 process was designed and optimised to manufacture diamond at an industrial pace. These conditions were found to be inadequate for processing crack-free MgB_2 which is much more brittle than diamond. In fact, all specimens presented here fell apart when taken

out of their Nb case. For this reason, no connectivity measurements or STEM analysis could be performed as they require relatively large crack-free pieces for the sample preparation.

Sample details

Table 4.13 describes the processing conditions of the four samples selected to compare the FAST and UHP hot pressing process. The four specimens were made with similar sintering conditions except for the pressure which was 110 times larger in the case of the UHP process.

Initial Powder	Sintering T [°C]	Sintering time [min]	Heating rate [°C/min]	Pressure [MPa]
MgB_2 FAST	900	5	120	50
MgB_2 UHP	900	15	50-100	5500
0.5 wt.% Y_2O_3 milled 12 h FAST	950	5	120	50
0.5 wt.% Y_2O_3 milled 12 h UHP	900	15	50-100	5500

Table 4.13: Processing conditions of 0.5 wt.% Y_2O_3-MgB_2 ODS and unmodified MgB_2 bulks manufactured by FAST and UHP hot pressing.

XRD and density measurements

Table 4.14 summarises the XRD analysis and the density measurements for unmodified MgB_2 and 0.5 wt.% Y_2O_3-MgB_2 ODS specimens manufactured by FAST and UHP hot pressing. The relative density for both UHP samples was estimated to $> 99\%$ since no porosity was observed by SEM.

A few common trends were observed when comparing the samples processed by FAST and UHP hot pressing. First, both UHP samples showed a small increase in MgO content, and a much smaller fraction of MgB_4. MgB_4 has a lower theoretical density than MgB_2, thus the decomposition reaction $2MgB_2 \rightleftharpoons MgB_4 + Mg_{(g)}$ that occurs above $\sim$ 900 °C [26, 32] is less favourable with increasing pressure.

As discussed in section 1.3.1, pressure has a positive effect on the sintering process and enhances densification. This is clearly observed in the UHP samples which were fully dense, whereas the FAST samples showed much lower density values. UHP specimens showed finer crystallite sizes, indicating that pressure is also useful to keep a fine microstructure by reducing grain growth. The inhomogeneous strain was higher in both UHP specimens compared to their FAST equivalent. This can be explained by the huge pressure applied on the UHP specimens, 110 times higher than for the FAST samples. The ODS sample sintered by UHP hot pressing showed very fine

$\sim$ 10 nm MgO particles, half the size of the ODS specimen made by FAST. This suggests that pressure also had a refining effect on MgO particles.

In terms of microstructure, the UHP process has significant advantages over FAST. Indeed, UHP samples showed much higher density values, and also finer microstructures, which are both expected to influence positively J_c values.

Sample	MgO [wt.%]	MgB_4 [wt.%]	Relative density [%]	MgB_2 crystallite size [nm]	MgB_2 strain [%]	MgO crystallite size [nm]	MgB_2 a-axis [Å]	MgB_2 c-axis [Å]
MgB_2 FAST	7	11	68	120	0.12	30	3.085	3.525
MgB_2 UHP	8	6	$> 99^*$	70	0.29	40	3.086	3.520
ODS FAST	16	18	72	60	0.27	22	3.085	3.527
ODS UHP	20	8	$> 99^*$	40	0.35	11	3.085	3.522

Table 4.14: XRD characterisation and relative density of 0.5 wt.% Y_2O_3-MgB_2 ODS and unmodified MgB_2 bulks manufactured by FAST and UHP hot pressing.*Estimated from backscattered SEM images.

SEM

Figures 4.18 (a) and (b) show backscattered SEM images of 0.5 wt.% Y_2O_3-MgB_2 ODS samples sintered at 950 °C by FAST and 900 °C by UHP hot pressing respectively. Whereas the sample sintered by FAST did not show much sintering, the specimen made by UHP hot pressing has sintered to full density. In contrast with the FAST specimen, no spherical particles and no porosity could be found in the UHP sample. This clearly highlights the large effect of pressure on densification. Only a few large $100 - 500$ nm MgO particles can be seen in Figure 4.18 (b), suggesting that most of the MgO particles (20 wt.% estimated by XRD) were too small to be resolved by SEM, consistent with the $\sim$ 10 nm size estimated by XRD.

Magnetic measurements

Figure 4.19 (a) shows that unmodified MgB_2 samples processed by FAST and UHP had very similar curves and high T_c values of $\sim$ 38 K. Both ODS specimens also had similar curves but with much lower T_c values, slightly above 31 K. This suggests that the type of process does not have a significant influence on T_c or the shape of the superconducting transition, as shown

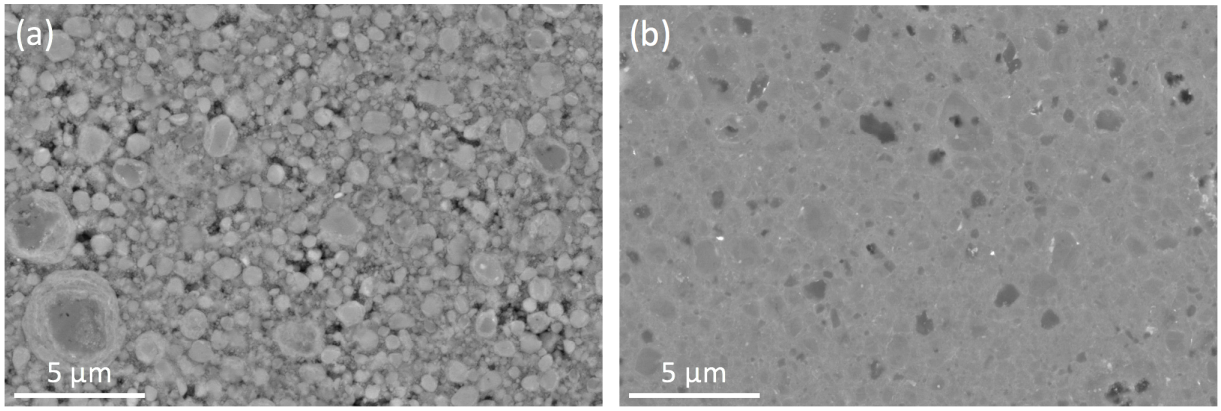

Figure 4.18: SEM backscattered images of 0.5 wt.% Y_2O_3-MgB_2 ODS samples sintered at (a) 950 °C by FAST and (b) 900 °C by UHP hot pressing.

in Figure 4.19 (a). On the other hand, Figure 4.19 (b) shows that the UHP process had a significant effect on J_c(4.2 K) values. The J_c(4.2 K) curves of both unmodified MgB_2 and ODS specimens manufactured by UHP hot pressing were pushed upward and outward (to higher fields) compared to their FAST equivalent. These improvements can be correlated to the difference in microstructure observed in Table 4.14. Indeed, the most noticeable difference between UHP and FAST samples were the significantly higher density and finer microstructure of the UHP samples compared to the FAST specimens. Higher density (in the absence of cracks) leads to better connectivity and larger superconducting fractions while finer microstructures improve pinning.

Figure 4.19 (c) shows that the J_c(20 K) curves of both ODS specimens are much closer to unmodified MgB_2 than at 4.2 K. In particular, unmodified MgB_2 made by UHP hot pressing is now as good at high field and better at low field than the UHP ODS sample. This can be explained by the significantly reduced T_c of the ODS specimens which is relatively close to the measurement temperature of 20 K. Consequently the J_c(20 K) values of the ODS specimens were drastically reduced by their low T_c. Table 4.15 shows that J_{c0}(20 K) was higher in both UHP samples compared to their FAST equivalent, suggesting that connectivity was improved by the UHP process. This is consistent with the large improvement in density observed in UHP samples.

Figure 4.19 (d) shows the pinning force curves of unmodified MgB_2 and the ODS sample made by UHP hot pressing. Unmodified MgB_2 has a hybrid shape between the GB and point pinning models, as indicated by its peak located at $b_{peak} = 0.26$ in Table 4.15. The low field side of the curve (before the peak) is also much closer to the GB pinning model than the point pinning

model, suggesting that GB pinning is the dominant pinning mechanism in unmodified MgB_2. In contrast, the pinning curve of the ODS specimen shifted to higher fields (arrow in Figure 4.19 (d)) and had a shape very similar to the point pinning model, confirmed by its peak located at $b_{peak} = 0.34$ (almost identical to the predicted 0.33 value). This suggests that the dominant pinning mechanisms was changed from GB pinning to point pinning by the creation of new point pinning centres. This is in good agreement with the microstructural characterisation which showed that the ODS specimen contained very fine $\sim$ 10 nm MgO particles, and probably equally fine YB_4 precipitates. Future work could include a detailed STEM analysis of the ODS sample prepared by UHP hot pressing to confirm the average size of the MgO particles estimated by XRD, and also to investigate the size distributions and locations of the YB_4 and MgO particles. It would also make sense to investigate if YB_4 and MgO particles can be refined further by using different processing conditions. In particular, it would be very interesting to observe the evolution of the superconducting properties for ODS bulks in which the size of these nano particles gradually becomes closer to (and eventually smaller than) the coherence length in MgB_2.

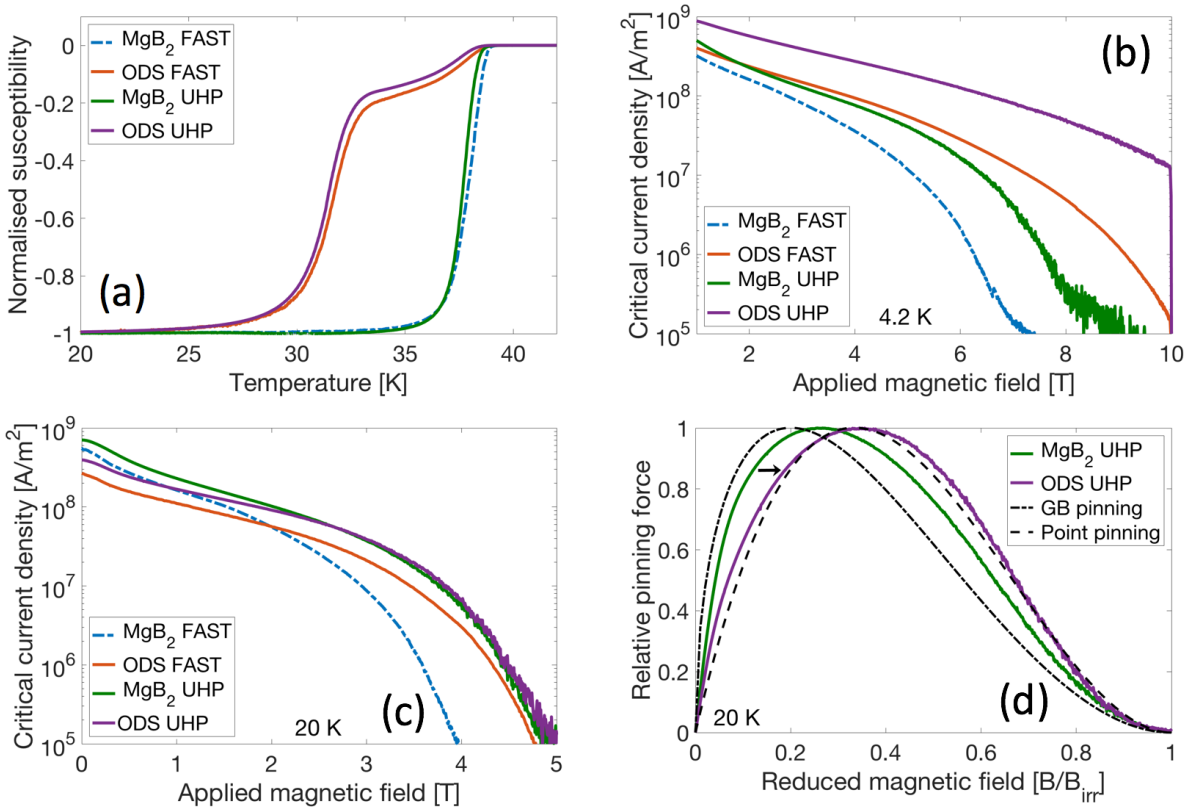

Figure 4.19: Superconducting properties of the 0.5 wt.% Y_2O_3-MgB_2 and unmodified MgB_2 samples sintered by FAST and UHP hot pressing. J_c values were estimated using the macro-scale model.

Sample	T_c [K]	ΔT_c [K]	B_{irr}(4.2 K) [T]	B_{irr}(20 K) [T]	b_{peak}(20 K)	J_c(7 T,4.2 K) [A/m^2]	J_c(0 T,20 K) [A/m^2]
MgB_2 FAST	38.2	1.7	6.8	3.8	0.3	1.5 $\times 10^5$	5.5 $\times 10^8$
MgB_2 UHP	37.6	1.4	8.1	4.7	0.26	4 $\times 10^6$	7 $\times 10^8$
ODS FAST	31.5	2.9	10.0	4.7	0.33	1.3 $\times 10^7$	2.7 $\times 10^8$
ODS UHP	31.4	2.4	12.2	4.8	0.34	8 $\times 10^7$	4 $\times 10^8$

Table 4.15: Superconducting properties of the 0.5 wt.% Y_2O_3-MgB_2 and unmodified MgB_2 samples sintered by FAST and UHP hot pressing. J_c values were estimated using the macro-scale model.

In conclusion, this chapter has shown strong evidence that the ODS concept can be applied to MgB_2 bulk superconductors. Similar to ODS steels, optimal properties are obtained for low Y_2O_3 fractions and relatively long ball milling times. These conditions ensure that a fine and homogeneous dispersion of nano particles is obtained. These particles were found to act as efficient pinning centres for magnetic vortices and led to significant J_c improvements, in particular when their size approached the coherence length of MgB_2. On the other hand, both the ball milling process and the addition of Y_2O_3 had a detrimental effect on densification and also led to a reduction in T_c.

It was further shown that density and T_c both benefit from higher sintering temperatures, however at the expense of J_c at high field due to microstructure coarsening. In fact, the magnetic measurements showed that there was a compromise between low and high field J_c performance which could not be enhanced at the same time by conventional FAST. Sintering MgB_2 under extreme pressure provided a way around this compromise and led to J_c improvements over the entire field range. Despite the promising results showed at the scale of PPMS specimens, large bulks made by UHP hot pressing contain macrocracks which prevent their use in real applications. The UHP process first needs to be redesigned completely for manufacturing MgB_2, rather than diamond, if solid crack-free bulks are to be made.

In the next section, a concept is developed to investigate if the density and connectivity of MgB_2 bulks can be improved without using high sintering temperatures or extreme pressures.

Chapter 5

Mg-MgB_2 bulks

In this section a novel approach that I developed to sinter pre-synthesised MgB_2 powder is reported. The results presented in Chapters 3 and 4 suggested that high sintering temperatures are necessary to obtain dense and well connected MgB_2 bulks, but are detrimental to the intraparticle J_c performance due to microstructure coarsening. I thus decided to find a method to enhance densification without using high processing temperatures. As discussed in section 1.4, higher pressure and heating rates promote densification, however the maximum values were already used in the DSP 507 FAST apparatus.

Liquid phase sintering (LPS) and reactive sintering have been used for decades to consolidate ceramic materials that are difficult to sinter by conventional methods [106–108]. In LPS, a liquid forms in the green body and enhance sintering by pulling the powder particles together through capillary force and by improving the transport mechanisms responsible for densification. A popular example of LPS is WC-Co cermets where Co is used to bond together WC particles at 1300-1500 °C [109]. In reactive sintering two (or more) precursor powders react together to form a new phase during the consolidation process. This often allows the use of cheaper precursor powders and lower sintering temperatures. In fact, many research groups manufacture MgB_2 samples using the so called in-situ method (described in section 1.2.2), where elemental Mg and B powders react together to form MgB_2 during sintering. Although MgB_2 can be manufactured at lower temperature ($700 - 900$ °C) by using this reactive sintering technique, the large difference in density between the Mg-B mixture and MgB_2 leads to very porous samples [38, 41]. On the other hand, it was shown in Chapter 3 that very dense samples can be obtained by sintering pre-synthesised MgB_2 powder, but higher sintering temperatures (≥ 1200 °C) were necessary to

obtain well connected bulks with density values $> 90\%$.

The approach investigated here involves mixing a small fraction of elemental Mg with pre-synthesised MgB_2 in an attempt to enhance densification and improve connectivity in the bulks sintered at lower temperature. My idea was that Mg (which melts at 650 °C) would act as a liquid phase and/or react with MgB_4, and promote densification at lower temperature. Different Mg-MgB_2 composite powders were thus sintered in the aim to develop a liquid phase and/or reactive sintering processing route.

5.1 Effect of Mg fraction

Sample details

In contrast with the ODS powders that were manufactured using the time consuming mechanical alloying route, the Mg-MgB_2 composite powders were simply mixed. Mg and MgB_2 powders were weighed and then enclosed in a small glass jar in a glove box filled with Ar[1]. The powders were mixed by shaking the glass jar manually for approximately 5 min. The composite powders were then poured into a graphite die and cold compacted inside the glove box following the procedure described in section 2.1.2.

Table 5.1 summarises the processing conditions for four Mg-MgB_2 samples containing different amount of Mg, and unmodified MgB_2 made by FAST. The MgB_2 and MgB_2 + 3 wt.% Mg specimens were sintered using the processing route described in section 2.1.2. All the other specimens containing Mg were processed using the same route, except for the cooling step. After the high temperature dwell, the pressure was gradually released and the sample was cooled under power at a slow rate of 30 °C/min during the first 2 min of the cooling step. Then, the upper piston[2] was raised to allow the sample to cool slowly. The sample cooled from 900 to 200 °C in approximately 50 min. This slower cooling method was used to avoid cracking problems that sometimes occurred with faster cooling rates. The MgB_2 and MgB_2 + 3 wt.% Mg specimens were made a second time using the slow cooling method, but could not be fully characterised due to time constraints. Further work should involve further characterisation of these two samples to

[1] Fine Mg powders (< 45 μm in my case) are extremely flammable and even become explosive when airborne. It is crucial to handle these powders with care and in a controlled inert atmosphere at all times.

[2] The upper piston is water cooled and provide fast conduction cooling when in contact with the graphite punch.

make sure that the cooling step did not have any major effect on the results observed. However, XRD characterisation and density measurements revealed that these two duplicates had very similar characteristics whether cooled fast or slow.

Initial Powder	Sintering T [°C]	Sintering time [min]	Heating rate [°C/min]	Pressure [MPa]
MgB_2*	900	5	120	50
MgB_2 + 1 wt.% Mg	900	5	120	50
MgB_2 + 3 wt.% Mg*	900	5	120	50
MgB_2 + 6 wt.% Mg	900	5	120	50
MgB_2 + 10 wt.% Mg	900	5	120	50

Table 5.1: Processing conditions of Mg-MgB_2 bulks manufactured by FAST. *These two samples were cooled more quickly using the procedure described in section 2.1.2.

XRD and density measurements

Figure 5.1 shows the XRD patterns for 3 wt.% and 10 wt.% Mg-MgB_2 and unmodified MgB_2 sintered by FAST. It is clear that Mg additions had a drastic effect on the composition of the consolidated samples, in particular on the fractions of residual Mg and MgB_4.

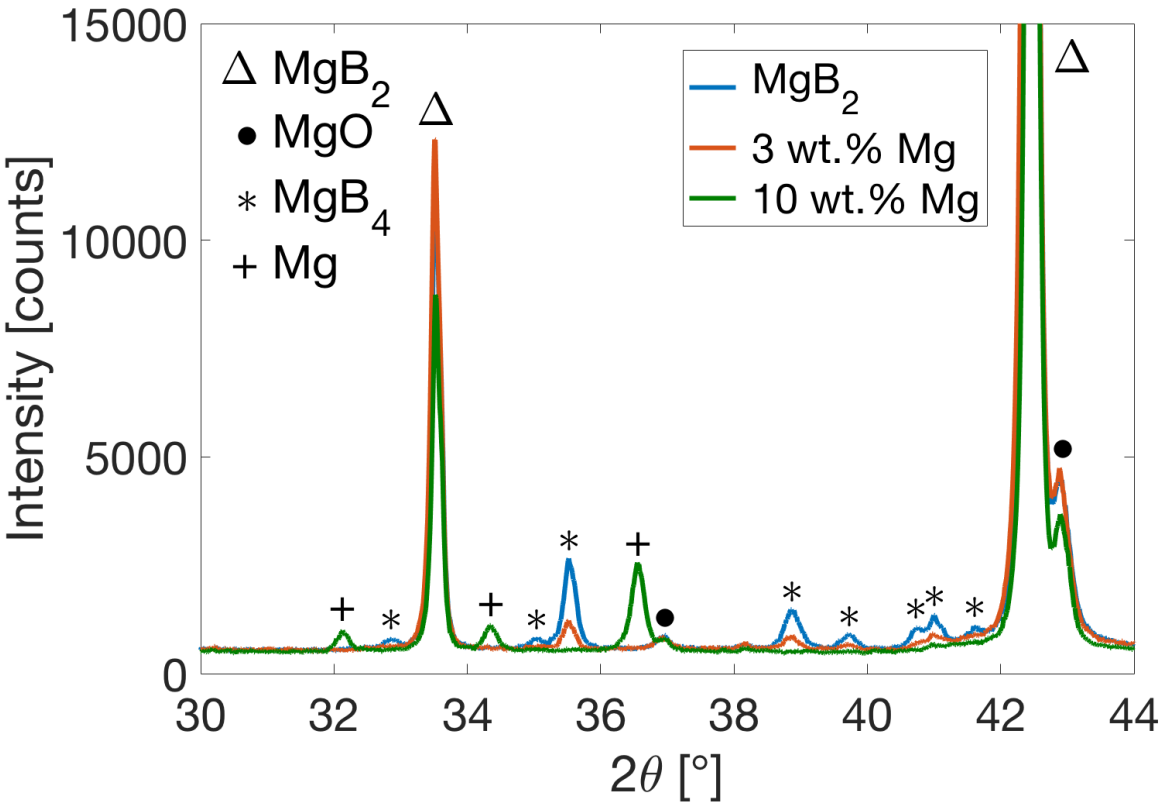

Figure 5.1: XRD patterns for Mg-MgB_2 samples and unmodified MgB_2.

Sample	MgO [wt.%]	MgB_4 [wt.%]	Relative density [%]	MgB_2 crystallite size [nm]	MgB_2 strain [%]	MgO crystallite size [nm]	MgB_2 a-axis [Å]	MgB_2 c-axis [Å]
MgB_2	7	11	68	120	0.12	30	3.085	3.525
1 wt.%	8	9	69	120	0.12	30	3.085	3.525
3 wt.%	8	4	72	120	0.12	34	3.085	3.525
6 wt.%	8	0*	76	130	0.10	39	3.085	3.523
10 wt.%	8	0*	79	130	0.10	44	3.085	3.523

Table 5.2: XRD characterisation and density measurements of Mg-MgB_2 composite bulk samples manufactured by FAST. *No MgB_4 peaks were detected.

XRD patterns of all 5 specimens have been analysed by Rietveld refinement and the results are summarised in Table 5.2. The fraction of MgO was identical in all four Mg-MgB_2 specimens and unmodified MgB_2. In contrast, the amount of MgB_4 decreased drastically in samples containing Mg additions, and even disappeared in the 6 and 10 wt.% specimens. In fact, these two samples contained 0.4 and 4 wt.% of residual Mg respectively. The evolution of the composition with Mg additions is also shown graphically in Figure 5.2. This can be explained by applying Le Chatelier's principle[3] to the decomposition reaction $2MgB_2 \rightleftharpoons MgB_4 + Mg_{(g)}$ that occurs around 900 °C [32]. In the absence of Mg additions, the forward reaction is favoured and MgB_2 decomposes into MgB_4 and $Mg_{(g)}$ until the dynamic equilibrium for these particular conditions is reached. Indeed, table 5.2 shows that the sample consolidated from unmodified MgB_2 contained 11 wt.% MgB_4. However, in the samples containing Mg additions, presumably some Mg evaporated and created a positive pressure of $Mg_{(g)}$ thus moving the dynamic equilibrium of the decomposition reaction to the left, as predicted.

It was shown in Chapter 3 that as-received MgB_2 powder contained 7 wt.% MgB_4 prior to sintering. This means that in the Mg-MgB_2 samples containing 3, 6 and 10 wt.% Mg, Mg additions not only suppressed MgB_2 decomposition but reacted with pre-existing MgB_4 to form "fresh" MgB_2 during sintering. In other words, Mg additions converted pre-existing MgB_4 impurities into MgB_2 in-situ.

The DSP 507 FAST apparatus is equipped with a pressure gauge which allows the operator to check the quality of the vacuum before starting a program and also during sintering. The pressure data recorded while sintering Mg-MgB_2 samples provided valuable insight on the reactions that occurred during sintering. When a sintering program is running, the vacuum pump is constantly

[3] Le Chatelier's principle states that if a dynamic equilibrium is disturbed by a change in the reaction conditions, the position of the equilibrium moves to counteract this change.

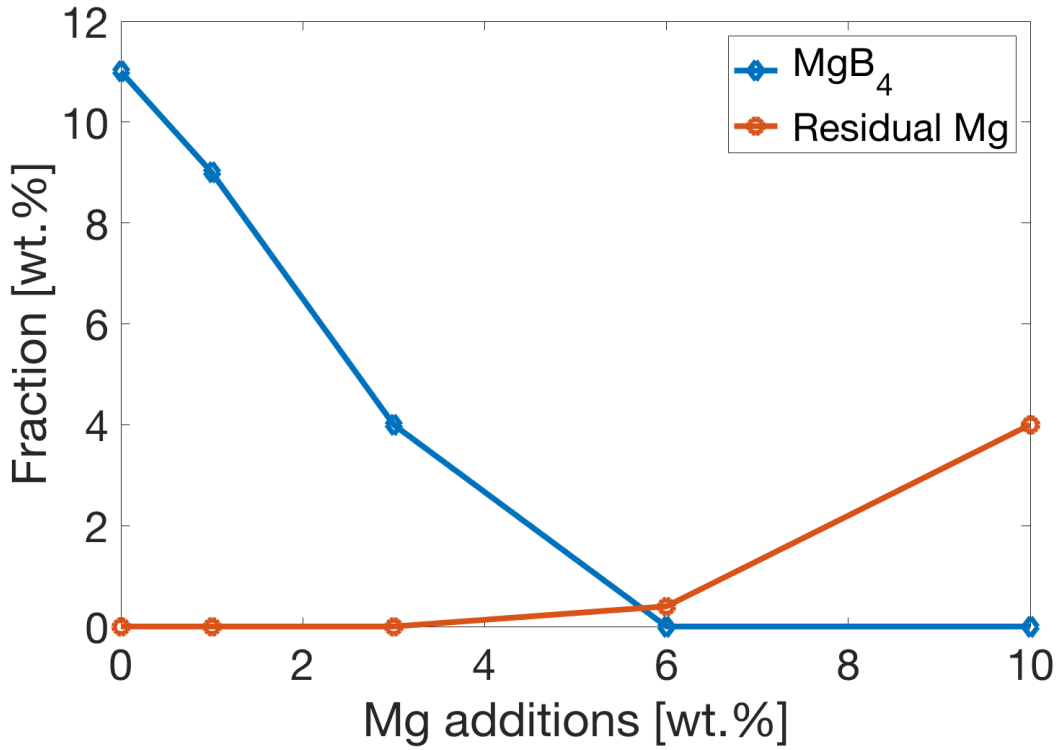

Figure 5.2: Fraction of MgB_4 and residual Mg estimated by XRD analysis for Mg-MgB_2 samples and unmodified MgB_2.

working and the chamber pressure drops rapidly from ambient pressure and reaches a plateau around 0.5 mbar after a few minutes. Therefore, constant and subtle phenomena cannot be detected using the pressure data. However, if a significant reaction involving a gas phase occurs in a relatively narrow temperature range, the sudden change in pressure can be detected as a peak in the pressure baseline.

Figure 5.3 shows the pressure in the sintering chamber as a function of the temperature during the first heating step. Unmodified MgB_2 powder showed a broad peak in pressure at $600-800\,^{\circ}C$ which corresponds to the MgB_2 decomposition reaction. In contrast, this peak disappeared in the samples containing Mg additions and was replaced by a narrower peak at $400-600\,^{\circ}C$ which corresponds to Mg evaporation. These results suggest that Mg evaporated at lower temperatures and formed a positive $Mg_{(g)}$ pressure within the green body that suppressed the decomposition of MgB_2. This is in good agreement with the XRD results and confirms the explanation based on Le Chatelier's principle.

Table 5.2 shows that the Mg-MgB_2 sample containing 1 wt.% Mg had almost the same density as unmodified MgB_2. This suggests that most of the Mg probably evaporated during sintering and

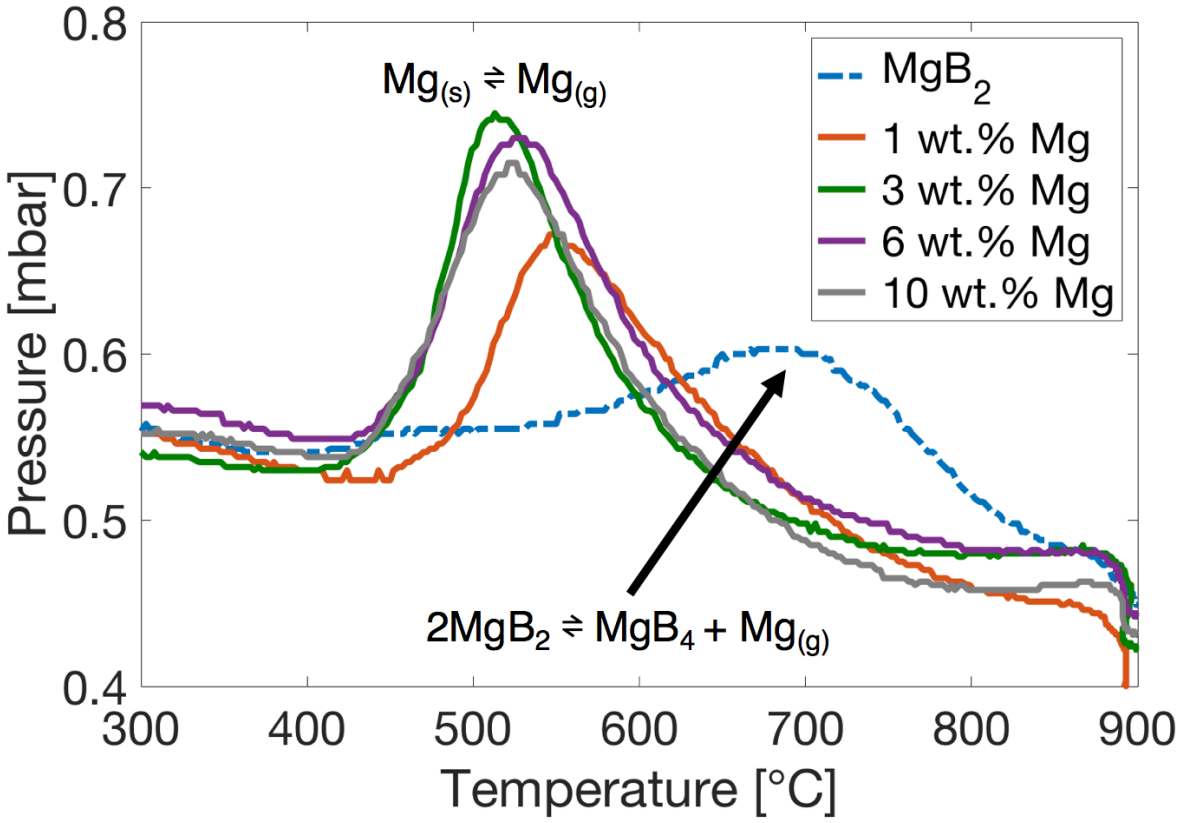

Figure 5.3: Pressure in the FAST chamber during the heating step of the sintering process. Data is shown for Mg-MgB_2 samples and unmodified MgB_2.

did not significantly enhance densification. However, the Mg-MgB_2 samples containing larger Mg fractions showed a significant increase in density, reaching 79% in the 10 wt.% sample compared to 68% in unmodified MgB_2. This indicates that for higher Mg concentrations, not all Mg evaporated and some Mg formed a liquid phase and enhanced diffusion rates leading to faster densification. In addition, Mg in gas phase probably also reacted with MgB_4 to form MgB_2. In order to confirm this theory, the piston travel data has been analysed for the Mg-MgB_2 samples and unmodified MgB_2. Figure 5.4 shows the relative piston travel in function of the temperature during the first heating step of the sintering program. In unmodified MgB_2, the curve has two distinct parts: a linear decrease between room temperature and 800 °C followed by a sudden drop above 800 °C. The first part corresponds to the compaction of the powder due to the pressure which increased linearly from room temperature to reach 50 MPa at 900 °C. The second part corresponds to sintering of the powder with the onset of sintering at 800 °C.

The curve of the 1 wt.% sample was almost identical to unmodified MgB_2 with the onset of sintering also located at 800 °C. This is in good agreement with the density measurements and

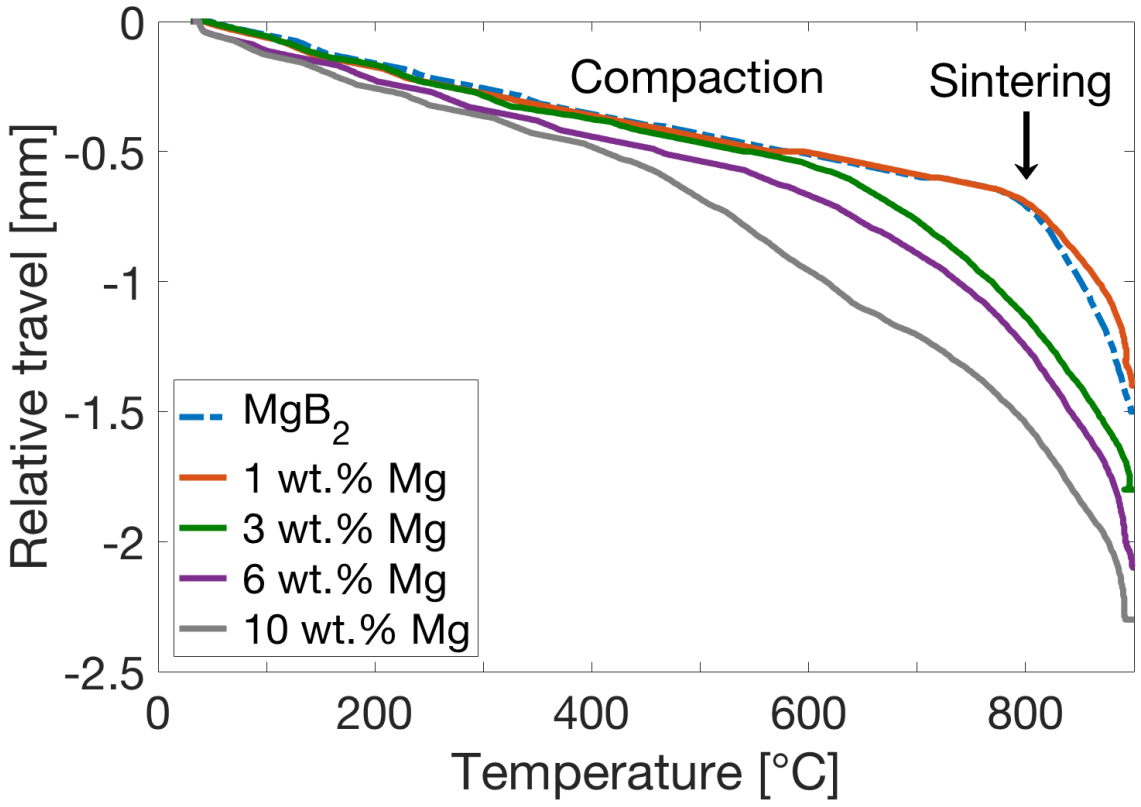

Figure 5.4: Relative travel of the piston during the heating step of the sintering process. Data is shown for Mg-MgB_2 samples and unmodified MgB_2. The data was smoothed for better legibility.

confirms that all the Mg evaporated at lower temperatures and did not form a liquid phase. In contrast, the composite specimens containing larger Mg fractions showed very different sintering curves. Indeed, the 3 wt.% sample had a very similar curve to unmodified MgB_2 up to $600-650$ °C, but then diverged significantly and showed a rapid decrease above $600-650$ °C. The onset of sintering was thus pushed to lower temperatures, around $600-650$ °C, which coincides with the melting temperature of Mg at 650 °C. This confirms that Mg formed a liquid phase and enhanced densification, as shown in Table 5.2. The 6 wt.% specimen showed a travel curve very similar to the 3 wt.% sample, only slightly shifted downward indicating better compaction. On the other hand, the 10 wt.% sample showed a relatively different behaviour with a first change in slope at approximately 450 °C, much lower than for the specimens containing 3 and 6 wt.% Mg at $600-650$ °C. However, this change in slope at 450 °C was not the onset of sintering but rather a change in compaction behaviour. At 450 °C, Mg might become soft enough to be hot extruded in between hard MgB_2 particles, leading to a more effective compaction regime. It is likely that this second compaction regime can only occur for relatively large Mg fractions, above

a critical concentration, which explains why this behaviour was only observed in the 10 wt.% specimen. The real onset of sintering was thus hidden by this new "hot extrusion" compaction regime, and was probably also located at $600 - 650$ °C as the 3 and 6 wt.% specimens.
The effects of Mg additions are summarised in the following:

- 1 wt.%: All the Mg evaporated during sintering and generated a positive $Mg_{(g)}$ pressure which modified the dynamic equilibrium of the MgB_2 decomposition reaction causing less MgB_4 to be formed. No liquid phase was formed and thus no increase in density was observed compared to unmodified MgB_2.

- 3 wt.%: Some Mg evaporated and MgB_2 decomposition was suppressed. A transient liquid was formed which enhanced densification and also reacted with pre-existing MgB_4 to form "fresh" MgB_2. No residual Mg was detected and the density increased compared to unmodified MgB_2. In addition, a reduction in the MgB_4 fraction compared to the as-received MgB_2 powder was observed.

- 6 wt.%: More liquid phase was formed and led to further density improvements and reduction in MgB_4. No MgB_4 was detected and a very small amount (0.4 wt.%) of residual Mg remained in the bulk after the sintering process.

- 10 wt.%: The volume fraction of Mg was enough to activate a new "hot extrusion" compaction mechanism. A liquid phase was then formed at higher temperature and led to further improvements in density. No MgB_4 was detected and a larger fraction of residual Mg (4 wt.%) was present in the sample.

Table 5.2 shows that all four Mg-MgB_2 samples and unmodified MgB_2 had very similar MgB_2 crystallite size which suggests that Mg additions did not affect the MgB_2 coarsening rate. All five samples also had similar inhomogeneous strain values and a and c-axis lattice parameters. However, the MgO crystallite size increased with higher Mg concentrations, reaching 44 nm in the 10 wt.% sample compared to 31 nm for unmodified MgB_2. Since all the composite specimens and unmodified MgB_2 had the same MgO content, this suggests that the liquid Mg phase increased MgO coarsening during the sintering process.

SEM analysis

Figure 5.5 shows typical low magnification backscattered SEM images for unmodified MgB_2 and the 10 wt.% Mg-MgB_2 sample. As discussed in section 3, unmodified MgB_2 sintered at 900 °C did not show any sign of sintering and had a very porous microstructure. In contrast, the Mg-MgB_2 sample showed a much more connected microstructure and less porosity, indicating that densification was significantly enhanced compared to unmodified MgB_2. This is in good agreement with the large increase in density observed for the Mg-MgB_2 sample. No MgB_4 could be seen by SEM, which is consistent with the XRD results (Table 5.2). However, the XRD analysis indicated the presence of residual Mg ($\sim$ 4 wt.%), but Mg could not be detected by SEM and EDX mapping. This could come from a lack of backscattered electron contrast between the Mg and MgB_2 phase or the fact that Mg regions were too small to be resolved by EDX.

Ceramics based on the Si_3N_4 or SiC structures are sintered using LPS by adding metal oxides and/or nitrides which react with the surface silica present in the starting powder to form a liquid phase that acts as a transport medium and thus promotes densification. Liquid phase sintered Si_3N_4 and SiC usually contain thin films (few nm) of residual glassy material at the grain boundaries and larger pockets (few tens of nm) at triple grain junctions [110].

It was shown above that Mg melted during the sintering process and also promoted densification, which suggests that liquid Mg wets MgB_2. Therefore, similar to the glassy phase found in LPS Si_3N_4 and SiC, Mg in Mg-MgB_2 samples could also form thin layers at the grain boundaries and/or small pockets of residual Mg. Such small features cannot be resolved by SEM, but TEM/STEM analysis could confirm the presence of residual Mg.

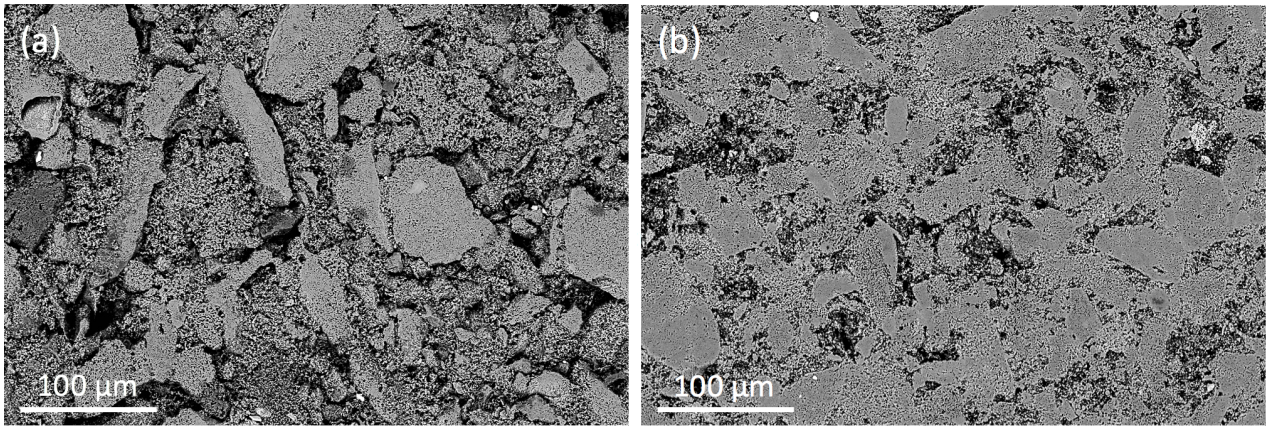

Figure 5.5: Typical backscattered SEM images for (a) unmodified MgB_2 and (b) 10 wt.% Mg-MgB_2 sintered 5 min at 900 °C by FAST. These images were taken by Dr Tayebeh Mousavi.

STEM analysis

The 10 wt.% Mg-MgB_2 specimen was further analysed by STEM, and Figure 5.6 shows a typical HAADF image depicting a triple grain junction (arrow) and an EDX linescan running through the small pocket located at the junction. The pocket is richer in Mg and depleted in B, which supports the theory that Mg wets MgB_2 and forms a liquid phase during sintering with some residual Mg forming pockets at triple grain junctions. This is consistent to what is observed in liquid phase sintered Si_3N_4 and SiC [110]. Although no significant change in composition could be detected at grain boundaries, it does not rule out the hypothesis that Mg also forms thin films (few nm) at grain boundaries. The EDX resolution of the STEM instrument used (the JEOL 3000f described in section 2.2.5) is similar to the thickness of the films, and will not be likely to detect these thin grain boundary films. Future work could involve further analysis on an aberration-corrected STEM to investigate finer details of the microstructure, in particular at grain boundaries.

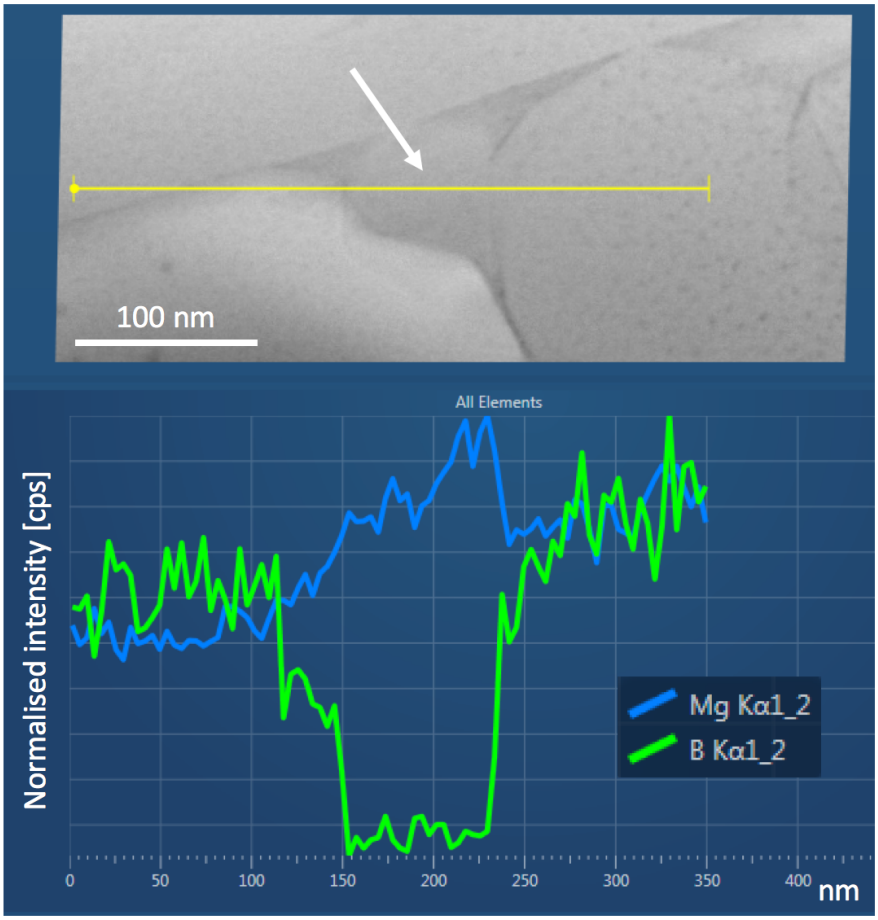

Figure 5.6: Typical STEM HAADF image of 10 wt.% Mg-MgB_2 showing a triple grain junction (arrow). An EDX linescan was performed across the triple grain junction.

Magnetic measurements

Figure 5.7 (a) shows that the superconducting transition becomes narrower with increasing Mg additions. ΔT_c decreased from 1.7 K in unmodified MgB_2 to 0.6 K in the sample containing 10 wt.% Mg, as shown in Table 5.3. A similar reduction in ΔT_c was observed in unmodified MgB_2 samples sintered at higher temperature, as discussed in section 3. This was attributed to heterogeneities (composition and/or disorder) initially present in the as-received powder being annealed out at high temperature. Here, all four samples were sintered at 900 °C suggesting that the reduction in ΔT_c is an effect of the Mg additions. Higher sintering temperatures and larger Mg fractions both lead to an increase in the diffusion rate, as suggested by the higher density of the 10 wt.% Mg-MgB_2 sample. As discussed in section 3, it is likely that as-received MgB_2 powder contained defects and/or local chemical heterogeneities which resulted in the relatively large ΔT_c value in the sample made from unmodified MgB_2. A possible explanation for the effect of Mg additions on ΔT_c could be that even though the sintering temperature is low (900 °C) the higher diffusion rate and excess Mg present as gas and/or liquid during sintering acts to smooth chemical heterogeneities and thus makes the sample more homogeneous, reducing ΔT_c.

Sample	$T_{c,onset}$ [K]	ΔT_c [K]	B_{irr}(4.2 K) [T]	B_{irr}(20 K) [T]	b_{peak}(20 K)	J_c(5 T,4.2 K) [A/m^2]	J_c(0 T,20 K) [A/m^2]
MgB_2	38.6	1.7	6.8	3.8	0.3	1.2×10^7	0.55×10^9
1 wt.%	38.6	1.1	6.8	3.9	0.26	2.3×10^7	1×10^9
3 wt.%	38.6	0.7	7	3.9	0.21	3.9×10^7	1.7×10^9
6 wt.%	38.6	0.6	7	3.8	0.26	3.8×10^7	2.6×10^9
10 wt.%	38.5	0.6	5.4	3.1	0.3	1.8×10^7	2.4×10^9

Table 5.3: Superconducting properties of unmodified MgB_2 and Mg-MgB_2 samples containing 1, 3, 6 and 10 wt.% Mg. J_c values were estimated using the macro-scale model.

Figure 5.7 shows that the J_c-B curves for the 1 and 3 wt.% Mg samples seemed simply translated vertically compared to unmodified MgB_2, maintaining a very similar shape. The $J_c - B$ curve of the 6 wt.% sample was very similar to the 3 wt.% specimen at high field (> 5 T), but J_c values at low field were further improved. On the other hand, the 10 wt.% sample showed a relatively different shape; low field J_c values were similar to the 6 wt.% specimen, but high field J_c was reduced compared to unmodified MgB_2 and all three Mg-MgB_2 samples containing fewer Mg additions. The 10 wt.% sample also had an irreversibility field B_{irr} approximatively 1.5 T lower than the other four specimens, as shown in Table 5.3. This suggests that the MgB_2 lattice of the 10 wt.% sample was "cleaner" (following the definition of Anderson [89]). As discussed

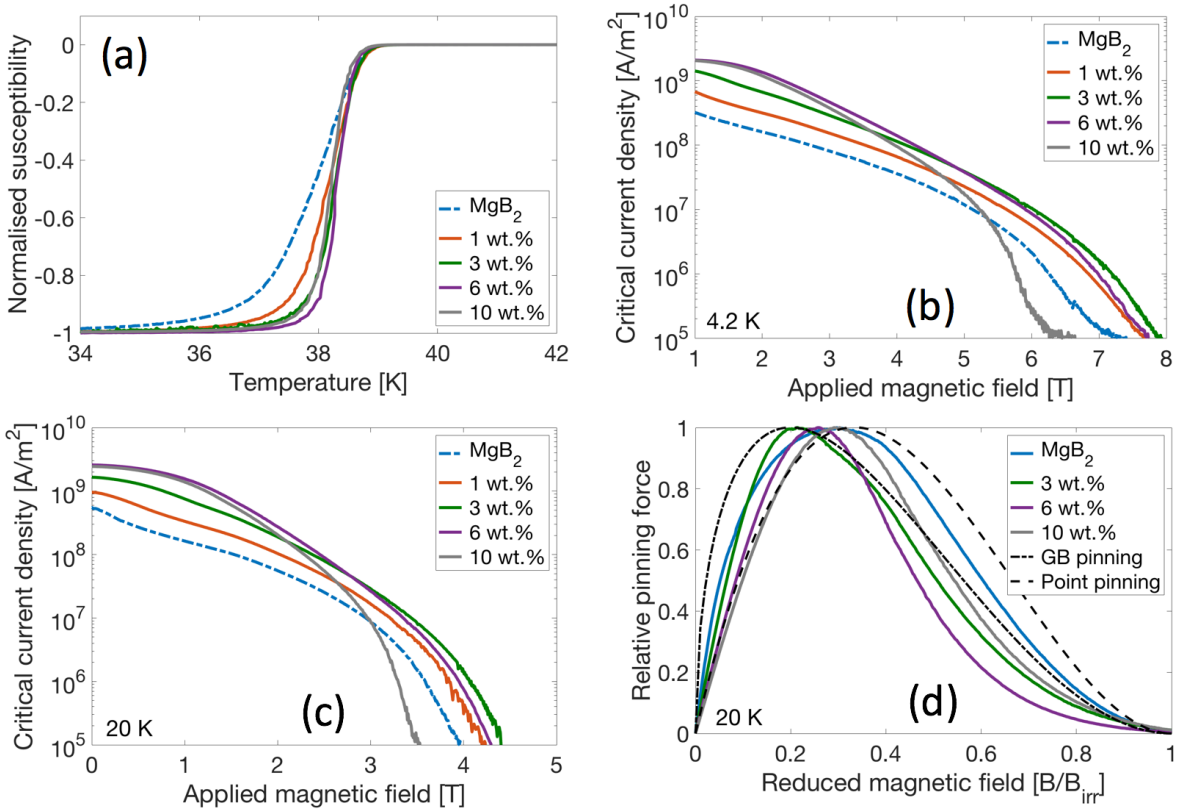

Figure 5.7: Superconducting properties of unmodified MgB_2 and Mg-MgB_2 samples containing 1, 3, 6 and 10 wt.% Mg. J_c values were estimated using the macro-scale model.

earlier, the 10 wt.% sample was the only specimen to contain a significant fraction of residual Mg ($\sim$ 4 wt.%) after the sintering process, and also showed the largest increase in density, attributed to the effect of Mg acting as a liquid phase during consolidation. It was shown that the liquid phase in Si_3N_4 and SiC act as an impurity well due to the much larger solubility of impurities in the liquid phase than in the solid phase [110]. It is likely that the Mg liquid phase during sintering also acts as an impurity well and thus makes the MgB_2 lattice "cleaner", explaining the significant reduction in B_{irr} observed in the 10 wt.% Mg-MgB_2 bulk.

At 20 K, the evolution of the $J_c - B$ curves with increasing Mg additions is very similar to that observed at 4.2 K. Self field J_c(20 K) increased more than 4 fold by adding 6 and 10 wt.% Mg compared to unmodified MgB_2. This is consistent with the SEM analysis (Figure 5.5) showing that the microstructure of the 10 wt.% Mg sample sintered to a much greater extent than unmodified MgB_2. These results suggest that well connected samples can also be obtained by using Mg additions instead of higher sintering temperatures. The liquid phase sintering method developed here thus offers a faster and cheaper alternative to the conventional ex-situ route.

The shape of the pinning force curve of unmodified MgB_2 sintered at 900 °C was discussed in section 3, and interpreted as showing a hybrid behaviour between grain boundary pinning and point pinning. Figure 5.7 shows that the pinning curve of the 3 wt.% Mg sample had a relatively different shape compared to unmodified MgB_2. The shape was relatively similar to the GB pinning model and had a peak located at $b_{peak} = 0.21$, which is very close to the theoretical value of 0.2 for the GB pinning model. This suggests that GB pinning had a larger contribution in the 3 wt.% Mg sample than for the specimen made from unmodified MgB_2. The 6 and 10 wt.% Mg specimens showed narrower curves with a concave shape on the high field side of the peak, which is typical of well connected samples, as discussed in Chapter 3 (pinning force analysis section). Due to anisotropy effects, the shape of these curves and the position of the peak are difficult to interpret, and no solid conclusions can be made on the nature of the pinning mechanism is these specimens.

Connectivity measurements

To estimate the effective cross-sectional area for macroscopic current transport in the bulk samples, four-point transport measurements and analysis of connectivity have been performed to obtain the normal state electrical resistivity as a function of temperature. Following the analysis of Collings *et al.* [85], values of connectivity were extracted from the data using the procedure described in section 2.2.7.

Figure 5.8 shows that connectivity increased significantly with Mg additions compared to unmodified MgB_2. In particular, the connectivity increased from only 6% in unmodified MgB_2 up to 25% in the sample containing 10 wt.% Mg. This increase in connectivity almost exactly matches the increase in self field J_c(20 K) discussed above. A strong correlation between connectivity and self field J_c values was already observed in unmodified MgB_2 sintered at temperatures ranging from 900 to 1200 °C, as discussed in Chapter 3. This confirms that connectivity has a significant effect on J_c values at low field, and also suggests that connectivity can be improved not only with higher sintering temperatures but also by using Mg additions. The residual resistivity also decreased with increasing Mg fractions, suggesting that Mg additions made the bulks microstructure cleaner (lower impurity content). This probably comes from the drastic reduction in MgB_4 with increasing Mg additions, as shown in Figure 5.2.

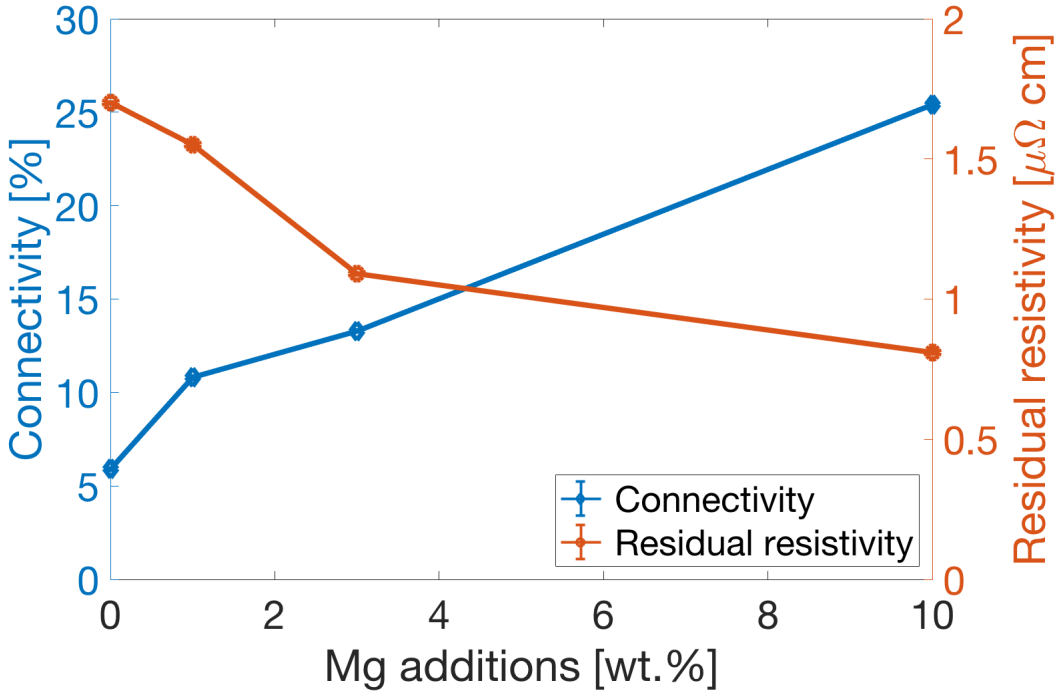

Figure 5.8: Connectivity and residual resistivity of the bulk samples estimated from normal state electrical transport measurements following the analysis outlined by Collings *et al.* [85]. The measurements and analysis were performed by Runsen Ma.

Kinetics of the liquid phase sintering process

A second 10 wt.% sample was made using a different sintering program, as shown in Figure 5.9. The fast cooling program was composed of the same first heating step but had no dwell at 900 °C and a much faster cooling rate. In this program, the sample was cooled from 900 to 200 °C in approximately 10 min, compared to 50 min for the slow cooling program. This program was designed to simulate a quench in order to capture the state of the microstructure just after the first heating step to 900 °C. The idea behind this experiment was to investigate how fast was the liquid phase sintering effect.

The quenched sample was analysed by XRD and had very similar characteristics to the sample cooled slowly except for a slightly higher residual Mg fraction of 6 wt.%. Both samples had the same density of 79%. This suggests that the reaction between pre-existing MgB_4 and Mg additions to form MgB_2 was relatively fast and occured entirely during the first heating step. The slow cooled specimen contained less residual Mg simply because it was exposed to high temperatures for longer and thus more Mg evaporated. Since both samples had the same density, most of the densification also occurred during the first heating step. Consequently, for a sintering

temperature of 900 °C the dwell and cooling steps did not have any effect on the final density value. These results suggest that dense Mg-MgB_2 specimens can be manufactured very quickly, without any dwell at high temperature, through the liquid phase sintering route developed in this work. This could have significant implications for the design of future MgB_2 industrial process due to the large energy and time savings that could be made with this efficient processing route. Future work could include additional quenching work, in particular at lower temperatures ($650 - 800$ °C) in order to investigate the evolution of the density and composition of the sample during the early stages of the liquid phase sintering process.

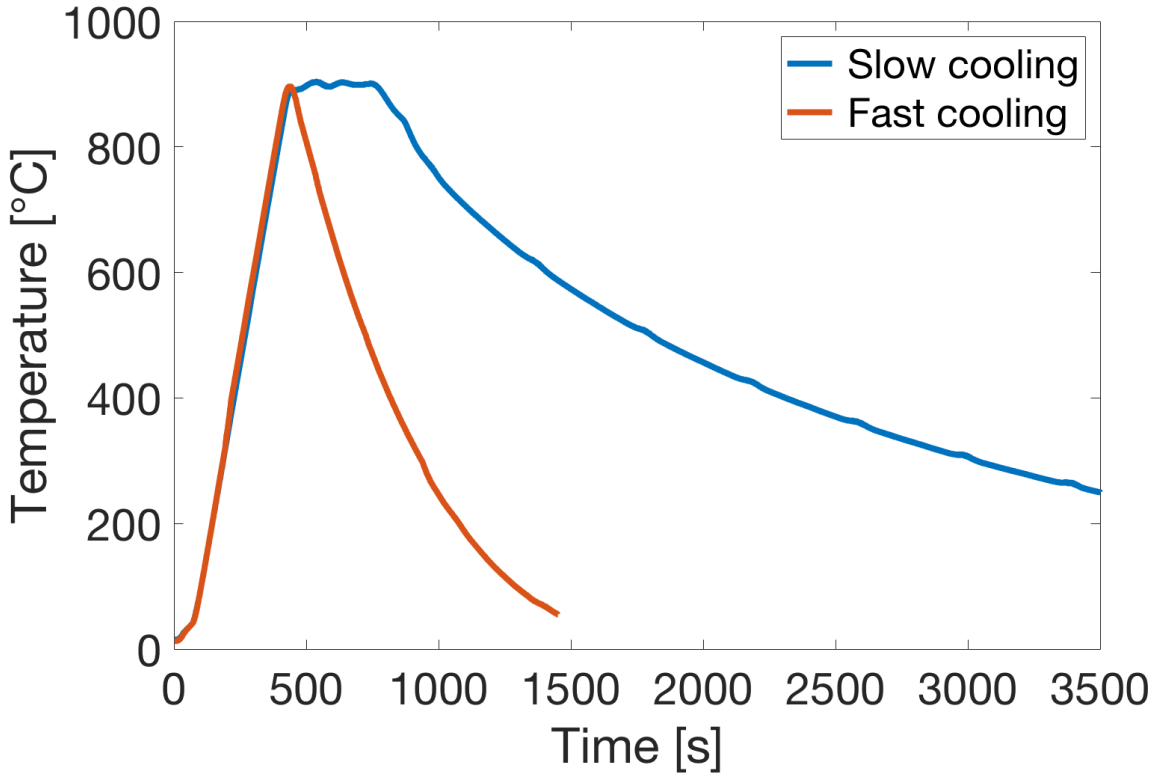

Figure 5.9: Sintering programs used to manufacture 10 wt.% Mg-MgB_2 samples by FAST.

5.2 Effect of sintering temperature

The effect of the sintering temperature on the microstructure of Mg-MgB_2 specimens was investigated by manufacturing 3 wt.% Mg-MgB_2 samples at 900, 1000 and 1100 °C. The sintering conditions are summarised in Table 5.4. The 1000 and 1100 °C samples were cooled slowly, by the procedure described in the previous section.

Sample details

Initial Powder	Sintering T [°C]	Sintering time [min]	Heating rate [°C/min]	Pressure [MPa]
MgB_2 + 3 wt.% Mg*	900	5	120	50
MgB_2 + 3 wt.% Mg	1000	5	120	50
MgB_2 + 3 wt.% Mg	1100	5	120	50

Table 5.4: Processing conditions of 3 wt.% Mg-MgB_2 bulks manufactured by FAST. *This sample was cooled more quickly using the procedure described in section 2.1.2.

XRD and density measurements

Overall, higher sintering temperatures had the same effect on the microstructure of Mg-MgB_2 samples as for unmodified MgB_2 (described in detail in Chapter 3). Mainly, the fraction of MgB_4 and density increased, and the microstructure coarsened with increasing sintering temperature. However, compared to unmodified MgB_2 sintered at the same temperature, the Mg-MgB_2 samples showed much higher density values and a large reduction in MgB_4. For instance, unmodified MgB_2 processed at 1100 °C contained 16 wt.% MgB_4 and had a density of 86% whereas the 3 wt.% Mg-MgB_2 sample sintered at the same temperature only contained 6 wt.% MgB_4 and showed a density of 95%. These results suggest that Mg additions are also very effective to increase density and suppress MgB_2 decomposition even at higher temperatures. The evolution of density with sintering temperature for 3 wt.% Mg-MgB_2 and unmodified MgB_2 is shown in Figure 5.10. Similar density values were obtained for 3 wt.% Mg-MgB_2 samples by using sintering temperatures $\sim$ 100 °C lower than for unmodified MgB_2. This is in contrast with ODS samples that showed much lower density values than unmodified MgB_2 sintered at the same temperature, as shown in Figure 4.14.

Sample	MgO [wt.%]	MgB_4 [wt.%]	Relative density [%]	MgB_2 crystallite size [nm]	MgB_2 strain [%]	MgO crystallite size [nm]	MgB_2 a-axis [Å]	MgB_2 c-axis [Å]
900 °C	8	4	72	120	0.12	34	3.085	3.525
1000 °C	8	6	83	130	0.12	44	3.084	3.526
1100 °C	9	6	95	140	0.14	48	3.083	3.527

Table 5.5: XRD characterisation and density measurements of 3 wt.% Mg-MgB_2 bulk samples manufactured by FAST.

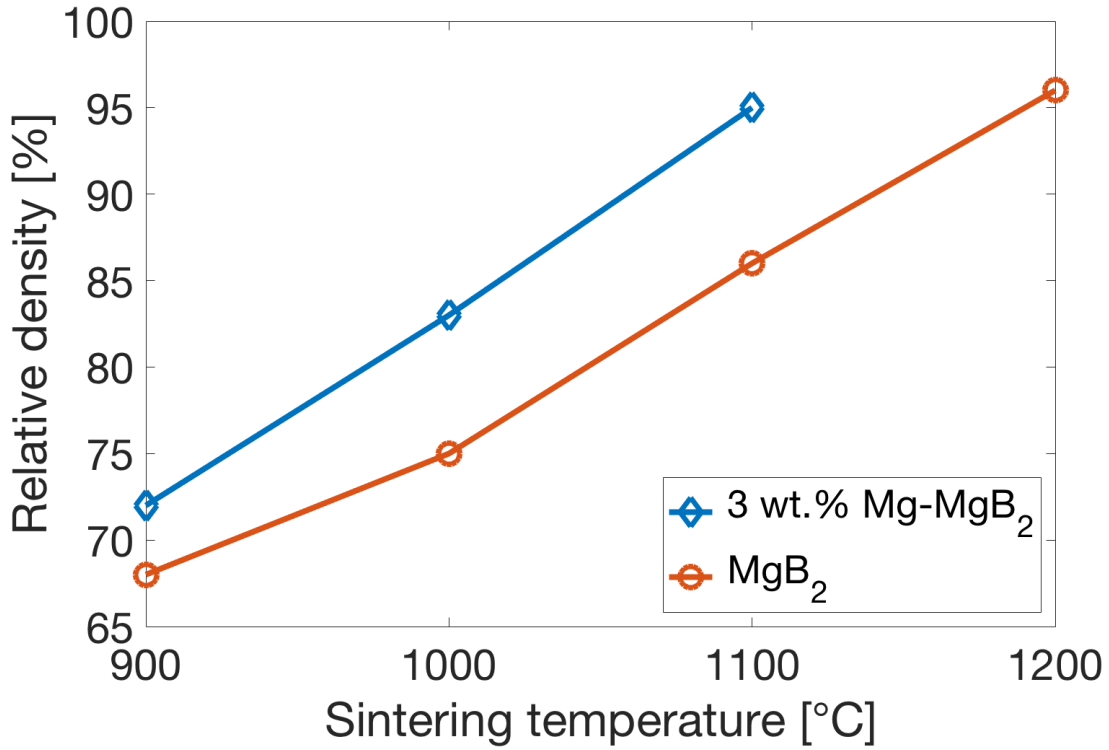

Figure 5.10: Relative density in function of the sintering temperature for 3 wt.% Mg-MgB_2 and unmodified MgB_2.

Magnetic measurements

The superconducting properties of 3 wt.% Mg-MgB_2 samples sintered between 900 and 1100 °C and unmodified MgB_2 processed at 1200 °C are summarised in Figure 5.11 and in Table 5.6. The effect of the temperature on the superconducting properties of Mg-MgB_2 samples was very similar to the effect observed in unmodified MgB_2 specimens, as discussed in Chapter 3. ΔT_c values decreased and J_c values at low field increased with increasing sintering temperature. The temperature had a negligible effect on B_{irr} values that were relatively similar for all three Mg-MgB_2 specimens and unmodified MgB_2. This is consistent with the microstructure evolution with the sintering temperature decribed above, which was identical to the observations made for unmodified MgB_2 sintered between 900 and 1200 °C (Chapter 3). Increasing sintering temperatures led to higher density values, a small increase in the fraction of MgB_4 and some microstructure coarsening (MgB_2 and MgO crystallite size). This is not suprising as Mg mainly acts as a sintering aid and is expected to react with MgB_2/MgB_4 in a similar way within the temperature range investigated here ($900 - 1100$ °C). The 3 wt.% Mg-MgB_2 specimen sintered at 1000 °C showed almost identical (even slightly better) J_c values both at 4.2 and 20 K to unmodified MgB_2 pro-

cessed at 1200 °C. This suggests that bulk samples showing equal performance can be obtained at much lower temperature (∼ 200 °C lower) by using Mg additions. The simplicity of this new processing route (mixing Mg and MgB_2 together for a few minutes without any specialised equipment) makes it very attractive to reduce the tooling and energy costs of the manufacturing process.

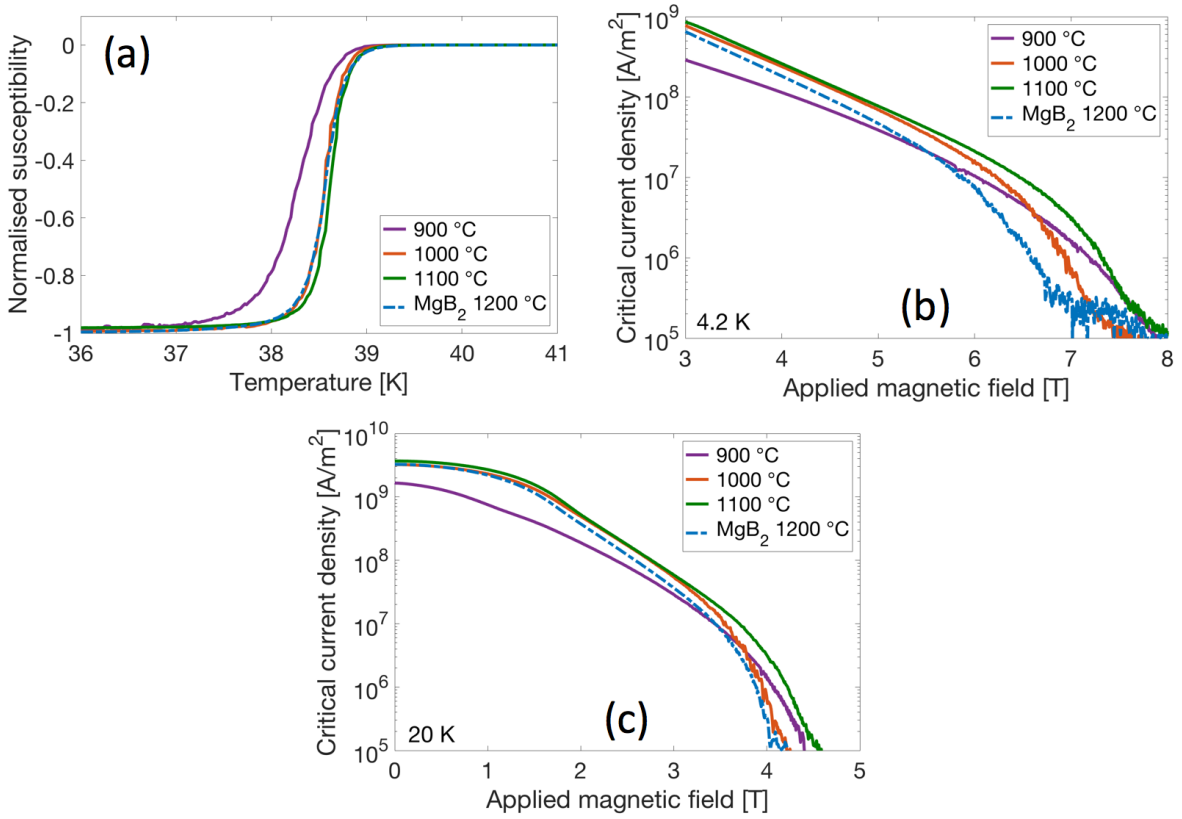

Figure 5.11: Superconducting properties of unmodified MgB_2 sintered at 1200 °C and 3 wt.% Mg-MgB_2 samples sintered at 900, 1000 and 1100 °C. J_c values were estimated using the macro-scale model.

Sample	$T_{c,onset}$ [K]	ΔT_c [K]	B_{irr}(4.2 K) [T]	B_{irr}(20 K) [T]	b_{peak}(20 K)	J_c(5 T,4.2 K) [A/m^2]	J_c(0 T,20 K) [A/m^2]
900 °C	38.6	0.7	7	3.9	0.21	4×10^7	1.7×10^9
1000 °C	38.7	0.5	6.9	3.8	0.3	7×10^7	3.3×10^9
1100 °C	38.8	0.4	7.2	4	0.29	7.7×10^7	3.7×10^9
MgB_2 1200 °C	38.7	0.4	-	3.8	0.28	4.6×10^7	3.3×10^9

Table 5.6: Superconducting properties of unmodified MgB_2 sintered at 1200 °C and 3 wt.% Mg-MgB_2 samples sintered at 900, 1000 and 1100 °C. J_c values were estimated using the macro-scale model.

5.3 Mg-Y_2O_3-MgB_2 composites

In this final result section, the additions investigated in Chapters 4 and 5 are combined together to produce Mg-Y_2O_3-MgB_2 composite bulks. It was concluded at the end of Chapter 4 that ODS MgB_2 samples had improved J_c values at high field but did not perform as well as unmodified MgB_2 at low field. Presumably, the ball milling process and Y_2O_3 additions hinder the sintering process and lead to lower electrical connectivity causing a decrease in J_c values at low field. It was also shown that J_c improvements at high field were significant for samples sintered at low temperatures where only limited microstructure coarsening took place during the manufacturing process. However, higher sintering temperature led to a drastic decrease in J_c improvements at high field. The results presented in section 4.2.3 thus suggests that the nature of these ODS specimens is such that low field J_c can only be improved at the cost of J_c at high field.

On the other hand, it was demonstrated in Chapter 5 that Mg additions had the opposite effect. Mg additions significantly improve connectivity, even at low processing temperatures and also enhance sintering by acting as a liquid phase sintering agent. In particular it was shown that similar electrical connectivity values and almost identical J_c performance could be obtained at temperatures approximately 200 °C lower than that required for unmodified MgB_2 by using Mg additions.

Consequently, the effect of Mg additions is complementary to the improvements observed in Y_2O_3-MgB_2 ODS specimens. This naturally led to the idea of combining both additions in a "composite" approach to investigate if they could work in synergy. Two bulk specimens were sintered at 900 °C for 5 min using very similar processing conditions to unmodified MgB_2 and 10 wt.% Mg-MgB_2 samples introduced in Chapter 3 and section 5.1 respectively, as shown in Table 5.7. Two different powders were prepared to investigate the effect of Y_2O_3 and Mg additions independently and then combined together. The 0.5 wt.% Y_2O_3-MgB_2 ODS powder was manufactured by ball milling nano Y_2O_3 and MgB_2 together for 6 h, using the procedure described in section 2.1.1. The 10 wt.% Mg - 0.5 wt.% Y_2O_3-MgB_2 composite powder was produced by simply mixing Mg additions with the 0.5 wt.% Y_2O_3-MgB_2 ODS powder.

Initial Powder	Sintering T [°C]	Sintering time [min]	Heating rate [°C/min]	Pressure [MPa]
MgB_2*	900	5	120	50
10 wt.% Mg	900	5	120	50
0.5 wt.% Y_2O_3	900	5	120	50
0.5 wt.% Y_2O_3 + 10 wt.% Mg	900	5	120	50

Table 5.7: Processing conditions of unmodified MgB_2, Mg-MgB_2, Y_2O_3-MgB_2 and Mg-Y_2O_3-MgB_2 bulks manufactured by FAST. *This sample was cooled more quickly using the procedure described in section 2.1.2.

XRD and density measurements

The XRD patterns of the ODS specimen and Mg-ODS composite are shown in Figure 5.12. Whereas the ODS sample showed numerous MgB_4 XRD peaks, none were detected in the Mg-ODS composite. In fact, a very small peak of residual Mg was seen in the composite specimen. As already discussed in section 5.1, large fractions of Mg additions suppress completely any MgB_2 decomposition during sintering and even react with pre-existing MgB_4 in the powder to form "fresh" MgB_2 in-situ.

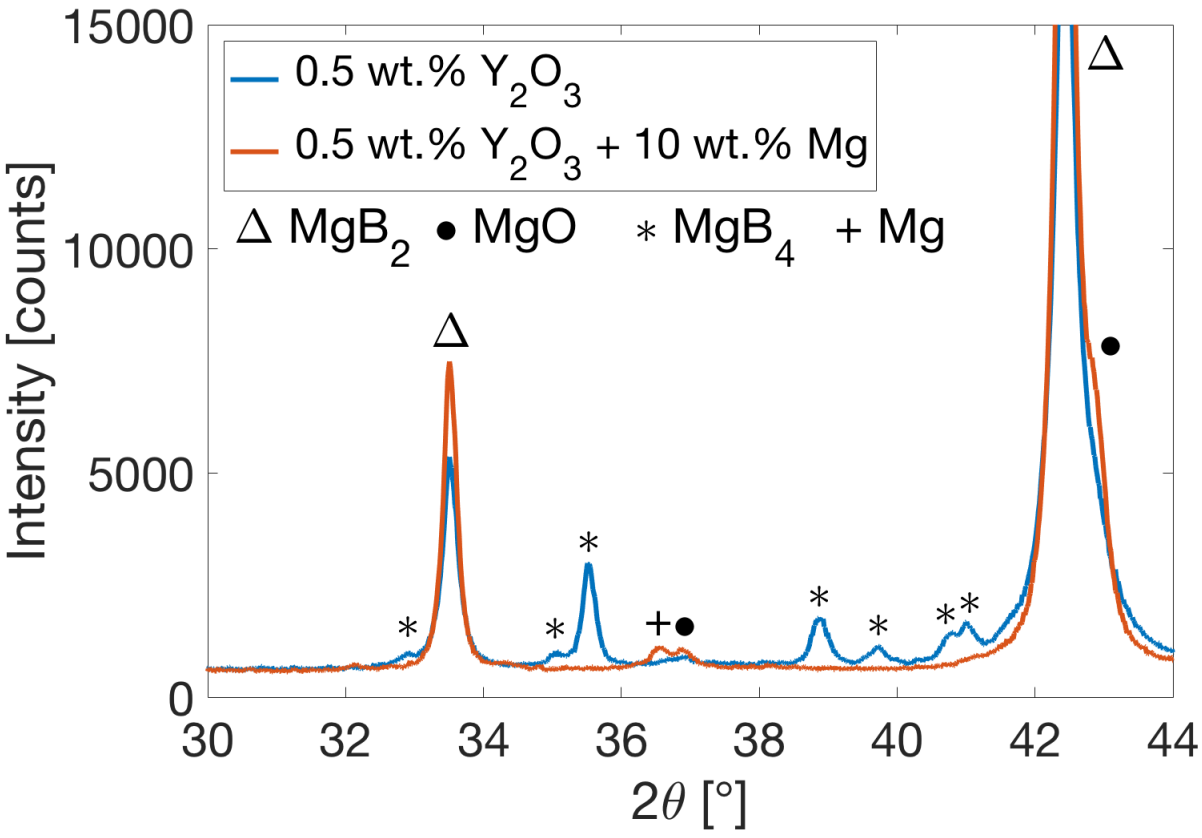

Figure 5.12: XRD patterns for Y_2O_3-MgB_2 and Mg-Y_2O_3-MgB_2 bulk samples.

Table 5.8 shows that by adding 10 wt.% Mg, the fraction of MgB_4 dropped from almost 20 wt.% in the ODS specimen down to $\sim$ 0 wt.%. This significant reduction in MgB_4 is beneficial for several reasons. First, lower fractions of MgB_4 lead to higher superconducting fractions and thus presumably better connectivity. Second, it is likely that reducing the fraction of MgB_4 will also improve the mechanical properties of the bulk, in particular its fracture strength. Coefficient of thermal expansion (CTE) values for MgB_4 could not be found in the literature but it is reasonable to assume that the CTEs of MgB_2 and MgB_4 are not identical, in which case the difference in CTE might lead to crack initiation upon cooling from high temperature. In addition, SEM analysis performed on unmodified MgB_2 samples (Chapter 3, SEM section) revealed that MgB_4 "islands" were very porous and are thus presumably preferential sites for crack initiation. Therefore, reducing the fraction of MgB_4 is likely to improve the mechanical properties of the bulk samples, which is also crucial in the design of superconducting magnets used in high field applications.

Sample	MgO [wt.%]	MgB_4 [wt.%]	Relative density [%]	MgB_2 crystallite size [nm]	MgB_2 strain [%]	MgO crystallite size [nm]	MgB_2 *a*-axis [Å]	MgB_2 *c*-axis [Å]
MgB_2	7	11	68	120	0.12	30	3.085	3.525
Mg-MgB_2	8	$\sim 0^*$	79	130	0.10	44	3.085	3.523
ODS	17	19	70	90	0.24	16	3.085	3.526
Mg-ODS	16	$\sim 0^*$	73	80	0.21	32	3.085	3.524

Table 5.8: XRD characterisation and density measurements of unmodified MgB_2, Mg-MgB_2, Y_2O_3-MgB_2 and Mg-Y_2O_3-MgB_2 bulk samples manufactured by FAST. *No MgB_4 peaks were detected.

The fraction of MgO was almost identical in the ODS and Mg-ODS specimens, which is consistent with the observations made earlier in section 5.1. Table 5.8 shows that adding 10 wt.% Mg to the ODS powder only slightly increased the density of the bulk specimen, from 70 to 73 wt.%. This increase in density is much smaller than that observed for the 10 wt.% Mg-MgB_2 specimen which reached a density of 79% compared to 68% for unmodified MgB_2, as shown in Table 5.8. However, this is consistent with the observations made in section 4.2.3 on ODS specimens processed at temperatures between 950 and 1200 °C. It was shown that Y_2O_3 and the ball milling process had a detrimental effect on sintering and led to smaller density values in ODS specimens compared to unmodified MgB_2 sintered at the same temperature (Figure 4.14). This probably explains why the increase in density in the Mg-ODS composite was smaller than in Mg-MgB_2 specimens. The ODS sample and Mg-ODS composite had very similar MgB_2 crystallite size and

strain values, which is consistent with the results on Mg-MgB_2 specimens discussed in section 5.1. However, the MgO crystallite size doubled with the addition of Mg, suggesting that the higher diffusion rate caused by the liquid sintering process led to coarsening of MgO particles. This was also observed in Mg-MgB2 specimens containing large fractions of Mg additions (section 5.1). In conclusion, the effect of Mg additions observed in the Mg-ODS composite is very similar to that observed in Mg-MgB_2.

Magnetic measurements

The magnetic properties of unmodified MgB_2, Mg-MgB_2, Y_2O_3-MgB_2 and Mg-Y_2O_3-MgB_2 samples are summarised in Figure 5.13 and Table 5.9. The ODS sample showed a very broad superconducting transition with a step, as already observed for ODS specimens processed at low temperature presented in section 4.2.3. This step was explained by a "two powders" model, presented in section 4.2.3. The first powder is composed of particles that were heavily altered during the mechanical alloying process and contain a large defect concentration and/or elements in solid solution. This first powder is associated with the main transition at low temperature. The second powder is made of the particles only mildly (or not) affected by the ball milling process and is responsible for the small step in the transition at higher temperature. The ODS specimen had a drastically reduced T_c of 27 K, compared to $\sim$ 38 K for unmodified MgB_2. In addition, the ODS sample showed a large ΔT_c value of 9 K, 5 times larger than for unmodified MgB_2. These results suggest that the ODS specimen was heterogeneous and contained a high concentration of defects and/or element in solid solution. This is consistent with the observations made on the ODS specimen sintered at 950 °C in section 4.2.3.

On the other hand, the Mg-ODS specimen had a much narrower transition ($\Delta T_c = 1.4$ K) and a much higher T_c of 36 K. This suggests that Mg additions had a significant effect on the microstructure of the Mg-ODS composite by reducing drastically heterogeneities in the bulk and also enhancing the MgB_2 lattice recovery (after ball milling the crystal structure of the ODS powder is heavily damaged). This is consistent with the reduction in ΔT_c observed in Mg-MgB_2 specimens containing larger Mg fractions (section 5.1). A significant increase in T_c and reduction in ΔT_c was also observed in ODS specimens processed at higher temperature, which was attributed to higher diffusion rates (section 4.2.3). Since Mg additions had the exact same effect on T_c and the width of the superconducting transition, it is reasonable to think that Mg

additions also increase the diffusion rate during the sintering process, in a similar way to higher temperatures. This is in good agreement with the results presented in section 5.1 showing that Mg-MgB_2 samples containing large fractions of Mg additions sintered to much higher density values than unmodified MgB_2 and ODS MgB_2.

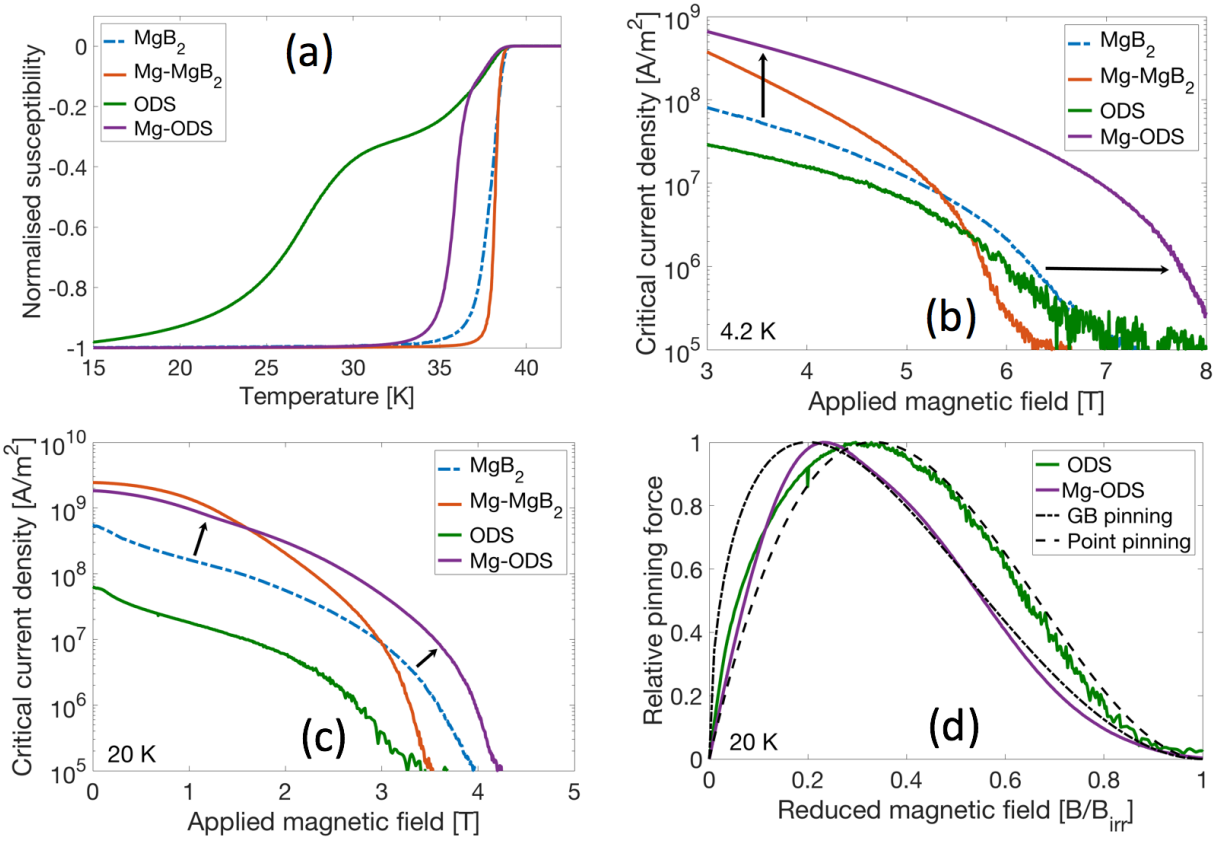

Figure 5.13: Superconducting properties of unmodified MgB_2, Mg-MgB_2, Y_2O_3-MgB_2 and Mg-Y_2O_3-MgB_2 bulk samples sintered at 900 °C by FAST. J_c values were estimated using the macro-scale model.

Sample	T_c [K]	ΔT_c [K]	B_{irr}(4.2 K) [T]	B_{irr}(20 K) [T]	b_{peak}(20 K)	J_c(5 T,4.2 K) [A/m^2]	J_c(0 T,20 K) [A/m^2]
MgB_2	38.2	1.7	6.8	3.8	0.3	1.2×10^7	0.55×10^9
Mg-MgB_2	38.2	0.6	5.4	3.1	0.3	1.8×10^7	2.4×10^9
ODS	27	9.1	6.8	3.4	0.32	6.1×10^6	6.4×10^7
Mg-ODS	35.9	1.4	8	4	0.23	1.3×10^8	1.8×10^9

Table 5.9: Superconducting properties of unmodified MgB_2, Mg-MgB_2, Y_2O_3-MgB_2 and Mg-Y_2O_3-MgB_2 bulk samples sintered by FAST. J_c values were estimated using the macro-scale model.

Figure 5.13 (b) shows that on their own, Mg and Y_2O_3 additions do not perform much better than unmodified MgB_2. In fact, unmodified MgB_2 outperformed the ODS specimen over the entire field range. This is due to the poor connectivity of the ODS sample and its low T_c, reducing drastically J_c. On the other hand, the Mg-MgB_2 specimen showed higher J_c values at low field but did not perform as well as unmodified MgB_2 at high field. However, the combination of both additions in the Mg-ODS composite led to impressive J_c improvements over the entire field range ($3-8$ T) compared to unmodified MgB_2. This suggests that the additions are indeed complementary and work in synergy to provide a true "composite" effect and enhance J_c values both at low and high field (shown by the arrows in Figure 5.13 (b)), which was not possible to achieve in ODS specimens, as discussed in section 4.2.3. The fine MgO and YB_4 particles found in ODS specimens provided additional pinning centres and were responsible for the improvements at high field, whereas Mg additions drastically increased connectivity and thus enhanced J_c at low field. J_c(5 T, 4.2 K) was improved 20 fold by adding 10 wt.% Mg to the ODS specimen.
Figure 5.13 (c) shows that at 20 K, a similar trend was observed. In particular, J_c(0 T, 20 K) almost increased by a factor 30 in the Mg-ODS composite compared to the ODS specimen. The composite also outperformed unmodified MgB_2 over the entire field range. These results suggest that Mg additions are crucial to improve the superconducting properties of ODS MgB_2 sintered at low temperature, and work in synergy with Y_2O_3 to produce high-performance Mg-Y_2O_3-MgB_2 composite bulks.
As expected, the ODS specimen showed a broad pinning force curve with a shape very close to the theoretical point pinning model (section 4.2.3), as shown in Figure 5.13. The Mg-ODS sample showed a different shape with a peak located at $b_{peak} = 0.23$ instead of 0.32 for the ODS specimen. This peak shift to lower reduced field might indicate that the contribution of GB pinning was higher in the Mg-ODS specimen than in the ODS sample. This is consistent with the microstructure observations presented above (Table 5.8). The MgO crystallite size was twice as large in the Mg-ODS specimen, which could lead to less effective point pinning from MgO particles. However, the high J_c(0 T, 20 K) value of the Mg-ODS sample suggests that the composite bulk was well connected and thus anisotropy effects can significantly modify the shape of the curve and the position of its peak (discussed in Chapter 3, pinning force analysis section), which does not allow to draw any firm conclusion.

It was concluded in section 5.2 that Mg-ODS samples showed very similar superconducting properties and connectivity values to unmodified MgB_2 specimens sintered ~ 200 °C higher. In order to investigate if this was also the case for Mg-ODS and ODS specimens, the susceptibility and $J_c - B$ curves at 4.2 K of an ODS specimen processed at 1100 °C and the Mg-ODS composite sintered at 900 °C (both containing 0.5 wt.% Y_2O_3) are compared in Figure 5.14 (a) and (b) respectively. The susceptibility curves of both specimens were almost identical which confirms that Mg additions have a very similar effect to high sintering temperatures on the superconducting properties of ODS bulks. Figure 5.14 (a) shows that the Mg-ODS specimen sintered at 900 °C outperformed the ODS sample processed at 1100 °C over the entire field range, in particular at high field (> 6 T). The composite specimen also showed a larger B_{irr} value of 8 T compared to ~ 7 T for the ODS sample. This suggests that the effect of Mg additions on J_c is similar to an increase in sintering temperature, while also being less detrimental to high field properties.

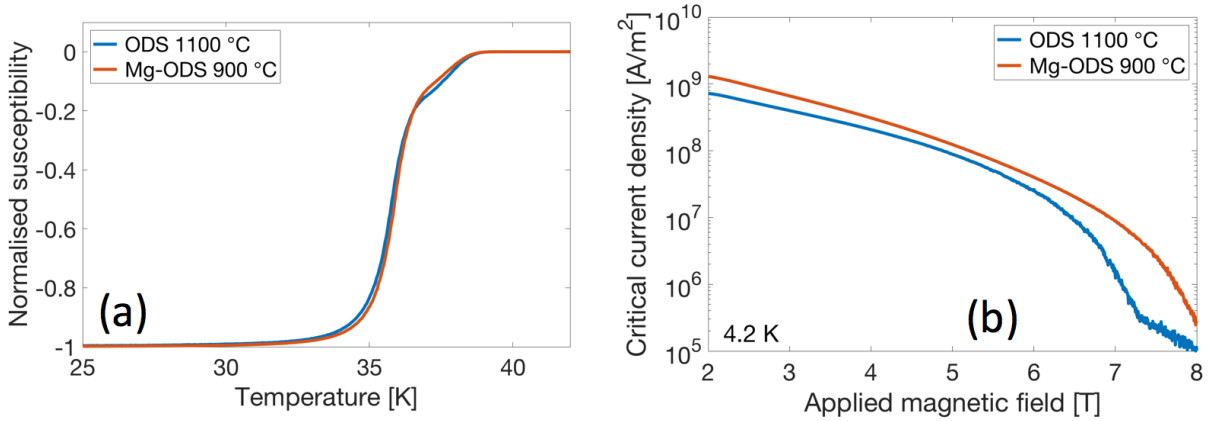

Figure 5.14: Superconducting properties of 0.5 wt.% Y_2O_3-MgB_2 and 10 wt.% Mg - 0.5 wt.% Y_2O_3-MgB_2 samples sintered at 1100 and 900 °C respectively. J_c values were estimated using the macro-scale model.

It was concluded in section 4.2.3 that higher sintering temperatures led to coarsening of MgO and YB_4 particles in ODS bulks, which was associated with a large decrease in J_c at high field, and a significant reduction in B_{irr}.

XRD characterisation of the Mg-ODS and ODS specimens showed that they had almost identical MgO fraction and MgB_2 and MgO crystallite size. One would thus expect similar properties at high field due to the similar fraction and average size of MgO. However, this was not observed and the Mg-ODS composite showed enhanced high field properties compared to the ODS sample. A possible explanation is that, whereas temperature had a similar coarsening effect on both MgO

and YB_4 particles, Mg additions might have only affected MgO precipitates. This seems reasonable since YB_4 particles are extremely stable and do not contain any Mg, unlike MgO. While both specimens had MgO particles of similar size, the Mg-ODS composite probably had finer YB_4 particles due to the "selective" coarsening effect of Mg additions that mostly affected MgO precipitates. This could explain the improvements in high field J_c observed in the composite specimen compared to the ODS sample sintered at higher temperature.

Future work should involve a detailed STEM characterisation of the MgO and YB_4 precipitates and connectivity measurements in order to better understand the subtle differences in microstructure that led to the superior performance of the Mg-ODS composite bulk.

Conclusion

MgB_2 bulk superconductors have been manufactured using unmodified and modified MgB_2 powders containing Y_2O_3 and/or Mg additions. The aim of this work was to investigate if the superconducting properties of MgB_2 could be improved by a combination of innovative processing methods and additions. The modified MgB_2 powders were manufactured by mechanical alloying and/or simple mixing, and the bulk samples were sintered using the Field Assisted Sintering Technique (FAST). The powders and bulks were characterised using a broad range of techniques: X-ray diffraction, density measurements, laser diffraction, scanning electron microscopy, scanning transmission electron microscopy and electrical transport measurements. The superconducting properties of the powders and bulks were also investigated by performing magnetic measurements.

Chapter 3 focussed on the effect of sintering temperature on the microstructure and superconducting properties of unmodified MgB_2 bulks manufactured at $900 - 1200$ °C. XRD and SEM analyses revealed that temperature had no effect on the fraction of MgO in the bulks, whereas the fraction of MgB_4 increased slightly with the processing temperature. As expected, higher sintering temperatures also led to coarsening of MgB_2 and MgO. Temperature also had a significant effect on the density of the bulks, increasing from 68% in the 900 °C sample to 96% in the specimen sintered at 1200 °C. Transport measurements revealed that temperature had a drastic effect on electrical connectivity, improving 6 fold by increasing the sintering temperature from 900 to 1200 °C. Magnetic measurements showed that temperature did not have a significant effect on T_c and B_{irr}. In contrast, J_c values at low field were improved significantly with higher sintering temperatures, in particular J_c(0 T, 20 K) was improved by a factor 6 when increasing the processing temperature from 900 to 1200 °C. This increase exactly matched the improvement in electrical connectivity, suggesting that in unmodified MgB_2 bulks, the main effect of temperature is to improve macroscopic connectivity and thus increase the size of the current loops circulating

in the bulks. Therefore, higher sintering temperatures lead to large improvements in macroscopic J_c, although microstructure characterisation and finer critical current analysis (performed with a more precise model developed in this work) suggested that microscopic (intraparticle) J_c decreased with temperature. Future work on unmodified MgB_2 bulks could involve new processing techniques and/or different sintering parameters, in order to achieve better connectivity and lower impurity content. The best samples only had connectivity values $< 40\%$ and a total impurity content (MgO and MgB_4) exceeding 20 wt.%, suggesting that there is still room for improvement.

In Chapter 4, the concept of Oxide Dispersion Strengthened (ODS) superconductors was investigated. The aim was to develop a new processing route and manufacture ODS MgB_2 bulks containing a dispersion of nano precipitates acting as pinning centres for magnetic vortices, in the same way as they pin dislocations and grain boundaries in ODS superalloys and steels. ODS powders were manufactured by mechanically alloying MgB_2 and nano Y_2O_3 powders for durations between 10 min and 12 h. XRD and STEM analyses suggested that Y_2O_3 particles gradually dissolved (and dissociated as Y and O) in the MgB_2 matrix during the ball milling process. After 12 h of milling, no trace of Y_2O_3 could be detected by STEM and XRD, even in ODS powders containing up to 10 wt.% Y_2O_3. This is consistent with the behaviour commonly observed for ODS superalloys and steels.

ODS MgB_2 bulks were prepared by FAST and three parameters were investigated: milling time, Y_2O_3 fraction and sintering temperature. STEM analysis of the bulks made from the ODS powders milled for 1 and 12 h revealed very different microstructures. The sample milled for only 1 h, mainly showed large YB_4 agglomerates at grain boundaries, whereas the specimen milled for 12 h had a much more homogeneous distribution of fine $(20-60$ nm) YB_4 and MgO precipitates inside MgB_2 grains. STEM, XRD and TKD analyses confirmed that ODS samples contained YB_4 precipitates and did not show any trace of Y_2O_3 after sintering, in contrast with ODS steels where mainly Y_2O_3 is re-precipitated.

Magnetic measurements showed that the $J_c - B$ curves of unmodified MgB_2 and the ODS sample milled for 1 h were almost identical. On the other hand, the ODS specimen milled for 12 h showed significant J_c improvements at high field and larger B_{irr}. These different J_c behaviours can be correlated to the microstructural observations and suggest that the ODS concept can be successfully applied to MgB_2 bulk superconductors providing that a homogenenous dispersion of

nano YB_4 and MgO precipitates can be achieved.

Increasing the fraction of Y_2O_3 led to lower density values, suggesting that Y_2O_3 additions had a detrimental effect on densification. The ODS samples containing 0.2, 0.5 and 2 wt.% Y_2O_3 had relatively similar $J_c - B$ curves with the 0.5 wt.% sample showing the best improvements at high field. As expected, STEM analysis revealed that the 2 wt.% specimen contained higher fractions of YB_4 and MgO particles, mostly located at grain boundaries. The magnetic measurements and STEM observations suggested that J_c improvements were a compromise between increasing the number of nano precipitates and decreasing interparticle connectivity. Increasing fractions of Y_2O_3 also led to a gradual reduction in T_c from 38.7 K in unmodified MgB_2 to 37.2 K in the 2 wt.% sample. This small decrease in T_c was attributed to residual Y and/or O dissolved in the MgB_2 lattice.

The effect of sintering temperature was investigated by manufacturing 0.5 wt.% Y_2O_3 ODS specimens at $950 - 1200$ °C. Higher sintering temperatures had the same effect on the microstructure of ODS samples than that observed for unmodified MgB_2, mainly a significant increase in density and coarsening of MgB_2, MgO and YB_4. In particular, the size of MgO and YB_4 precipitates doubled (~ 20 nm $\rightarrow 40 - 50$ nm) by increasing the sintering temperature from 950 to 1200 °C. The superconducting properties of the ODS bulks were drastically affected by the sintering temperature. T_c increased significantly with the processing temperature from 31.5 to 37.5 K in the specimens processed at 950 and 1200 °C respectively. This was attributed to higher diffusion rates which promoted the recovery of the damaged MgB_2 lattice after mechanical alloying. The ODS samples sintered at low temperature (950 and 1000 °C) showed large improvements in J_c at high field, in particular J_c(4.2 K, 7 T) was increased by two orders of magnitude compared to unmodified MgB_2. This significant improvement probably came from the size of MgO and YB_4 precipitates ($\sim$ 20 nm) which was very close to the diameter of flux vortices in MgB_2 ($2\xi = 8 - 20$ nm), and thus acted as very effective pinning centres. On the other hand, low sintering temperatures were detrimental to J_c at low field, in particular J_c(20 K, 0 T) was one order of magnitude lower in the 950 °C specimen compared to the sample sintered at 1200 °C. This was attributed to poor connectivity in the ODS bulk sintered at low temperature. These results suggest that there exist a compromise between coarsening and increase in connectivity which prevents J_c to be improved both at low and high field. Future work should include a detailed STEM analysis in order to confirm the average size of YB_4 and MgO particles and

investigate their size distribution and location. Electrical transport measurements would also provide quantitative information on the effect of temperature on the connectivity of ODS bulks. In an attempt to overcome this compromise and improve J_c over the entire field range, a 0.5 wt.% Y_2O_3 ODS sample was made by ultra high pressure (UHP) hot pressing at 900 °C and 5.5 GPa (110 times higher than the pressure used in FAST). Although the sample showed numerous macroscopic cracks, the magnetic measurements performed on a small ($\sim$ 2x2x3 mm) specimen showed colossal improvements in J_c and B_{irr}. J_c(4.2 K, 7 T) was 500 times higher in the UHP ODS than unmodified MgB_2 manufactured by FAST, and B_{irr} was also increased from 7 to 12 T. In contrast with the FAST ODS specimen sintered at low temperature, SEM analysis revealed that the UHP ODS sample was fully sintered and did not show any porosity. Ultra high pressure significantly enhanced densification at low sintering temperatures, thus reducing drastically coarsening. Therefore, the UHP process enabled to maintain a very fine microstructure while also improving the connectivity of the bulks, leading to J_c improvements both at low and high field. Future work should explore different processing parameters such as temperature and pressure, and also a suitable cooling step that does not lead to sample cracking.

Chapter 5 focussed on a new processing method that I developed to improve the connectivity of MgB_2 bulks at low sintering temperatures. Mg additions ($1-10$ wt.%) were mixed to pre-synthesised MgB_2 to make composite powders that were sintered at 900 °C by FAST. Mg had a drastic effect on the density of the bulks and their composition. Density increased from 68 to 79% and the fraction of MgB_4 was reduced from 11 to $\sim$ 0 wt.% by adding 10 wt.% Mg to unmodified MgB_2. Pressure and dilatometry data recorded in-situ during the sintering process revealed that Mg additions led to different mechanisms depending on the Mg fraction. For small Mg fractions (1 wt.%) all the Mg evaporated during sintering and generated a positive $Mg_{(g)}$ pressure which modified the dynamic equilibrium of the MgB_2 decomposition reaction causing less MgB_4 to be formed. No liquid phase was formed and thus no increase in density was observed. For intermediate Mg fractions (3 wt.%) some Mg evaporated and MgB_2 decomposition was suppressed. A transient liquid was formed, enhancing densification and reacting with pre-existing MgB_4 to form "fresh" MgB_2. No residual Mg was detected and the density increased compared to unmodified MgB_2. For large Mg fractions (6 and 10 wt.%) more liquid phase was formed and led to further density improvements, and all pre-existing MgB_4 was transformed

into MgB_2. A small amount of residual Mg remained in the bulks after the sintering process. Connectivity was also improved with Mg additions, increasing 4 fold in the 10 wt.% Mg-MgB_2 sample compared to unmodified MgB_2. J_c values at low field were also significantly improved by Mg additions, in particular the 6 and 10 wt.% Mg-MgB_2 specimens showed J_c(20 K, 0 T) values $4-5$ times higher than for unmodified MgB_2. Similar J_c improvements were obtained by sintering unmodified MgB_2 at 1200 °C, suggesting that Mg additions enabled the production of well connected bulks at much lower temperatures. However, J_c values at high field were lower in the 10 wt.% Mg-MgB_2 sample. This was attributed to residual Mg (4 wt.%) acting as an impurity well during the sintering process and thus reducing B_{irr}. It was concluded that Mg additions had the opposite effect of Y_2O_3 on the superconducting properties.

The liquid phase/reactive sintering method developed in this work provides a clever alternative to the conventional ex-situ process by allowing well connected and MgB_4-free bulks to be manufactured at lower temperatures, minimising the detrimental effect of coarsening, improving the production rate and significantly reducing the production costs. Future work should investigate further this innovative processing route by finding the optimal combination of sintering temperature and Mg additions, and also by exploring different parameters such as sintering time.

Since Y_2O_3 and Mg additions had complementary effects on the superconducting properties of MgB_2, the final section looked at the concept of Mg-Y_2O_3-MgB_2 composite bulks to combine both additions in an attempt to enhance J_c both at low and high field. A 10 wt.% Mg-ODS composite and an ODS specimen made from 0.5 wt.% Y_2O_3 ODS powder were sintered at 900 °C by FAST. The composite showed higher density and was free of MgB_4, whereas the ODS sample contained 20 wt.% MgB_4. The superconducting properties were drastically improved by Mg additions with J_c values increasing more than 20 fold over the entire field range. T_c also increased significantly from 27 K in the ODS specimen to 36 K in the Mg-ODS composite. These results suggest that both additions worked in synergy to provide a true composite effect, overcoming the compromise in J_c observed in samples containing only one type of addition. Future work should involve a detailed microstructural characterisation of Mg-ODS composites to understand better the origin of their superior superconducting properties. A careful STEM analysis should be performed to investigate the size and spatial distributions of YB_4 and MgO precipitates. In addition, a parametric study of the Mg-ODS bulks should be undertaken to optimise the superconducting properties of these novel composites. In particular, the fractions of Y_2O_3 and Mg

additions should be adjusted to make the most of their synergy and maximise J_c both at low and high magnetic fields. The sintering temperature and time are also crucial processing parameters that should be investigated to achieve the optimal combination of high connectivity and reduced microstructure coarsening. The liquid phase sintering route developed in this work should also be studied further by capturing the microstructure evolution during the early stages of sintering. This can be done by designing quenching experiments that "freeze" the microstructure of the sample at different stages of a typical sintering cycle. Finally, trapped field measurements should be performed on large disc-shaped specimens having different diameters and aspect ratios. Experimental trapped field values should then be compared with theoretical values calculated from the microscopic properties measured in this work by conducting modelling experiments. This analysis should provide insight into the macroscopic connectivity of large-scale specimens, and help us to refine further the processing parameters leading to the production of high-performance bulk superconducting magnets.

In conclusion, innovative ODS microstructures can be engineered in MgB_2, and further improved by using the liquid phase/reactive sintering route developed in this work, producing Mg-ODS composites that significantly outperform conventional MgB_2.

Bibliography

[1] J. Nagamatsu, N. Nakagawa, T. Muranaka *et al.* Superconductivity at 39 K in magnesium diboride. *Nature*, 410:63–64, 2001.

[2] J.S. Benjamin. Dispersion strengthened superalloys by mechanical alloying. *Metallurgical Transactions*, 1(10):2943–2951, 1970.

[3] J.S. Benjamin and P.S. Gilman. Mechanical Alloying. *Annual Review of Materials Science*, 13:279–300, 1983.

[4] R.L. Klueh, J.P. Shingledecker, R.W. Swindeman *et al.* Oxide dispersion-strengthened steels: A comparison of some commercial and experimental alloys. 341:103–114, 2005.

[5] L. Zhang, S. Ukai, T. Hoshino *et al.* Y_2O_3 evolution and dispersion refinement in Co-base ODS alloys. *Acta Materialia*, 57(12):3671–3682, 2009.

[6] H. Zhang, M.J. Gorley, K. Chong *et al.* An in-situ powder neutron diffraction study of nano-precipitate formation during processing of oxide-dispersion-strengthened ferritic steels. *Journal of Alloys and Compounds*, 582:769–773, 2014.

[7] L. Dai, Y. Liu and Z. Dong. Size and structure evolution of yttria in ODS ferritic alloy powder during mechanical milling and subsequent annealing. *Powder Technology*, 217:281–287, 2012.

[8] Q. Zhao, L. Yu, Y. Liu *et al.* Morphology and structure evolution of Y_2O_3 nanoparticles in ODS steel powders during mechanical alloying and annealing. *Advanced Powder Technology*, 26(6):1578–1582, 2015.

[9] P. Mangin and R. Kahn. *Superconductivity: An introduction.* 2017.

[10] W. Meissner and R. Ochsenfeld. Ein neuer Effekt bei Eintritt der Supraleitfähigkeit. *Naturwissenschaften*, 21(44):787–788, 1933.

[11] H. London and F. London. The Electromagnetic Equations of the Supraconductor. *Proceedings of the Royal Society A*, 149:71–88, 1934.

[12] S. Speller. Superconducting Materials, 2018.

[13] V.L. Ginzburg and L.D. Landau. On the theory of superconductivity. *Zh. Eksp. Teor. Fiz.*, 20:1064–1082, 1950.

[14] L. Piraux. PHY2273: Superconductivity. 2014.

[15] D. Dew-Hughes. Flux pinning mechanisms in type II superconductors. *Philosophical Magazine*, 30(2):293–305, 1974.

[16] C.P. Bean. Magnetization of hard superconductors. *Physical review letters*, 8(6):250–253, 1962.

[17] J. Bardeen, L.N. Cooper and J.R. Schrieffer. Theory of Superconductivity. *Phys. Rev.*, 108(5):1175–1204, 1957.

[18] H. Fröhlich. Theory of the Superconducting State. I. The Ground State at the Absolute Zero of Temperature. *Phys. Rev.*, 79(5):845–856, 1950.

[19] L.N. Cooper. Bound Electron Pairs in a Degenerate Fermi Gas. *Phys. Rev.*, 104(4):1189–1190, 1956.

[20] J.H. Durrell, A.R. Dennis, J. Jaroszynski *et al.* A trapped field of 17.6 T in melt-processed, bulk Gd-Ba-Cu-O reinforced with shrink-fit steel. *Superconductor Science and Technology*, 27(8):82001, 2014.

[21] M. Ainslie and H. Fujishiro. *Fundamentals of bulk superconducting materials*. 2019.

[22] T.C. Cosmus and M. Parizh. Advances in whole-body MRI magnets. *IEEE Transactions on Applied Superconductivity*, 21(3):2104–2109, 2011.

[23] B.D. Josephson. Possible new effects in superconductive tunnelling. *Physics Letters*, 1(7):251–253, 1962.

[24] C. Buzea and T. Yamashita. Review of superconducting properties of MgB_2. *Superconductor Science and Technology*, 14(11):115–146, 2001.

[25] Y. Takano, H. Takeya, H. Fujii *et al.* Superconducting properties of MgB_2 bulk materials prepared by high-pressure sintering. *Applied Physics Letters*, 78(19):2914–2916, 2001.

[26] Z. Liu, D.G. Schlom, Q. Li *et al.* Thermodynamics of the Mg–B system: Implications for the deposition of MgB_2 thin films. *Applied Physics Letters*, 78(23):3678, 2001.

[27] G. Balducci, S. Brutti, A. Ciccioli *et al.* Thermodynamics of the intermediate phases in the Mg–B system. *Journal of Physics and Chemistry of Solids*, 66:292–297, 2005.

[28] Y. Guo, W. Zhang, D. Yang *et al.* Decomposition and oxidation of magnesium diboride. *Journal of the American Ceramic Society*, 95(2):754–759, 2012.

[29] C.E.J. Dancer, P. Mikheenko, A. Bevan *et al.* A study of the sintering behaviour of magnesium diboride. *Journal of the European Ceramic Society*, 29(9):1817–1824, 2009.

[30] W. Häßler, J. Scheiter, P. Hädrich *et al.* Properties of ex-situ MgB_2 bulk samples prepared by uniaxial hot pressing and spark plasma sintering. *Physica C: Superconductivity and its Applications*, 551:48–54, 2018.

[31] G. Aldica, S. Popa, M. Enculescu *et al.* Dwell Time Influence on Spark Plasma Sintered MgB_2. *Journal of Superconductivity and Novel Magnetism*, 31(2):317–325, 2018.

[32] A. Kario, R. Nast, W. Häler *et al.* Critical current density enhancement in strongly reactive ex-situ MgB_2 bulk and tapes prepared by high energy milling. *Superconductor Science and Technology*, 24(7):075011, 2011.

[33] S. Lee, T. Masui, A. Yamamoto *et al.* Carbon-substituted MgB_2 single crystals. *Physica C*, 397(1-2):7–13, 2003.

[34] H. Fujii, A. Iwanade, S. Kawada *et al.* The reduction of optimal heat treatment temperature and critical current density enhancement of ex-situ processed MgB_2 tapes using ball milled filling powder. *Cryogenics*, 89:76–84, 2018.

[35] J.H. Kim, S. Oh, Y. Heo *et al.* Microscopic role of carbon on MgB_2 wire for critical current density comparable to NbTi. *Nature*, 4(1), 2012.

[36] D. Batalu, G. Aldica, S. Popa *et al.* GeO_2 added MgB_2 superconductor obtained by Spark Plasma Sintering. *Solid State Sciences*, 48:23–30, 2015.

[37] G.A.B. Matthews, C.R.M. Grovenor, P.S. Grant and S.C. Speller. Effect of the sintering temperature on the microstructure and superconducting properties of MgB_2 bulks manufactured by the field assisted sintering technique. *Superconductor Science and Technology*, 33(5):054003, 2020.

[38] A.V. Pan, S. Zhou, H. Liu *et al.* Properties of superconducting MgB_2 wires: In-situ versus ex-situ reaction technique. *Superconductor Science and Technology*, 16(5):639–644, 2003.

[39] C.E.J Dancer, D. Prabhakaran, M. Başoğlu *et al.* Fabrication and properties of dense ex-situ magnesium diboride bulk material synthesized using spark plasma sintering. *Superconductor Science and Technology*, 22(9):095003, 2009.

[40] A.G. Bhagurkar, A. Yamamoto, A.R. Dennis *et al.* Microstructural evolution in infiltration-growth processed MgB_2 bulk superconductors. *Journal of the American Ceramic Society*, 100(6):2451–2460, 2017.

[41] A. Yamamoto, H. Tanaka, J. Shimoyama *et al.* Towards the Realization of Higher Connectivity in MgB_2 Conductors: In-situ or Sintered Ex-situ? *Japanese Journal of Applied Physics*, 51(1):010105, 2012.

[42] S. Lee, S. Yoo, Y. Kim *et al.* Preparation of Dense MgB_2 Bulk Superconductors by Spark Plasma Sintering. *Journal of the American Ceramic Society*, 86(10):1800–1802, 2003.

[43] S. Shim, K. Shim and J. Yoon. Superconducting characteristics of polycrystalline magnesium diboride ceramics fabricated by a spark plasma sintering technique. *Journal of the American Ceramic Society*, 88(4):858–861, 2005.

[44] G. Aldica, M. Burdusel, S. Popa *et al.* The influence of heating rate on superconducting characteristics of MgB_2 obtained by spark plasma sintering technique. *Physica C: Superconductivity and its Applications*, 519:184–189, 2015.

[45] P.J. Jacques. LMAPR2672: Matériaux frittés et traitements de surface, 2015.

[46] O. Guillon, J. Gonzalez-Julian, B. Dargatz *et al.* Field-Assisted Sintering Technology/Spark Plasma Sintering: Mechanisms, Materials, and Technology Developments. *Advanced Engineering Materials*, 16(7):830–849, 2014.

[47] Z.A. Munir, U. Anselmi-Tamburini and M. Ohyanagi. The effect of electric field and pressure on the synthesis and consolidation of materials: A review of the spark plasma sintering method. *Journal of Materials Science*, 41(3):763–777, 2006.

[48] J.P. Kelly and O.A. Graeve. Spark Plasma Sintering as an Approach to Manufacture Bulk Materials: Feasibility and Cost Savings. *JOM*, 67(1):29–33, 2015.

[49] T. Nishimura, X. Xu, K. Kimoto *et al.* Fabrication of silicon nitride nanoceramics-powder preparation and sintering: A review. *Science and Technology of Advanced Materials*, 8(7-8):635–643, 2007.

[50] Z. Shen, M. Johnsson, Z. Zhao *et al.* Spark Plasma Sintering of Alumina. *Journal of the American Ceramic Society*, 85(8):1921–1927, 2002.

[51] Y. Zhou, K. Hirao, Y. Yamauchi *et al.* Densification and grain growth in pulse electric current sintering of alumina. *Journal of the European Ceramic Society*, 24(12):3465–3470, 2004.

[52] B. McWilliams and A. Zavaliangos. Multi-phenomena simulation of electric field assisted sintering. *Journal of Materials Science*, 43(14):5031–5035, 2008.

[53] B. McWilliams, J. Yu and A. Zavaliangos. Fully coupled thermal–electric-sintering simulation of electric field assisted sintering of net-shape compacts. *Journal of Materials Science*, 50(2):519–530, 2014.

[54] E. Olevsky and L. Froyen. Constitutive modeling of spark plasma sintering of conductive materials. *Scripta Materialia*, 55(12):1175–1178.

[55] A.M. Locci, R. Orrù, G. Cao *et al.* Synthesis of bulk MgB_2 superconductors by pulsed electric current. *American institute of chemical engineers*, 52(7):2618–2626, 2006.

[56] G. Aldica, D. Batalu, S. Popa *et al.* Spark plasma sintering of MgB_2 in the two-temperature route. *Physica C: Superconductivity*, 477:43–50, 2012.

[57] J. Schmidt, W. Schnelle, Y. Grin *et al.* Pulse plasma synthesis and chemical bonding in magnesium diboride. *Solid State Sciences*, 5(4):535–539, 2003.

[58] S.M. Kazakov, R. Puzniak and A.V. Mironov. Single crystal growth and properties of MgB_2 and $Mg(B_{1-x}C_x)_2$. *Physica C*, 410:123–124, 2004.

[59] R.H.T. Wilke, S.L. Bud, P.C. Canfield *et al.* Systematic Effects of Carbon Doping on the Superconducting Properties of $Mg(B_{1-x}C_x)_2$. *Physical review letters*, 92(21):2–5, 2004.

[60] R.A. Ribeiro, S.L. Bud, C. Petrovic *et al.* Effects of boron purity, Mg stoichiometry and carbon substitution on properties of polycrystalline MgB_2. *Physica C*, 385:16–23, 2003.

[61] A. Yamamoto, J. Shimoyama, S. Ueda *et al.* Effects of B_4C doping on critical current properties of MgB_2 superconductor. *Superconductor Science and Technology*, 18(10):1323–1328, 2005.

[62] S.R. Ghorbani, G. Farshidnia, X.L. Wang *et al.* Flux pinning mechanism in SiC and nano-C doped MgB_2: evidence for transformation from δT_c to δl pinning. *Superconductor Science and Technology*, 27(12):125003, 2014.

[63] G. Aldica, M. Burdusel, S. Popa *et al.* Graphene addition to MgB_2 superconductor obtained by ex-situ spark plasma sintering technique. *Materials Research Bulletin*, 77:205–211, 2016.

[64] M. Burdusel, G. Aldica, S. Popa *et al.* B_4C in ex-situ spark plasma sintered MgB_2. *Current Applied Physics*, 15:1262–1270, 2015.

[65] S. Deemyad, T. Tomita, J.J. Hamlin *et al.* Dependence of the superconducting transition temperature of single and polycrystalline MgB_2 on hydrostatic pressure. *Physica C*, 385:105–116, 2003.

[66] G. Aldica, S. Popa, M. Enculescu *et al.* Enhancement of critical current density and irreversibility field by Te or TeO_2 addition to MgB_2 bulk processed by spark plasma sintering. *Scripta Materialia*, 66:570–573, 2012.

[67] M. Burdusel, G. Aldica, S. Popa *et al.* MgB_2 with addition of Bi_2O_3 obtained by spark plasma sintering technique. *Journal of Superconductivity and Novel Magnetism*, 26(5):1553–1556, 2013.

[68] G. Aldica, S. Popa, M. Enculescu *et al.* Addition of Ho_2O_3 of different types to MgB_2 in the ex-situ Spark Plasma Sintering: Simultaneous control of the critical current density at low and high magnetic fields. *Materials Chemistry and Physics*, 146(3):313–323, 2014.

[69] J. Wang, Y. Bugoslavsky, A. Berenov *et al.* High critical current density and improved irreversibility field in bulk MgB_2 made by a scalable, nanoparticle addition route. *Applied Physics Letters*, 81, 2002.

[70] Q. Cai, Y. Liu, Z. Ma *et al.* Superconducting properties of Y_2O_3/SiC co-doped bulk MgB_2. *Journal of Superconductivity and Novel Magnetism*, 25:357–361, 2012.

[71] G.J. Xu, J.C. Grivel, A.B. Abrahamsen *et al.* Enhancement of the irreversibility field in bulk MgB_2 by TiO_2 nanoparticle addition. *Physica C*, 406(1-2):95–99, 2004.

[72] M. Muralidhar, K. Inoue, M.R. Koblischka *et al.* Effects of Silver Addition on Critical Current Densities and Mechanical Properties in Bulk MgB_2. *Advanced Engineering Materials*, 17(6):831–838, 2015.

[73] Y. Sun, L. Zhu, X. Song *et al.* Superconducting Properties and Microstructure of Nanocrystalline MgB_2 Bulk Prepared by Sintering of Ball Milled Powders. *Journal of Superconductivity and Novel Magnetism*, 25:1735–1741, 2012.

[74] D. Rodrigues, B.J. Senkowicz, J.M. Hanson *et al.* Preparation and characterization of MgB_2 bulk samples using high-energy ball milling and hot isostatic pressing. *AIP Conference Proceedings*, 986:359–366, 2008.

[75] T. Naito, Y. Endo, and H. Fujishiro. Optimization of vortex pinning at grain boundaries on ex-situ MgB_2 bulks synthesized by spark plasma sintering. *Superconductor Science and Technology*, 30(9):095007, 2017.

[76] H. Fujii, A. Ishitoya, S. Itoh *et al.* Improved critical current density in ex-situ processed MgB_2 tapes by the size reduction of grains and crystallites by high-energy ball milling. *Cryogenics*, 82:15–24, 2017.

[77] J. Hill and J. Howard. Quantitative Phase Analysis from Neutron Powder Diffraction Data Using the Rietveld Method. *Journal of Applied Crystallography*, 20:467–474, 1987.

[78] H.G. Scott. The Estimation of Standard Deviations in Powder Diffraction Rietveld Refinements. *Journal of Applied Crystallography*, 16:159–163, 1983.

[79] D. Schwarzenbach and S.C. Abrahams. Statistical Descriptors in Crystallography. *Acta Crystallographica*, 45:63–75, 1989.

[80] B.H. Toby. R factors in Rietveld analysis: How good is good enough? *Powder Diffraction*, 21(1):67–70, 2006.

[81] J.J. Friel. *Practical Guide to Image Analysis.* ASM International, 2000.

[82] G. Wang, M.J. Raine, and D.P. Hampshire. The cause of 'weak-link' grain boundary behaviour in polycrystalline $Bi_2Sr_2CaCu_2O_8$ and $Bi_2Sr_2Ca_2Cu_3O_{10}$ superconductors. *Superconductor Science and Technology*, 31(2):024001, 2018.

[83] E. Martínez, P. Mikheenko, A. Millán *et al.* Flux pinning force in bulk MgB_2 with variable grain size. *Physical Review B*, 75:1–8, 2007.

[84] I.A. Golovchanskiy, A.V. Pan, and J. George *et al.* Vibration effect on magnetization and critical current density of superconductors. *Superconductor Science and Technology*, 29(7):075002, 2016.

[85] E.W. Collings, M.D. Sumption, M. Bhatia *et al.* Prospects for improving the intrinsic and extrinsic properties of magnesium diboride superconducting strands. *Superconductor Science and Technology*, 21(10):103001, 2008.

[86] A. Yamamoto, J. Shimoyama, K. Kishio *et al.* Limiting factors of normal-state conductivity in superconducting MgB_2: an application of mean-field theory for a site. *Superconductor Science and Technology*, 20:658–666, 2007.

[87] Y. Eltsev, S. Lee, K. Nakao *et al.* Anisotropic superconducting properties of MgB_2 single crystals probed by in-plane electrical transport measurements. *Physical Review B*, 65(14):140501, 2002.

[88] M. Eisterer. Magnetic properties and critical currents of MgB_2. *Superconductor Science and Technology*, 20:47–73, 2007.

[89] P.W. Anderson. Theory of dirty superconductors. *Journal of Physics and Chemistry of Solids*, 11:26–30, 1959.

[90] D.C. Larbalestier, L.D. Cooley, M.O. Rikel *et al.* Strongly linked current flow in polycrystalline forms of the superconductor MgB_2. *Letters to nature*, 410:186–189, 2001.

[91] D.A. Cardwell, N.H. Babu, M. Kambara *et al.* Magnetic properties and critical currents of bulk MgB_2 polycrystalline superconductor. *Physica C*, 372:1262–1265, 2002.

[92] E.J. Kramer. Scaling laws for flux pinning in hard superconductors. *Journal of Applied Physics*, 44(3):1360–1370, 1973.

[93] R. Labusch. Elasticity Effects in Type-II Superconductors. *Physical Review*, 170(2), 1968.

[94] D. Hampshire, H. Jones and E. Mitchell An in depth characterization of $(NbTa)_3Sn$ filamentary superconductor. *IEEE Transactions on Magnetics*, 21(2):289–292, 1985.

[95] E.H. Brandt. Elastic and plastic properties of the flux-line lattice in type-II superconductors. *Phys. Rev. B*, 34(9):6514–6517, 1986.

[96] G.A.B. Matthews, C.R.M. Grovenor, P.S. Grant and S.C. Speller. Design and characterisation of ex-situ bulk MgB_2 superconductors containing a nanoscale dispersion of artificial pinning centres. *Superconductor Science and Technology*, 33(3):034006, 2020.

[97] R. Bjørk and C.R.H. Bahl. Demagnetization factor for a powder of randomly packed spherical particles. *Applied Physics Letters*, 103(10), 2013.

[98] A.M. Campbell, F.J. Blunt, J.D. Johnson *et al.* Quantitative determination of percentage superconductor in a new compound. *Cryogenics*, 31(8):732–737, 1991.

[99] T. Gupta. Sintering of MgO: Densification and Grain Growth. *Journal of Materials Science*, 6:25–32, 1971.

[100] J.A. Zaykoski, M.M. Opeka, L.H. Smith *et al.* Synthesis and Characterization of YB_4 Ceramics. *Journal of the American Ceramic Society*, 94(11):4059–4065, 2011.

[101] P. Mikheenko, S.K. Chen and J.L. MacManus-Driscoll. Minute pinning and doping additions for strong, 20 K, in-field critical current improvement in MgB_2. *Applied Physics Letters*, 91:1–4, 2007.

[102] A.L. Micheli, D.F. Dungan and J.V. Mantese. High-Density Yttria for Practical Ceramic Applications. *Journal of the American Ceramic Society*, 75(3):709–711, 1992.

[103] C. Zener. *Trans. Met. Soc. AIME*, 175:15, 1948.

[104] E. Nes, N. Ryum and O. Hunderi. On the Zener drag. *Acta Materialia*, 33(1):11–22, 1985.

[105] T. Nishizawa, I. Ohnuma and K. Ishida. Examination of the Zener Relationship between Grain Size and Particle Dispersion. *Materials Transactions, JIM*, 38(11):950–956, 1997.

[106] H. Katzman and W.F. Libby. Sintered Diamond Compacts with a Cobalt Binder. *Science*, 172:1132–1134, 1971.

[107] H. Zhao and Y. Cheng. Formation of TiB_2-TiC composites by reactive sintering. *Ceramics International*, 25:353–358, 1999.

[108] R.M. German, P. Suri and S.J. Park. Review: liquid phase sintering. *Journal of Materials Science*, 44:1–39, 2009.

[109] J. García, V. Ciprés, A. Blomqvist *et al.* Cemented carbide microstructures: a review. *International Journal of Refractory Metals and Hard Materials*, 80:40–68, 2019.

[110] L.K.L. Falk. Imaging and microanalysis of liquid phase sintered silicon-based ceramic microstructures. *Journal of Materials Science*, 39:6655–6673, 2004.